ADVANCED GEOMETRIES FOR DRYOUT MITIGATION IN TEMHD-DRIVEN LIQUID LITHIUM SYSTEMS

BY

MATTHEW MICHAEL SZOTT

DISSERTATION

Submitted in partial fulfillment of the requirements
for the degree of Doctor of Philosophy in Nuclear, Plasma, and Radiological Engineering
in the Graduate College of the
University of Illinois at Urbana-Champaign, 2020

Urbana, Illinois

Doctoral Committee:

Professor David N. Ruzic, Chair
Adjunct Professor Jean Paul Allain
Research Assistant Professor Daniel Andruczyk
Professor Shiv Kapoor
Assistant Professor Mariana Kersh

ABSTRACT

The promise of nuclear fusion as an energy source is unparalleled, but the technological challenge is arguably the most difficult humanity has faced. As progress continues toward bringing sustained fusion power production to the grid, the conditions inside fusion devices are becoming more extreme. A common method of producing sustained fusion reactions is by heating isotopes of hydrogen until they are a plasma and confining them magnetically in a toroidal vacuum system. High plasma density, long confinement time, and extremely high plasma temperatures must be achieved in order to create efficient fusion. Plasma facing components (PFCs) must bear the brunt of these extreme conditions, which can result in a myriad of damage mechanisms on even the most resilient materials.

One method of mitigating the damage in solid PFCs is through the use of liquid metals, specifically liquid lithium. Liquid lithium PFCs reduce erosion and thermal stress damage, prolonging device lifetime, and have been shown to enhance plasma performance, decrease edge recycling, and reduce impurities. Flowing open surface liquid metal concepts utilize flowing liquid lithium to provide a constantly refreshing PFC surface and can remove impurities from the device, though potential concerns include surface stability, wetting control, hydrogen retention, and heat flux handling.

The Liquid Metal Infused Trench (LiMIT) concept pioneered at the University of Illinois harnesses the heat and magnetic fields already present in fusion devices to drive lithium flow via thermoelectric magnetohydrodynamics (TEMHD). Proof of concept testing at the Center for Plasma Material Interactions and larger scale testing in the HT-7 and EAST tokamaks and the Magnum PSI linear plasma device have shown sustained flow and improved plasma performance. Continued development of the system has focused on mitigating potential concerns, including defining stability criteria, enhancing ability to control lithium wetting and flow, and designing systems to recover the hydrogenic fuel species from lithium.

Under high localized heat fluxes present in fusion devices, TEMHD forces can cause a depression of the lithium surface below the solid structures, minimizing the benefits of the flowing liquid system and risking damage. This is known as the lithium dryout phenomenon. This work adapts the standard LiMIT trench design to improve heat flux handling and eliminate the presence

of lithium dryout on the free surface. Improvements to the design focus on extending the 1-D trench design to 2-D and 3-D flow channels, which result in post and foam structures. Using extensive COMSOL Multiphysics modeling and experimental testing, the propensity for TEMHD flow and the resistance to dryout in the face of high localized heat flux is investigated.

The 3 post TEMHD designs exhibit effective TEMHD drive with maximum velocities on the order of 0.2 to 0.9 m/s, depending on the geometry and the peak heat flux applied. The addition of secondary flow channels improves dryout resistance, though swirling flow and eddies develop around the posts. Experimental testing verifies the usefulness of the crosstalk to distribute flow, and velocities match numerical modeling of the system.

A disordered foam geometry and 3 ordered foam geometries are tested as concepts to improve capillary action and surface stability while still allowing TEMHD flow. While the internal structure of the disordered foam as manufactured did not prove compatible with liquid lithium, a new pipeline was developed to incorporate arbitrary geometries into TEMHD modeling. The ordered designs exhibit sustained TEMHD flow of slower maximum magnitude than the post geometries, between 0.05 and 0.35 m/s. This reduction in flow speed comes with improved resistance to dryout. Experimental testing of proof of concept cases showed velocities that matched numerical modeling. Electron beam testing of the foam proves heat flux handling capabilities of the designs and increases the operating regime of the LiMIT system by 127%, to 6.8 MW/m^2, with no signs of dryout or impending damage.

New capabilities of multiphysics modeling of the TEMHD systems were developed to capture the motion of the free surface. Using a level set multiphase model, TEMHD flow under low heat flux proof of concept conditions was replicated. Applying a high heat flux stripe to the free surface resulted in lithium dryout and pileup in the trench domain, which was reduced in the post and foam designs. The inclusion of surface tension in the model steadies the free surface against dryout. Surface tension values near that of liquid lithium, up to 0.3 N/m, were applied. The surface tension simulations displayed successful elimination of dryout in a 3 MW/m^2 peak heat flux scenario, but the large surface forces induced spurious wave motion in the free surface.

ACKNOWLEDGEMENTS

It is truly shocking how many people have helped me along the path toward this degree. I would love to acknowledge some of them here.

My parents Brian and Kathy and aunt Susan sparked an insatiable curiosity and wonder about the world around me and have always been there to help me along the way. My sister Emily's reminders to 'hide my stupidity' got me this far. The support and encouragement from my grandparents and other extended family has always been very appreciated. My girlfriend Lindsey has given me the strength and motivation to finish this degree, and her love and unceasing encouragement has really kept me going. I could not have done this without you. To all above, and to all my friends who have always been there for hanging out and/or amusing shenanigans, I thank you from the bottom of my heart. I love you all.

I would like to thank my advisor, David Ruzic, for leading me through my college career and shaping me as a researcher in both undergrad and graduate studies. Your intuition and belief in the future of fusion have been instrumental in guiding this work. I also thank J.P. Allain, Daniel Andruczyk, Shiv Kapoor, and Mariana Kersh for being a part of my doctoral committee. Your input has guided my research and made it better.

I really appreciate the help of all undergraduate and graduate researchers who have worked with me throughout the years. To my fellow grad students, both past and present, thank you. The friendships made will be treasured, and this work could not have been completed without your help and valuable discussions. Whether it was all-nighters to prepare for a conference, sipping beer at a bar (probably Legends), or chugging the 6^{th} coffee of the day, it has been a wild ride. Thanks for sharing the journey with me.

Thank you to all the professors and staff of the NPRE department. You have taught me so much and helped me through my college career. Without the departmental machine shops, especially ECE, our visions of experimental contraptions could never become reality. Thanks to the Beckman Institute Visualization Laboratory for imaging equipment and simulation capabilities. To the DOE and commercial fusion companies who have funded these studies, thanks for being willing to experiment with lithium technologies and opening doors to practical application, so we can continue the goal of bringing fusion power to the world.

TABLE OF CONTENTS

LIST OF FIGURES

LIST OF ABBREVIATIONS

ALPS – Advanced Limiter-divertor Plasma-facing Systems
APEX – Advanced Power Extraction
CAD – Computer-aided design
CDX-U – Current Drive Experiment-Upgrade
CFD – Computational fluid dynamics
CPMI – Center for Plasma Material Interactions
CPS – Capillary porous structures
CVD – Chemical Vapor Deposition
D-D – Deuterium-deuterium
DEMO – Demonstration power plant
DEVEX – Divertor Edge and Vapor Shielding Experiment/
DIII-D – Doublet III, D-shape tokamak
DMLS – Direct metal laser sintering
D-T – Deuterium-tritium
D_α – Deuterium alpha
EAST – Experimental Advanced Superconducting Tokamak
e-beam – Electron beam
EC – Electric currents
EDM – Electronic discharge machining
ELM – Edge localized mode
EM – Electromagnetic
Emf – Electromotive force
FLiLi – Flowing liquid lithium limiter
FLIT – Flowing Liquid Torus
FTU – Frascati Tokamak Upgrade
HT – Heat transfer
HT-7 – Hefei Tokamak-7
IFMIF – International Fusion Materials Irradiation Facility
IR – Infrared
ITER – International Thermonuclear Experimental Reactor
JET – Joint European Torus
LCFS – Last closed flux surface
LF – Laminar flow
Li – Lithium
LiH – Lithium hydride
LiMIT – Liquid Metal Infused Trenches
LIPES – Lithium and Plasma Evaluation System
LS – Level set

LSVOF – Coupled level set volume of fluid
LTX – Lithium Tokamak Experiment
MAST – Mega Ampere Spherical Tokamak
MCATS – Materials Characterization Test Stand
MHD – Magnetohydrodynamics
MM – Moving mesh
NiCr – Nickel-chromium
NSTX/NSTX-U – National Spherical Torus Experiment Upgrade
PECVD – Plasma enhanced chemical vapor deposition
PFC – Plasma facing component
PIV – Particle image velocimetry
PMI – Plasma material interactions
Ppi – Pores per inch
PPPL – Princeton Plasma Physics Laboratory
SiC – Silicon carbide
SLiDE – Solid-Liquid Lithium Divertor Experiment
Sn – Tin
SnLi – Tin-lithium
SOL – Scrape off layer
TELS – Thermoelectric-Driven Liquid-Metal Plasma-Facing Structures
TEMHD – Thermoelectric magnetohydrodynamics
TFTR – Tokamak Fusion Test Reactor
UIUC – University of Illinois at Urbana-Champaign
VCR – vacuum coupling radiation
Z – Atomic number
Z_{eff} – Effective atomic number

CHAPTER 1 – INTRODUCTION

1.1 Fusion Power

As humans continue reaching forward in this age of technology, the accelerating speed of advancement requires ever more power. On a large scale, human productivity and standard of living tends to be highly linked to power consumption. For generations, fossil fuels such as coal, oil, and natural gas have satisfied this need. However, constant pollution through combustion of these fuels threatens the constant improvement of quality of life, so methods of producing large amounts of power without the harmful side effect of destroying the planet are needed. Arguably the most effective way to generate large amounts of baseload, (essentially) zero-carbon energy is through nuclear power. Nuclear fission, the splitting of heavy atomic nuclei to produce energy, was quickly realized as a viable power source after the world careened into the atomic age during WWII. For decades, nuclear fission power plants have produced high levels of power with minimal downtime and an impressive safety record. Unfortunately, truly widespread global adoption has been hindered by concerns about storing highly radioactive nuclear waste, as well as public fear of accidents and radiation.

Long hailed as the holy grail of energy generation, the successful harnessing of fusion power stands to be one of the greatest achievements in the history of humanity. This zero-emission power source promises low levels of (and eventually no) radioactive byproducts, high efficiency, and nearly unlimited fuel in the form of deuterium, found naturally in water. There is also no risk for nuclear accidents, as the reaction cannot runaway. Nuclear fusion entails smashing light atomic nuclei together to create heavier byproducts. The mass difference between reactants and products is released as byproduct energy. In order to create a fusion event, the repulsive Coulomb force between atomic nuclei must be overcome by providing the fuel species with large amounts of energy. If this can be accomplished, the payoff is enormous. While there are several pathways fusion reactions, the deuterium-tritium (D-T) and deuterium-deuterium (D-D) reactions are favored as they have the highest likelihood of fusion at the lowest energies. The D-T reaction is shown below.

$$ {}_{1}^{2}D + {}_{1}^{3}T \rightarrow {}_{2}^{4}He(3.5\ MeV) + n^{0}(14.1\ MeV) $$

Here the deuterium (D) and tritium (T) fuse to create a helium nucleus (He, also known as an alpha particle) and a neutron (n), which have a combined energy of 17.6 MeV. When converted from energy release per reaction to energy released per mass, the potential for nuclear fusion becomes more apparent. The 3.38×10^{8} MJ/kg released by the D-T reaction is over 8 million times higher than that of gasoline (40 MJ/kg) and even over 4 times that of nuclear fission (7.9×10^{7} MJ/kg) [1]!

Unfortunately, exorbitantly high temperatures are required to initiate and sustain fusion reactions, and the development of fusion power has progressed for over half a century without creating controlled net power output, to the dismay of many proponents of the technology. Likened to trapping the sun on Earth, the challenges associated with fusion power development are plentiful. At the temperatures required to increase the reaction cross section enough to make fusion viable, gases become ionized plasmas. Over time, huge strides have been made in the areas of plasma and nuclear physics, reaching ever closer to this coveted goal.

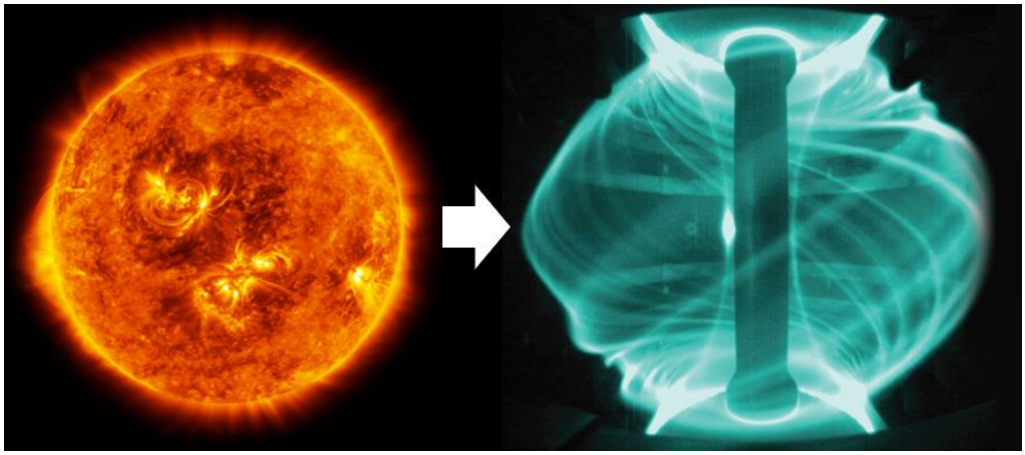

Figure 1.1 – The sun is proof that fusion power works. The challenge is bringing this process to Earth. Common fusion devices confine hot plasma in a toroidal geometry, as seen in the MAST device on the right [2].

In describing the energy balance in a hot fusion plasma, the Lawson criterion was developed to describe how energy relates to the temperature, density, and confinement time of fuel components [3]. A close corollary became known as the "triple product", a multiplicative metric that any concept of fusion power production must achieve in order to produce net energy. For self-sustaining deuterium-tritium fusion, the easiest fusion reaction to achieve, this is given by

$$nT\tau_E \geq 5 \times 10^{21} \ \frac{keV\ s}{m^3}$$

Where n is the electron density (due to quasi-neutrality in a fusion plasma, electron and ion densities are assumed equal ($n = n_e = n_i$), T is the plasma temperature, and τ_E is the confinement time. Above the value given, the fusion energy released will exceed the power required to heat and confine the fuel. While many methods of creating and containing plasmas have been proposed, the most noteworthy can be grouped into 2 main categories: inertial confinement fusion and magnetic confinement fusion.

Inertial confinement fusion typically utilizes laser beams to impact a small fuel pellet, quickly condensing and heating the fuel inside. The strategy attempts to maximize n_e and T while τ_E is quite low, on the order of nanoseconds. In the United States, the National Ignition Facility is one of the pioneers of this technique, using 192 beams to compress and blow apart a hohlraum structure that surrounds fusion fuel. The destruction of the hohlraum creates x-rays meant to create further compression. In many cases, the perfect symmetries required and instabilities of the plasma at very high pressure cause density and confinement time to suffer [4].

Magnetic confinement fusion has received the overwhelming bulk of focus and funding over the years. It approaches the triple product using lower n_e than inertial confinement but hopes to reach high T with τ_E on the order of seconds. It takes advantage of the fact that plasmas can be controlled by electric and magnetic fields. Ionized particles and electrons tend to stay confined to field lines, orbiting them and travelling along them rather than diffusing across them. Since particles will continue to travel along said field lines indefinitely, the brilliant idea was proposed to loop the field lines back upon themselves. In this way, the magnetic field lines, and therefore the plasma, form a torus, allowing for continuous confinement and heating of the plasma. This led to the toroidal magnetic confinement concept, and the development of tokamaks and stellarators. In these devices, the toroidal and poloidal magnetic fields within the vessel provide closed magnetic flux surfaces which confine the charged particles of the plasma and allow them to heat to fusion temperatures.

1.2 Plasma Facing Components

As tokamak plasmas get larger and hotter, leading to the development of the International Thermonuclear Experimental Reactor (ITER), the world's largest tokamak [5], material constraints of wall materials have not changed much. PFCs must contend with heat flux from diffusion and instabilities. Neutrons also carry a majority of the released energy of the fusion reaction and, since they are not affected by the magnetic fields, travel straight to the walls. Wall materials must contend with this high heat load and irradiation without exhibiting catastrophic damage. These heat loads are also only expected to increase. Even with flux spreading and plasma shaping techniques meant to minimize heat flux impingement on the divertor, plasmas in ITER are expected to reach over 10 MW/m2 at the divertor surface [6]–[8].

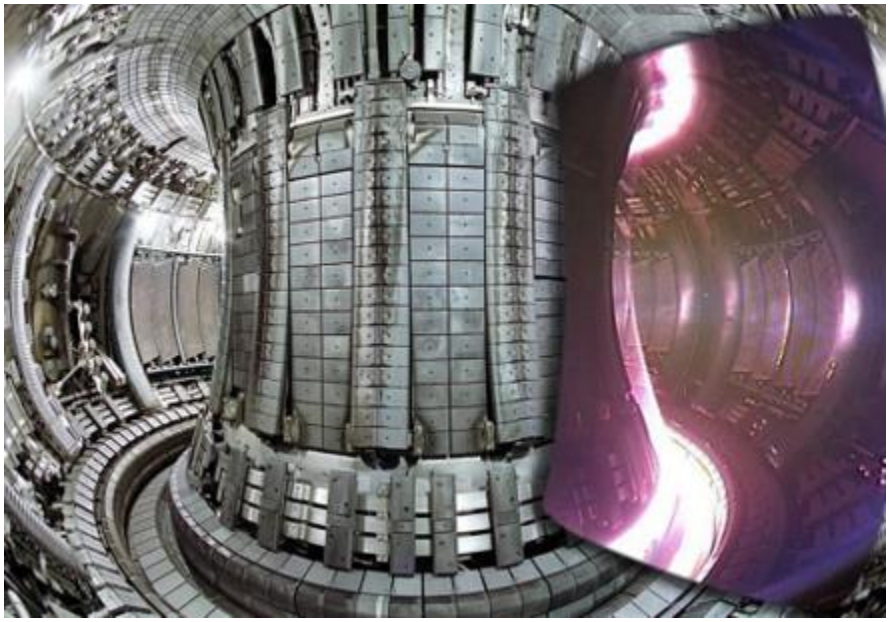

Figure 1.2 – The JET device in the UK showing the internal structure of a tokamak, with the bright pink glows in the inset displaying the regions the plasma is interacting with the PFCs [9].

As plasma systems were bent into toroidal geometries, plasma particles began to defy classical transport theories. New drifts and instabilities were discovered in these plasmas due to magnetic field, density, temperature, and pressure gradients, and this led to reduced confinement and lower temperatures [10]–[13]. A tokamak contains plasma many times hotter than the center of the sun, and this diffusion and drift result in inevitable plasma-material interaction (PMI) at the wall. As new confinement techniques and better operating modes (such as the H-mode) were discovered [14], it seemed as though the improvement was usually tempered by new instabilities.

These pressure and current driven instabilities can lead to large disruptions and edge localized modes (ELMs) that cause plasma ejection from the core to deliver a substantial fraction of the total energy to the wall of the device within a fraction of a second.

Furthermore, recycling from the wall can cool the plasma, hindering fusion. If a particle diffuses to the wall and rebounds, it can thermalize and rebound at the temperature of the wall, cooling the edge plasma. If the particle was neutralized at the wall, it can easily diffuse into the core, causing massive cooling in the hottest parts of the plasma. This recycling is enhanced if the plasma sputters high atomic number (high-Z) particles from the wall and back into the core. When sputtered, high-Z materials like tungsten or molybdenum also heavily contribute to plasma cooling via Bremsstrahlung radiation losses that are proportional to Z^2 [3].

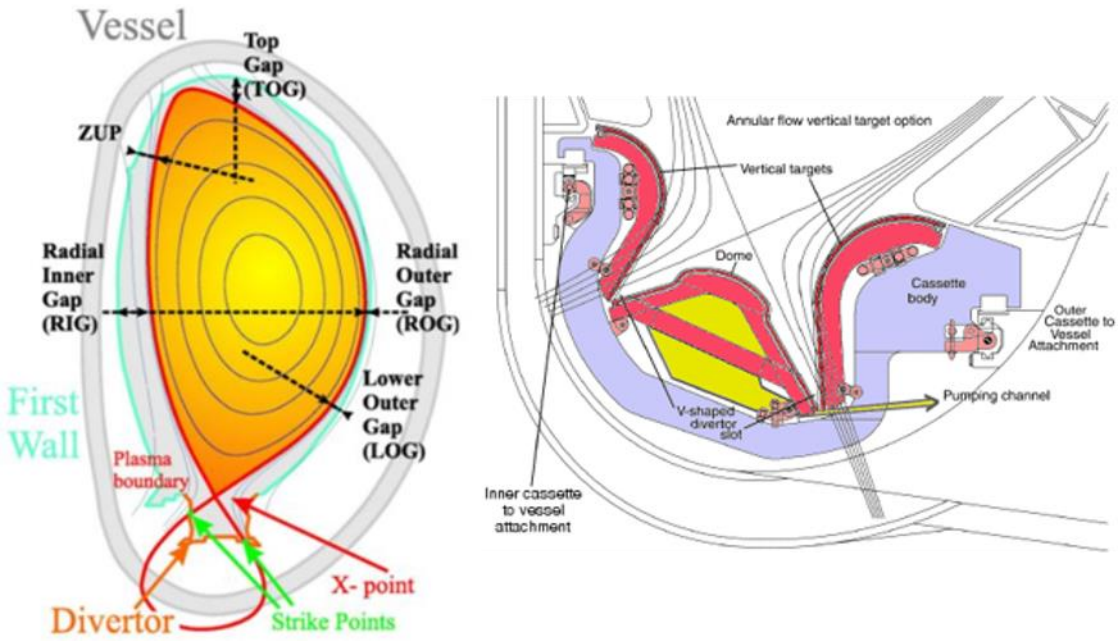

Figure 1.3 – Left: The shape of a typical toroidal fusion plasma, with the LCFS outlined in red. The divertor, first wall, and divertor strike points are also labeled [15]. Right: A close-up view of a standard divertor cassette, with the magnetic field lines displaying how the plasma will interact with the plasma facing surface [16].

In order to protect the main wall (or first wall) of the fusion device, plasma facing components (PFCs) were developed specifically to receive the bulk of heat and particle loads that stream out of a tokamak plasma. These PFCs must have high melting points, good thermal conductivity, and low sputtering. A limiter is a PFC that is inserted into the fusion vessel in order to stop the core plasma from expanding to impact the first wall. This provides a way to control which surfaces encounter the highest heat and particle fluxes and maintains better confinement

due to less expansion of the plasma. However, limited plasmas are more susceptible to egress of limiter impurities into the core, which increases the radiated power and lowers core temperatures. Plasma shaping to a divertor configuration allowed the main point of contact to move farther from the core of the fusing plasma. In this case, divertor tiles are positioned toroidally around the bottom (and sometimes top) of the device. The magnetic field is shaped in such a way that there is some point where the magnetic flux surfaces are no longer closed. Between this last closed flux surface (LCFS) and the vessel walls lies the scrape-off layer (SOL), a region in which the magnetic fields direct particles toward the divertors. Here the impurity concentration from the PFCs is more removed from the core plasma, but the intensity of the heat and particle fluxes along the LCFS increases the risk of damage from thermal shock and long-term particle loading.

Current PFC solutions generally utilize solid materials, including low-Z carbon and beryllium as well as high-Z metals such as stainless steel, molybdenum, and tungsten. When exposed to the high intensity conditions of fusion devices, several issues with solid materials arise. Melting and thermal damage arise from the high heat fluxes [17]–[19]. Even tungsten, the element with the highest melting temperature, can sustain heavy damage, and longer term effects of neutron irradiation damage and fuzz formation from plasma interaction degrade the material [20]. Erosion and ablation due to sputtering increase PFC damage, and this wall material is then introduced into the core. When first wall components are all high-Z substances, impurity egress into the core plasma can be quite damaging to the plasma performance. It takes less than 0.1% impurity fraction of molybdenum in the core plasma to effectively radiate away 10% of fusion power [21]. Low-Z materials are much less damaging; it takes roughly 10% impurity fraction of beryllium to effect a 10% loss in fusion power. However, low-Z solids tend to exhibit enhanced erosion, which minimizes this benefit and places an unsustainable limit on device lifetime [22].

While progress is still being made in plasma shaping techniques, operating regimes, and materials science to combat these issues, conditioning PFC surfaces with low-Z materials such as boron [23], beryllium [24], and lithium (see below) has shown improved plasma performance and wall viability. This work focuses on the promise of lithium, specifically liquid lithium, as an alternative PFC and wall material, with the goal of eliminating many of the problems mentioned above.

1.3 Liquid Metals in Fusion

Since current systems are struggling to be sufficient for use with solid PFCs, a growing section of the fusion community is studying the benefits of liquid metals in fusion applications. Liquid surfaces can provide a self-healing PFC surface that is much less vulnerable to irreparable damage from heat and particle loading. The liquid surface can be regenerated or recirculated, improving PFC lifetime. In addition to simple conduction, liquid surfaces allow for more methods of dealing with the extreme fusion heat loads, including convection and evaporation. While many of these ideas have existed for some time, the increasingly intense conditions expected in reactor relevant fusion devices has led to a resurgence of study in these areas. The Advanced Limiter-divertor Plasma-facing Systems (ALPS) and Advanced Power Extraction (APEX) initiatives have received extensive funding to develop novel methods of using liquid metal systems as PFCs [25]–[27]. The liquid metal solutions being developed promise more durable and economically viable fusion PFCs.

1.3.1 Liquid Metal Comparisons

Multiple materials have been proposed for liquid metal PFCs, including lithium (Li), tin (Sn), tin-lithium (Sn-Li), gallium (Ga), and Galinstan (Ga-In-Sn eutectic). While lithium is a highly reactive and corrosive liquid, it offers some of the best wetting and corrosion characteristics of the candidate materials. However, the vapor pressure of lithium becomes quite high at temperatures above 450 ºC, limiting the effective temperature window. Tin has been proposed as an alternative, since it maintains an extremely low vapor pressure, but poor wetting ability and corrosion characteristics limit the use of tin in many applications. Sn-Li alloys/eutectics have shown some promise as a liquid that would exhibit the best characteristics of lithium and tin. Lithium segregation to the surface could allow a pure lithium surface to face the plasma, while the stability of tin would govern bulk material properties. Issues with preferential sputtering, as well as the need for extensive research into other important material properties such as wetting and corrosivity limit the current application of Sn-Li alloys. The handling ability of gallium and Galinstan is a major advantage, as they are stable in atmosphere. They also exhibit low melting points, high boiling points, and low vapor pressures. Unfortunately, both materials are high-Z and

are extremely corrosive at high temperatures. Therefore, their use is limited to stand-in materials in test-bed studies of liquid metal technology.

1.3.2 Benefits of Liquid Lithium

Of the liquid metals under investigation, lithium has found the most support, due to several spectacular benefits it provides in fusion systems. Lithium is a low-Z element, the lowest besides hydrogen and helium, meaning if it is sputtered or evaporated into the plasma it will effect minimal losses on core plasma performance. The thermo-physical properties of lithium, namely the high thermal capacity and latent heat of melting and vaporization, make it an attractive candidate for heat removal and protection of PFC surfaces. The vapor pressure of liquid lithium creates a vapor shielding effect at relatively low temperatures (>500 ºC). Coupled with a low ionization energy, this can lead to small clouds of vapor near the PFC surface that are extremely effective at dispersing incoming heat and radiating it away. This effect may be very important in power exhaust handling of PFCs and be critical in reducing loads to the surrounding first wall. The use of lithium can also be quite beneficial to fusion device operation.

Since the first definitive results of lithium-driven performance increases in TFTR [28], lithium has been shown to provide low recycling, increased confinement time, increased and more stable density profiles, and even ELM mitigation. Since 2005, the FTU device in Italy has been operating with a lithium limiter and has experimented with lithium wall conditioning. They saw sudden increases in core density as soon as lithium use began, as well as reliable 20% increases in confinement time [29]. Due to its reactivity, lithium is an excellent getter material, effectively reacting with and absorbing essentially all particles and impurities that impact the surface. CDX-U at PPPL installed a fully toroidal liquid lithium limiter and observed much lower recycling at the wall, along with fewer oxygen and carbon impurities. Z_{eff} of the core was reduced 50%, and they achieved a 25% increase in core temperature [30], [31]. The reduction in recycling tends to reduce the temperature gradients at the edge of the plasma, allowing a larger volume of plasma to stay hot and effective for fusion. The LTX experiment even recently announced a completely flat radial temperature profile, with no reduction in temperature at the edge, due to the effects of lithiated walls [32].

NSTX and NSTX-U at PPPL has also experimented extensively with lithium, developing a liquid lithium divertor and lithium evaporators to cover sections of the wall [33], [34]. Increasing coating thickness of lithium on the walls of the device was shown to decrease recycling, improve energy confinement, and reduce the edge density gradient profile [35]. The lithium coating affected edge plasma profiles by lowering the density, pressure, and current gradients, rendering them more stable to the instabilities that lead to ELMs. This led to periods of ELM-free H-mode operation, known as the quiescent H-mode [36]. Confinement was also markedly improved during the periods of quiescent discharges.

Another concept utilizing the benefits of lithium is ELM pacing. Instead of allowing instabilities to grow and crest into large, relatively unpredictable ELMs or disruptions that could quench the plasma, pellet injection was found to be able to produce a pseudo-quiescent H-mode where pellets would trigger small ELMs at a regular frequency, essentially releasing tension in the plasma and allowing for more stable operation. DIII-D had proposed this method in conjunction with fueling by deuterium pellet injection as a mitigation strategy for ITER [37]. Recently, lithium pellet injection was also attempted on DIII-D [38], [39] and EAST [40], [41], successfully triggering ELMs at a higher rate with lower peak heat flux. The lithium also lowered impurity concentrations in the plasma core, and resulted in good H-mode energy confinement and pedestal characteristics [38], [39].

1.3.3 Challenges of Liquid Metal Systems

While liquid metal systems, specifically those utilizing liquid lithium, can alleviate many issues with PFC design and improve fusion plasma performance, there are several potential issues that have been raised by the community. These include surface stability, wetting control, fuel retention, and heat flux handling. Different liquid metal PFC solutions must successfully address these issues before they can be incorporated into large scale devices.

Surface stability – Any liquid metal surface must remain stable in the face of highly intense electromagnetic conditions inside fusion devices. The ejection of material from the surface can trigger ELMs and disruptions, which quench the plasma and can lead to damage on exposed first wall surfaces. During large plasma impulses and sharp magnetic field transients, strong electromagnetic forces in the liquid can trigger Rayleigh-Taylor and Kelvin-Helmholtz

instabilities which may lead to ejection. These instabilities can be countered by surface tension, so it is important that liquid metal systems maintain critical dimensions that enhance surface tension to remain immune to ejection [34], [42].

Wetting control – Liquid metal PFCs require a consistent coating of the solid surfaces, so that damage to the surface is avoided. In order to ensure uniform surface coatings, the liquid metal must be able to adequately wet the surface. While high surface tension liquids tend to exhibit strong capillary action and wicking effects once wetting has begun, this can become detrimental if the liquid metal wicks onto surfaces that should remain unwetted. Control of wetting temperature is important to maintain liquid metal adhesion to the solid substrate surface while ensuring corrosion sensitive areas remain free of liquid metal impingement.

Fuel retention – Large particle fluxes to PFC surfaces result in retention of fuel and impurity species in both solid and liquid materials. While the excellent gettering characteristics of liquid lithium provide impressive improvements to the temperature and density profiles of the plasma, the strong interaction of lithium with hydrogen isotopes results in fuel retention concerns. Deuterium and tritium, both fuel species and isotopes of hydrogen, can be absorbed by liquid lithium up to a 1:1 saturation. Aggressive retention of fuel can alter several aspects of device operation. Hydrides and oxides can passivate the lithium surface, impeding flow and reducing the beneficial aspects of a clean lithium PFC. Retention of tritium can drastically impact the amount of highly controlled tritium that must be manufactured and stored onsite, raising issues with regulatory authorities and even the more basic issue of reliable tritium manufacturing. Due to the high cost of tritium and the safety concerns of retaining tritium onsite, liquid metal PFCs must limit the hydrogenic species uptake or have systems to recover the deuterium and tritium in real time.

Heat flux handling – Liquid metal systems have additional methods of heat removal in comparison to purely solid PFCs. In order to protect the underlying solid surfaces, the liquid metal components must surpass solid PFC solutions in the ability to survive under high heat loads. Liquid surfaces must stay steady in high plasma impulse and high local heat flux environments. If evaporation, plasma impulse, or divertor/limiter heat stripes thin or eliminate the liquid surface, underlying solids can be directly impacted by the plasma, leading to overheating and damage.

1.4 Flowing Liquid Lithium Technologies

As seen above, many devices have examined the effects of incorporating solid or liquid lithium into device operation, to encouraging results. However, lithium also has its drawbacks. It is a highly reactive metal that acts as a strong getter to many common impurities in tokamaks. While this makes its low recycling ability possible, it makes it very difficult to keep lithium pure, both in atmosphere and in vacuum. Lithium also has a large affinity for hydrogen and its isotopes, requiring fueling rates to be largely increased when lithium is present. Many devices have just used open pools or evaporated films of lithium, and the high reactivity of liquid lithium can lead to diminished performance over the course of run campaigns. To this end, researchers have developed ways to utilize flowing liquid lithium in PFCs to maintain clean surfaces and provide continuous enhancement of plasma properties. These systems can be classified into 3 main categories: slow flow, medium flow, and fast flow.

1.4.1 Slow Flow Systems

Slow flow systems have near stagnant lithium flow that can be integrated more easily than medium and fast flow systems due to the lack of active pumping. Standard flow velocities are on the order of millimeters per second or below. The capillary porous structure (CPS) system and the lithium vapor box divertor are summarized here.

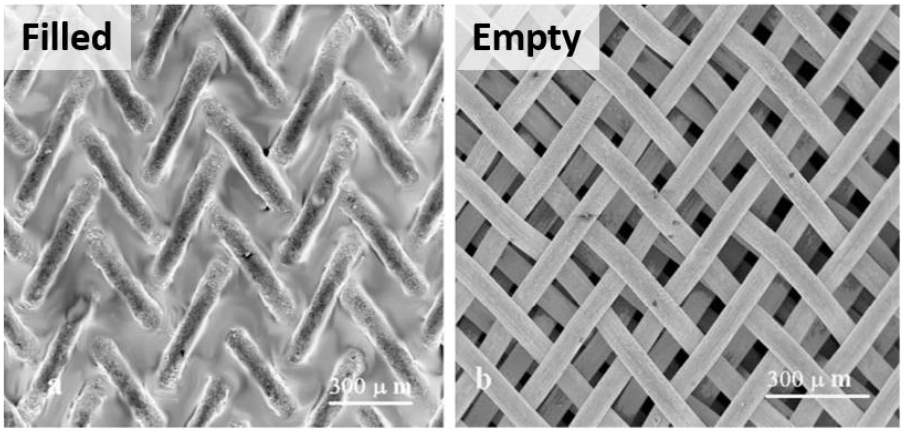

Figure 1.4 – SEM images of a molybdenum CPS mesh filled with lithium (left) and empty (right) [43].

The CPS system relies on surface tension and capillary forces to maintain a macroscopic static liquid metal surface that is quite stable under high MHD and electromagnetic forces produced by the intense magnetic fields in fusion devices. The system comprises of a micrometer

scale mesh into which a liquid metal intercalates. As the surface is eroded and evaporated from the plasma facing region, capillary forces drive flow upward to replenish the topside liquid. Active cooling is generally included in CPS systems to remove heat, and evaporation of the liquid can also produce a vapor shielding effect to further enhance radiation. Liquid metals tested in CPS systems include lithium, tin, and tin-lithium alloys. CPS systems have demonstrated impressive inhibition of droplet ejection and effective protection of the underlying solid mesh substrate. In the FTU tokamak, a CPS liquid lithium limiter showed sustained performance at 5 MW/m^2 heat flux with no damage to the substrate [44]. In the T11 tokamak, plasma loads up to 10 MW/m^2 were survived during short pulses of 50 ms. Electron beam exposure experiments have demonstrated steady state power handling of 10 MW/m^2 and even subjected the system to transient events up to 50 MW/m^2 [45].

While CPS systems display superior heat flux handling and surface stability, wetting control and fuel retention become drawback for the system. Liquid lithium has the most beneficial wetting characteristics of standard CPS liquid candidates, requiring temperatures of 600-700 ºC to effectively wet the mesh. For tin and tin-lithium alloys, the wetting temperature climbs beyond 1000 ºC, making effective wetting difficult before operation. Due to the nearly stagnant nature of the liquid surface, passivation due to high impurity flux can inhibit effective upwelling of the liquid through the small pores. Additionally, there is no outlet for the liquid once injected into the device. Lithium and the impurities and fuel it getters will eventually be evaporated and redeposited around the walls of the vessel. This limits the long-term benefits and viability of CPS systems, as fuel retention presents a severe concern.

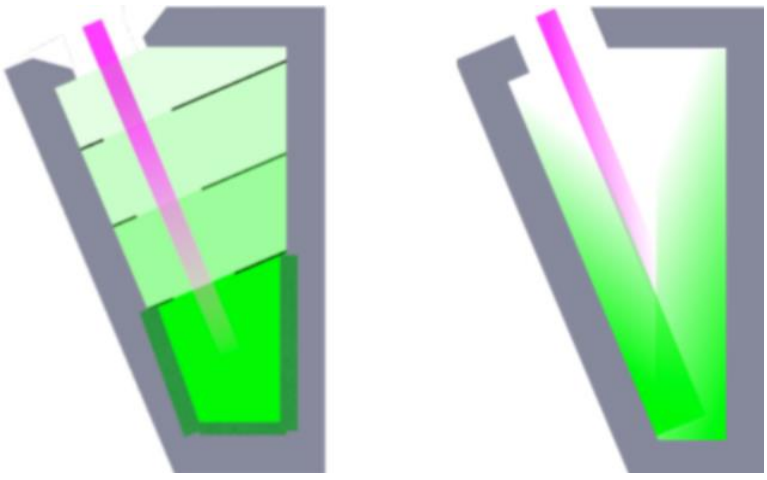

Figure 1.5 – Diagrams of the vapor box divertor concept, both with (left) and without (right) baffles [46].

The lithium vapor box divertor is a concept recently proposed at PPPL to harness the strong vapor shielding effects of liquid lithium. This slow flow/stagnant system comprises of a series of baffled stages held at successively lower temperatures as they progress toward the main chamber. The divertor heat stripe entering the vapor box would encounter progressively higher densities of evaporated lithium. The resulting volumetric heat dissipation limits both heat impingement on (and therefore damage to) the solid surfaces and particles sputtered back into the core plasma. The cooler stages near the outlet of the divertor allow for lithium condensation to prevent high lithium efflux into the vessel. In order to protect the solid surfaces during transient events, the entirety of the device must remain covered in liquid lithium, presenting a wetting control challenge. However, vapor flow simulations of the device suggest that baffled section may not be necessary, making fabrication and effective wetting much simpler [46].

As with the CPS system, fuel and impurity retention are a significant concern with the vapor box design. With no method of liquid removal, deuterium and tritium retention become a limiting factor for device lifetime. Hydrides and oxides will continue to form as the lithium getters impurities, and while these species will decompose in the hottest regions, lower temperature condensation areas could see passivation in lithium impurities, hindering wetting and surface protection.

1.4.2 Medium Flow Systems

Medium flow systems harness some form of active or passive pumping technique to drive liquid metal flow at 0.1-100 cm/s. The faster flow speeds allow for a clean, constantly refreshing liquid surface to face the plasma. Faster flowing systems allow the liquid to remove gettered impurities and fuel particles and can provide faster heat removal from the vessel. However, convection alone cannot provide the entirety of heat removal needed from the divertor strike point region, and while the flow allows for impurity removal, the filtration and fuel removal techniques provide an additional challenge for system integration. This section presents the Flowing Liquid Lithium Limiter (FLiLi) and the Liquid Metal Infused Trench (LiMIT) concepts.

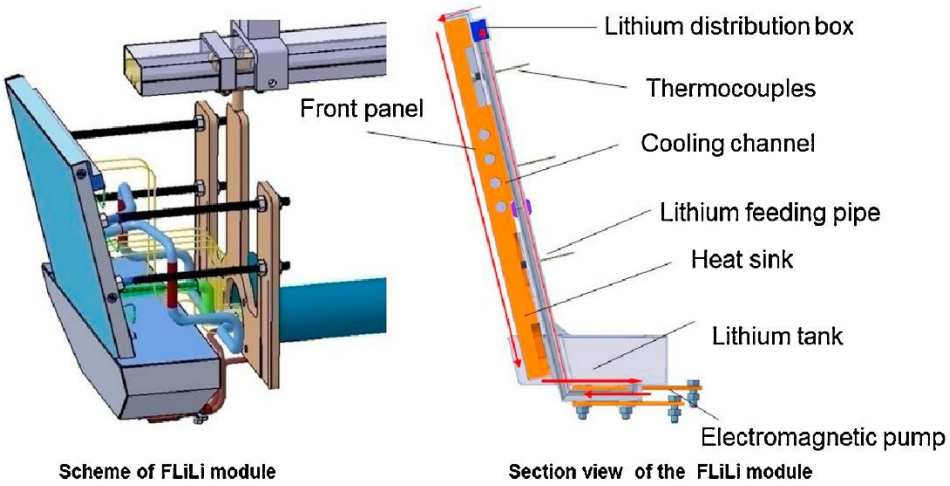

Figure 1.6 – Left: Drawing of the FLiLi system attached to the EAST transfer arm. Right: Side view of the FLiLi system with main components labeled [47].

The FLiLi concept was pioneered by PPPL and is still in development through domestic and international collaborations [48]. This limiter design has been through several iterations of testing in the HT-7 and EAST tokamaks in Hefei, China. Consisting of a flat plate topped in a distribution manifold, the FLiLi system relies on thin film lithium flow of <1 cm/s over a solid backing plate. EM pumping supplies lithium to the top of the plate, and a series of small holes in the distributor spread the lithium film. The first generation consisted of a stainless-steel plate bonded to a copper heat sink to keep the lithium surface below the high evaporation regime. Lithium flowed from an inlet tube into a collector below the plate. Later generations of FLiLi developed into a self-contained loop system. The plate was sunk into a small reservoir containing approximately 1.5 L of lithium. An EM pump included beneath the reservoir supplied lithium to the distributor, and lithium flows down the plate back into the reservoir. As in the first generation, a thin film of lithium flows under gravity down the plate surface. The most recent versions of FLiLi do away with the plate bonding and consist of a single TZM plate to reduce material compatibility and erosion concerns. Tests in both HT-7 and FLiLi successfully demonstrated the ability of the lithium limiter to improve plasma characteristics. Plasma stored energy increases, loop voltage decreases, and D_α decreases by ~16%, which indicates a significant reduction in recycling from the limiter surface due to the presence of lithium.

The FLiLi system relies on thin open surface flow and is therefore susceptible to MHD instabilities and ejection from the surface. Maintaining a thin wetted surface is also imperative, as formation of rivulets on the surface increases the risk for ejection. Distribution systems have proven to be a significant challenge as well. Issues with blockage and impurity buildup in the 0.8 by 0.8 mm distributor holes has resulted in uneven lithium coverage on the limiter surface, allowing the backing plate to be in direct exposure to the plasma.

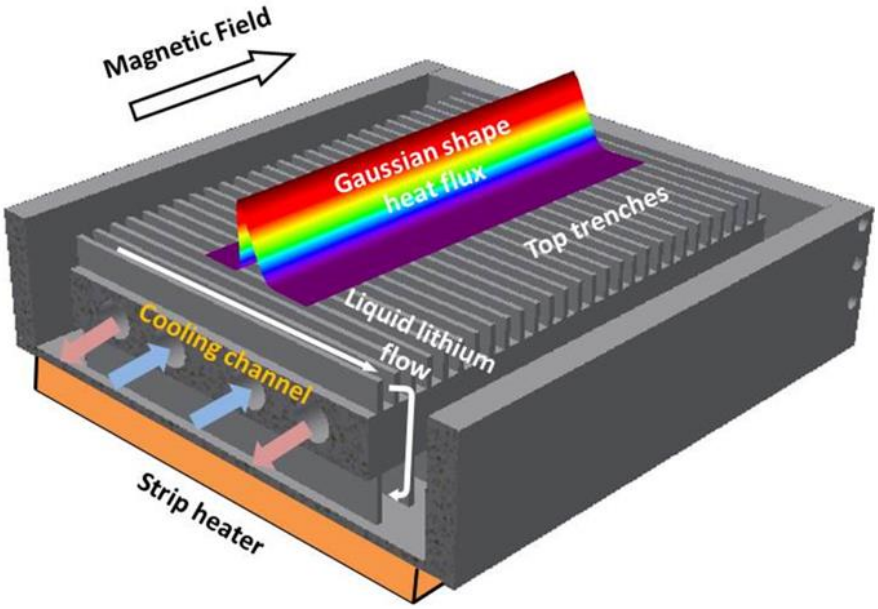

Figure 1.7 – Diagram of the LiMIT system, including bottom side and topside heating, central cooling lines, transverse magnetic field component, and the direction of TEMHD-driven flow.

The LiMIT system, developed at the CPMI at UIUC, will be briefly introduced here. LiMIT is the basis of this work and will be discussed in more detail in Chapter 2. The LiMIT concept consists of an array of solid metal trenches (usually stainless steel, though molybdenum and tungsten have been studied) that are filled with liquid lithium. When 2 different metals share an interface and a temperature gradient is applied along that interface, a voltage difference is developed due to the Seebeck effect. As a result, a thermoelectric current begins to circulate around the junction between the 2 metals. In the case of LiMIT, a thermal gradient is created along the height of the trenches, either by coolant passing through the device or by a plasma impinging on the top of the lithium surface. This generate a thermoelectric current that circulates through the liquid lithium. Then, a transverse magnetic field creates a J×B Lorentz volume force that can passively drive the lithium through the trenches. When trenches continue along the underside of the device, full recirculation of the liquid lithium is possible. This thermoelectric

magnetohydrodynamic (TEMHD) driving force is the key to the LiMIT system. As a PFC, the LiMIT device can utilize the plasma heat flux and toroidal magnetic field to create self-driven TEMHD flow, without the need for any external pumping. TEMHD and the LiMIT system is described in more detail in Chapter 2, along with the progressing development of the concept to address all liquid metal PFC challenges.

1.4.3 Fast Flow Systems

Fast flow systems exhibit thermal handling benefits in comparison to medium flow systems, and outlet the liquid flow from the vessel to allow for external processing. These systems require liquid flow on the order of 1-10 m/s, which allows the liquid to remove most of the heat flux from the device in a single pass. High velocity flows may be susceptible to splashing and particle ejection, however, and flow instabilities could be detrimental to PFC operation. On site liquid metal volume must also be quite high and required pumping and power systems are quite extensive. The fast flow systems for the International Fusion Materials Irradiation Facility (IFMIF) and the Flowing Liquid Torus (FLIT) are summarized here.

Material response to long term neutron exposure at fusion-relevant energies of 14 MeV is a large open-ended question for fusion power. There is currently no facility that can supply sufficiently large fluxes to apply to the conditions that will be experienced in large scale fusion power devices like ITER, DEMO, or future power plants [49]. The IFMIF plans to change that by firing two 40 MeV deuteron beams at a stream of fast flowing lithium to create D – Li-7 neutrons. These beams will impart roughly 1 GW/m^2 heat flux on the surface of the lithium. To cope with this extreme heat, IFMIF will utilize a lithium jet system capable of sustaining a 2.5 cm thick wedge of lithium at a velocity of 15 m/s around a hyperbolic target arc onto which the beams are focused. The lithium removes the heat from the system, as well as the impurity species and reaction products. Evaporation is suppressed by the large centrifugal forces the lithium surface experiences as it moves through the vessel [50].

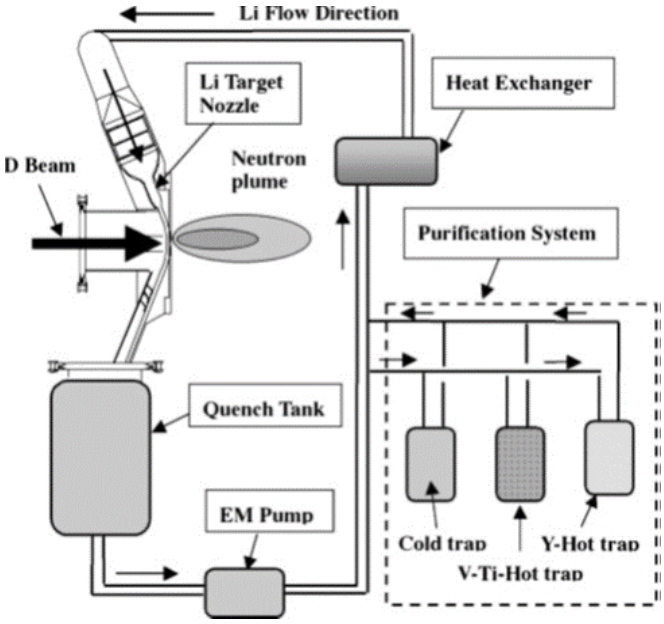

Figure 1.8 – Diagram of the IFMIF design, including pumping systems, purification systems, and the beam interaction arc where a jet of lithium is impacted by a high power deuterium beam [49].

While planning for the lithium system on IFMIF has progressed significantly, and the designs incorporate the collection, filtration, and purification systems that will be needed for medium flow systems, IFMIF has yet to enter proof of concept phases of testing. Bulky external components, the potential for splashing and ejection, and the nascent technology readiness of the system are challenges that need to be overcome.

The FLIT design is a proof of concept, recirculating, toroidal liquid metal system, meant to demonstrate fast liquid metal flow. The free surface is designed to recirculate poloidally in an annular geometry. EM pumping will drive a 5 mm film of liquid metal at 2.6 m/s, required to remove a heat flux of 10 MW/m^2. To minimize costs and safety concerns, Galinstan is proposed as an initial test material. The system aims to demonstrate 30 cm of stable free surface flow in order to be relevant to ITER conditions. The system allows for a multitude of adjustments to the flow configuration, in order to optimize the flow profile [51].

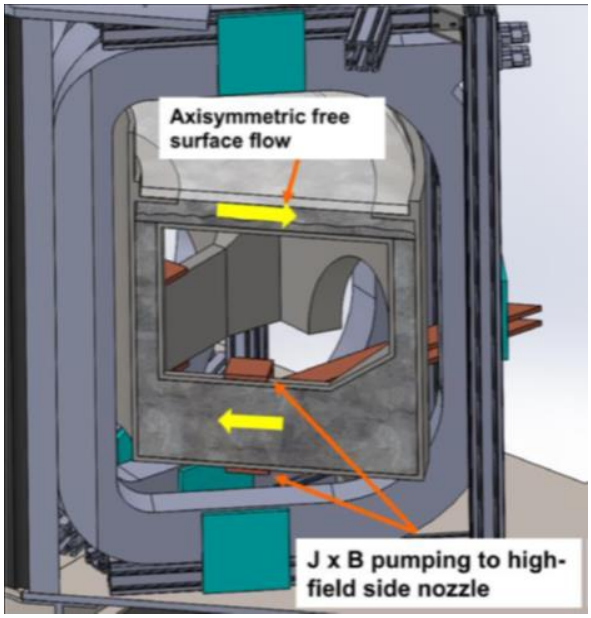

Figure 1.9 – Drawing of the FLIT experiment, showing the magnetic field coils, pumping system, and recirculating flow setup [51].

For the FLIT experiment, maintaining a stable surface is a concern. As a fully open surface, ejection may be an issue. Even distribution and flow thinning as radial position increases are important challenges that must be overcome. Once constructed, the ease of changing flow patterns and distribution manifolds may allow for the study and resolution of many flow stability issues.

CHAPTER 2 – TEMHD AND THE LiMIT SYSTEM

2.1 Thermoelectric Magnetohydrodynamics

The key to TEMHD driven flow is the thermoelectric effect. This principle is used in thermocouples to measure temperature. It states that when 2 dissimilar metals share a junction and a temperature gradient is present along the junction, a voltage difference develops between the top and bottom of the interface. The induced voltage difference is a result of the Seebeck effect. The Seebeck coefficient, also known as the thermoelectric power or thermopower, is an inherent material property that describes the magnitude of thermoelectric voltage that can be induced across a material. A difference in thermopower between the 2 materials gives rise to the voltage difference of the thermoelectric effect. Where there is a voltage difference, current flows. A simple diagram of this thermoelectric current can be seen in Figure 2.1. Adapting and generalizing Ohm's law to account for the thermoelectric current generation yields,

$$\frac{\boldsymbol{J}}{\sigma} = \boldsymbol{E} + \boldsymbol{u} \times \boldsymbol{B} - S\nabla T$$

Where $\boldsymbol{J}$ is the current density vector, σ is the electrical conductivity, $\boldsymbol{E}$ is the electric field vector, $\boldsymbol{u}$ is the velocity vector, $\boldsymbol{B}$ is the magnetic field vector, S is the Seebeck coefficient, and ∇T is the temperature gradient. The term including the Seebeck coefficient describes the electromotive force (emf) from the Seebeck effect, and the $\vec{u} \times \vec{B}$ is used to capture any emf that results from the velocity of the conductive material.

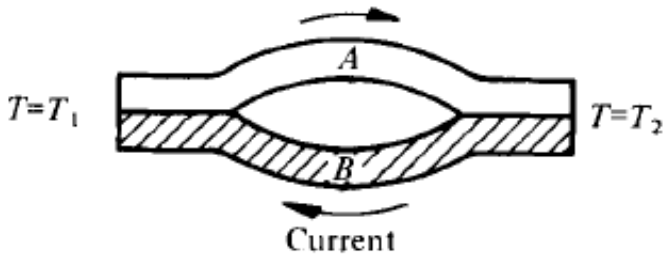

Figure 2.1 – A simple diagram of the current flow in a thermoelectric junction, where materials A and B share a junction at 2 different temperatures, T_1 and T_2 [52].

If one of the metals in the thermoelectric current loop is liquified, the current will still flow from the solid through the liquid as long as contact is maintained. Therefore, the application of an

external magnetic field with a transverse component will generate a $j \times B$ Lorentz force that will begin to drive flow in the liquid metal. Therein lies the basis for the concept of TEMHD flow. Assuming the fluid is incompressible, and the magnetic Reynolds number of the fluid is small enough that the flow does not impact the magnetic field strength, the MHD equations can be written as follows.

$$\nabla \cdot \boldsymbol{u} = 0$$

$$\nabla \cdot \boldsymbol{J} = 0$$

$$\boldsymbol{J} = \sigma(\boldsymbol{E} + \boldsymbol{u} \times \boldsymbol{B} - S\nabla T)$$

$$\rho\left(\frac{\partial \boldsymbol{u}}{\partial t} + \boldsymbol{u} \cdot \nabla \boldsymbol{u}\right) = -\nabla P + \mu \nabla^2 \boldsymbol{u} + \boldsymbol{J} \times \boldsymbol{B}$$

$$\rho C_p\left(\frac{\partial T}{\partial t} + \boldsymbol{u} \cdot \nabla T\right) = \nabla \cdot (k \nabla T)$$

Here, ρ is the density, P is the pressure, μ is the dynamic viscosity, C_p is the heat capacity of the liquid, and k is the thermal conductivity. From here it is possible to describe the TEMHD driven motion in a variety of ideal geometries.

While the idea of pumping conductive liquids using the electromagnetic force has existed since the 1800s [53], the concept of harnessing the thermoelectric effect for liquid metal flow was proposed in the mid-1960s as a method of pumping liquid metals for cooling in nuclear fission reactors [54], [55]. Through the late 1970s and early 1980s, Shercliff provided a wealth of new work on TEMHD flow and suggested the use of TEMHD in fusion applications, such as liquid lithium blanket designs [52]. He examined the MHD equations adjusted for inclusion of thermoelectric effects, then developed the expected flow profiles for Hartmann flow between 2 parallel plates and 2D flow in a circular pipe. He went on to provide solutions of TEMHD driven flow in closed containers with walls perpendicular [56] and parallel [57] to the magnetic field, as well as flow in a finite closed pipe [58]. Initially, these solutions were developed assuming a known, steady temperature gradient across the domain. From there, Shercliff investigated the effects of heat transfer and convection on the development of TEMHD in closed systems and showed that heating and cooling can cause perturbations in the flow [59], [60].

TEMHD work for fusion applications was revived by Jaworski, when he observed swirling liquid lithium motion in stainless steel containers. The swirling lithium velocity, tracked via impurity motion on the surface of the lithium, closely matched theoretical estimates of flow velocity based on the thermal gradients measured throughout the container [61]. This experiment led to a reconsideration of bulk swirling lithium flow seen in the CDX-U tests mentioned in Section 1.3.2. Both experiments witnessed e-beam impingement providing strong temperature gradients that drove TEMHD flow in bulk liquid lithium. These results gave a new focus to liquid lithium research in the CPMI at UIUC. The goal was to develop systems capable of utilizing and constraining TEMHD flow, so it can be used as an effective liquid metal PFC for large-scale fusion applications.

2.2 The Liquid Metal Infused Trench System

The developments in TEMHD led to the Liquid Metal Infused Trench (LiMIT) device. LiMIT is comprised of a series of stainless-steel trenches into which lithium is melted. In order to provide effective thermal contact and enhanced recirculation, both the topside open surface and the bottom side return channels contain trenches (see Figure 1.7 and Figure 2.2). When the center of the module is cooled, a temperature gradient develops from the backside heating provided from a heater plate and/or topside e-beam or plasma heat flux. A thermoelectric current begins to flow top to bottom along the trench-lithium junction, providing the driving force to push lithium flow along the length of the narrow trenches, as seen in Figure 2.2. The current flow is illustrated in Figure 2.3. The system has been developed and tested extensively at UIUC, where horizontal [62]–[64] and vertical flow [65] have been sustained. The high surface tension of liquid lithium helps to constrain the surface to the trenches while still allowing flow. This results in smooth, even films of liquid lithium that are constantly refreshing in the face of plasma impingement. The TEMHD circulation aids in heat transfer and reduces the effects of high heat flux divertor heat stripes. Figure 2.4 shows a well wetted lithium surface in the LiMIT trench module. TEMHD-driven velocities >20 cm/s have been measured in LiMIT systems.

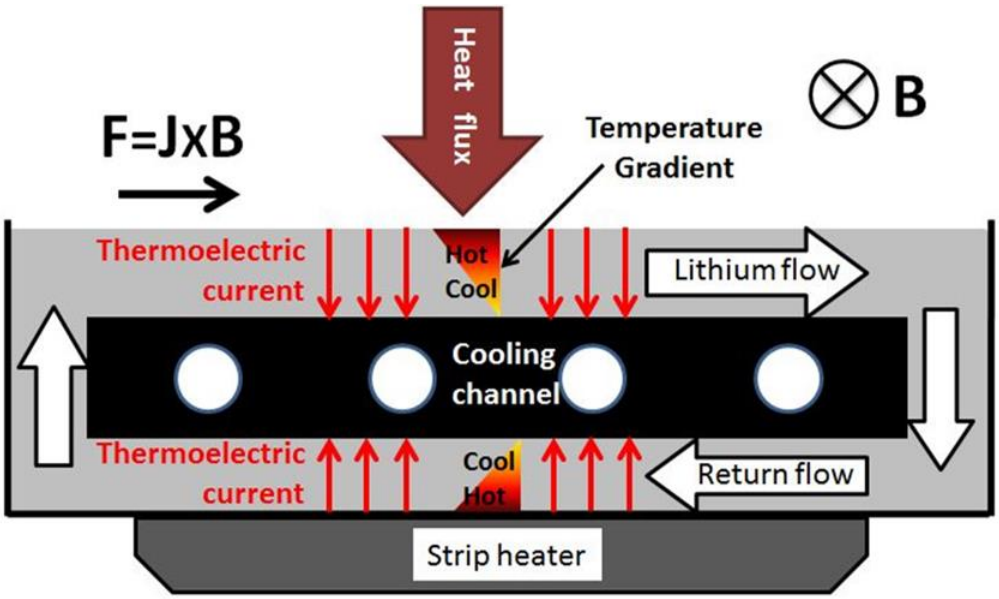

Figure 2.2 – Diagram of the LiMIT system showing how the heat flux and resultant thermoelectric current drive lithium flow through solid trenches.

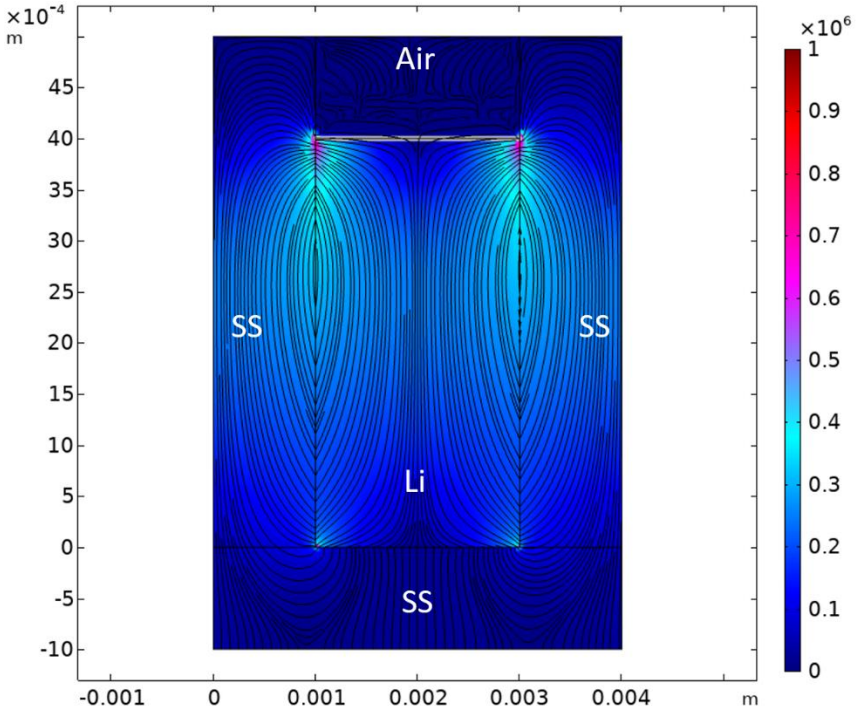

Figure 2.3 – Simulated current flow in a LiMIT trench. The background color map represents current density in A/m^2. The streamlines follow the circulation of the thermoelectric current flow.

The module can operate with or without a strong topside heat flux. A backside heater plate provides latent heat to the system, and central cooling lines develop thermal gradients on the topside and bottom side series of trenches to initiate flow recirculation. In high heat flux operations, a homemade electron beam provides a linear heat stripe down the center of the module

with a standard deviation of approximately 5 mm. In standard operation, this e-beam can supply up to 20 MW/m^2, with transient excursions of ~40 MW/m^2 [61].

Figure 2.4 – An example of the of the standard LiMIT system as viewed through a mirror placed in the chamber to see around the e-beam. The trenches are perfectly filled with liquid lithium.

Proof of concept tests rotated a small LiMIT module past horizontal, testing the ability for the lithium surface tension to constrain the liquid within the trenches [65]. In-operando rotation of the vacuum chamber allowed for TEMHD flow to be investigated at arbitrary angles to horizontal. Up to 90º, higher inclination angles show better agreement with theoretical prediction. Lower angles have a lower measured velocity than predicted, which is hypothesized to be due to lithium overfill. The observed reduction in velocity implies an overfill of approximately 1 mm at low angles, which is reduced as the system rotates and the excess falls into a small reservoir pool. When rotated to 180º from horizontal, with the open surface facing downward, the lithium surface stayed stable, flow was sustained, and no spilling occurred.

LiMIT has been tested in several large-scale devices around the world. LiMIT was installed in the final run campaign of the HT-7 tokamak in China, alongside the first generation of the FLiLi plate [40], [66], [67]. Lithium was injected down a ramp that led to a trench system similar to that being tested at UIUC. While there were issues with full plate wetting, selective full trench wetting occurred. During exposure, these wetted trenches sustained a velocity of

3.7 ± 0.5 cm/s in a 1.8 T magnetic field, and the lithium contributed to lowered impurity concentration and increased confinement time.

To test the effectiveness of LiMIT under high heat and particle fluxes, a module was installed in the Magnum-PSI linear plasma device [68]. Over the course of 73 shots, effective performance was demonstrated at B-fields up to 0.3 T and heat fluxes up to 3 MW/m^2, with measured velocities up to 60 cm/s. Inadequate drainage in the Magnum-PSI design hindered effective recirculation and lithium refill at the highest heat flux, eventually leading to melt damage that ended the experimental campaign.

2.3 Overcoming Liquid Metal Challenges

As referenced in Section, several potential issues with open surface liquid metals PFCs have been raised by the community, namely propensity for droplet ejection, lithium control and wetting, hydrogenic species retention, and heat flux handling. Development of the LiMIT concept has proceeded at the CPMI to address these issues.

2.3.1 Surface Stability

Liquid metal PFCs must eliminate the risk of droplet ejection to avoid the influx of material into the core plasma. MHD forces are more than strong enough to cause droplet ejection in open surface pools of lithium when there are no structures present to stabilize the surface. Both static and flowing liquid lithium systems have exhibited disrupted surface stability. After observing minor droplet ejection in the LiMIT testing on Magnum-PSI [68], research at the CPMI focused on investigating the stability of a LiMIT style trench. A static lithium module with varied representative trench sizes was exposed to a coaxial plasma gun on the DEVeX/TELS experiment. The propensity for ejection in trenches between 1 and 14 mm was characterized based on trench dimension and plasma impulse. Results were then matched with wave simulations meant to represent a lithium surface being struck by a plasma. The study [42] built upon previous stability regimes [34] and established a stability criterion that demonstrates the effectiveness of LiMIT trenches against ejection.

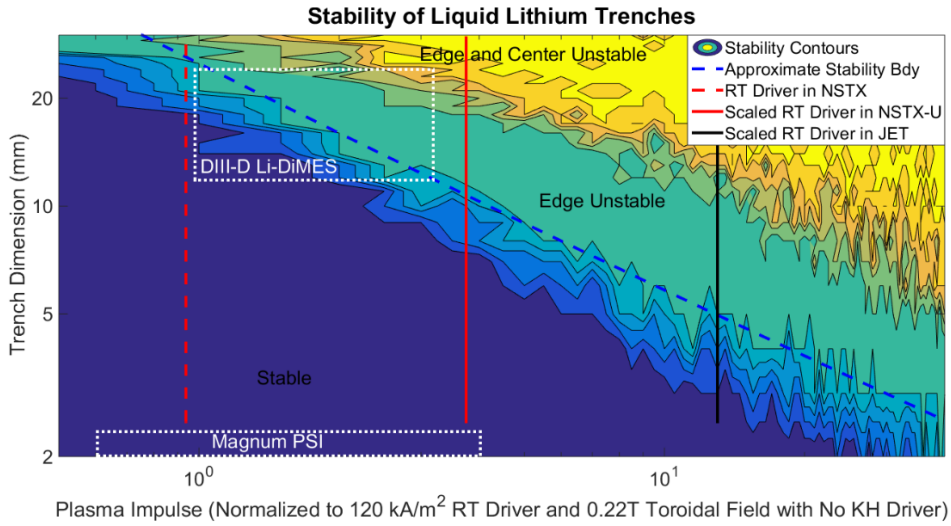

Figure 2.5 – Stability contours of LiMIT trench dimensions against droplet ejection at various levels of plasma impulse, as modeled using the shallow wave equations. Standard 2 mm LiMIT trenches remain stable up to estimated JET conditions, though larger dimensions can exhibit edge instability droplet breakoff and eventually bulk droplet ejection [42].

2.3.2 Wetting Control

While effective lithium wetting is desired on the entire surface of the PFC, lithium wicking outside of that region is generally not desirable. Developing methods of controlling liquid lithium wetting temperatures can result in more effective flow control. This can be achieved using local surface modification. By controlling the roughness of substrate materials, work at the CPMI demonstrated that the temperature at which lithium will wet those materials can be controlled. A laser structuring process was developed that induces micro and nanostructure formation on the surfaces of molybdenum and stainless-steel samples. Structuring of the surface was shown to increase the wetting temperature of both molybdenum (nominal wetting at 324 ºC) and stainless steel (nominal wetting at 315 ºC) by approximately 80 ºC [69], [70]. On the flip side, mirror finishing of a surface demonstrates liquid lithium wetting as soon as melting occurs (181 ºC). These results provide a large operating regime in which structured surfaces will not readily wet and non-structured or polished surfaces will wet easily, a range in which lithium flow can be directed. The change in wetting temperature can be predicted based on the size and shape of the structures [71], so if the process can be enhanced for tighter controls, selective flow control can improve, aiding effective thermal management and prevention of material failure.

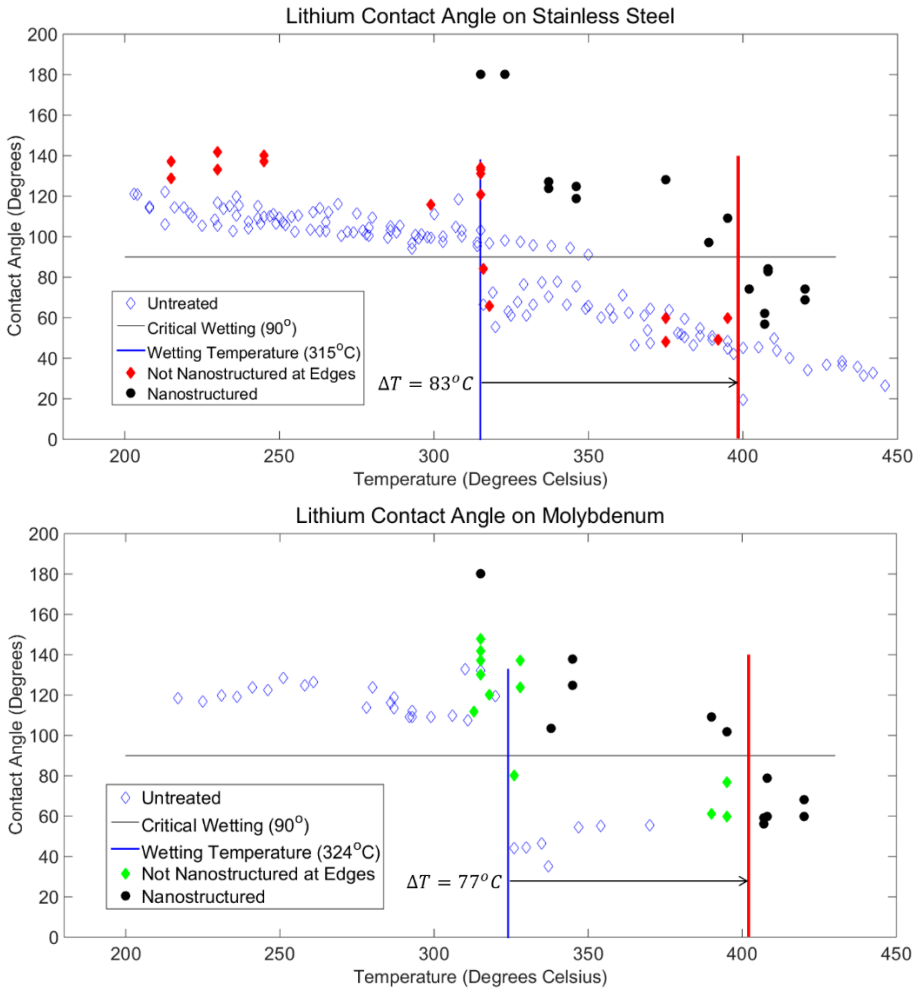

Figure 2.6 – Contact angle measurements showing the decrease of wettability with surface structuring. Wetting temperature increases by 83 ºC on stainless steel and 77 ºC on molybdenum [69].

2.3.3 Hydrogen Retention

Recent research at the CPMI has improved the understanding of, and developed initial solutions to, the challenge of fuel retention. Static lithium exposure to hydrogen, as an analog to deuterium and tritium, showed the characteristics of absorption, surface passivation, hydrogen dissolution, and the formation of lithium hydride (LiH) [72]. In order to prove flowing liquid metal systems are viable with regards to hydrogenic species retention, a prototype distillation column was machined to demonstrate the ability to remove hydrogen from Li/LiH melts [73]. The hydride mixtures are heated to over 700 ºC via induction heating to reach dissociation temperatures. Baffled stages condense the lithium as it evaporates and/or dissociates, while allowing gaseous hydrogen to escape out of the top of the column. Future flowing loop systems will include distillation columns in line with the flow, cleaning the lithium and reinjecting it into

the PFC, while funneling deuterium and tritium back to fueling systems. Preliminary testing showed that a distilling area of 1.53 m^2 is needed to balance the hydrogen wall losses expected in ITER [74].

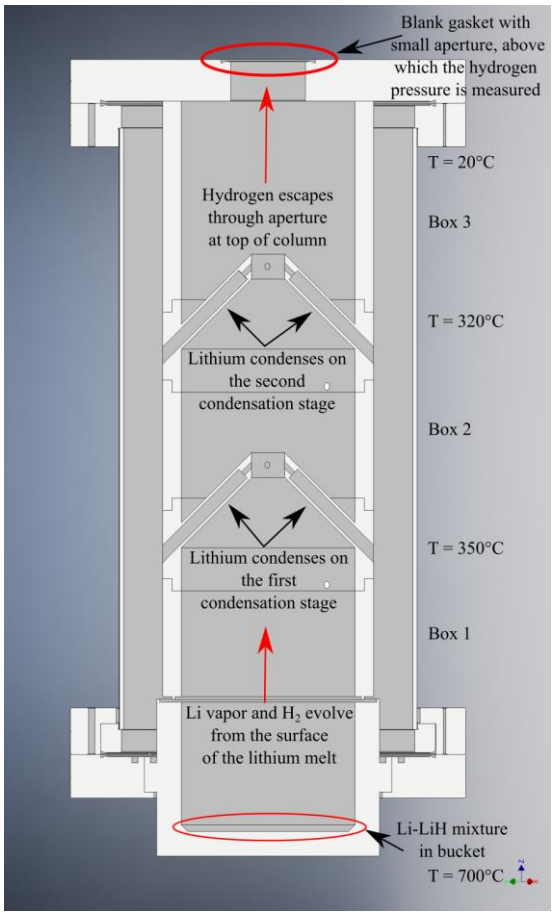

Figure 2.7 – Drawing of the distillation column as designed and tested at CPMI. Li-LiH mixtures are inductively heated in the bottom bucket, 2 condensation stages are included to recapture evaporating lithium, and the upper aperture allows hydrogen capture [73].

2.4 Thesis Motivation

As UIUC and others in the liquid metal fusion community have developed flowing lithium PFC technology, several potential issues with open surface lithium flow have been brought to light. These include (1) droplet ejection, (2) wetting control, (3) tritium retention, and (4) heat flux handling. After conducting many successful proof-of-concept tests of TEMHD-driven lithium flow, the CPMI has focused on addressing these issues in order to advance the technological readiness level of this system.

The first 3 topics have been addressed through previous work at the CPMI (see Section 2.3), and this thesis falls into the fourth category – heat flux handling. In order to consider the concept a true solution to PFC issues, it must be proven in current device heat flux regimes of single digit MW/m^2, up to ITER conditions of ~10 MW/m^2, and eventually, DEMO power plant scenarios of 10s of MW/m^2.

This work will focus on examining the propensity for TEMHD-driven flow in several advanced geometries, with the overall goal of reducing or eliminating dryout. An investigation into the behavior of liquid lithium flow in these geometries branches away from the standard LiMIT concept, looking for methods of enhancing the viability of flowing lithium systems in transient high heat flux environments. The work presented herein provides evidence that this goal can be realized.

In addressing the fourth and final issue outlined above, this thesis will aim to tackle a final outstanding topic on the road to full systems integration. The combination of this and prior work will lead to and inform the development of a full-scale flowing liquid lithium loop system, including the dryout and ejection resistant plasma facing surface, lithium reservoirs and pumping, flow control, and lithium cleaning and degassing before reintroduction to the plasma.

The methods for increasing system performance under high heat flux impingement are framed in the context of advancing the development of fusion power, but the new geometries presented here are also applicable in several areas where thermoelectric currents are present in conductive liquid flow, including but not limited to metallurgy and liquid metal fission systems.

For fusion systems, this work applies to both passive systems like LiMIT, as well as slow-to-medium flow active pumping scenarios expected to be used in the first full lithium loop systems. In either case, the improved geometries will aid in viability of the system under high heat flux. Near-term application comes through collaboration with commercial fusion initiatives. As companies progress through an iterative design process building successively larger devices, they reach junctures where PMI becomes a major concern. For the solutions hoping to develop economical fusion power for the world, this technology can be developed to fit their PFC needs.

While the examples and experiments presented here showcase horizontal open surface flow, previous work on the LiMIT concept has shown that TEMHD-driven lithium flow can work effectively at any angle [65]. These new TEMHD geometries will be designed to be easily contoured to fit the surface of any wall or PFC, providing heat flux protection and mitigating the risk of dryout. The ultimate goal is improvement of fusion power production through inclusion of flowing liquid lithium surfaces throughout the interior of the vacuum vessel.

The goals of this work were approached using numerical modeling in COMSOL Multiphysics and experimentation in the SLiDE device at the CPMI at UIUC. Chapter 3 presents the background of the dryout phenomenon, early attempts at modeling the lithium depression, and describes the possibility of directly shaping the LiMIT trenches to combat dryout. The dryout solutions proposed as the main driver of this study are introduced in Chapter 4, along with the experimental and computational setup for investigating the development of TEMHD flow in the 2-D and 3-D adaptations of the standard 1-D LiMIT flow channels. Chapter 5and Chapter 6 detail the numerical and experimental results of the 2-D post TEMHD designs and 3-D foam TEMHD concepts, including high heat flux e-beam testing of the foam designs in Chapter 6. Chapter 7 describes a new multiphase model of TEMHD flow that captures the real motion of the lithium free surface. Finally, a summary of the work, discussion of the major results, and suggestions for continuing the development of novel geometries for TEMHD flow are presented in Chapter 8.

CHAPTER 3 – DRYOUT BACKGROUND

A remaining issue seen in open surface bulk flow lithium systems, and the focus of this work, is known as lithium dryout. Dryout typically refers to the onset of film boiling after a liquid system surpasses the critical heat flux [75]. For liquid metals, this usually pertains to liquid metal cooling in nuclear fission [76], [77], though some studies have begun to examine film boiling potential in fusion applications [78], [79]. In this case, dryout is used to refer to a different phenomenon relating to open surface flows. In applications where high localized heat fluxes exist, such as divertor heat stripes or transient events striking the first wall, large thermal gradients develop in areas of the lithium surface. These gradients drive high thermoelectric currents, which translates to TEMHD forces much larger than in the surrounding bulk. As the lithium responds to this higher acceleration, the increased velocity leads to a depression of the lithium surface, which has the potential to expose the underlying solid structure. Additionally, the liquid downstream experiences 'pileup' as the accelerated flow runs into the bulk lithium. A diagram of open surface dryout can be seen in Figure 3.1.

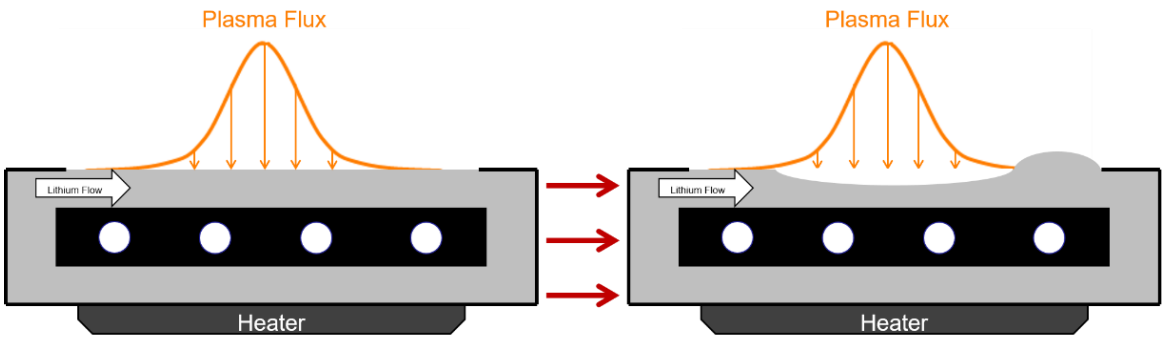

Figure 3.1 – A diagram depicting the development of lithium dryout and pileup in a LiMIT style system under high heat flux impingement.

Throughout the work presented here, dryout is used to refer to this exposure of solid structures under the liquid lithium driven by localized high TEMHD forces. If this occurs in large scale applications, overheating and damage to the underlying structures can occur, and the desire to protect the solid walls is one of the initial reasons for the use of liquid metal systems. The thinning lithium layer must also continue absorbing the same heat flux, leading to large increases in temperature and higher lithium evaporation.

The series of images shown in Figure 3.2 to Figure 3.6 illustrates the component physics that works to develop a dryout condition. These were adapted from a free surface simulation (see Chapter 7) where the volume forces in the fluid were disabled, and therefore fluid advection does not occur. This offers a clean/ideal example of the profiles that develop to cause lithium dryout, though note this is distorted once flow begins.

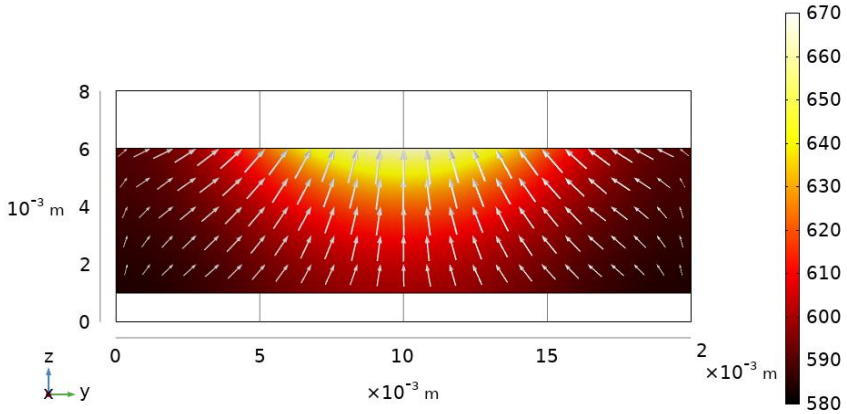

Figure 3.2 – Temperature plot from the side of a single LiMIT trench with high local heat flux impingement. The color map shows temperature in K and the arrows follow the temperature gradient, which is noticeably non-vertical in most places.

Figure 3.2 shows the temperature profile resulting from a Gaussian heat flux centered at 10 mm, with a standard deviation of 5 mm. The arrows display the direction of the temperature gradient. The TEMHD effect aims to utilize the purely vertical temperature gradient to drive flow down the channel, however, there is a distinctly non-vertical component to the temperature gradient profile on either side of the center. This is due to the non-uniformity of the heat flux and standard dissipation of heat through the lithium.

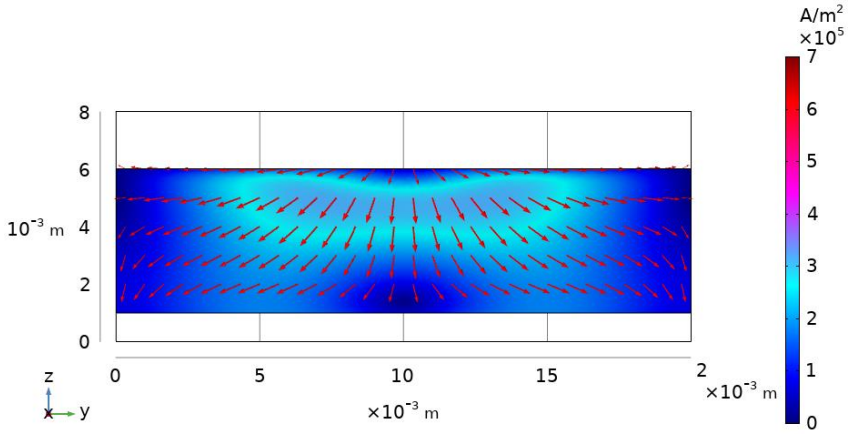

Figure 3.3 – Current density plot from the side of a single LiMIT trench with high local heat flux impingement. The color map shows current density in A/m^2 and the arrows follow current flow direction, highlighting non-vertical thermoelectric currents in the lithium.

The temperature gradients develop thermoelectric currents. Again, it is expected that a circulating current develops between the trenches and the lithium in the X-Z plane (the trenches are present over the same area of this image slice, 1 mm into and out of the page). Instead, the changing temperature gradients lead to the formation of non-zero currents in the Y direction, as shown by the arrows in Figure 3.3.

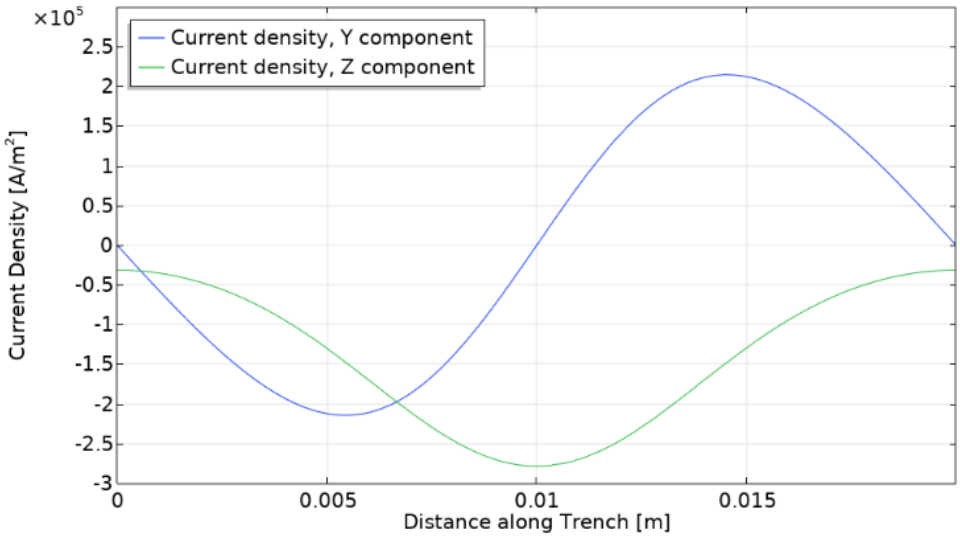

Figure 3.4 – Line plot of the Y and Z components of current density along the center of the simplified LiMIT trench. Solely Z-directed current is desired for TEMHD drive through the trench.

The relative strengths of the components of the current density are shown in Figure 3.4. Typical LiMIT-style TEMHD flow is driven by the Z-component. When localized heat fluxes are present, they can spur the existence of significant thermoelectric current densities in the upstream

(+Y) and downstream (-Y) directions. In this case, these suboptimal currents are approximately 75% of the magnitude of the primary flow-driving current.

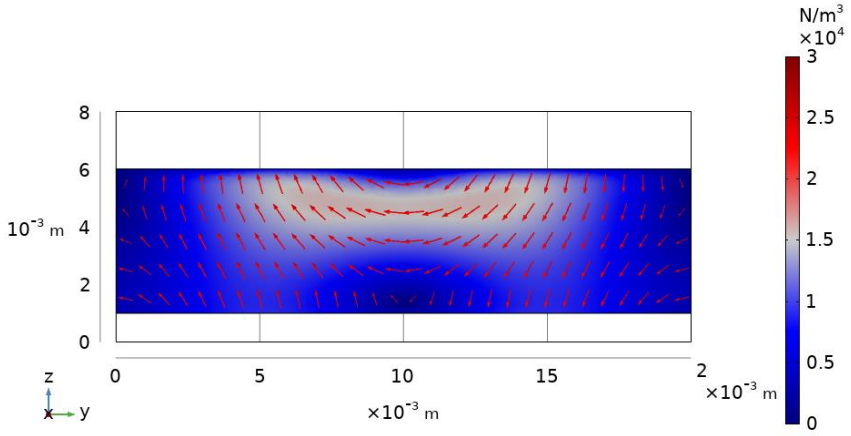

Figure 3.5 – Volume force plot from the side of a single LiMIT trench with high local heat flux impingement. The color map gives volume force magnitude in N/m^3 and the arrows follow the volume force direction, clearly displaying the forces that lead to the development of lithium dryout and pileup.

Obviously, this results in a less than ideal volume force distribution which acts to drive TEMHD flow. Figure 3.5 shows the strength of the resulting volume force, with the arrows displaying the downward dryout force on the upstream side of the heat load and the upward pileup force on the downstream side.

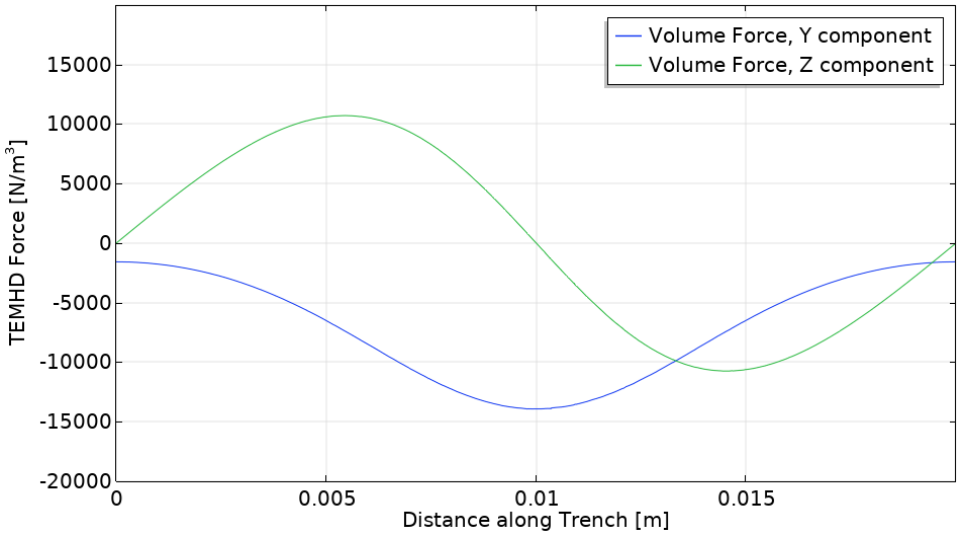

Figure 3.6 – Line plot of the Y and Z components of the volume force along the center of the simplified LiMIT trench. Y-directed volume forces drive standard TEMHD flow while the Z-directed forces act to depress or lift the lithium surface.

The line plot of the volume forces given in Figure 3.6 is closely related to the current plot seen in Figure 3.4, with different units. This shows the Z-directed TEMHD volume forces that arise due to spatially transient heat fluxes. The Y component still drives flow through the trench system as expected, but the considerable forces acting in Z work to disrupt the stability of the surface. When the fluid is in motion these profiles become skewed, generally downstream due to convection effects from the flow, but the potential for dryout remains.

3.1 Experimental Observations

Lithium dryout has been observed in the LiMIT system in both laboratory and larger-scale system testing. In the SLiDE system at UIUC (described in more detail in Section 4.2), the linear e-beam is capable of producing a theoretical maximum heat flux of 45 MW/m^2. Most LiMIT testing occurs between 1-3 MW/m^2 of topside e-beam heat flux, but tests have been done at heat fluxes ≥10 MW/m^2 to stress the limits of the device. Rapid departures from nominal operation during conditioning of the e-beam filaments can also occur, resulting in brief periods of heat flux >10 MW/m^2. This has led to experimental observation of dryout in SLiDE, seen in Figure 3.7, and melt damage to one version of the LiMIT trench module, seen in Figure 3.8. These images come from a 10 MW/m^2 heat flux test.

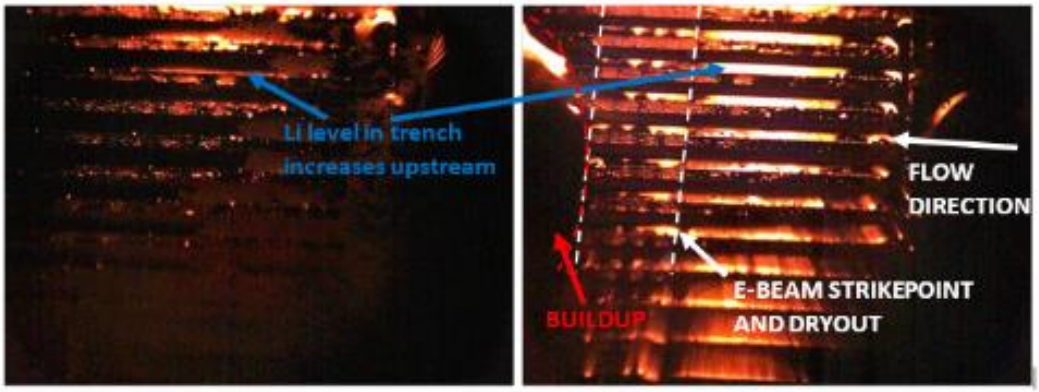

Figure 3.7 – Experimental observation of dryout in LiMIT trenches under e-beam heat flux at UIUC [80]. The left frame shows the stationary lithium flow level, and the right frame shows the dryout and pileup during e-beam operation.

Figure 3.8 – Melt damage on a LiMIT trench module due to 10 MW/m^2 e-beam heat flux driving lithium dryout and exposure of the underlying solid substrate [80].

In the beginning of the video from which the images in Figure 3.7 are pulled, lithium sits stationary slightly under the level of the trenches. This is the static case shown in the left image. While this test begins in an underfilled scenario (lithium level starts below the level of the trenches), the characteristic behaviors of lithium dryout conditions are seen. As the flow begins, lithium velocity increases in the e-beam strike point region and lithium buildup occurs downstream. The right image shows the LiMIT module shortly after flow begins and includes the 2 to 3 mm buildup from the high velocity lithium exiting the e-beam region, small waves in the e-beam region from the accelerating flow, and ~1 mm increase in upstream lithium height. As the video progresses, the pileup is drained out from the downstream region through the return flow channels. The 1 to 1.5 mm lithium depression formed in the high heat flux region persists through the video and high velocity flow continues downstream of the impingement area.

Another example of dryout observed in experimental testing occurred in LiMIT tests under high heat loads at Magnum-PSI [68]. Due to the larger heat flux spread from the linear plasma device, an apt comparison is not as direct. However, lithium dryout and pileup are still seen qualitatively in the image in Figure 3.9. The infrared snapshot from a video of one of the Magnum PSI tests of the LiMIT module shows trenches becoming more visible as lithium thins above them and they receive more heat from the plasma. The trenches become visible from the top left to the bottom right of the 'Progressing Dryout' region as the test progresses. Due to small recirculation

channels in this version of the LiMIT apparatus, pileup occurs downstream, but does not drain as in the test in Figure 3.7. This is indicated by the disappearance of the trenches in the 'Pileup' region of the IR image.

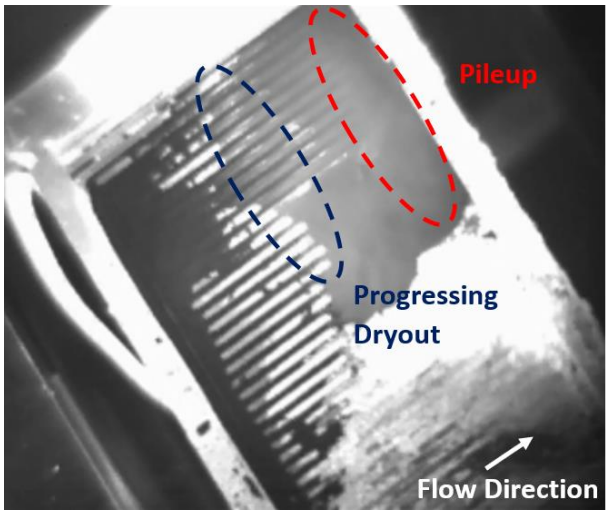

Figure 3.9 – Infrared camera image of dryout beginning during LiMIT testing at the Magnum PSI linear plasma device [68]. Trenches progressively become more visible as they heat up due to the lithium level reduction. Note that there is still lithium coverage throughout most of the device, though it is being reduced in the indicated region. Though some trenches appear fully uncovered, this is due to the differences in emissivity between lithium, stainless steel, and surface impurities.

3.2 Numerical Observations

Computational studies [64] of the flowing liquid lithium in the LiMIT system have generally constrained the lithium in a rigid domain. While this may be fully accurate if the liquid is truly constrained, such as in pipe flow, the solution lacks completeness when an open surface exists. Fluids slosh around when forces act upon them, and this behavior cannot be captured when a rigid domain is used. The usual solution is to make the top surface a slip boundary condition, which mimics an open surface by eliminating the frictional force from the walls. This treatment is generally effective in describing flow conditions, and has been used to model and predict flow velocities in LiMIT trenches [64]. However, the shape of some velocity profiles in constrained surface flow models imply a dryout condition would occur.

To that end, initial modeling of the dryout phenomenon used COMSOL Multiphysics to develop a 2-D simulation approximating free surface lithium flow under high heat flux, with the goal of replicating the dryout phenomenon and taking steps to alleviate it.

3.2.1 Model Setup

The preliminary simulation work shown here, first developed for [71] and refined in [81], helped solidify the need for further study on dryout reduction in open surface liquid lithium PFCs. The simulation was performed in a 2-D simplified domain in COMSOL v4.3. In order to reduce computational constraints, a 2-D slice of a 3-D trench is modeled in the domain shown in Figure 3.10. Previous modeling of TEMHD flow in the LiMIT system relied on a fixed topside lithium boundary that approximated an open surface by including a slip boundary condition. In order to accurately capture the behavior of the free surface, this model simplifies the system to 2-D and couples the Laminar Flow (LF) interface with the Moving Mesh (MM) interface.

For the two test cases presented here, 1 cm/s and 10 cm/s flow, the Reynolds number is 50 and 500, respectively, allowing the laminar flow interface to be used. Assuming a steady state flow case with low 500 K/m temperature gradient before a topside heat flux is introduced, this corresponds to a magnetic field of 1 T and 0.05 T. The Single Phase Flow, Laminar Flow physics interface solves the Navier-Stokes continuity and momentum equations to find the pressure and velocity field of the liquid [82]. Assuming incompressibility, these equations become

$$\rho \nabla \cdot \boldsymbol{u} = 0$$

$$\rho \frac{\partial \boldsymbol{u}}{\partial t} + \rho(\boldsymbol{u} \cdot \nabla)\boldsymbol{u} = \nabla \cdot [-p\boldsymbol{I} + \mu(\boldsymbol{\nabla u} + (\boldsymbol{\nabla u})^T)] + \boldsymbol{F}$$

Where ρ is the density, $\boldsymbol{u}$ is the velocity vector, p is the pressure, $\boldsymbol{I}$ is the identity matrix, μ is the dynamic viscosity, and $\boldsymbol{F}$ is the force vector. The inlet and outlet are included using zero pressure boundary conditions with suppressed backflow. An attempt was made to link the inlet and outlet using a periodic flow condition, but the dryout deformation passing from the outlet to the inlet side of the domain caused errors to amass and the solution to diverge. The top surface is a free surface modeled as an open boundary with 0 normal stresses on the surface. The bottom surface is a no slip boundary condition.

The development of the thermoelectric current is dependent on the junction between the lithium and a wall, and inherently 3-dimensional (looping into and out of the page in the domain view), and therefore the full coupling between heat transfer, magnetic field, and electric currents cannot be included via physics modules in this model. Instead, a Gaussian volume force term is

included in the LF interface that takes the entirety of the TEMHD effect into account. In a 3-D domain, a Gaussian heat flux leads to a thermoelectric current, which in turn is used to calculate a volume force. In COMSOL post-processing, the volume force data was examined. The vertical volume force is a combination of the velocity and fluid effects, as well as the errant thermal gradient effects. From 3-D simulations, the volume force data was extracted and input into this 2-D domain, in the form

$$F = F_{max} \exp\left(\frac{-(x - x_{centerpoint})^2}{FWHM^2}\right) \left[N/m^3\right]$$

The F_{max} value for the slow 1 cm/s flow case is set at 10 N/m^3, mimicking a 1 MW/m^2 peak heat flux, while the F_{max} for the medium flow 10 cm/s case is set to 1000 N/m^3, indicative of a 3 MW/m^2 peak heat flux. These values are based on 3-D fixed surface models of a LiMIT trench.

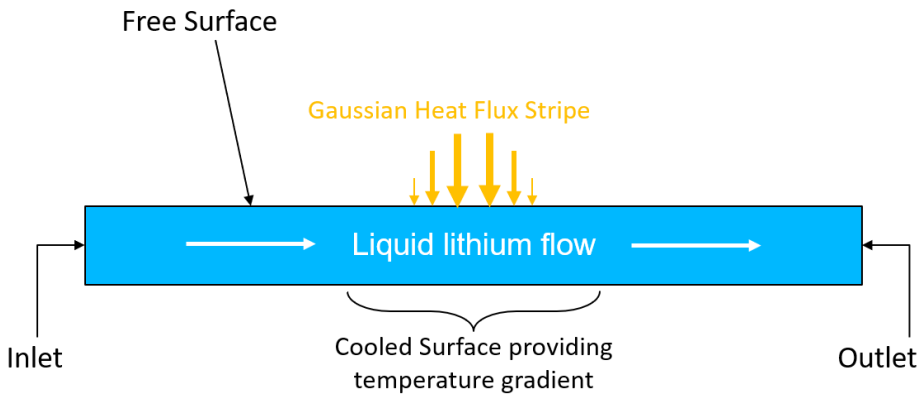

Figure 3.10 – 2-D COMSOL domain used to simulate the dryout phenomenon. The top surface is modeled as a free surface and the Moving Mesh interface allows deformation to follow liquid motion.

The MM interface allows the free surface to deform in response to the fluid flow on the top surface. This allows the mesh movement to be coupled with the driving force provided by the TEMHD effect. Typically, physical systems are set up and solved computationally in one of two coordinate systems. The spatial coordinate system, known as the Eulerian formulation, fixes the coordinate axes in space, and the material coordinate system, known as the Lagrangian formulation, fixes the coordinates to the reference material and follows the material as it deforms. For fluid solutions, the Eulerian formulation tends to be more convenient, since following the particles becomes quite computationally intensive. However, since the grid points are fixed to a

spatial system, an Eulerian method cannot follow moving domain boundaries, which are a staple in open surface flow. One way to get around this problem is to use a convenient feature that is always included in COMSOL – the mesh. The mesh points created in COMSOL have a direct mapping to material domain points. Therefore, if the mesh were to deform and follow the mobile domain, it is possible to use an Eulerian mapping to solve for a deforming Lagrangian-type system. This is known as an arbitrary Lagrangian-Eulerian (ALE) process, and it is included as the solver in the MM interface [82]. As the domain deforms, the mesh is stretched and compressed along with the domain motion. While this deformation can cause degradation of the mesh quality that can lead to a buildup of solver error, small disturbances can be effectively solved with a fine mesh.

Implementation of the MM interface requires choosing what boundaries and domains can deform, and in what way. For this system, there is only one domain, which is allowed free deformation. In order to constrain that deformation, and hold it in its trench shape, prescribed displacements are used on the edges. The bottom surface is a no slip surface that has a prescribed displacement of 0 meters in both the horizontal and vertical directions. This keeps the bottom fixed at all times. The inlet and outlet edges on the sides of the domain have a prescribed displacement of 0 meters in the horizontal direction, and no constraint vertically. This allows the edges to follow any vertical motion in the domain, such as dryout or pileup, while still acting as a fixed inlet or outlet. The free surface on the top, meanwhile, is modeled using a prescribed mesh velocity. Velocities solved by the laminar flow interface are coupled with this step, and the mesh deforms to match the true behavior of the fluid in the horizontal and vertical directions.

Using the arbitrary Lagrangian-Eulerian system to solve for a variable v, COMSOL defines a frame time derivative on the spatial frame, and a mesh time derivative on the fixed mesh points

$$v_t(x_0, y_0) = \left.\frac{\partial v}{\partial t}\right|_{x_0, y_0}$$

$$v_{TIME}(X_m, Y_m) = \left.\frac{\partial v}{\partial t}\right|_{X_m, Y_m}$$

And relates them using

$$v_t = v_{TIME} - v_x x_{TIME} - v_y y_{TIME}$$

Where (x_{TIME}, y_{TIME}) is the mesh velocity. Within deforming domains, a mesh displacement equation is solved to determine how the region deforms. A Winslow smoothing algorithm is chosen to deform the mesh, which leads the software to solve

$$\frac{\partial^2 X}{\partial x^2} + \frac{\partial^2 X}{\partial y^2} = 0 \ \ and \ \ \frac{\partial^2 Y}{\partial x^2} + \frac{\partial^2 Y}{\partial y^2} = 0$$

Here X and Y are the material frame coordinates, and x and y are the coordinates of the spatial frame [82]. Solutions in 2-D require less memory, so a MUMPS direct solver is used to solve the fully coupled system.

3.2.2 Model Results

The model was run for up to 3 seconds after heat flux impingement begins. Two separate cases were examined, a slow flow case with 1 cm/s velocity, and a fast flow case where the velocity is 10 cm/s. These can be thought of as low heat flux and high heat flux cases, as the volume force is adjusted accordingly based on the amount of flux the flow speed can handle. The system is initialized with aforementioned velocities, as though lithium flow was established using an alternative heat flux, such as heaters on the bottom of the trench. The impingement heat flux is centered at 0 centimeters in the domain and starts at t = 0 seconds.

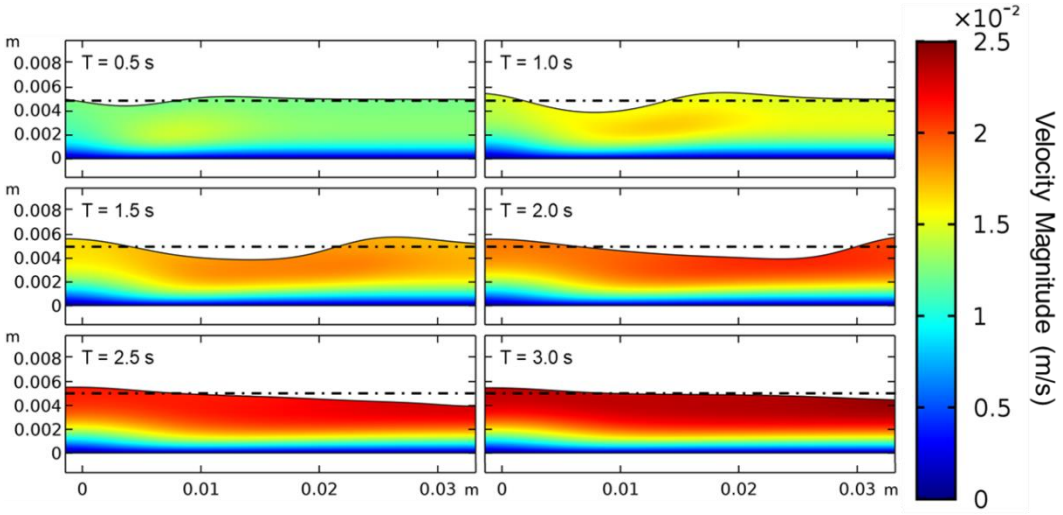

Figure 3.11 – Frame-by-frame (every 0.5 seconds) results of slow flow dryout development. Initial velocity is 1 cm/s. The color map shows flow velocity, and the dotted line marks the trench level/nominal lithium level.

The slow flow case is shown in the series of images in Figure 3.11. Again, the color map represents lithium velocity. As the simulation begins, the dryout begins to form in the center,

directly under the highest heat flux. This is due to the preferential heating of the lithium in the depressed region, which is then accelerated by the large thermal gradient resulting from passing through the heat stripe. The dryout is then propelled down the trench by the flow. Lithium pileup occurs downstream of the high heat flux region, as high velocity lithium accelerates into slower downstream flow. As this reaches the end of the trench, spillover could occur, damaging other components that are not necessarily compatible with the hot liquid lithium. It is also interesting that as the dryout forms, there is upstream buildup that occurs during its transient development. This is due to lithium building up against the reduced cross-sectional area of the flow before accelerating through the high heat flux region. Additionally, as the initial heat flux impact depresses the lithium surface, the pressure from that quick acceleration extends in both directions. This causes upwelling on either side of the depression like when a rock impacts shallow water and the entire area around it wells up before splashing. This effect starts the upwelling, and the continuation of flow into these regions helps maintain the pileup.

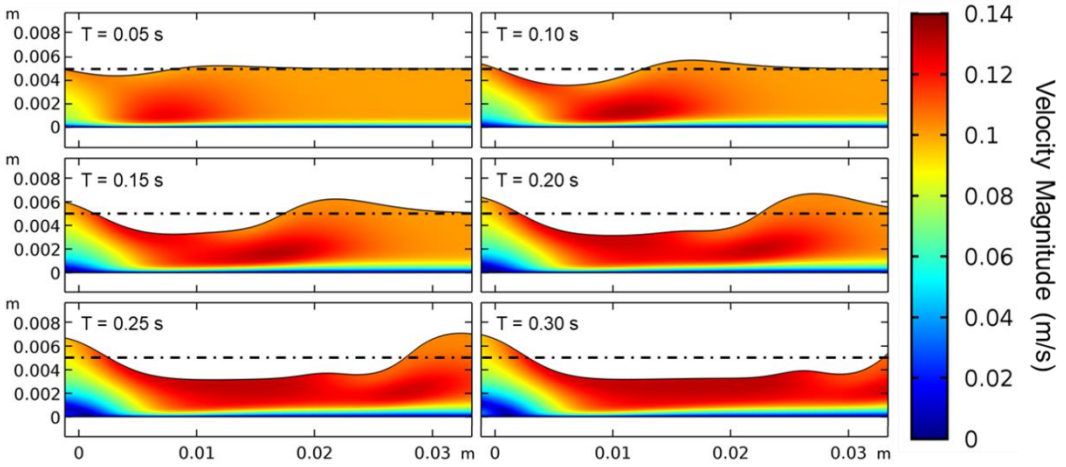

Figure 3.12 – Frame-by-frame results (every 0.05 seconds) of fast flow dryout development. Initial velocity is 10 cm/s. The color map shows flow velocity, and the dotted line marks the trench level/nominal lithium level.

The fast flow case exhibits the same behavior, albeit faster than the slow flow tests. The set of images describing this case is given in Figure 3.12. Dryout forms under the heat flux region and extends downstream. The pileup quickly moves toward the end of the trench, and eventually leaves the domain, meaning half of the length of the trenches are potentially exposed. Note any lithium level below the initialized 5 mm will expose trench material.

These models directly mimic what has been observed in experimental testing. While the tests shown above were not originally set up to measure dryout, so the video quality is not

conducive to quantifying the exact height, the 1 to 3 mm buildup in the model is very similar to what is seen in experiment. Lithium depression on the order of 1 to 2 mm also matches the experimental cases. The domain setup in this case more closely mirrors the LiMIT setup at UIUC, where there is ample drainage for the initial downstream pileup and the dryout propagates downstream from the high heat flux region with some rippling effects due to the initial impulse. The model also shows the upstream upwelling seen in the LiMIT testing.

3.3 Trench Shaping TEMHD

Originally, ideas for protecting the LiMIT system against dryout centered around shaping the trenches, such as machining or inserting material in the bottom of the trenches to adjust flow or reducing the height of the trench walls underneath the highest heat flux region. The simple concept of a single step height increase in the bottom of the trench proved to be an effective solution. The trench step-up was slightly offset from center to allow the liquid buildup from impact on the obstruction to occur directly underneath the highest heat flux area. This fluid level increase could help provide extra thermal protection to the trenches in the most intense regions. The increase in the height of the bottom of the trench maintained a higher lithium level throughout the remainder of the trench, combating the extension of dryout downstream of the highest heat flux region.

3.3.1 2-D Modeling

While an exact experimental comparison may not be possible due to the 2-D nature of the model and the simplifications it requires, the behavior captured in this model provides a starting point for engineering decisions regarding a solution to the dryout problem. Of the potential mitigation strategies described above, perhaps the most straightforward is shaping the bottom of the trenches, either by machining or inserting additional material into the bottoms of the trenches. This method is also testable in the COMSOL model. The effect of trench insert shapes can be investigated before real world application. This allows for quick iteration through possible designs. Several different strategies were tested, and while they may have provided a solution to the dryout, in most cases the eventual return to original trench depth caused a small waterfall-like depression in the lithium surface. This may be acceptable since the depression occurs outside of the high heat flux area, but for now that effect was avoided.

It appears what may be one of the simplest ideas could become an effective solution to the dryout effect. A simple step increase in the height of the bottom of the trench provided multiple benefits in both the slow and fast flow cases. First, the extended region of the narrowed trench height directly combated the extended region of the dryout by compensating for the depression caused by the high velocity flow. Second, the slight offset from center allowed the buildup that generally occurs in front of underwater flow obstructions to be placed directly underneath the area of strongest heat flux. The initial strong depression of the surface is directly opposed by this upwelling from the trench step, providing additional thermal protection of the underlying solid trenches. Third, the height of the pileup above the dryout is diminished. In other words, deviations from an average flow height are decreased. Instead the bulk flow from the center of the trench continuing downstream is raised slightly, which will not severely impact flow velocity and will also provide more protection for the trenches.

The strength of the above effects varies based on the magnitude of the trench-bottom height increase. This was investigated with the COMSOL model by running a parametric sweep over the height of the step increase. The height was varied from 0.3 mm to 3 mm (initial depth is 5 mm) with a step of 0.3 mm, and various metrics of the flow properties were extracted for each parametric solution. These parameters of the flow are diagramed in Figure 3.13 for clarity.

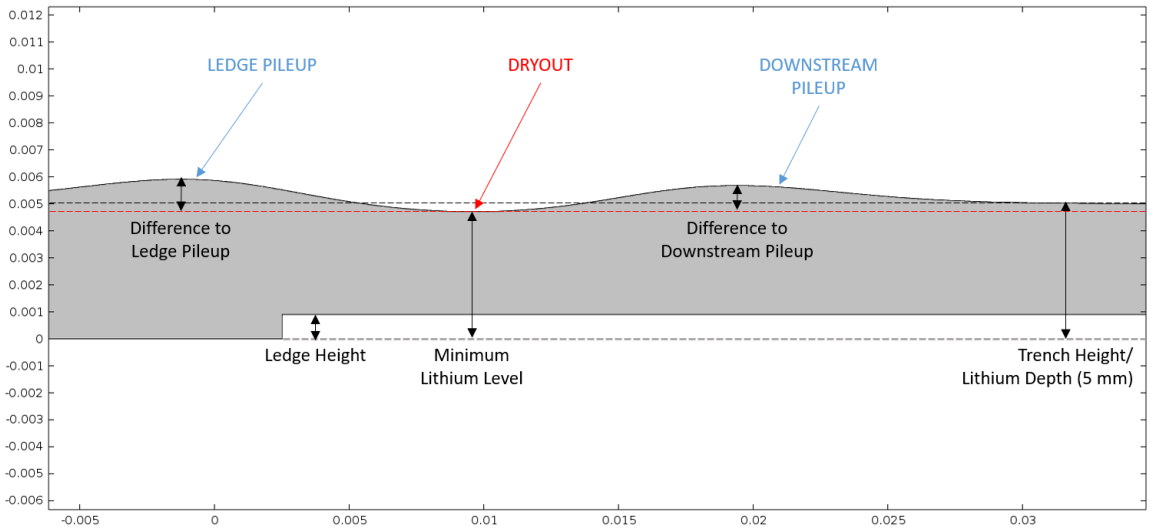

Figure 3.13 – Diagram of different flow metrics measured during testing of trench shaping dryout mitigation techniques in the COMSOL model.

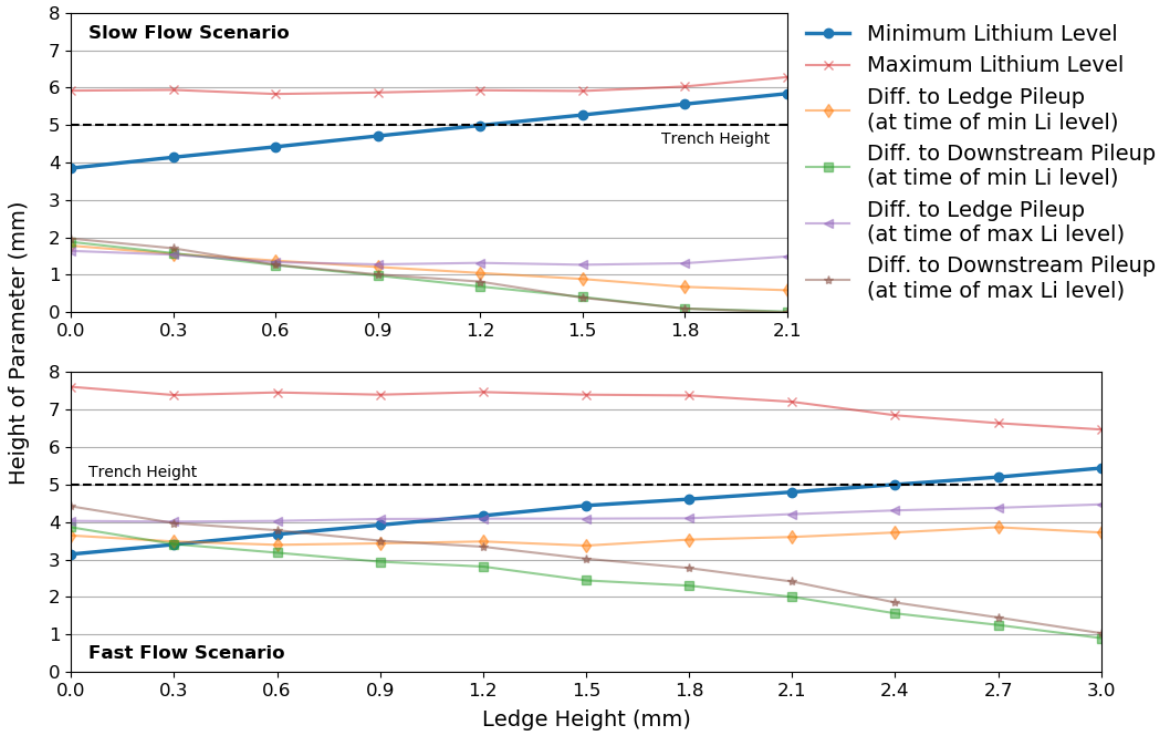

Figure 3.14 – Change of various dryout-relevant metrics measured from the parametric COMSOL study of increasing ledge height bottom in the bottom of the trench. Refer to Figure 3.13 for a diagram of the metrics plotted. Minimum lithium level is the most important me measure of dryout, as the lithium must stay above the solid trench material. The maximum lithium level indicates the highest levels of pileup – this should be kept low to minimize risk of droplet ejection. The remaining values represent the peak to peak differences in lithium level when dryout is most severe (min Li level) and when pileup is most pronounced (max Li level).

The results of the parametric analysis are presented in Figure 3.14 for the slow flow and the fast flow scenarios. First, it is worth noting that the trends plotted above for the slow flow case terminate at a step size of 2.1 mm. At heights greater than 2.1 mm, the dryout minimum fully disappears, and the upwelling caused by the trench step just pushes downstream into the small initial downstream pileup. At this point, the ledge effect causes lithium to rise several millimeters above the initial level, so these heights are discounted. As expected, increasing the ledge in the bottom of the trench helps to decrease the minimum lithium level. By a height of 1.5 mm, the minimum is above the level of the 5 mm trench, meaning dryout would be avoided. One can also see that while the pileup slightly increases, the difference between the maximum and minimum lithium level continues to drop as ledge height increases. While the ledge effect pileup keeps increasing, for a 2.1 mm ledge the lithium height is still within 3 mm of the trench, which should provide good protection for the trenches in the high heat flux region without causing too much turbulence. After consideration of the trends, 1.8 mm seems to be an ideal height for the trench

ledge. At this height, there is a very small difference between the maximum and minimum lithium levels at both time of minimum and time of maximum. The ledge and downstream pileups are limited, while ensuring the dryout minimum stays above the level of the trenches. In all cases, the recirculation zone or drain area should be expanded to account for inevitable lithium pileup. However, instead of being a single wave, the lithium level will be relatively sustained. To further illustrate the ledge effects, the series in Figure 3.15 shows the comparison between step sizes using the same time step for each of the tested ledge heights, up to 2.1 mm, and Figure 3.16 gives an example of how the flow develops in time for one of those ledge heights (1.8 mm).

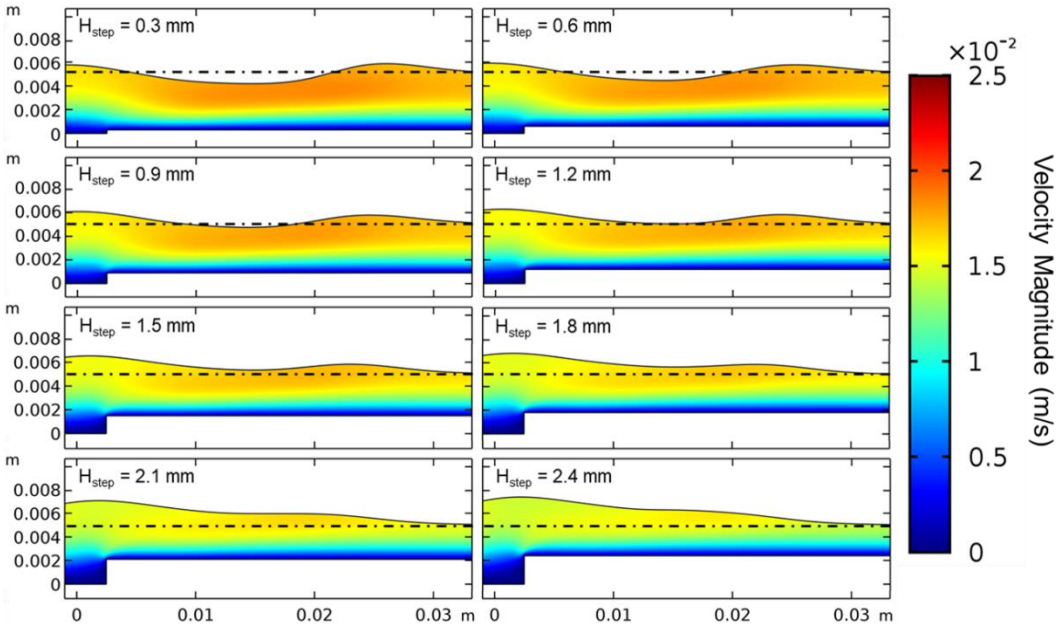

Figure 3.15 – The same time step (1.5 seconds) presented for differing trench ledge heights, showing the mitigating effect trench shaping has on development of dryout. The color map shows flow velocity (initial 1 cm/s velocity), and the dotted line marks the trench level/nominal lithium level. Refer to Figure 3.11 for a reference dryout case with no trench shaping.

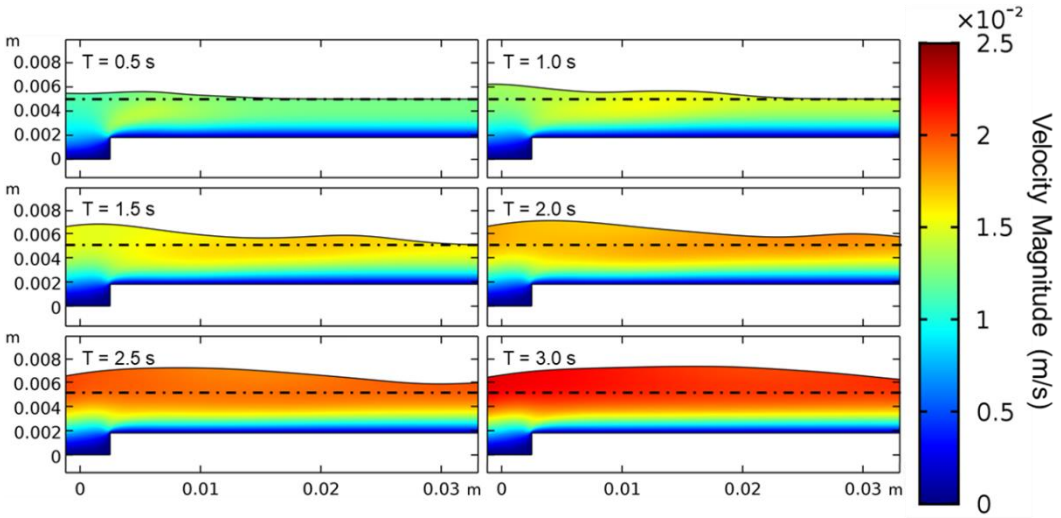

Figure 3.16 – Frame-by-frame (every 0.5 seconds) of the best case for slow flow dryout mitigation using trench shaping (1.8 mm insert). The color map shows flow velocity (1 cm/s initial velocity), and the dotted line marks the trench level/nominal lithium level.

For the fast flow case, the high velocity makes for a more turbulent scenario. High ledge effect lithium levels are unavoidable, but again, this helps to protect the trenches facing the largest heat fluxes. It takes at least a 2.4 mm step increase in the height of the bottom of the trench to fully counteract the effect of dryout. This is expected, since the higher heat flux and faster velocity should combine to create a stronger dryout scenario. In this fast flow case, the maximum pileup tends to decrease slightly as ledge height is increased. While the ledge effect lithium level keeps increasing, it does not adversely affect the drainage like the downstream pileup would, so it is decided that a ledge height of 2.7 to 3.0 mm would work for a high heat flux, high velocity case. These heights maximize dryout alleviation and minimize downstream pileup.

3.3.2 3-D Fixed Surface Modeling

In the interest of examining the relationship of the 2-D moving mesh and the 3-D constrained surface models, some test cases were run using the fully coupled 3-D model described in Section 4.3. Similar transient behavior that would drive ledge pileup is seen as the flow develops in the constrained model (Figure 3.18 and Figure 3.19). Note that these simulations were run with much higher bottom side temperature conditions, which acts to drive rapid recirculation channel flow.

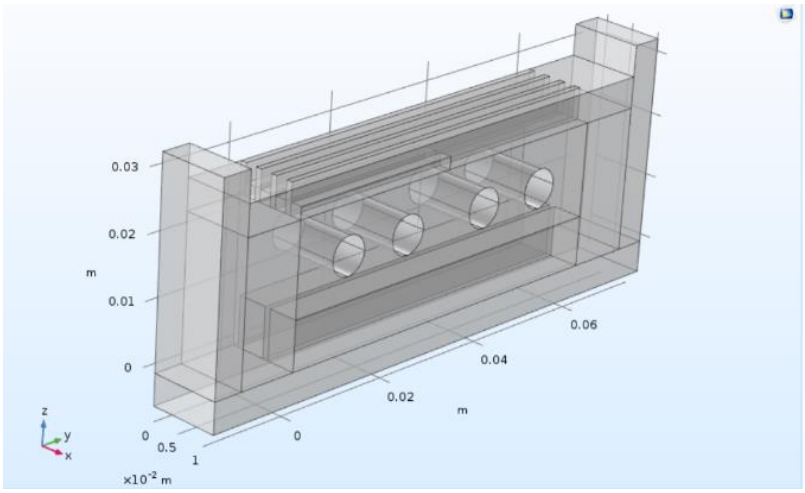

Figure 3.17 – Standard COMSOL model domain for trench shaping TEMHD. The ledge inserts can be seen along one half of the trench bottoms.

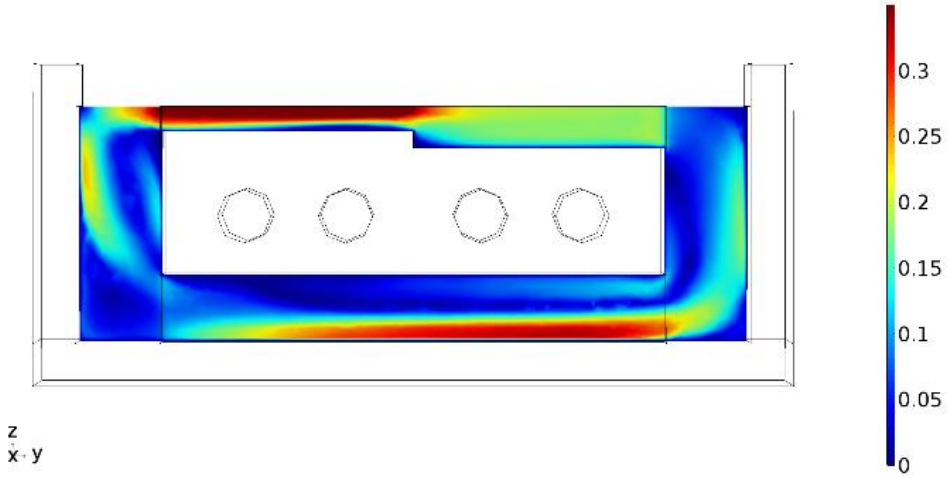

Figure 3.18 – Representative case of TEMHD flow in an 'exact fill' trench shaping simulation. The step causes high velocity lithium flow against the constraining top surface, but no heat flux turbulence/indicated dryout is seen. Note that this simulation includes larger bottom side heating than other simulations presented, resulting in higher recirculating flow velocities. Color bar gives velocity in m/s.

The lithium begins to well up around the ledge but remains locked by the top lithium surface. High speed lithium flow continues through the downstream half of the trench without eddies or turbulence, suggesting the ledge is dominating flow characteristics rather than the central heat flux. In the overfill case seen in Figure 3.19, there is stronger swirling flow due to the temperature gradients through the lithium.

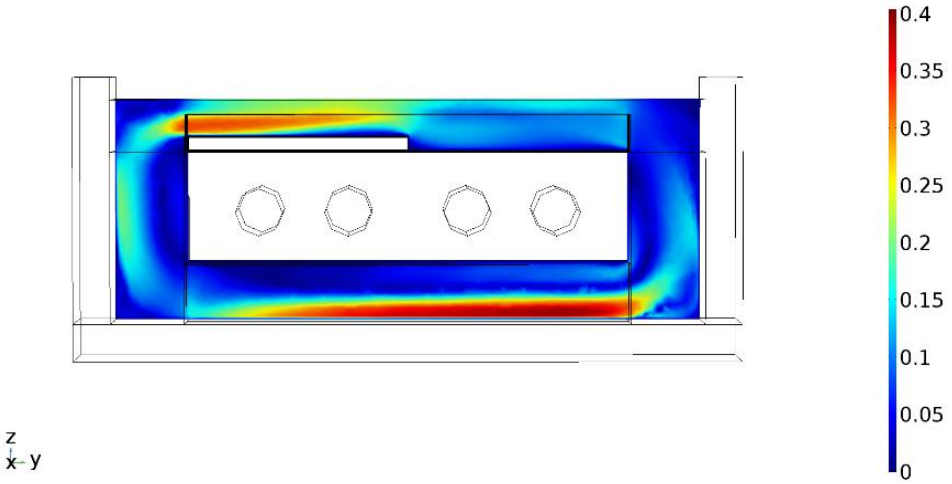

Figure 3.19 – Representative case of TEMHD flow in an 'overfill' trench shaping simulation. The higher top constraining surface allows for better visualization of the expected liquid jump over the step. Note that this simulation includes larger bottom side heating than other simulations presented, resulting in higher recirculating flow velocities. Color bar gives velocity in m/s.

The higher lithium level indicates low levels of dryout may still be possible as the flow develops. This is believed to result from the fact that the flow is starting from rest when the high topside heat flux is initiated. In contrast to the 2-D simulations, which had a velocity field already established, the no-flow start condition allows the top heat flux to dominate flow startup and cause dryout. As flow develops toward the 1 second simulation end, expected flow profiles develop. To gain better confirmation of trench shaping as a viable option for dryout mitigation, the 3-D simulations should be allowed to develop a steady flow profile before top heating is enabled. This would also more closely resemble actual experimental conditions, where the flowing liquid lithium PFCs would be in operation before device startup.

While the trench shaping shown above may have the ability to reduce the risk of dryout, the solution is limited in scope due to the precision required in the design. The ledge placement must be accurate to within 1-3 cm, or the liquid response from the step height will not be impacted by the highest heat flux and dryout could occur. Any shift in divertor configuration would lessen the effectiveness of this trench shaping, and transient events elsewhere on the wall cannot be predicted and therefore cannot be protected against. Thus, geometries with a more inherent resistance to dryout must be explored.

CHAPTER 4 – METHODOLOGY

The conceptual design behind adapting the LiMIT system to increase resistance to dryout focuses on modifying the standard trench geometry. The progression of module design begins with simple adjustments to the standard LiMIT concept and proceeds toward progressively complex geometries. Initially, dryout protection ideas were centered around shaping the trenches, such as machining down the trench walls or inserting material into the bottom of the trenches. Further improvements entail extending the geometry from the standard 1-D LiMIT trenches to 2 and 3 dimensions of flow channels, resulting in the post TEMHD and foam TEMHD concepts. In order to demonstrate effective flow in these systems, computational modeling and experimental testing were undertaken. These sections describe the design and manufacturing of the new test modules, including the modeling and experimental setup.

4.1 Advanced Geometries for TEMHD Flow

Brief descriptions of the several types of LiMIT system geometry modification are given here, along with the general goals that type of modification is aiming to achieve. For a more detailed examination of the modeling behavior and experimental performance, refer to the respective sections of the following chapters.

Shaping the LiMIT trenches was an early concept for potential dryout mitigation that was explored briefly in Chapter 3. Trench shaping TEMHD provides a simple change to the LiMIT system that could provide enhanced heat flux resistance. Initial modeling suggested that the simplest solution may be the most effective. Placing a single step increase in the bottom of the trench could offer a jump in lithium height that would counteract lithium dryout. The adjustment could be an insertable retrofit to current LiMIT systems which would not require a full redesign of the flow driving open surface. Modeling of step height can inform the design of trench adjustments based on initial trench geometry and expected device conditions. An example of a trench set with a step height increase is shown in Figure 4.1. Ultimately, the precision required in both PFC design and plasma-shaping control led to other, more generally applicable avenues of geometry adjustment to be explored in more detail.

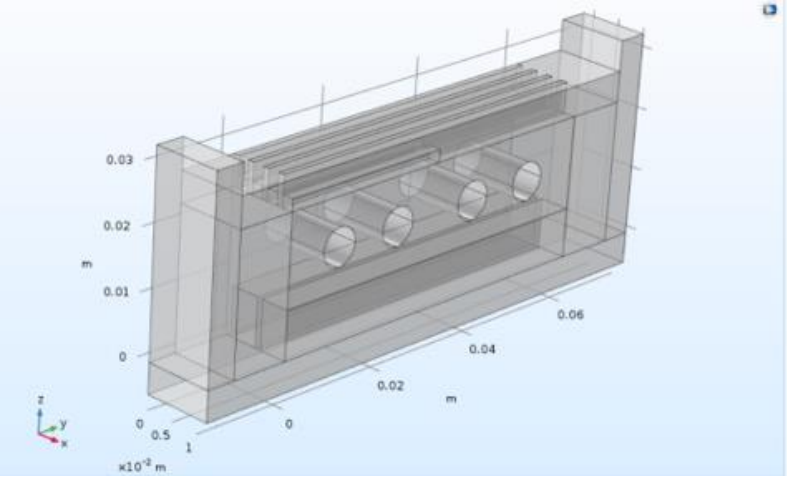

Figure 4.1 – Standard trench shaping design, using inserts in the bottom of the trenches to help resist the formation of dryout.

The post TEMHD design is meant to maintain the capillary action and surface tension forces that stabilize the liquid lithium surface, while introducing passages perpendicular to the main flow direction. The posts still provide an anchor for the lithium surface and maintain the resistance to droplet ejection. The passages reduce the amount of solid material directly under the heat stripe, lessening the potential for damage. The post system also enables crosstalk between the predominant flow channels. This reduces the isolation of a 1-D LiMIT trench and allows regions outside of the highest heat flux to more effectively refill the area under direct impingement. To study the effects of post size and spacing, 3 main post geometries of interest were designed, including 1x1 mm posts with 2 mm spacing, 2x2 mm posts with 2 mm spacing, and 2x2 mm posts with 4 mm spacing. These designs are shown in Figure 4.2.

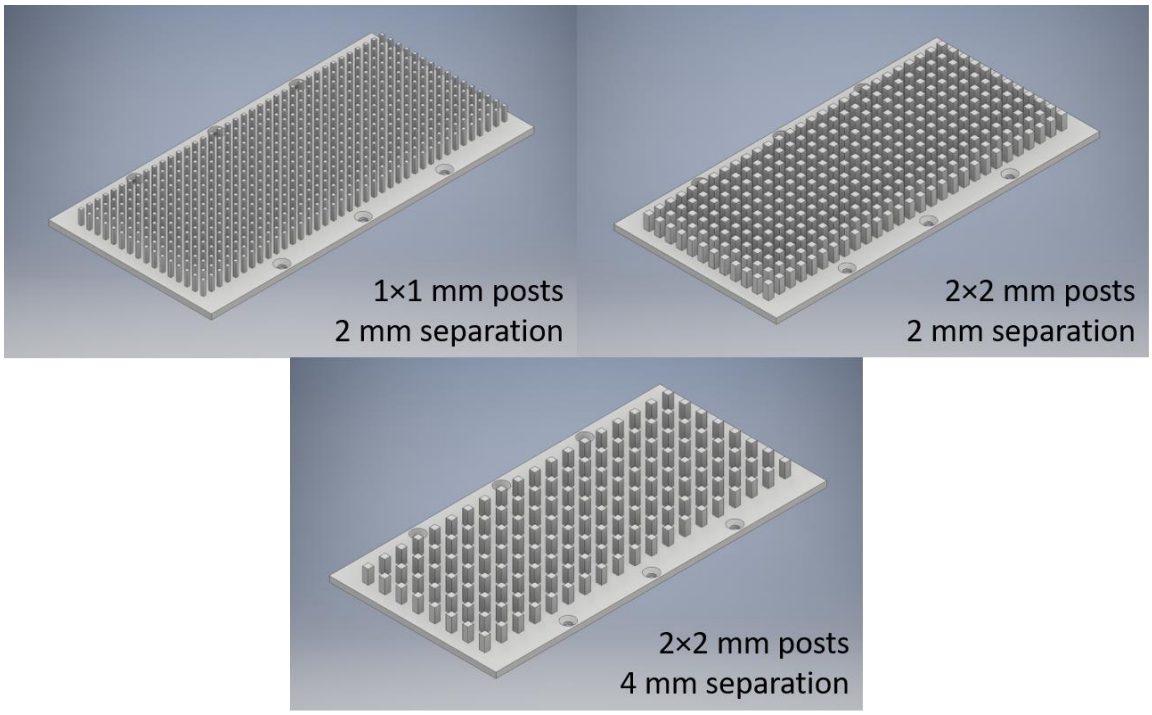

Figure 4.2 – Designs for 3 post TEMHD geometries machined onto base plates for testing in SLiDE with the modified base module.

The 3-D foam TEMHD concept aims to capitalize on the advantages of both LiMIT and CPS systems. Development of large pore foam enhances capillary action without a large impact on the TEMHD driving force, allowing flow to accelerate through the system. Extending the LiMIT concept to 3 dimensions allows for flow along all 3 major axes. The design will improve surface stability, both through stronger capillary action helping resupply the surface and through the 3-D nature of the foam arresting the characteristic dryout depression. Coupling this with sustained flow solves the passivation, evaporation, and ablation issues with CPS systems. Both disordered and ordered base foams were considered for this work. Disordered foams have a randomized structure, and the most easily controllable geometry parameter is pores per square inch (ppi). Several samples of disordered foam, from 3 ppi to 45 ppi, were considered; see Figure 4.3.

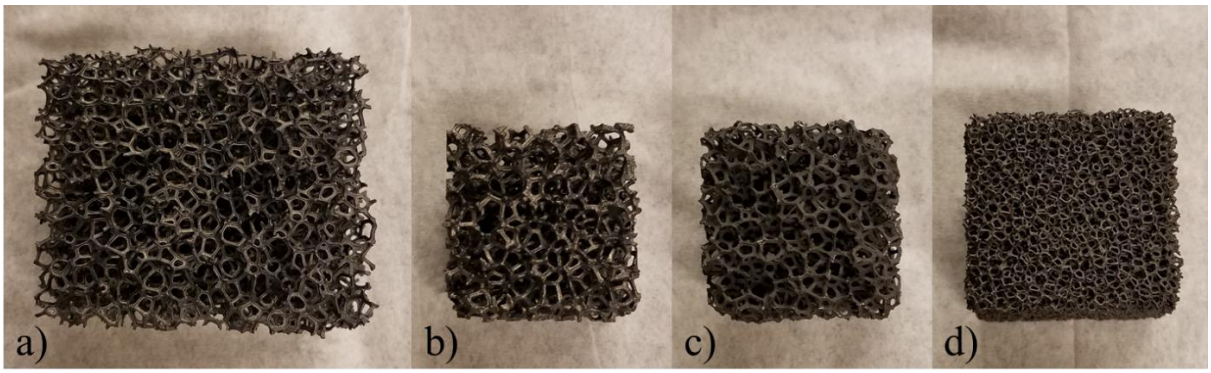

Figure 4.3 – A range of high-porosity SiC foams procured from Ultramet. Sample sizes are a) 3 ppi, b) 10 ppi, c) 20 ppi, and d) 45 ppi.

The ordered foam design focuses on improving machinability and heat transfer through a foam, while still utilizing the benefits of the 3-D structure. Arrays of wires or mesh are organized in a regimented cubic pattern. In this case, both wire size and separation can be controlled. Concepts to be studied include a 0.5x0.5 mm mesh structure with 3 mm separation in all directions, a 1x1 mm mesh with 3 mm separation, and a 1x1 mm mesh with 2 mm separation. See Figure 4.4 for examples of these designs.

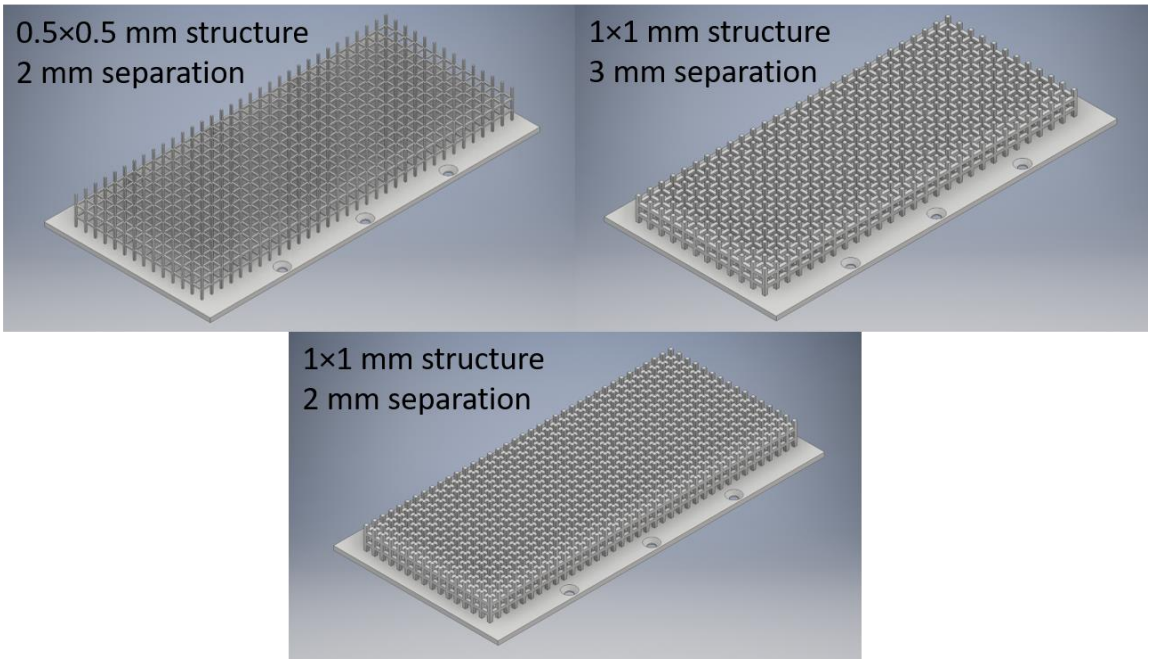

Figure 4.4 – Designs for 3 ordered foam geometries machined onto base plates for testing in SLiDE with the modified base module.

4.2 Experimental Setup

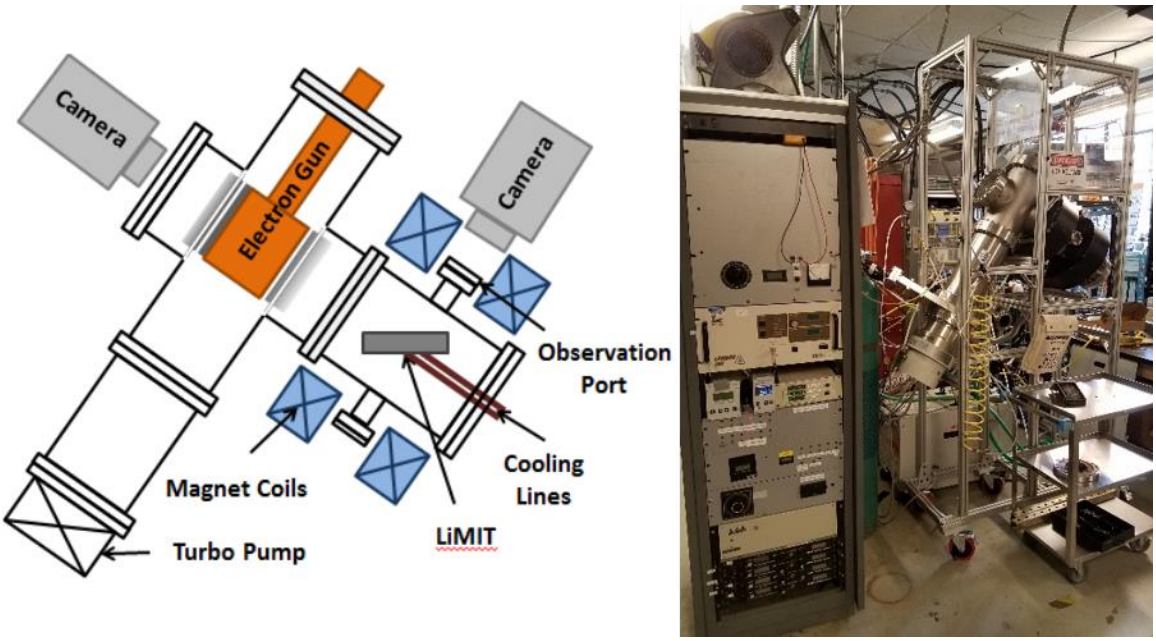

Figure 4.5 – The SLiDE chamber is a test stand for the LiMIT system, including an e-beam for heating, Helmholtz coils for e-beam focus and TEMHD drive, and module heating and cooling systems.

Flow testing of liquid lithium in the standard LiMIT module takes place in the Solid/Liquid Lithium Divertor Experiment (SLiDE) chamber, shown in Figure 4.5. A summary of pertinent experimental capabilities of the chamber are given here, as well as a description of system improvements that have been made. For a deeper dive into SLiDE systems, refer to [80]. The vacuum chamber is pumped using a roughing pump and turbomechanical pump to reach base pressures on the order of 1×10^{-6} Torr, required to mitigate lithium surface passivation. The system features electromagnetic Helmholtz coils arranged on either side of the module installation location to provide the transverse magnetic fields required for TEMHD flow. The coils are powered by 4 high current EMS power supplies providing a nominal maximum current of 130 A each. This results in a magnetic field strength of approximately 800 Gauss. To reach higher magnetic field strengths, power can be provided by a bank of up to 8 car batteries, which can provide up to 2300 Gauss. Power is transferred through 2 high current knife switches, allowing rapid operation of the magnetic field.

The design of the base flow module was altered for this work. Initially, the main body of the module had both top and bottom trenches directly machined into the surface. Instead of machining an entire new module for every geometry, the system was adjusted to allow for plates

containing each geometry to attach to a single base. This design drastically reduces cost and time to perform physical testing based on multiphysics modeling. The base plate design also improves heat transfer through conduction to the topside structure (especially the foam designs), increasing wettability once lithium is injected. In Figure 4.6, the new base module is shown with an example test plate geometry.

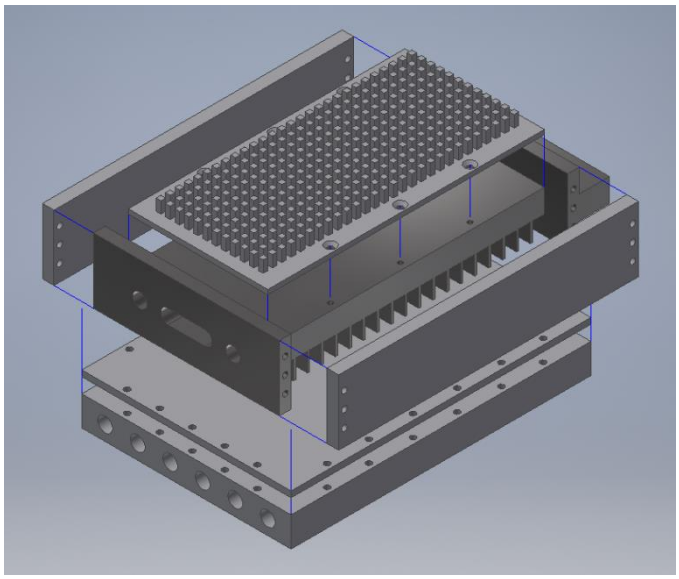

Figure 4.6 – Exploded drawing of the modified base module including a test plate geometry as well as side and heater plates.

Heating and cooling systems in the flow module provide the temperature gradients required to sustain TEMHD drive. Cooling lines snake through the center block of the device, developing temperature gradients on the topside structures and bottom side recirculation channels. Cooling lines were upgraded from Swagelok two-ferrule fittings to entirely VCR metal face seal connections, which provide a strong enough seal to enable forced helium cooling. Most of the experimental testing in this work was performed with 20 psi forced helium cooling. Heating systems include bottom side and topside heating. The heater plate at the bottom of the device provides latent heat through 6 Watlow E4J30-J6C8H cartridge heaters. These 120 V 200 W cartridge heaters have a 0.5 inch no-heat length at the lead end and braided metal shielding along the leads for overheating and lithium spill protection, respectively. Proof of concept testing of TEMHD flow propensity is carried out with cooling of the latent heating only, allowing for smoother flow conditions to develop. Topside heating is available through the addition of a homemade linear electron beam (e-beam). A variable AC transformer (Variac) is used to heat the

4 thoriated tungsten filaments (Goodfellow 0.15 mm diameter, 99% W, 1% Th) to emission temperatures, and the A.L.E. Systems high voltage power supply can provide up to 20 kV of bias for electron acceleration. The e-beam provides a Gaussian heat flux profile approximately a centimeter wide over a linear distance of approximately 15 cm, with a nominal peak sustainable heat flux of ≥10 MW/m^2 and excursions up to 40 MW/m^2. For more information on design and operation of the e-beam, refer to [61], [80]. The topside heating is built to provide a heat flux that simulates the conditions in much larger fusion devices, in order to prepare the system for high heat flux operation. The main chamber is tilted at approximately 55°, allowing the Helmholtz coils to both focus the e-beam and provide the transverse magnetic field component for TEMHD flow. To measure temperature, Omega K-type thermocouples are placed in 4 locations on the test module and 3 locations through the injection system, as shown in the diagram in Figure 4.7. These thermocouples measure the top and bottom of the topside open surface structures, the topside of the recirculation channels, and the base of the heater plate. Analyzing the temperature trends in these locations is useful for showing the bulk fluid motion throughout the module. Additionally, the injection system temperature is tracked at the reservoir, vacuum feedthrough, and nozzle. Temperature data is gathered with the help of a LabJack U6-Pro, along with a temperature tracking VI premade by LabJack and available for download.

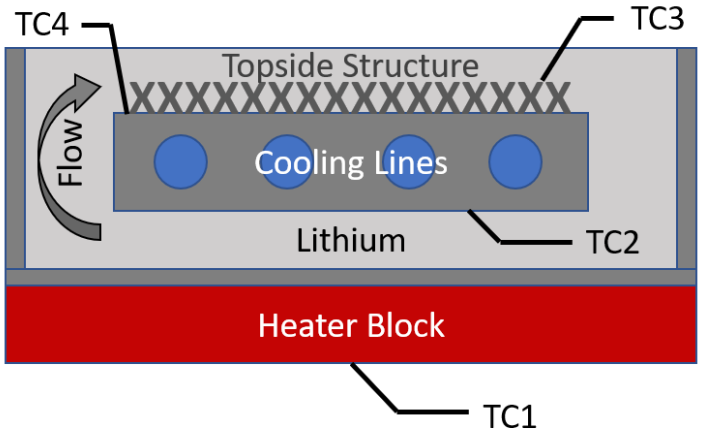

Figure 4.7 – Diagram of thermocouple placement in the flow module.

Lithium is loaded into the flow module via a separate injection system. Lithium is prepared in a glove box under argon atmosphere to slow passivation, and quickly transferred to an external reservoir that is bled with argon. Lithium is heated in the external reservoir and tubing by wrapped fiberglass heating ribbon(s), such as an Omegalux STH051-040 or similar model. External

Swagelok fittings that require disassembly for lithium cleaning were exchanged for VCR seals, for better vacuum tight sealing and lithium protection, and easier detachment. Internal tubing is isolated using Kapton tape and heated with a NiCr NCRR-34-100 resistance heating ribbon wire. Lithium is heated to approximately 220-250 ºC before injection. While this means lithium is injected below the wetting temperature and must be heated by the module before ample wetting is achieved, this strategy mitigates risk of injector nozzle wetting and leakage due to static lithium pressure in the reservoir. Argon backpressure powers lithium injection and fill control is achieved with needle valves and electric switches. Generally, 75-100 g of lithium in the reservoir allows for sufficient filling of any flow geometry.

After injection, the experimental focus shifts to effective wetting of the flow structure and observation of flow. While most initial lithium impurities remain in the reservoir, one benefit to this injection technique, the strong gettering effects of liquid lithium immediately pull impurities from the main vacuum chamber. Low base pressures are maintained, but remaining impurities can quickly build up an impurity layer and passivate the lithium surface. As a rule of thumb, a chamber pressure of 1×10^{-6} Torr passivates lithium at a rate of 1 monolayer per second. To remove this slag layer and simultaneously enhance the wetting of the surface structures, a temperature excursion to ~500 ºC is used. This allows most surface impurities to dissolve into the bulk lithium, cleaning the surface to a mirror finish. Higher temperatures lower the wetting angle of the lithium on the solid substrates [83], [84], allowing faster wicking and filling of the topside structures.

Current methods of flow visualization and velocity measurement rely on particle image velocimetry (PIV), in which surface particle motion is measured to determine the lithium flow speed. This presents a several challenges for quantifying open surface flow characteristics. Impurities on the top surface can block up flow and a passivation layer can hide bulk lithium motion from view. However, some impurities are required to track flow, so effective cleaning of the top surface with temperature excursions could remove the particles required for PIV. Particles floating on the top surface that become entrained in the flow will move at slower speeds than the bulk flow, depending on mass, so PIV gives a reliable but lower bound value of flow velocity. Lithium is also a highly inviscid liquid, so as floating particles are driven in one direction toward the return channels, they can easily spiral around to another part of the flow, creating surface eddy motion. While bulk flow remains recirculating, the surface can quickly develop eddies that mask

bulk flow velocities. Pulsing the magnetic fields for short TEMHD-driven tests of ~5-6 seconds can reset some particles and allow calming of surface eddies, but also introduces more transient effects. Temperature measurements of the open surface and the recirculation channels during pulsed B-field operation provide a clear picture of sustained recirculating flow but relating this data to flow speed is challenging. These challenges should be kept in mind, as they are present throughout experimental testing undertaken in this work, as well as any testing of liquid metal flow designs. Several cameras can be used for PIV, including infrared, which can identify impurities based on differences in emissivity, visible light fast-frame cameras, which have a higher temporal resolution but have reduced spatial resolution and require more lighting, and standard high resolution, lower frame rate cameras. See [80] for more information on the use of fast-frame and infrared cameras for LiMIT systems.

Post-test particle tracking is carried out in ImageJ, a powerful open-source, Java-based image processing tool built at the National Institutes of Health and the University of Wisconsin [85]. Videos of the experimental testing are trimmed to highlight each pulse and turned into image series using the open-source image processing tool FFmpeg [86]. The image series of each pulse is imported into ImageJ and the Cell Counter plugin allows frame-by-frame position measurements of many different particle tracks. A reference point is identified to eliminate motion of the camera or module during the pulse. Particle positions are output from ImageJ and analyzed in a Python script. It would be optimal to utilize computer vision techniques for particle identification, tracking, and trajectory analysis, which can be done reliably through Python scripting [87]. Unfortunately, the changes in color and contrast throughout the model create too much variability for reliable tracking, since the particles can be quite small and very similar in hue to other regions of the image. Potential changes that would allow for more effective use of automatic tracking instead of manual identification include larger use of IR imaging with tuned resistivity values to enhance contrast or attempting to identify motion of localized contrast changes to identify particle locations. These methods have not yet been applied in this work.

A variety of manufacturing techniques were used to produce the new flow geometries for study. Conventional milling and vacuum welding techniques were used for the module redesign, base plates, and adjustment of cooling lines, courtesy of the excellent machinists at the UIUC Electrical and Computer Engineering machine shop. The posts were machined with the help of

the Aerospace Engineering machine shop, using a wire-EDM process. Disordered foam samples were created by Ultramet using several CVD/PECVD steps on a base carbon foam. The ordered foam designs defy conventional machining, so samples were 3-D printed by Protolabs using DMLS. For more information on the machining processes and resulting surface characteristics, see the respective sections in the following chapters.

4.3 COMSOL Modeling Setup

COMSOL Multiphysics is an extremely powerful, verified tool for finite element analysis and multiphysics simulations [88]. The software package presents an integrated desktop environment into which the user can input relevant physics interfaces contained within large physics modules. Physical parameters can be quickly and directly specified using the predefined interfaces, or the user can enter their own PDEs to be solved. With built-in physics packages for mechanics, heat transfer, electromagnetics, fluids, chemistry, plasma, and more, COMSOL allows for extensive coupling of physics within complex systems. Previous modeling efforts at UIUC have showcased the ability of COMSOL to capture the physics of liquid lithium TEMHD flow and the use the resulting models to inform experimental design [64], [81]. The fully coupled TEMHD model has been validated by past experiments and provides a method of design iteration without physically building and testing each successive attempt. Improvements in computational power allow for larger domains exhibiting lithium flow propensity, including multi-channel flow and recirculation through the bottom side trenches.

This section describes the modeling setup, in COMSOL Multiphysics v5.4, valid for the majority of TEMHD modeling presented in this work. Except for the 2-D modeling presented in Chapter 3 and the extension to true free surface flow developed in Chapter 7, the coupled system is solved in a 3-D constrained surface domain. TEMHD relies on 3 main physics interfaces to develop and drive the lithium flow: Heat Transfer in Fluids (HT), Electric Currents (EC), and Laminar Flow (LF).

Geometry

The COMSOL geometry editor allows creation of most basic primitives. For this work, with the exception of the disordered foam simulation in Section 6.1.1, the domains can generally be constructed with blocks. Posts are entered using an Array of a single block. Elimination of

portions of a block to make way for a domain that will end up being a new material is done with a Difference Boolean. For ease of dealing with the solid and fluid domains, the Union Boolean is used to concatenate the domains of each type. For more complex geometries, COMSOL supports work planes, parametric curves and other primitives, and operations such as extrusions, sweeps, fillets, and chamfers, but taking full advantage of these tools can be less straightforward than most standard CAD software. Conveniently, COMSOL also includes an Import tool for importing external geometry files, as well as LiveLink interfaces with several CAD programs.

The example domain presented in Figure 4.8 shows the base LiMIT trench case prior to any geometry adjustment. The return channels on the bottom are 5 mm wide and 8 mm deep, with 1 mm thick walls. The topside trenches are 2 mm wide and 5 mm deep, also with 1 mm thick walls. The entire domain is 12 mm in width, allowing for 2 full return channels and 4 standard topside trenches. The walls upstream and downstream of the trenches continue 5 mm above the trench height, to allow for inclusion of lithium overfill in the simulations.

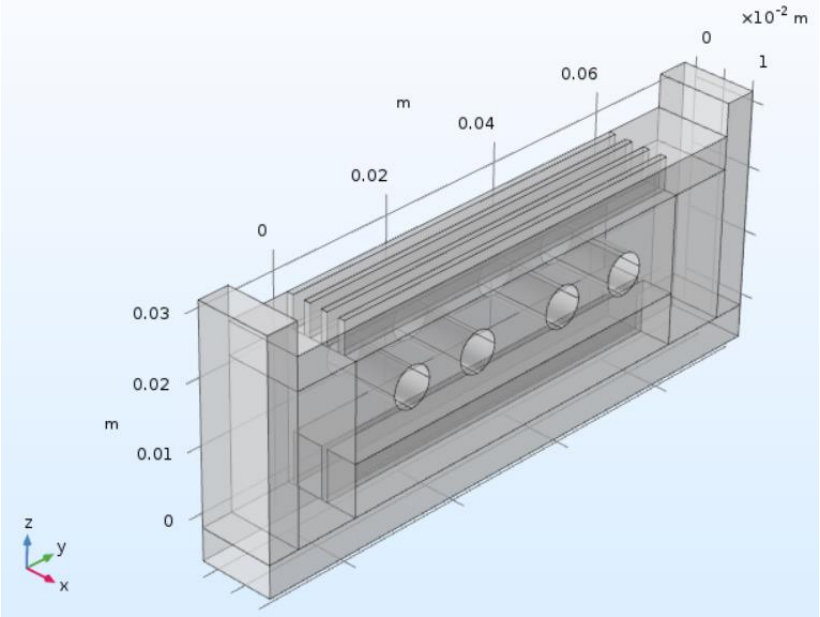

Figure 4.8 – COMSOL 3D model domain is large enough for multi-trench or multiple flow channel investigation.

Lithium surfaces on the edges of the domain, and of course the top open surface, are initialized as slip wall boundaries to allow for flow visualization and to imply that the lithium domain would continue in x on either side of the simulation domain. All other walls are non-slip boundary conditions. All solid structures are composed of stainless steel in these preliminary tests, and the ¼-inch cooling channels can be seen cutting through the domain.

Adjustments to the topside geometry generally maintain the overall dimensions of the Figure 4.8 domain. In the post TEMHD domains, trimming or extension of the domain in the X direction by 1 to 2 mm is needed to bound the main flow channels with a row of posts on each side. The ordered foam domains are assembled using a Difference Boolean to subtract away the flow channels, inserting a block across the topside, and carrying out another Difference Boolean while keeping input objects to eliminate overlapping domains.

Materials

The Materials interface requires the user to assign each domain in the finalized geometry to a material. COMSOL includes a built-in library of over 2500 materials with relevant properties included, though the user can change any property at will. Properties that require a value are based on the physics included in the rest of the model. For this work, stainless steel and lithium are used, and Table 4.1 gives the relevant properties. To minimize issues with parameters changing due to built-in property functions, it is assumed that the property values are constant.

Table 4.1 – Relevant material properties of stainless steel and lithium, as included in COMSOL Multiphysics modeling.

	Stainless Steel	Lithium
Thermal Conductivity [W/(m K)]	16	45
Heat Capacity [J/(kg K)]	500	4349
Electrical Conductivity [S/m]	1.3×10^{6}	3.6×10^{6}
Density [kg/m^3]	7900	508
Dynamic Viscosity [Pa s]	N/A	5.03×10^{-4}
Seebeck Coefficient relative to Stainless Steel [V/K]	0	2.5×10^{-5}

Heat Transfer in Fluids Interface

The HT interface in the Heat Transfer module solves the heat equation to model heat transfer from conduction, convection, and radiation. The basis of TEMHD is the thermal gradients present in the system, so this interface effectively solves for temperature variation within the

domain, accounting for all sources and sinks of heat. For this system, the conservation of energy equation distills to the energy balance equation, including terms for temperature change in time, convection, conduction, and heat sources.

$$\rho C_p \frac{\partial T}{\partial t} + \rho C_p \boldsymbol{u} \cdot \nabla T + \nabla \cdot (-k \nabla T) = Q$$

Here ρ is the material density, C_p is the heat capacity at constant pressure of the material, T is the temperature, t is time, $\boldsymbol{u}$ is the velocity vector, k is the thermal conductivity of the material, and Q is the net heat source to the system. While the default setup assumes a fluid domain everywhere, heat transfer in solids is easily included in a domain physics node. The initial temperature throughout the domain is set to 573 K (300 ºC) in order to match standard experimental conditions. By default, COMSOL sets all boundary conditions to thermal insulation, and as boundary physics nodes are added, these conditions are overwritten. Bottom side heating of the system is introduced via a heat flux on the bottommost surface of the domain. The heater block consists of six 200 W heaters, whose power is rated at wall voltage of 120 V. At experimental temperatures, they are run at approximately 50 V, and output 0.7 A each at this voltage. This gives a total of 210 W in a heater block that is 90 mm by 130 mm. If all power is transferred to the flow module, this gives a bottom side heat flux of 18 kW/m^2. Assuming the bottom surface of the heater block is radiating some of that power, then

$$q_{rad}\ [W/m^2] = 5.67 \times 10^{-8} \varepsilon T^4$$

Where ε is the emissivity coefficient of the stainless-steel block, estimated to be 0.1, and T is the temperature of the radiating body, in Kelvin. For a heater plate on the order of 573 to 673 K, radiation accounts for a loss of 0.6 to 1.2 kW/m^2. Therefore, the bottom side heat flux is input as a general inward heat flux set at 17 kW/m^2. Topside heating, included when modeling high heat flux conditions, is also introduced as a boundary heat flux node, general inward heat flux type boundary condition on the top surfaces of the domain. To mimic the shape of a heat stripe from a divertor or e-beam, the heat flux is added as a Gaussian profile in Y, with the form

$$q = q_{max} \exp\left(\frac{-\left(y - y_{centerpoint}\right)^2}{Stdev^2}\right) \left[W/m^2\right]$$

Here q_{max} is the maximum value of the curve, $y_{centerpoint}$ is where the peak is centered, and $Stdev$ is the standard deviation of the Gaussian distribution. For this domain, the heat stripe is centered at a $y_{centerpoint}$ of 3 cm, with a standard deviation of 5 mm and an initial q_{max} of 1×10^6. Cooling is included as a convective heat flux boundary condition on the cylindrical cutouts that represent the experimental cooling lines. The convective heat flux is given by $q = h(T_{ext} - T)$ where the heat transfer coefficient h is 500 W/m^{2}K and external temperature T_{ext} is room temperature, 293 K. The heat transfer coefficient is based off of generic values for forced gas convection, and matches previous simulation work [64] for comparison.

Electric Currents Interface

The EC interface in the AC/DC module solves for electric potentials and resultant currents in the domain and derives the next step in computationally modeling TEMHD-driven flow – the thermoelectric current. The interface solves a current conservation equation based on Ohm's law. The set of governing equations is as follows.

$$\nabla \cdot \boldsymbol{J} = Q_j$$

$$\boldsymbol{J} = \sigma \boldsymbol{E} + \frac{\partial \boldsymbol{D}}{\partial t} + \boldsymbol{J}_e$$

$$\boldsymbol{E} = -\nabla V$$

Here $\boldsymbol{J}$ is the current density vector, Q_j is the net current source, σ is the electrical conductivity of the material, $\boldsymbol{E}$ is the electric field, $\boldsymbol{D}$ is the electric displacement or electric flux density, t is time, $\boldsymbol{J}_e$ is any external current density vector, and V is the dependent variable electric potential. By default, all domains are included in the current conservation equation, and all boundaries are set as electric insulation. The initial value of the electric potential is 0 everywhere. A ground boundary condition is added on the bottom surface of the domain, as any flowing system will remain grounded in operation.

For the TEMHD system, it is assumed that the electric field and displacement are 0, or very small with respect to the external thermoelectric current. An external current density domain physics node is added to the lithium domains to capture the thermoelectric current. The additional current density term is given by

$$\boldsymbol{J}_e = \sigma(\boldsymbol{u} \times \boldsymbol{B} - S\nabla T)$$

Where $\boldsymbol{u}$ is the velocity vector, $\boldsymbol{B}$ is the magnetic field vector, S is the Seebeck coefficient, and ∇T is the temperature gradient. Expanding the $\boldsymbol{u} \times \boldsymbol{B}$ term yields

$$(\boldsymbol{u} \times \boldsymbol{B}) = (u\hat{x}, v\hat{y}, w\hat{z}) \times B_0\hat{x} = (0\hat{x}, wB_0\hat{y}, -vB_0\hat{z})$$

Here B_0 is the magnitude of the magnetic field, which is constant in the X direction in these simulations. Splitting the current into components gives the terms entered into the external current density node.

$$j_x = \sigma(-S\nabla T_x)$$

$$j_y = \sigma\left(wB_0 - S\nabla T_y\right)$$

$$j_z = \sigma(-vB_0 - S\nabla T_z)$$

Laminar Flow Interface

The COMSOL CFD module has many physics interfaces that are optimized to solve specific types of fluid flow. While COMSOL's fluid solvers have largely lagged well optimized fluid codes like OpenFOAM or ANSYS CFD, the interface options and solver stability have greatly improved through the 5.x versions, and the physics coupling of COMSOL that allows for TEMHD modeling is quite robust. While Chapter 7 details an extension of TEMHD modeling capabilities to true free surface flow, the majority of the models presented in this work include the lithium as a constrained block domain. While this eliminates the nature of the surface motion, it has been shown that this style of modeling can capture most pertinent characteristics of the flow [64], [80]. This setup therefore utilizes the single phase, laminar flow interface, which is used to calculate the velocity and pressure fields throughout the fluid domains. The flow can be assumed laminar if the Reynolds number stays below a critical value, usually on the order of 10^3. For these geometries, the critical dimension never exceeds 4 mm, and for the vast majority of conditions the velocity stays below 0.75 m/s. With the lithium density and dynamic viscosity given in Table 4.1 – Relevant material properties of stainless steel and lithium, as included in COMSOL Multiphysics modeling., the Reynolds number will generally stay below 3000. For the largest critical

dimensions and fastest velocities, the flow will be transitioning to a turbulent scenario, but most conditions remain in a laminar regime. To allow for effective simulation on relatively short timescales, it is assumed that flow is laminar. Future work should investigate transitional or turbulent scenarios. As is written earlier in this chapter, the LF interface solves the Navier-Stokes continuity and momentum equations to find the pressure and velocity field of the liquid [88]. Assuming incompressibility, these equations become

$$\rho \nabla \cdot \boldsymbol{u} = 0$$

$$\rho \frac{\partial \boldsymbol{u}}{\partial t} + \rho(\boldsymbol{u} \cdot \nabla)\boldsymbol{u} = \nabla \cdot [-p\boldsymbol{I} + \mu(\boldsymbol{\nabla u} + (\boldsymbol{\nabla u})^T)] + \boldsymbol{F}$$

Where ρ is the density, $\boldsymbol{u}$ is the velocity vector, p is the pressure, $\boldsymbol{I}$ is the identity matrix, μ is the dynamic viscosity, and $\boldsymbol{F}$ is the force vector. By default, all walls are a no slip boundary condition, so the velocity goes to 0, and initial velocity and pressure are 0 everywhere. Gravity is included in this model, so the pressure calculation compensates for hydrostatic (or 'lithistatic') pressure. In order to aid stability of the pressure calculation, a pressure point constraint point physics node is added. This node specifies a gauge pressure value, generally 0, at a point near which there should not be much change in pressure. For this model, it is specified at a corner of the top surface, specifically [0 mm, 70 mm, 28 mm] (though this varies slightly in Z for the foam models). The reference point required on the main LF settings page after enabling gravity is set to the same point for consistency. The free surface of the lithium is modeled using a wall node with a slip condition. While motion of the surface is not captured, the top surface velocity moves with no friction against the boundary. The open sides of the domain (in X) are included in a symmetry boundary node, representative of the extension of the flow volume in each direction. In order to include the final step in TEMHD drive, a domain volume force node is included. The Lorentz force arising from the thermoelectric current is input as follows.

$$\boldsymbol{F} = (\boldsymbol{J} \times \boldsymbol{B}) = \left(j_x\hat{x}, j_y\hat{y}, j_z\hat{z}\right) \times B_0\hat{x}$$

$$F_x = 0$$

$$F_y = j_z B_0$$

$$F_z = -j_y B_0$$

Meshing and Solution Methods

The quality of a simulation result is highly dependent on the mesh used to segment the domain. COMSOL includes a default meshing interface that attempts to optimize mesh generation based on the physics included in the model. The COMSOL v5.4 mesh solver has improved over previous versions, and the physics controlled meshes include automatic refinement near corners and through small features, as well as boundary layers along the edges between the fluid and the domain. Since the simulations are time dependent to show the transient development of flow in these new geometries, minimizing mesh size while maintaining element quality becomes important for getting results on reasonable time scales. With the aid of the UIUC Beckman Institute Visualization Laboratory, these simulations were run on 2 Intel Xeon E5-2670 processors and 128 GB of RAM, with an NVIDIA Quadro K600 graphical accelerator for more effective post processing and visualization. If RAM is limited, the COMSOL segregated solvers should be used. They are well optimized, splitting the solution by physics interface and iterating until a convergence criterion is reached for each dependent variable. Each variable can be calculated by a different solver and convergence criterion. With large amounts of RAM, it is possible to run time dependent studies in a fully coupled mode, where all physics is solved collectively.

COMSOL has many direct and iterative solver types with multitudes of options for fine-tuning solver efficacy and convergence, and adjusting these options becomes a daunting task. Due to the RAM included in the system, it was possible to forego the use of iterative solvers in favor of direct solvers. Iterative solvers use less memory but are more sensitive to initial conditions and ill-posed problems and can therefore diverge more easily or converge to an erroneous solution. Direct solvers are more robust, though they require more memory while calculating. Most of the simulations presented here use a segregated method, with a direct PARDISO solver for every physics interface. It is important to reorder the default segregated system so that the temperature is the first segregated step, followed by electric potential, and then velocity and pressure. Since the segregated solver looks at coupling in the order of the steps, maintaining the order of how TEMHD forces develop proves to be more effective at attaining good convergence and time stepping. COMSOL uses a variety of factors to predict and apply an adaptive time step as it solves a time dependent simulation, and desired output steps are interpolated from solution steps. In general, though this can vary by model, most simulations were run to several seconds in solution

time, RAM usage was typically >15-20 GB, and computation time varied from 30 minutes to 48 hours, depending on the complexity of the geometry.

CHAPTER 5 – POST TEMHD

The standard LiMIT trench and trench shaping solutions tend to suffer from isolation of the flow channels in perfect fill or slight underfill scenarios. If dryout begins to occur, there is no way for lithium in other regions of the module to aid in filling an isolated trench. So instead of having trenches cut in solely one dimension, the post TEMHD concept cuts trenches in two dimensions, leaving square posts separated by channels for lithium flow. It is believed that this type of geometry will still provide TEMHD currents in predominantly one direction. The inclusion of channels perpendicular to the standard flow should allow crosstalk between flow channels, removing the trench isolation of standard LiMIT and allowing lithium from areas not under direct high heat flux or transient impingement to provide relief. Errant TEMHD currents may produce some swirling flow, but this should serve to enhance channel crosstalk. The post design should be able to utilize capillary forces to aid in maintaining lithium fill, and the overall reduction in material under any heat stripe location reduces the potential for damage.

For preliminary testing, 3 sets of trench geometries were machined via EDM onto base plates for installation on the new base module, described in Section 4.2. These encompass 2 post sizes and 2 post separation sizes, in order to study how the main geometric parameters impact the flow. The sizes tested, shown in Figure 5.2, will be referred to as listed below.

A_p – 1×1 mm posts, 2 mm separation
B_p – 2×2 mm posts, 2 mm separation
C_p – 2×2 mm posts, 4 mm separation

Electrical discharge machining (EDM) ablates material from a part by creating a small arc discharge between a tool electrode and the part. In wire-EDM, material is slowly removed along a thin single strand of wire that passes along or through the part being machined. This technique, shown in Figure 5.1, is extremely useful in creating long thin trenches like those that make up a standard LiMIT system or the new post TEMHD plates.

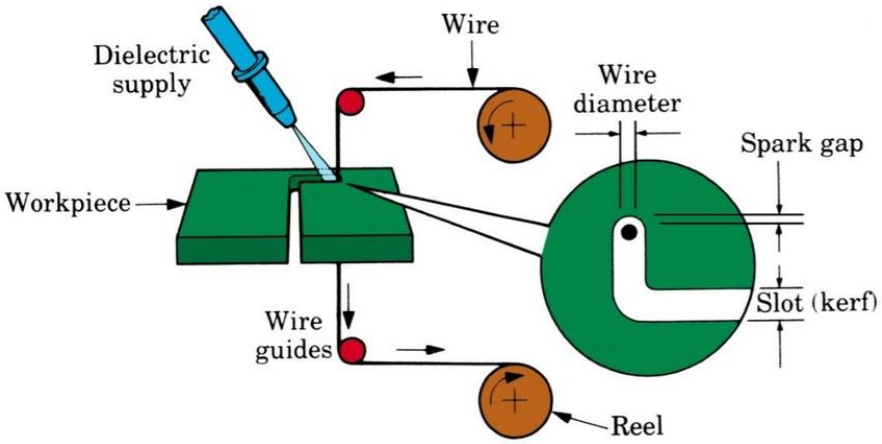

Figure 5.1 – Diagram of the wire-EDM process [89].

All 3 geometries mentioned above were manufactured as a separate full plate. Wire-EDM excels at cutting the 2 dimensions of trenches, producing even dimensions and sharp corners. The process was repeated 2-3 times in order to provide better smoothness throughout the piece. Dimensional accuracy is very high with this process, and surface roughness is kept to an R_a value below 1 µm, due to the increased smoothing of the repetitive EDM. There are no noticeable defects in manufacturing. The full post plates as manufactured are shown in Figure 5.2.

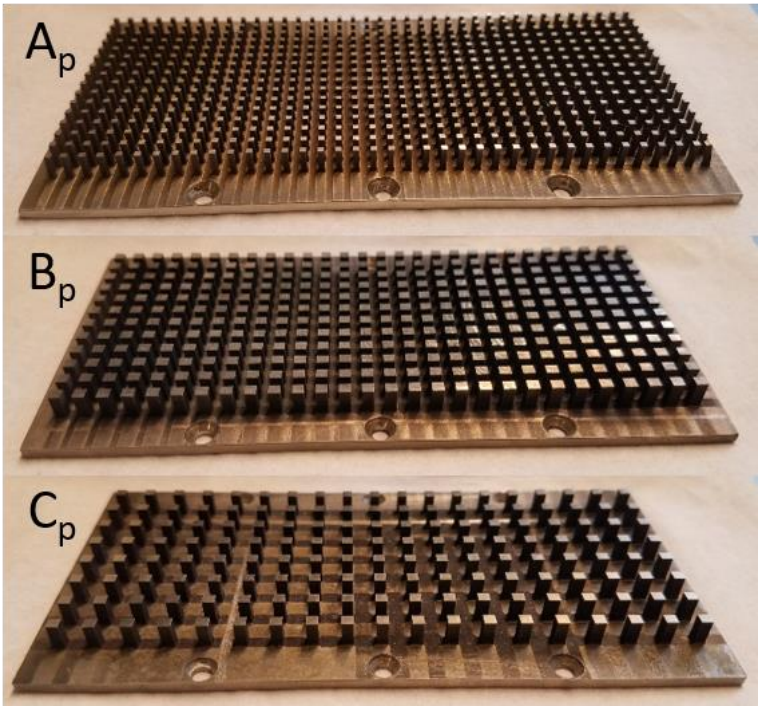

Figure 5.2 – Set of 3 posts plates as machined. The sharp corners and smoothness throughout are apparent, improved by repetition of the wire-EDM process.

5.1 Numerical Modeling

As machining began on the post plates, the 3 geometries were built into the COMSOL model described in Section 4.3 to investigate the expected flow profiles. The domains, shown in Figure 5.3, vary in width from 10 to 14 mm in the X direction, due to the need to have the main flow channels (in Y) be bounded by a row of posts. In initial modeling, any unbounded flow channel at the edge of the domain did not have appropriate current paths and therefore developed spurious velocities. These velocities could grow strong enough to effect at least one other flow channel, causing enhanced swirling and less stable flows.

The physics that creates TEMHD flow is a highly coupled interplay between temperature gradients, electric currents, and fluid flow. Additionally, the dryout phenomenon is a highly transient condition based on localized heat fluxes. This makes it difficult to distill information about the behavior of these geometries down to single sets of values, Therefore, in these forthcoming sections, equivalent snapshots of the time dependent simulations are presented for each geometry to illustrate the differences in temperature, current, and flow profiles between the geometries. The test conditions chosen for this comparison are 1 MW/m^2 topside heat flux in a 0.05 T magnetic field in the +X direction, a moderate heating case near the peak velocity magnetic field for TEMHD flow. The cooling lines resemble forced gas convection with a heat transfer coefficient of 500 W/m^2K, and the heater plate provides 17 kW/m^2 along the bottom surface of the system. This would resemble an e-beam test in SLiDE. Following this, the time-varying temperature and velocity behavior will be analyzed with respect to topside heat flux and magnetic field strength via parametric sweeps of these conditions.

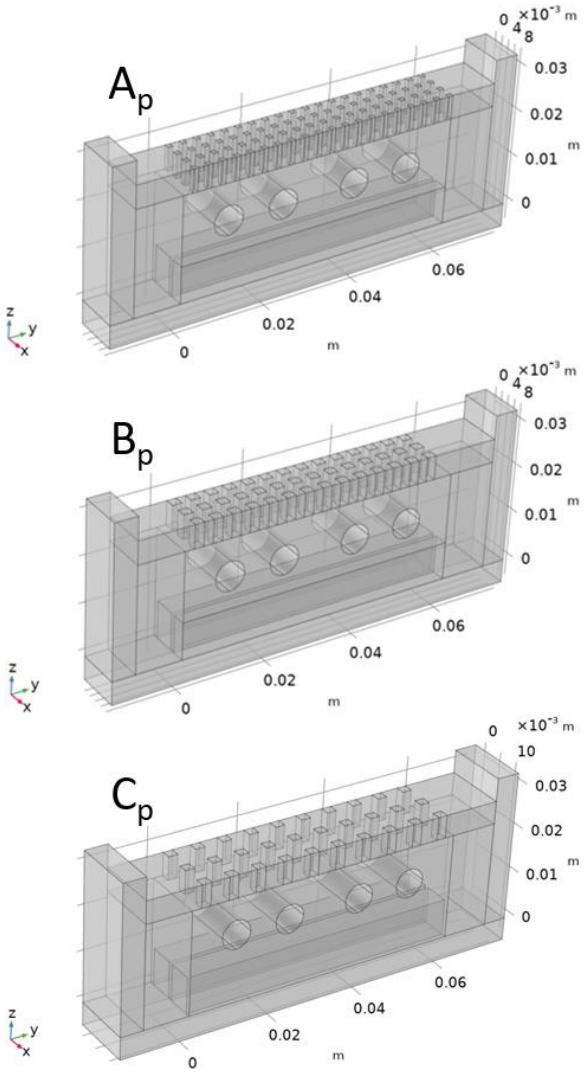

Figure 5.3 – COMSOL modeling domains for the 3 post geometries.

5.1.1 Temperature Profile

The temperature profiles in Figure 5.4 show the rapid convective cooling of the lithium flow. Lithium is an efficient thermal conductor, and the rapid development of TEMHD flow aids in the heat transfer by improving convective cooling. The lithium that is heated under the topside heat flux is accelerated away from that region and quickly exits downstream. The higher temperature lithium is recirculated into the bottom channels where it is cooled before reentering the topside. The cooling channels quickly create strong temperature gradients in the stainless steel that are reaching the lithium channels (see the bottom side velocity profile in Section 5.1.3), though the local topside heat flux obviously dominates the development of the temperature profile. As

expected, the bottom side heating is essentially negligible in the high heat flux scenarios, with very little noticeable temperature increase over initial conditions.

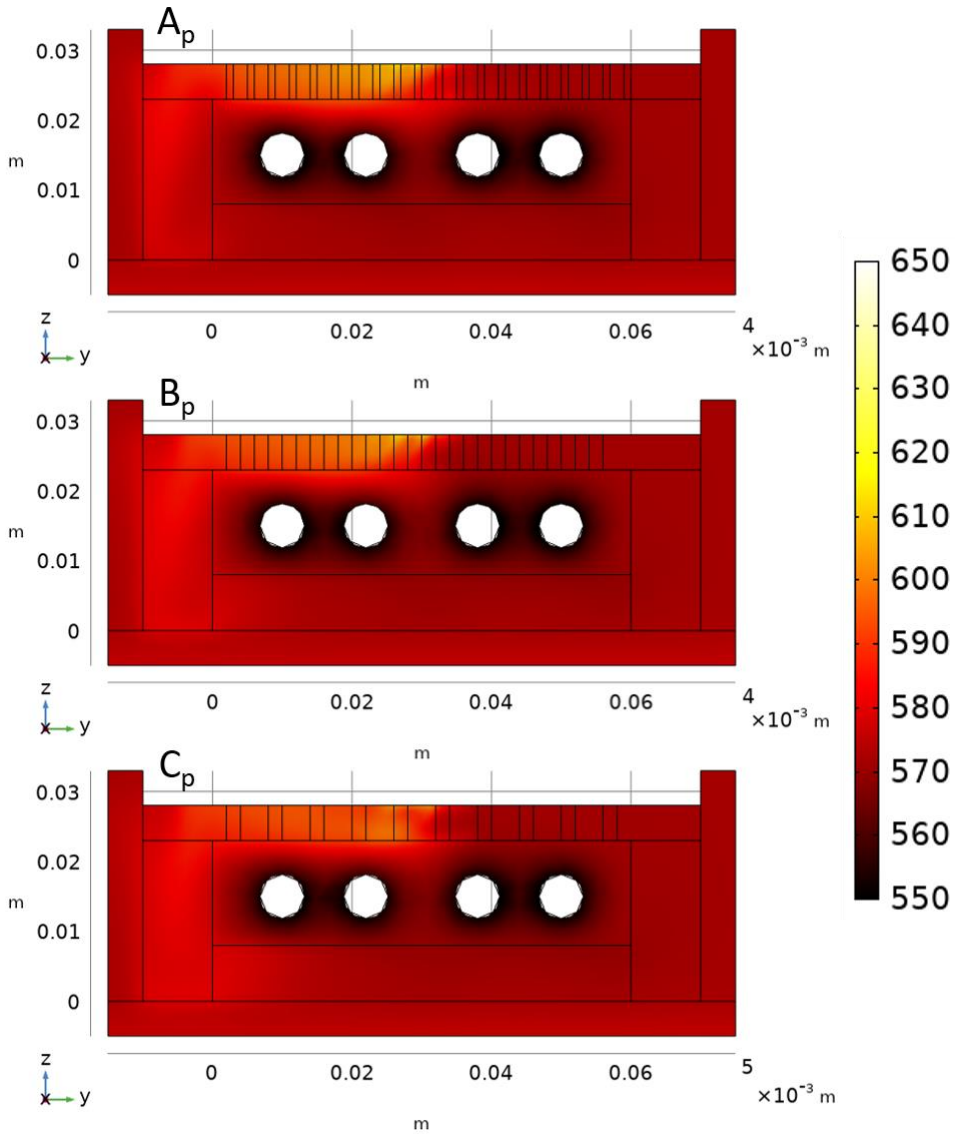

Figure 5.4 – Side view slice of the temperature profile in all post geometries. Color bar gives temperature in K. The effect of the centered topside heat flux and subsequent flow of hot accelerated lithium is visible.

It is important to consider the temperature profile on the open surface of the module when investigating viability of a design. This is important from liquid and solid standpoint. While lithium is excellent at dispersing heat via its high thermal conductivity, and the flow provides additional dissipation due to convection, the high vapor pressure of lithium above approximately 450 to 500 ºC (723 to 773 K) limits the operating temperature window of a lithium system (assuming extra vapor production is deemed undesirable). So, the flowing system should be

designed in a way that maintains a lithium temperature below this point. Most importantly, the heat removal by the lithium must keep the underlying solid structure from being damaged. In this case of no lithium overfill, both the lithium and stainless-steel surfaces are receiving the brunt of the heat flux. Cooling of the solid structure is only possible from conduction and convection to the lithium, with no additional dispersion of heat from lithium above the level of the posts. Figure 5.5 shows the topside temperature profile. There is no drastic difference in overall temperature range on the top surface between the geometries, but the larger posts in cases B_p and C_p exhibit more pronounced streamers of heat being carried away from the solid material. The small posts in case A_p are cooled more effectively by the lithium, displaying a smoother temperature gradient around the topside heating.

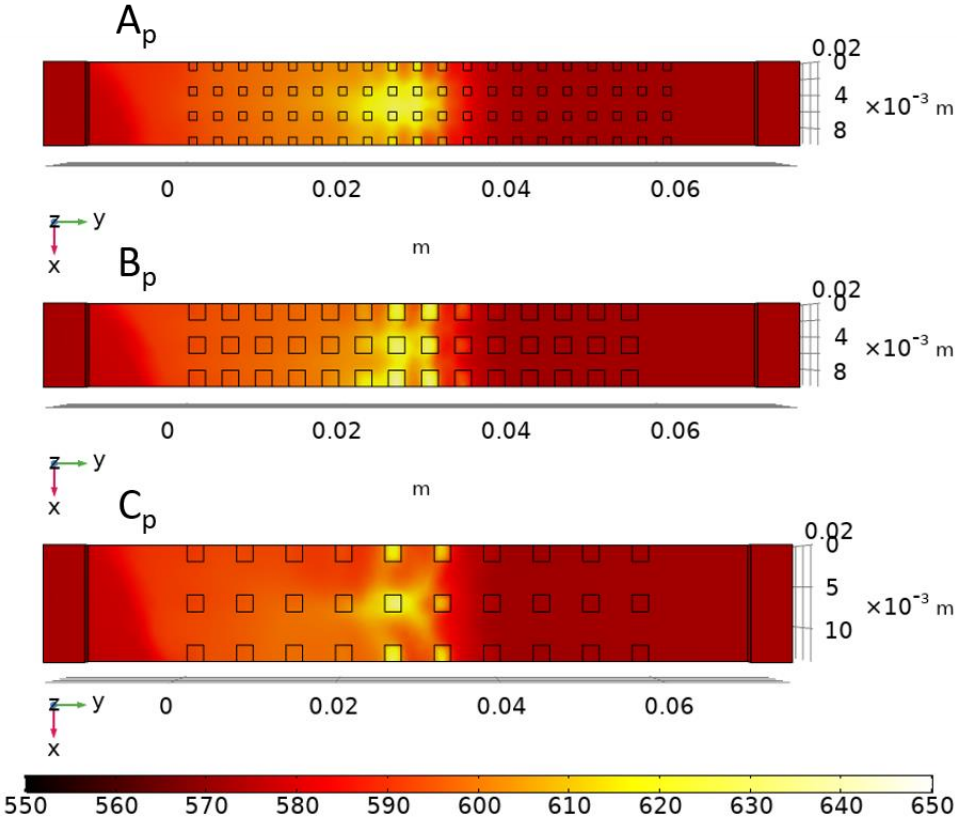

Figure 5.5 – Topside temperature profile of the 3 post designs. The color bar gives temperature in K. Cooling of the posts directly under the heat stripe is evident by high temperature streamers in the lithium.

The temperature profiles are obviously strongly coupled to the flow profile, as the temperature gradients that arise lead to the thermoelectric current and driving force for the flow, so the profiles are liable to change over time. Figure 5.6 shows the evolution of the maximum

surface temperature over the simulation duration. The 1x1 mm case A_p posts are indeed more quickly cooled by the lithium as flow develops and reach a lower overall maximum temperature. Case B_p heats faster than case C_p, though the overall maximum temperatures of both crest just above 650 ºC before falling into the 630 to 640 ºC range as flow steadies. The variability of case C_p is more pronounced than the other 2 due to the wider gaps and more eddy-ridden flow profile that develops in that geometry (see Section 5.1.3).

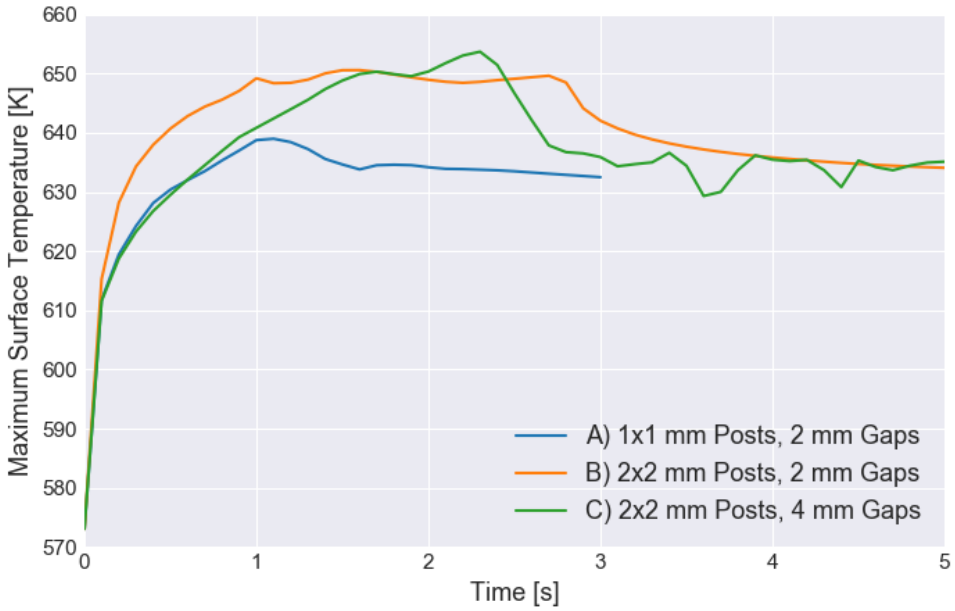

Figure 5.6 – Maximum surface temperature over time in the post geometries for a 1 MW/m^2 peak heat flux with 0.05 T magnetic field.

5.1.2 Current Profile

The temperature gradients from the heating and cooling of the module drive the development of the thermoelectric currents. These current profiles are not as smooth or straightforward as the ones depicted in the Figure 2.3 example, where a steady, linear temperature gradient exists. In these post geometries, the repetitive presence and lack of thermoelectric junctions (the posts), together with a highly local topside heat flux, create a current density and directionality that can be highly variable. Figure 5.7 shows the current density (color plot) and the direction (red arrows) of the currents that develop between the posts near the center of the topside heat flux. Note that the Y component of the current is not included in the arrow plot.

The maximum current density magnitude is similar in all 3 cases, at 1×10^6 A/m^2, though case B_p has a larger extent of high current near the upper corners of the posts. Case B_p also maintains a higher current throughout the lithium domain, never dropping below 1.4×10^5 A/m^2. Due to the large spacing between the posts, case C_p current density falls to 7.1×10^4 A/m^2, and the middle flow channel of case A_p has a minimum current density of 5.3×10^4 A/m^2 as a result of the smaller posts allowing more interference between the channels. In all cases, the current predominantly flows down (-Z) through the liquid lithium and up (+Z) through the solid posts, creating the typical current circulation necessary to drive TEMHD flow. In cases A_p and C_p, there is more deviation from this standard. The larger flow-channel-to-post ratio in these cases allows eddy formation and swirling flow that is not as readily controlled by a larger current drive (case B_p). Combined with the rapid thermalization of the lithium with respect to the posts, this develops non-standard thermal gradients that enhance these effects (again, the physics is highly coupled).

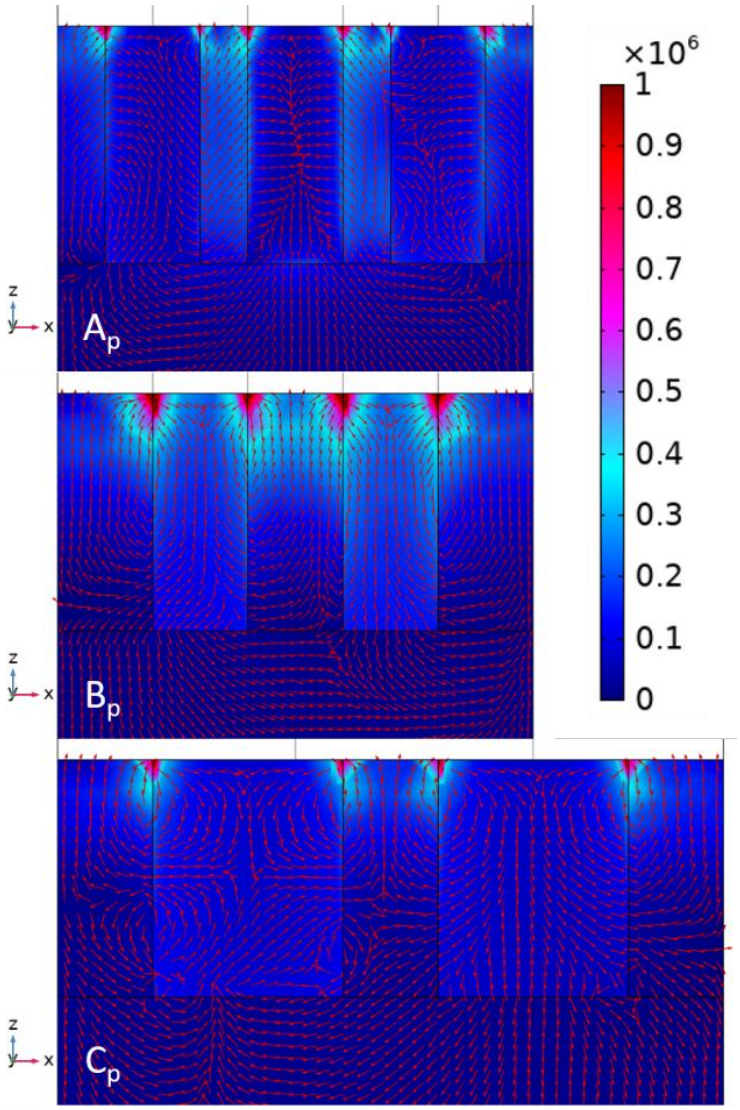

Figure 5.7 – Current density plot in an XZ slice through a set of posts near the peak of the topside heat flux, showing large peak values near the post corners. The color bar shows current density in A/m^2. The arrows follow XZ current direction.

The current profiles in the gaps between the posts illustrate the current dissipation when there is no standard 'parallel plate' typical for TEMHD drive (Figure 5.8). It is interesting to note that the current density magnitudes stay generally consistent with those in the bulk flow channels between the posts, just without the large corner currents. While there is more pronounced X-directed current flow, the current also predominantly flows in -Z throughout the domain, forcing the lithium out of the page due to the +X magnetic field. This will drive the lithium in -Y towards the posts in the secondary flow streams, and the post obstacles will split the flow and contribute to channel crosstalk.

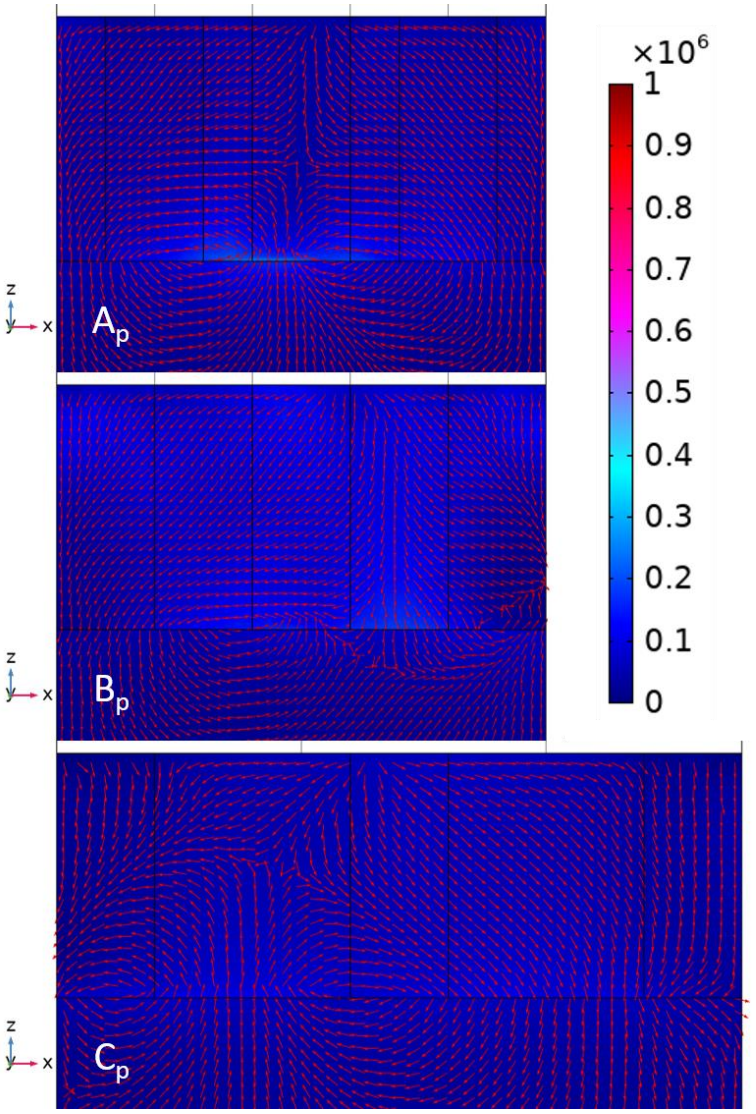

Figure 5.8 – Current density plot in an XZ slice in between sets of posts near the peak of the topside heat flux, showing more variability in current flow and smaller magnitudes. The color bar shows current density in A/m^2. The arrows follow XZ current direction.

The YZ current slices shown in Figure 5.9 help to explain the nature of the dryout phenomenon. In these images, only the Y and Z components of the current profile are plotted in the arrow surface, though the color plot still represents current density magnitude. The slices are positioned in the centers of the main flow channels, remaining within the lithium in the top domain. The pronounced Y-directed current throughout the flow channel is immediately apparent. This current is initiated by the Y variation of the topside heat flux causing Y-directed temperature gradients which persist as flow develops. This current, though typically below 5×10^4 A/m^2, can reach maximums of 1.0×10^5 A/m^2 in case A_p, 2.3×10^5 A/m^2 in case B_p, and 9.5×10^4 A/m^2 in case C_p, of the same order of magnitude of the Z-directed currents meant to drive the lithium

downstream. This implies a significant volume force will result that acts in the vertical (Z) direction, with a downward dryout force upstream of the topside heat flux and an upward pileup force downstream. The point at which the switch occurs shifts as the flow develops, as the moving lithium removes heat and changes the position of the temperature gradients. Ultimately, these current slices suggest that while case B_p should maintain faster, steadier flow than the other geometries, it could end up still being susceptible to dryout.

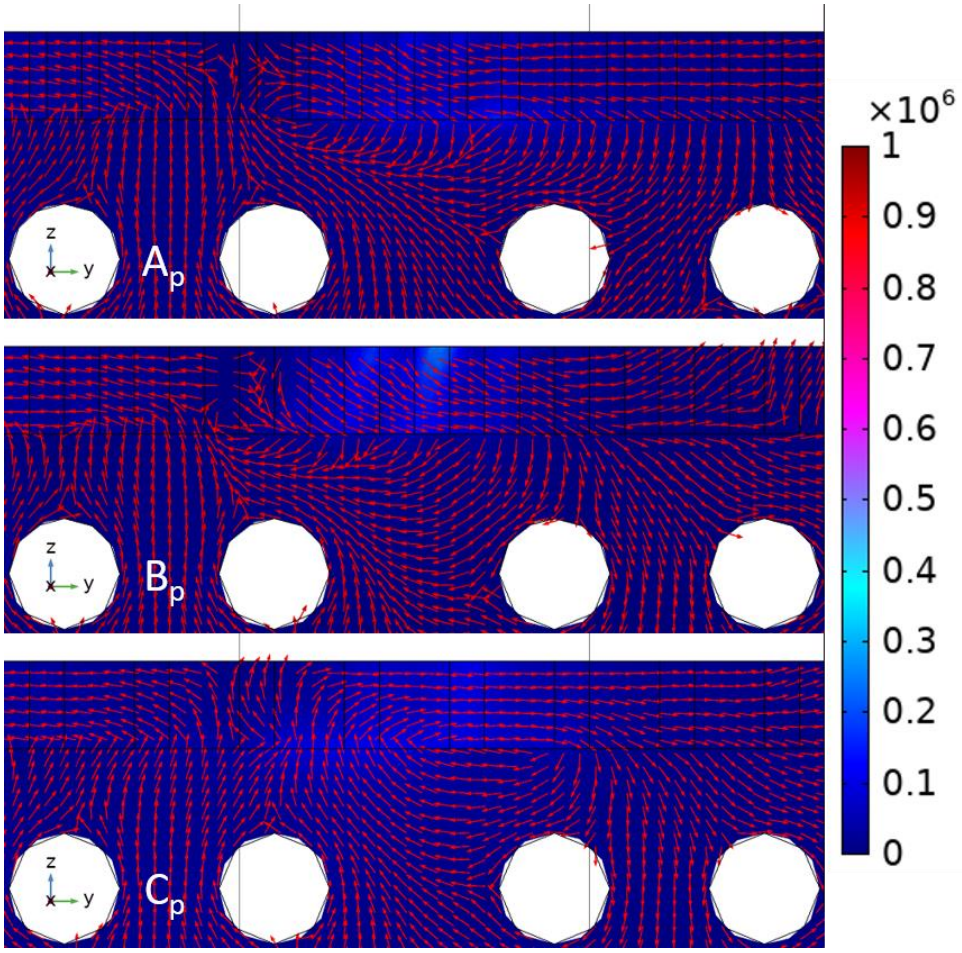

Figure 5.9 – Current density plot in a YZ slice in the center of a primary flow channel, showing the presence of the Y-directed currents that lead to dryout. The color bar shows current density in A/m^2. The arrows follow YZ current direction.

5.1.3 Flow Profile

As expected, the temperature gradients create thermoelectric currents based on the Seebeck effect, and the presence of a magnetic field creates a volume force that drives TEMHD flow. Figure 5.10 shows the volume force in the Y direction at 3 seconds on a slice that borders a row

of posts. As in the electric current profiles, the volume forces peak sharply near the boundaries of the posts, especially the top corners. The temperature gradients provided by the topside heat flux obviously dominate the TEMHD forces, and by 3 seconds, the convection of heat downstream of the center line extends the region of high magnitude driving forces. This is most apparent in case B_p. The effect of the cooling lines can be seen to a much lesser extent along the recirculation channel, in the light red hue.

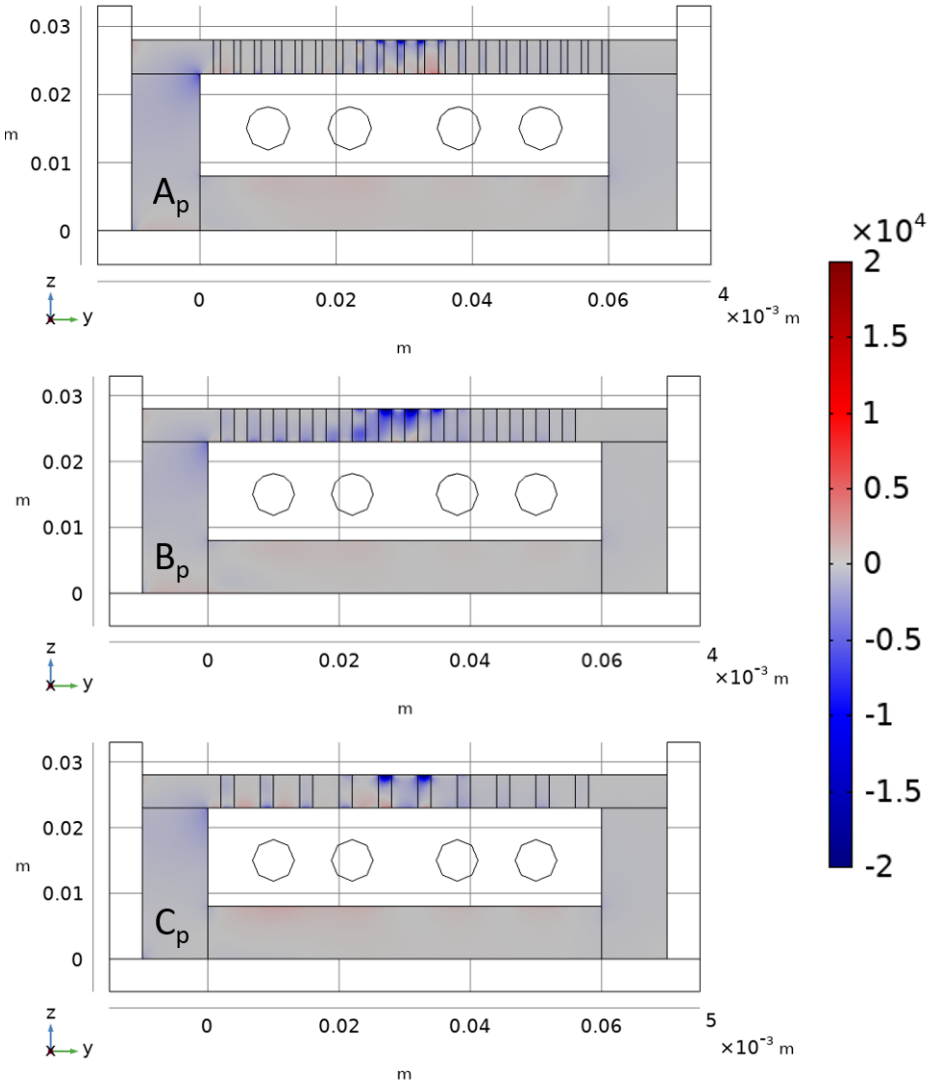

Figure 5.10 – Plot of the Y component of the volume force providing the primary TEMHD drive. The color bar gives volume force in N/m^3.

These volume forces lead to the final product, a TEMHD driven velocity. These velocity profiles, shown in Figure 5.11 show steady recirculating flow through all geometries. The lithium clearly accelerates under the central high heat flux, reaching velocities between 10 and 15 cm/s

through the topside domain, with case B_p reaching a maximum of 26 cm/s. Case B_p, with its lower fluid to solid ratio of 1:1, has more thermoelectric junction area along the main flow channels, and therefore exhibits stronger sustained flow. Cases B_p and C_p have a 2:1 fluid to solid ratio, resulting in lower velocities and more swirling flow along the topside domain. The presence of the cooling channels can be seen more clearly here than in the volume force plots, through the 2 regions of higher velocity flow hugging the topside of the recirculation channel. The central spacing between the cooling lines is slightly larger than the other 2, so the cooling effect is clumped to the right and left of center.

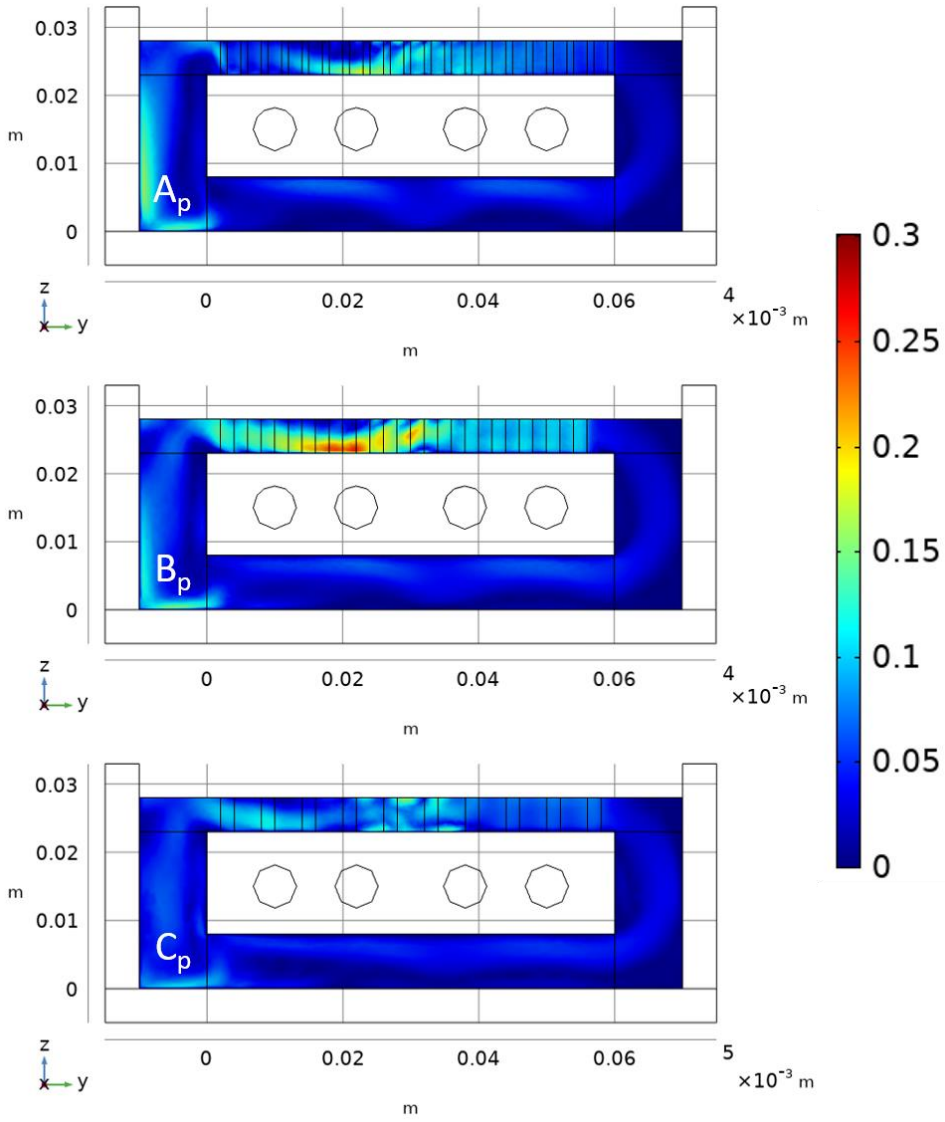

Figure 5.11 – Velocity profile at 3 seconds of simulation time, showing strong lithium circulation and indicating some depression of the high velocity lithium after acceleration through the central heat stripe. The color bar gives velocity magnitude in m/s.

However, the shape of the high velocity lithium profile directly under and downstream of the central high heat flux stripe suggests that dryout may still be an issue with these geometries. To investigate further, it is pertinent to examine the Z-directed volume forces through the domain, as shown in Figure 5.12. The dryout phenomenon hinges on these large volume forces in Z that are driven by the localized topside heat flux dissipating in Y. The sharp temperature gradients that result from the peaked Gaussian instigate a force downward on the upstream side, causing dryout, and a force upward on the downstream side, aiding the formation of lithium pileup. Over time, as the central temperature peak is dissipated downstream, the center of the upward and downward forces shifts downstream. This results in the high velocity lithium depression that extends downstream before rising to the surface to cause pileup, which is evident in both Figure 5.11 and the 2-D models of Chapter 3. The dryout forcing is most pronounced between the posts, as opposed to in the gaps/secondary channels, since the thermoelectric junction is most effective there. The repetition and spatial pulsing develop the swirling motion most evident in the case C_p flow profile directly underneath the central heat stripe. The 4 mm spacing in this geometry allows swirling to manifest more readily without being tempered by further strong volume forces. While the overall velocity profile is slower for case C_p, this effect could help to mitigate dryout, based on the less prominent high velocity lithium depression observed.

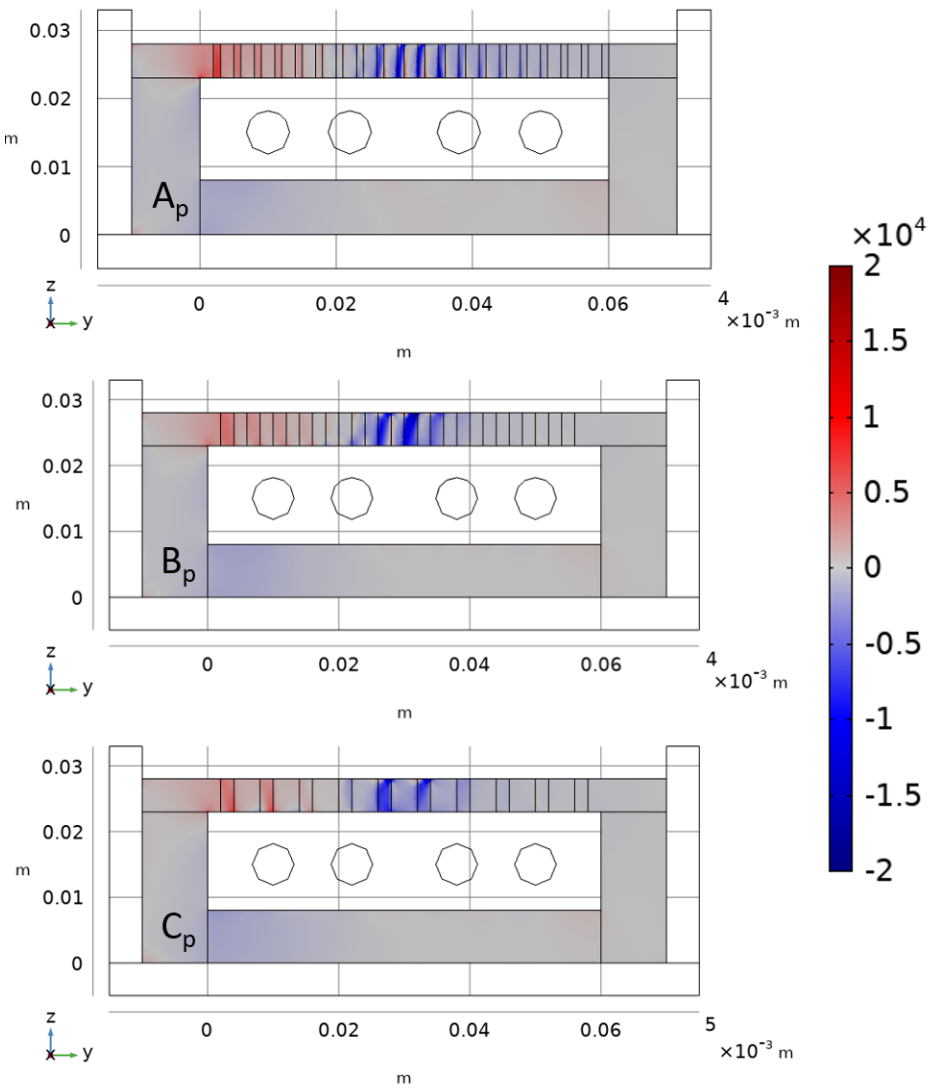

Figure 5.12 – Plot of the Z component of the volume force providing the impetus for dryout and pileup. The color bar gives volume force in N/m^3.

The interplay between the driving force in the main flow direction and the forces developing dryout can be illustrated by plotting the average and minimum volume forces over time in the Y and Z directions, as seen in Figure 5.13. After the initial rapid ramp from t=0, all geometries exhibit sustained overall TEMHD drive in the -Y direction. The magnitude of case B_p in relation to A_p and C_p agrees with the stronger velocity profile seen in B_p. Cases A_p and C_p maintain a similar Y-directed volume force average, suggesting (somewhat obviously) that the fluid to solid ratio of the posts to gaps is an important criterion for sustaining flow. Additionally, the overall post density resistance to flow is also a strong consideration, as the high post density of case A_p is able to keep the average Z volume force low by minimizing swirling, while the eddy

formation in case C_p eventually allows the average dryout force to grow larger than the Y volume force. Note that the average Z volume force also includes any upward pileup forces, so while the fact the average stays negative implies dryout is stronger than the pileup forces, the separation is not captured by the average. Figure 5.13 quantifies the extent to which the volume forces in TEMHD flow are peaked, and in all cases, the dryout force dominates the flow-developing force. The minimum here refers to the directionality of the force; the predominant topside flow is in -Y and dryout in -Z. The Y and Z force peaks are closest in case B_p, which means sustained flow can develop faster under high heat flux as any dryout effect begins. Case A_p maintains the highest peaks of both Y and Z forces, due to the small size of the posts concentrating the thermoelectric currents.

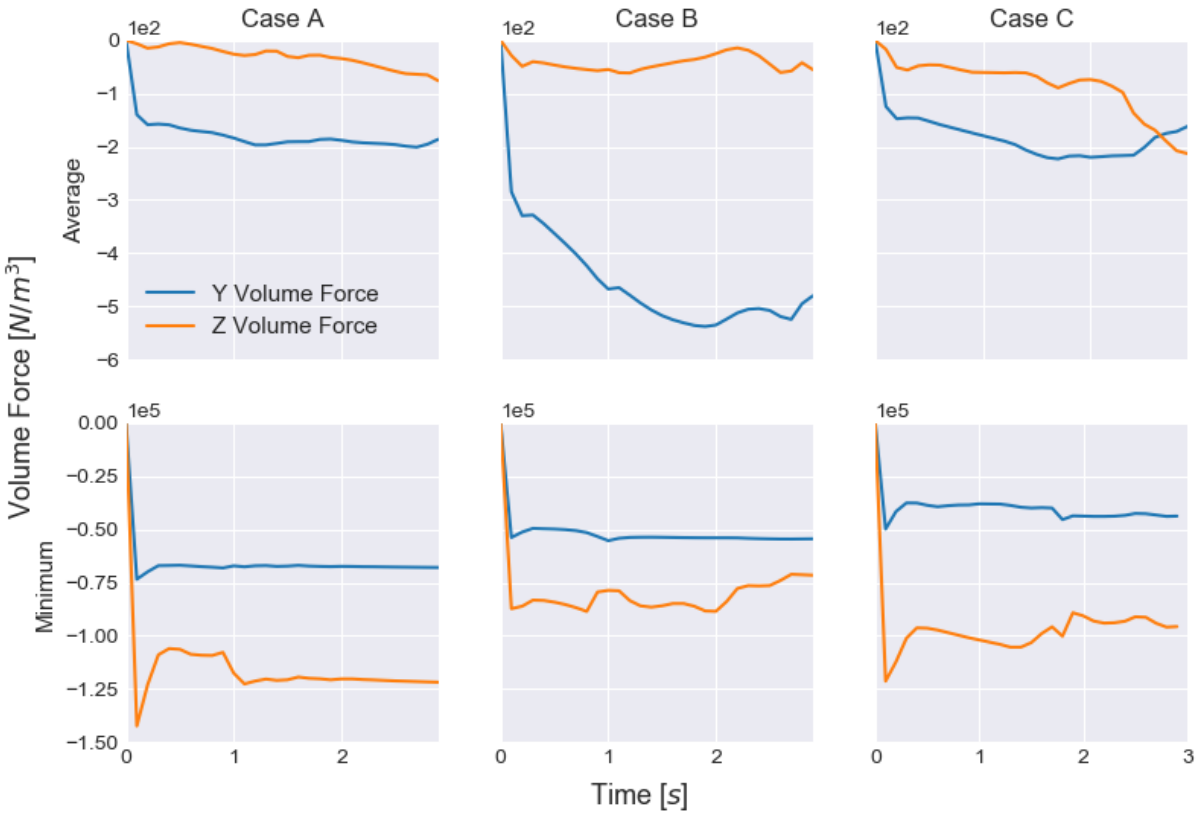

Figure 5.13 – Geometry comparison of minimum and average volume force components over time.

Considering this potential for dryout, the geometry should show sustained surface flow as an indication of resistance to dryout. The velocity magnitude on the top surface is shown in Figure 5.14. Surface velocity remains above at least 5 cm/s over most areas but is noticeably slower

downstream of the topside heat flux. In this region, the accelerated lithium is force downward as shown in Figure 5.11 above.

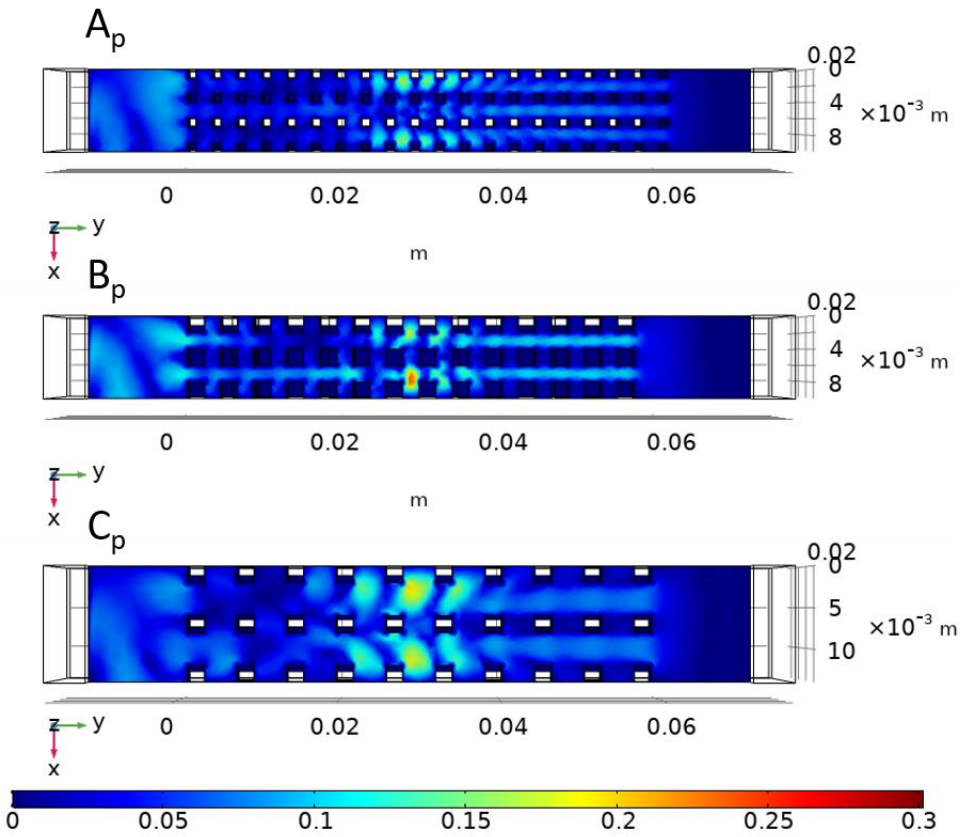

Figure 5.14 – Topside surface velocity magnitude. The color bar gives velocity in m/s.

While in this case the crosstalk is enhanced by the main flow channels entraining lithium from the secondary flow channels that border the boundary, this would be similar to a rapidly accelerating channel experiencing local heat flux pulling lithium from a neighboring channel with slower flow for lithium level support. There is no longer isolation between flow channels, allowing the lithium to flow to level the surface across the PFC. The efficiency of this process varies by geometry and is shown in Figure 5.15 with a color expression based on the X velocity. The post separation of case C_p allows for the highest crosstalk velocities, at around 15 cm/s, while cases A_p and B_p generally exhibit a maximum of 10 cm/s crosstalk velocity (apart from the centermost secondary flow channel in case B_p). The noticeable crosstalk velocities reside in the highest heat flux regions as expected, though low levels of crosstalk in the secondary flow channels is present throughout the domain.

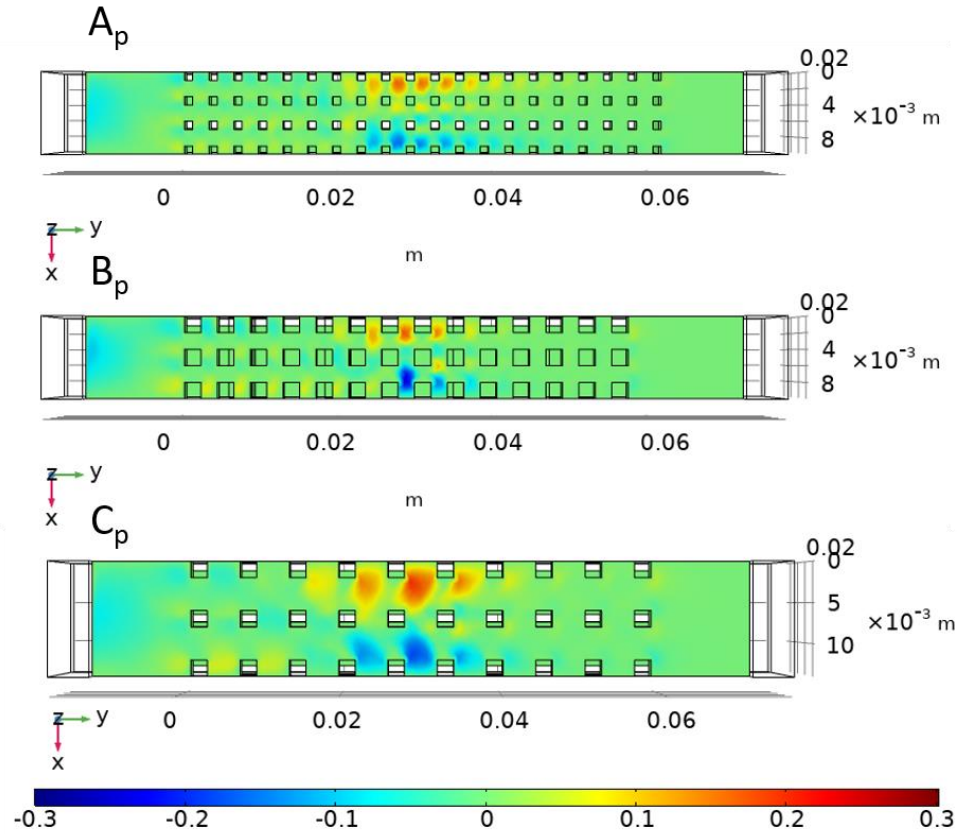

Figure 5.15 – Topside X component of velocity illustrates the crosstalk in the secondary flow channels. The color bar gives velocity in m/s.

5.1.4 Parameter Sweep Effect on Flow

The sets of profiles shown in the previous sections describe the development of TEMHD flow through the 3 different post geometries and provide a glimpse into a representative case that includes both high topside heat flux and rapid lithium velocities. However, this is but a glimpse into the 3-D, time dependent simulations that were run. While it can be difficult to distill information to a presentable format from simulations that are highly transient in both time and space, some key parameters of the open surface flow are shown here with respect to time, as well as modified heat flux and magnetic field. Values are plotted every 0.05 seconds for the duration of the simulation time. Due to differences in geometry and parameters, time stepping and convergence in COMSOL can vary significantly between simulation. Therefore, computational constraints limited the simulation time on select sets of parameters, generally at the highest heat flux and B-field values.

Figure 5.16 shows topside velocity characteristics for all 3 geometry cases as topside Gaussian heat flux is varied. The heat flux is denoted by the peak value of the Gaussian and varied from a low but topside flow significant 0.5 MW/m^2 through SLiDE e-beam relevant 1 MW/m^2 and 3 MW/m^2 to a large fusion device caliber of 10 MW/m^2. For these runs, the B-field is held at 0.05 T, and the heat transfer coefficient is 500 W/m^{2}K. The topside heating is immediately applied at t=0, resulting in rapid acceleration through the topside domain.

The trend in velocity magnitude with respect to heat follows the expected increasing trend. While all geometries develop similar magnitudes over time, the slight variations can yield insight into system resistance to dryout. The overall maximum velocity is achieved by case A_p, nearing 1 m/s, extremely fast with respect to the module size. This is due to the extent of peaking of current/volume force being higher in case A_p because of the small size of the posts. While the nature of TEMHD flow results in peaking of driving forces near the boundaries and corners of the posts, the relationship between the volume maximum velocity and the surface maximum velocity is one way to measure dryout, as a lower surface maximum indicates the highest velocity lithium sinks into the domain. Across the cases, there is a significant reduction in surface maximum velocity in comparison to the volume maximum. Case A_p is the worst scenario, with >50% lower surface velocity at the 10 MW/m^2 case. Cases B_p and C_p each show an approximate 35% and 22% decrease in velocity at 10 MW/m^2. This change reduces as heat flux decreases, as risk of dryout is lower. Case B_p and C_p maintain roughly similar velocities up to at least 1 MW/m^2. Overall, at the max heat flux studied, case C_p exhibits the closest volume-to-surface maximum velocity ratio.

The topside volume average velocities show similar acceleration of bulk lithium in all geometries due to the topside heat flux. Case A_p reaches lower average velocities at lower heat fluxes due to the smaller contribution of the topside posts but has smoother acceleration for all conditions. There is more variation in case C_p due to the larger spacing between the posts and development of eddy formation, as is seen in the velocity profiles in Figure 5.11. Overall, while it can get lost in the noise easily, especially for the high heat flux cases, these profiles display the cyclical nature of the high velocity topside flow visible in the simulations. As the lithium is accelerated under the heat stripe, the high velocity lithium is propelled away from the center. The uneven nature of this acceleration and any depression from dryout readily causes some swirling in the flow. Eventually, the high velocity profile can ‘collapse’ in a way that resembles a hydraulic

jump or a wave back toward the center, as would be expected in a true free surface fluid (refer to Chapter 7 for more insight on this). As this happens, the steady high velocity stream experiences mixing and eddies, dispersing the flow and lowering the maximum velocities, after which flow is reaccelerated under the heat stripe into a more stable high velocity stream once more. This cyclic wave-like motion is seen on shorter time scales of 0.3 to 0.5 seconds in cases A_p and B_p, and is most clearly shown in Figure 5.16 through case B_p at 3 MW/m^2 and case A_p at 3 and 10 MW/m^2 (examine the maximum velocity profiles after ~1.5 seconds). In case C_p, the larger post spacing and high overall eddy formation seems to extend this wave motion to 0.7 to 1.0 seconds, seen most clearly in the 3 MW/m^2 volume average curve and the 1 MW/m^2 volume maximum curve.

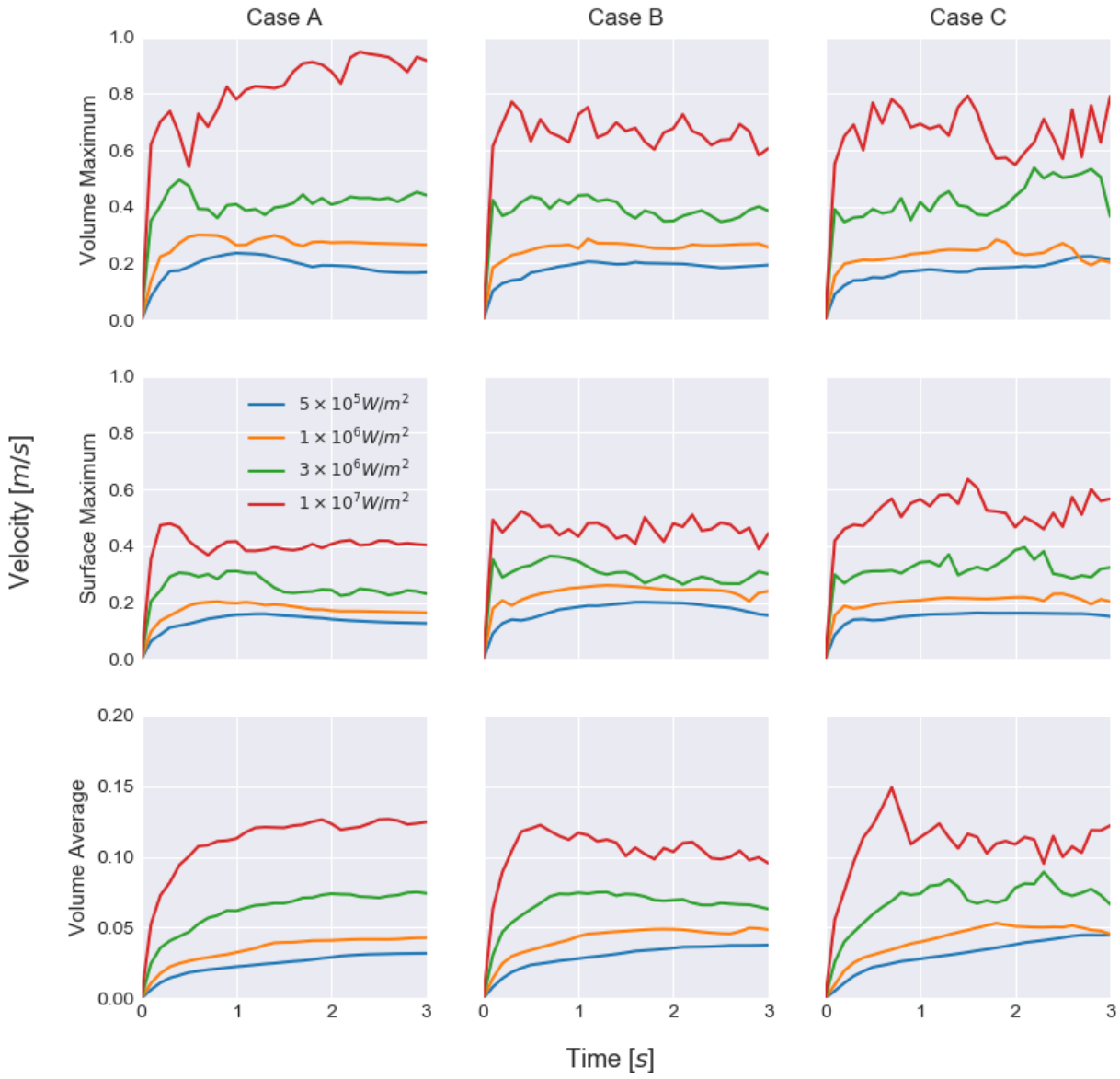

Figure 5.16 – Geometry comparison of several velocity profile characteristics over time, for various peak topside heat flux values.

The interplay between the thermoelectric driving forces and MHD drag presents a more complicated picture of velocity development in relation to increasing B-field. Figure 5.17 shows the topside maximums and average velocity development in time, along with the average recirculation channel velocity, for select B-fields from 0.05 to 1.0 T. These sweeps were done for a topside heat flux of 1 MW/m^2. The magnetic field strength is directly included through external source terms in the EC and LF COMSOL interfaces. As the magnitude of B increase, these source terms can become quite large, which can lead to issues with convergence and a decrease in the step size COMSOL can take in response to simulation error. To improve the solution quality,

these sweeps were carried out on smaller domains (generally a single primary flow channel) with finer meshes for more resolution, and the magnetic field was ramped from zero to the final value from t=0.1 to t=0.6 seconds. The adjusted domain size can lead to a difference in velocity profiles due to the relation between topside and recirculation channel flow volumes, and the magnetic field ramping obviously affects flow development due to the initial dominance of Lorentz force drive followed by the increasingly significant MHD drag.

Looking at the topside surface and volume maximum curves suggests an opposite trend than expected. Theoretically, the TEMHD velocity peaks around 0.5 to 0.1 T, depending on geometric factors, and falls off from there as MHD drag forces dominate fluid motion. However, in the topside domain, where the high heat flux is prescribed, the lowest maximum velocities are seen for the lower B-field values. Maximum velocity actually increases with increasing B-field. In the topside domain, the thermoelectric drive from the high local heat flux dominates over the MHD drag in a small area. It is expected that this behavior is most likely a result of the transient nature of the simulation, with rapid acceleration occurring throughout the fluid domain during the B-field ramp, especially in the regions with the largest thermal gradients. This high velocity is not damped by further increases in the B-field within the 1.5 to 3 second simulation time. The velocity magnitudes tend to stay relatively similar as well, suggesting the heat flux value is the dominant driver of maximum topside velocity. It is expected that this effect diminishes over longer time, as suggested by previous time-independent stationary parameter sweeps of TEMHD flow [64].

The average velocities of the topside domain and the recirculation channel present the expected relationship between flow velocity and magnetic field. In these profiles, the effect of the B-field ramp is easily observed, especially at high B values. The flow quickly accelerates and is then damped once the field reaches a critical value. The ramp time is kept constant through the sweep, meaning the period of rapid acceleration before damping is shorter as B increases, as indicated by the velocities. After drag limits flow speed, the post geometries exhibit, on average, a slow acceleration of flow. This is caused by the slowly increasing relevance of the cooling channels providing thermal gradients to drive flow. This provides an additional source of drive that become more relevant over time. The effect is more pronounced in cases A_p and C_p, which is posited to be due to the trench to flow ratio. The TEMHD drive from the posts in these 1:2 solid to fluid area cases, while always dominant under high heat flux, contributes less overall drive once

cooling starts to become relevant. Case B_p is more immediately resilient, especially in the recirculation channel flow, though it is expected that over longer simulation times this slow ramp would be observed.

While the ramping of the magnetic fields inserts more volatility into an already highly transient set of simulations, this sweep provides a glimpse into realistic startup conditions and how flow velocities are affected as the field coils are powered. While on average the flow speed reacts as expected to increased B-field, the regions under the highest heat flux may remain relatively indifferent in terms of flow acceleration. This is important to consider for device development, as external pumping or recirculation channel development can be tailored to account for this profile development depending on full power operating conditions.

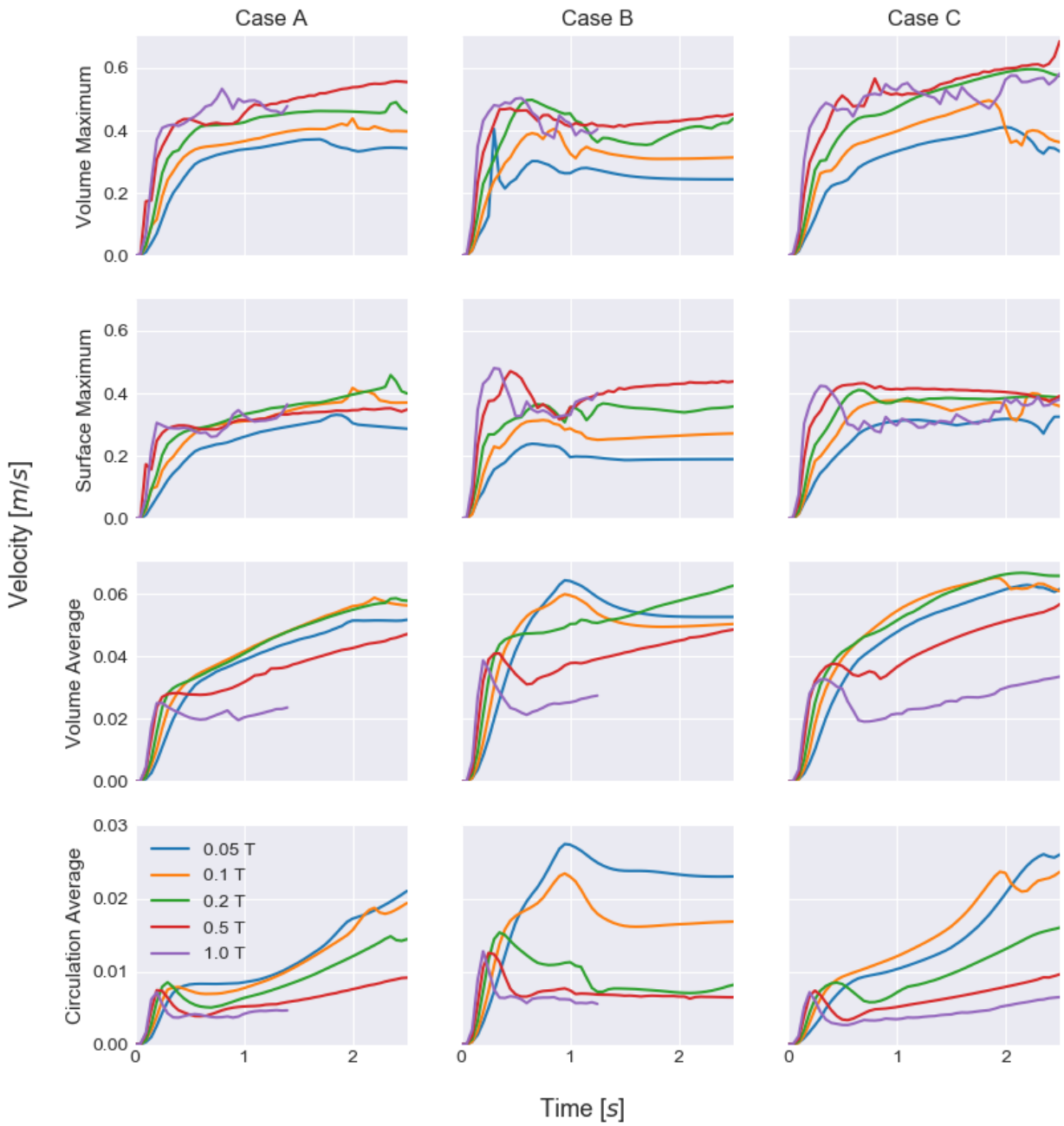

Figure 5.17 – Geometry comparison of several velocity profile characteristics over time, for various magnetic field strengths.

5.1.5 Relation to Heat Sink Optimization

Another method of analyzing performance of TEMHD flow structures is via heat transfer metrics. All geometries of LiMIT-style designs resemble types of heat sinks, from plate type (trenches) [90], to pin fin (posts) [91], to metallic foam or wire mesh (foams) [92]. Extensive work has been performed over many decades on heat sink testing, modeling, and optimization. While a

rigorous study on the design and optimization of heat sinks is not possible here, it is pertinent to generalize some metrics used to quantify heat sink performance in order to discuss the thermal performance of the post designs. Future studies should focus on combining knowledge of heat sink optimization methods, such as entropy minimization [93], [94], with TEMHD flow models. Here, common measurable metrics will be discussed in relation to the post designs, including total heat output, maximum surface temperature, thermal resistance, and pressure drop [95], [96]. The total heat output Q_{out} quantifies the amount of heat that is being removed from the system, and is defined as

$$Q_{out} = \dot{m} C_p (T_{out} - T_{in})_{avg}$$

Where $\dot{m}$ is the mass flow rate, taken at the outlet, C_p is the heat capacity at constant pressure, and $(T_{out} - T_{in})_{avg}$ is the difference between the average inlet temperature T_{in} and the average outlet temperature T_{out}. Maximum surface temperature is straightforward, and is taken across the entire fixed surface, including the lithium and stainless-steel surfaces. It should be noted that these values are conservative, since there is no lithium present above the posts to aid in convection or conduction. The structures can only be cooled from the side. In practice, lithium will always wick to cover the structure surfaces, and even a thin layer of lithium will drastically improve performance. Thermal resistance R_{th} measures the temperature increase versus applied power, and is defined as

$$R_{th} = \frac{(T_{max} - T_{in})}{Q_{tot}}$$

Where T_{max} is the maximum temperature, taken here as the maximum overall surface temperature including the stainless steel in order to present a conservative case. Q_{tot} is the total heat applied, calculated as a surface integral of applied topside heat flux. The pressure drop is calculated between the inlet and outlet of the topside structure. To ensure effective heat transfer and maximum convection, less pressure head and lower pressure drop is optimal. Since this is a recirculation system and not an inlet to outlet setup, these values may be less meaningful. The topside heat flux also leads to large swings in pressure in the topside domain due to the lithium acceleration, which could further skew the results.

These metrics are plotted over time in Figure 5.18, for the topside heat flux parametric sweep, as thermal performance at high heat fluxes is most important. In total heat output, case A_p lags the other designs. This is most apparent at the 10 MW/m^2 value, where the 2 mm post designs of case B_p and C_p show very large improvement over the 1 mm case A_p. Interestingly, case A_p exhibits lower topside maximum temperatures than the other designs. This is likely a result of the conservative nature of the simulations mentioned earlier. Since the tops of the posts are in direct line of the heat flux, they can only be cooled from the sides, with no lithium on the top to aid in convection or conduction. While this will not be true in practice, it leads to larger overall maximum temperatures due to the poor thermal conductivity of stainless steel, especially for the larger 2 mm posts. The 1 mm posts can be more effectively cooled by the lithium flow. Low thermal resistance is a sign of better heat transfer capabilities, as additional heat applied leads to less of a temperature increase in the fluid. All designs stay under 1 K/w for all values of heat flux. The larger TEMHD velocities driven by higher heat fluxes results in a reduction of thermal resistance and an increase in performance. Cases A_p and C_p have the lowest overall thermal resistance, and case C_p starts with a lower value at the lowest heat flux, indicating slightly less performance improvement with heat flux.

Pressure drop in all geometries begins with a small negative drop due to the topside heating pushing downstream. It then quickly ramps positive as flow accelerates, as expected since the topside structure impede flow. Since the module recirculates and has a fixed surface, it is expected that this pressure drop should begin to lower over larger time scales, and this happens at different rates and different times for each geometry and heat flux. The high post density of case A_p creates the highest sustained pressure drop of the designs, while cases B_p and C_p stay lower and display more variability. It is somewhat surprising that case B_p exhibits the lowest overall values, with the 10 MW/m^2 case even showing a drop back negative after approximately 2.1 seconds. As mentioned, these values are likely skewed by the high acceleration of the localized topside heat flux, so the fact that case B_p has more TEMHD drive area allows the topside heat flux to counteract pressure drop through the structures more effectively.

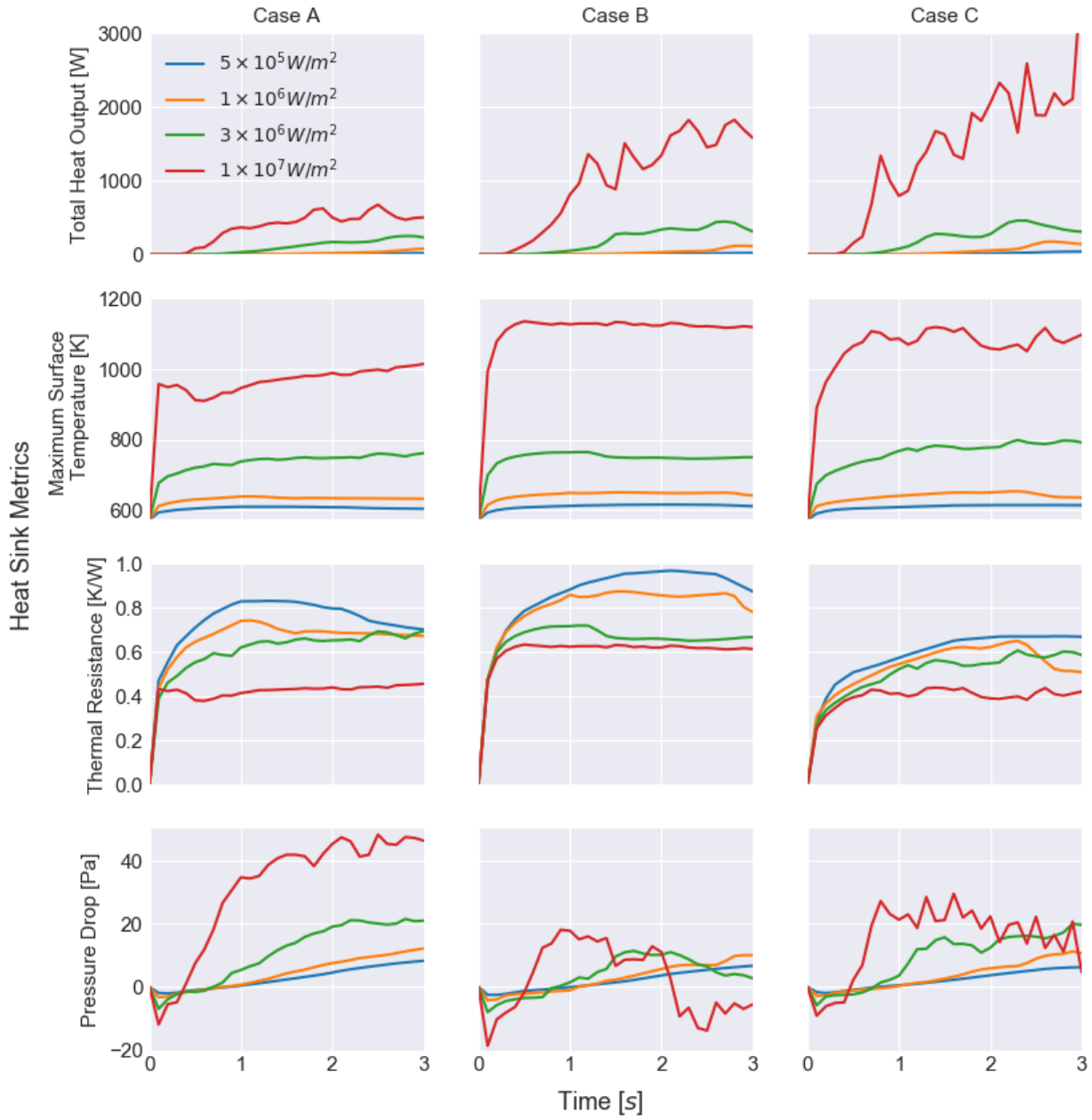

Figure 5.18 – Geometry comparison of heat sink optimization metrics over time, for various peak topside heat flux values.

5.2 Experimental Testing

The case B_p and case C_p post designs were loaded into the SLiDE apparatus for proof of concept TEMHD flow testing. Refer to Chapter 4 for a description of the SLiDE chamber components as well as general installation and lithium loading, testing, and disposal. A photograph of the machined case C_p plate installed on the top side of the flow module is shown in Figure 5.19. To enhance thermal conductivity between the base module and the base plate of the structures, a thin layer of thermally conductive silver paint was added under the structure base plate. The fit of the plates and small amounts of silver paint ensured minimal risk of lithium attack and passivation due to this impurity.

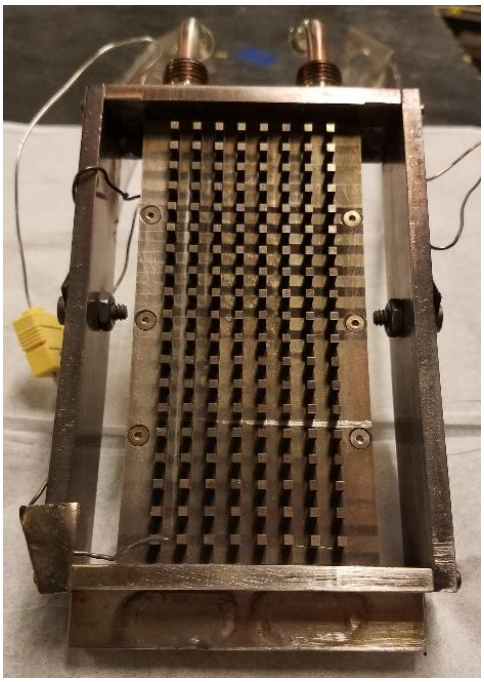

Figure 5.19 – A post plate installed in the test module, without the base plate and heater block.

Lithium is injected into the side channels of the module. Figure 5.20 shows the injector entering the frame from the right, and the nozzle is aiming down and into the page along the side channel. As mentioned in Section 4.2, lithium is injected below the wetting temperature of the stainless steel structure, to lower risk of leakage from the nozzle. This initially results in the lithium fill seen in Figure 5.20 Left. The lithium wicks through the hotter recirculation channels but is not immediately able to effectively wet the topside structure. After injection, module temperature is raised to 400 to 500 ºC to enhance wettability and clean the lithium surface. After cooling from these temperatures to optimal experimental temperatures of 250 to 350 ºC, a much

cleaner lithium surface exists, as seen in Figure 5.20 Right. In this image, the apparent splattered particles on the top surface is in fact a reflection of the top surface of the chamber, which was subject to high levels of lithium evaporation during the wetting and cleaning steps.

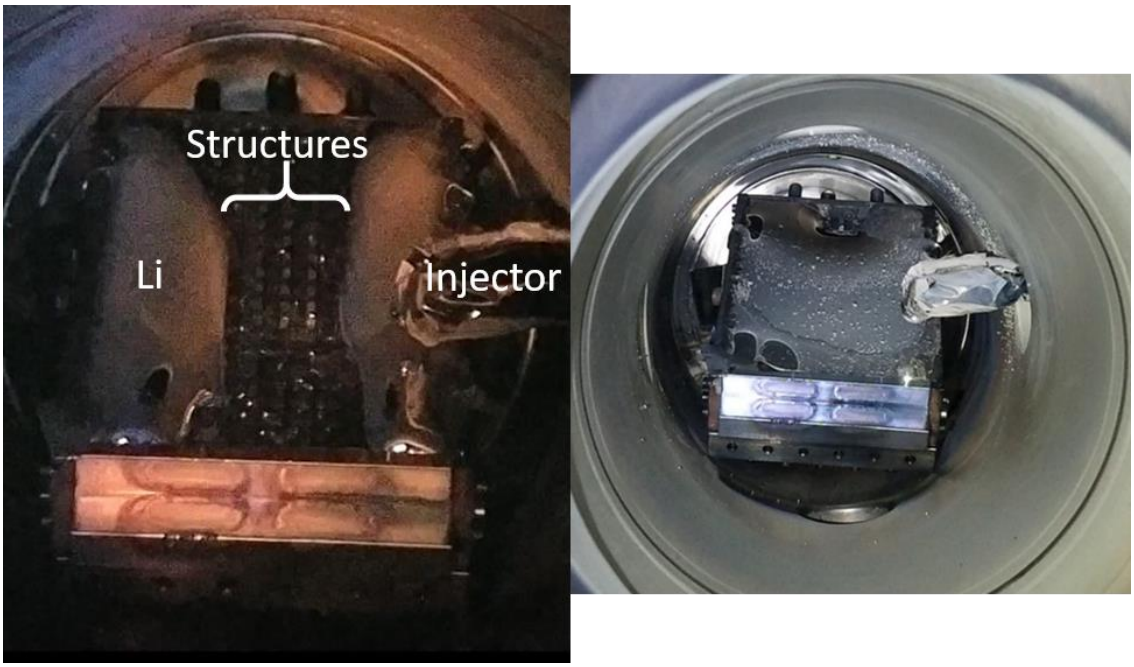

Figure 5.20 – Left: Intermediate step in lithium filling after injection but before complete wetting of the topside surface. Right: Lithium surface after near complete wetting and surface cleaning, with the mirrorlike surface reflecting evaporation droplets on the topside of the chamber.

SLiDE allows 2 views for visualizing flow – an 8-inch window at the end of the main chamber tube or a 2.75-inch shuttered window above the module at a 90º angle to the main tube. The view from the 8 inch windows yields images of the entire module as seen in Figure 5.20, but the view is obscured upon installation of the e-beam and limited to viewing around the e-beam with a mirror installed along the side of the chamber. The 2.75-inch view is seen in Figure 5.21, which shows the wetted, cleaned, even fill test of case B_p. From here, better views of a select portion of the module are possible, which works well for the post designs, but can limit visibility when the surface structure is varied (see Chapter 6).

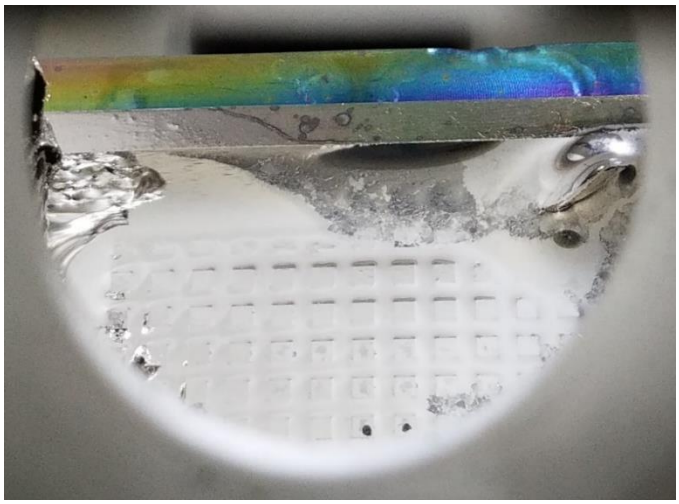

Figure 5.21 – Perfect fill scenario in the case B_p posts. The majority of the surface is clean, though some impurities exist near the top center of the module. The injector is reflected in the top left corner of the surface.

The proof of concept testing of the post designs was carried out with bottom side heating only, forced helium cooling at 20 psi, and a low magnetic field that was varied from 0.02 to 0.07 T (200 to 700 G) which corresponds to 2 V to 7 V on the 4 high-current magnet power supplies. The SLiDE setup contains a DC battery bank which allows short pulse magnetic field of up to 0.2 T, but this was not attempted here due to safety concerns. The range of magnetic fields studied encompasses the peak TEMHD flow region, before MHD drag forces begin to dominate the flow profiles. In order to visualize flow startup from a no-flow condition, the magnetic fields are typically off for proof of concept testing. Around 10 seconds after cooling is activated, the B-field is pulsed on for 5 to 7 seconds before disengaging.

5.2.1 Temperature Measurements

Temperature measurement of any PFC is necessary to monitor system performance. When the PFC includes TEMHD driven liquid lithium, temperature data informs loading and wetting potential, provides an assessment of whether current conditions are optimal for operation, tracks the development of thermal gradients required for TEMHD, and provides evidence of flow through the system. As diagramed by Figure 4.7, there are 7 thermocouples in use on this testing module to measure temperature over time. The 4 placed on the module measure the temperature of, from bottom up (or generally hottest to coldest), the heater block, the recirculation channels, the bottom of the structures, and the top of the structures. As cooling is activated, a hot to cold temperature gradient is formed from the topside to the center, and from the heaters to the center. Though there

is no additional topside heating applied in the proof of concept testing, the latent heat in the module is slow to dissipate, allowing for significant runtime before the entirety of the topside is cooled. With 20 psi helium cooling, the latent heat on the topside is enough for a conservative estimate of 3 minutes of continuous operation, based on the 50 ºC drop in the temperature of the post bottoms seen in Figure 5.22 below. It is expected that the heat capacity and thermal conductivity of lithium could extend this time if needed.

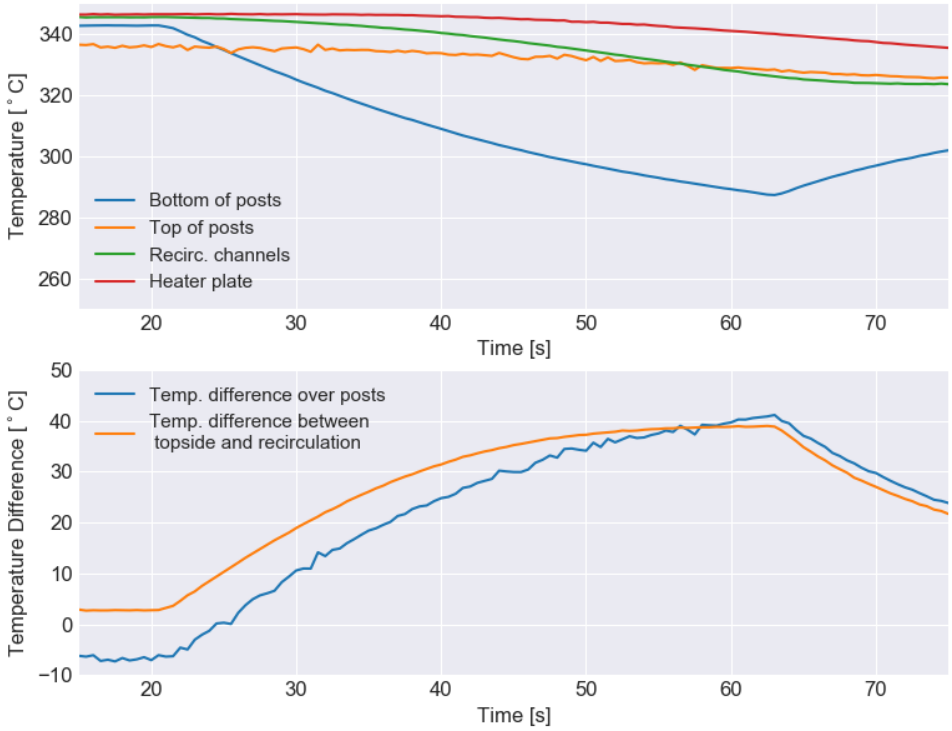

Figure 5.22 – Thermocouple response for reference case of module cooling with no magnetic field pulsing to drive TEMHD flow.

As implied above, Figure 5.22 establishes a base case of temperature behavior in time with 20 psi forced helium cooling in the cooling channels. The top plot displays the response of all 4 module thermocouples, while the bottom plot shows the temperature differences that develop along the topside structures as well as between the topside and bottom side channels. Note that while initial conditions can vary extensively between tests based on a myriad of heating and cooling trends, the relative shapes of the profiles signify important development of temperature gradients and therefore flow. Here, the post bottom thermocouple records the fastest and most pronounced decrease of temperature, as this location maintains the most effective thermal contact to the stainless-steel base plate and resides closest to the cooling lines. Over the course of cooling,

the other thermocouples begin to register declines of various magnitudes, before beginning the thermalization process once cooling is turned off.

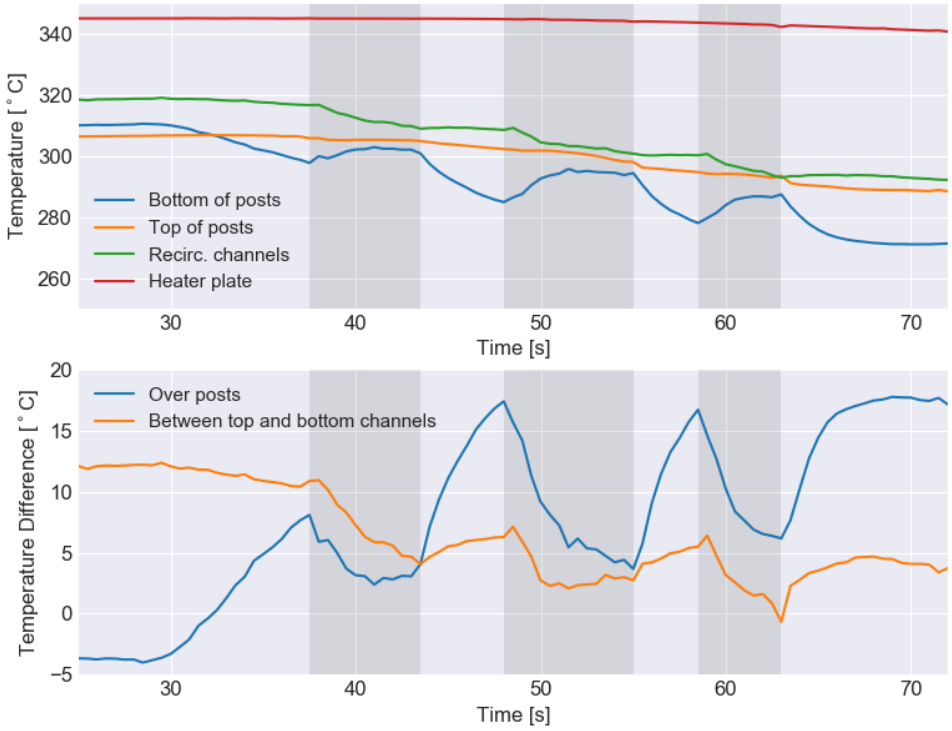

Figure 5.23 – Representative thermocouple response for a set of TEMHD pulses at 0.05 T magnetic field. The shaded bars represent the times the magnetic field is activated.

Figure 5.23 shows a representative set of temperature curves for the post TEMHD proof of concept testing. The initial conditions differ between tests because full thermalization between the heater plate and the module in its entirety is not feasible between experimental runs, however this is not expected to drastically effect development of TEMHD flow. Regardless, the differences in the temperature profiles are immediately apparent. This plot comes from a 0.05 T test of the case B_p posts that included 3 pulses of the same magnetic field. The darker shading indicates the periods of time in which the magnetic field is on.

Cooling is activated 28 seconds into the run. Again, the post bottom thermocouple is the fastest to respond, and after roughly 4 seconds the bottom plot indicates the development of the desired positive temperature gradient along the topside structures of the module. At 38 seconds, the magnets are activated, and the fun begins. TEMHD flow is instantly driven by the presence of the magnetic field. The temperature trend of the bottom of the posts reverses course and rises toward the top of post temperature, indicating temperature equilibration as flow and channel

crosstalk mix the topside lithium. The post top temperature pauses its decline, then slowly continues to fall. Taken together, the profiles of the topside thermocouples indicate the recirculation of lithium, as hotter lithium from the recirculation channels is pushed to the topside via TEMHD. Likewise, the recirculation channels display enhanced cool down during the pulses as cooler lithium from the topside is driven into the recirculation channels.

Looking closely at the curves reveals a slight (~0.5 s) delay between the sharp changes in temperature profile between the bottom of the posts and the recirculation channel, which persists over each pulse (and different runs). This time delay is based on the relative positions of the thermocouples and further indicates bulk circulation. The underside thermocouple is place approximately 2.5 cm into the recirculation channel, while the thermocouple at the bottom of the posts was placed less than 1 cm from the side channels.

After the pulse is turned off, thermal gradients quickly reestablish themselves as the pre-flow cooling trends restart once flow stops. This allows for reliable restart over the course of several pulses, as TEMHD relevant temperature gradients develop over the topside structure height. Before the second pulse, a maximum temperature gradient of 3400 ºC/m is established on the topside. While not a driving temperature gradient, the difference between the topside and bottom side channels indicates the mixing taking place, as they trend to the same temperature over each pulse.

This strong indication of flow persists across all testing conditions and provides a non-visual indication of bulk TEMHD circulation through the module. Unfortunately, quantifying flow speed using this technique is not yet reliable. The changing initial conditions and pulse-to-pulse error dwarf any change due to flow speed. There is not enough difference between the velocity profiles that develop in this range of magnetic field, but after testing in regions that exhibit large difference in TEMHD flow velocity, it may be possible to correlate temperature data to velocity.

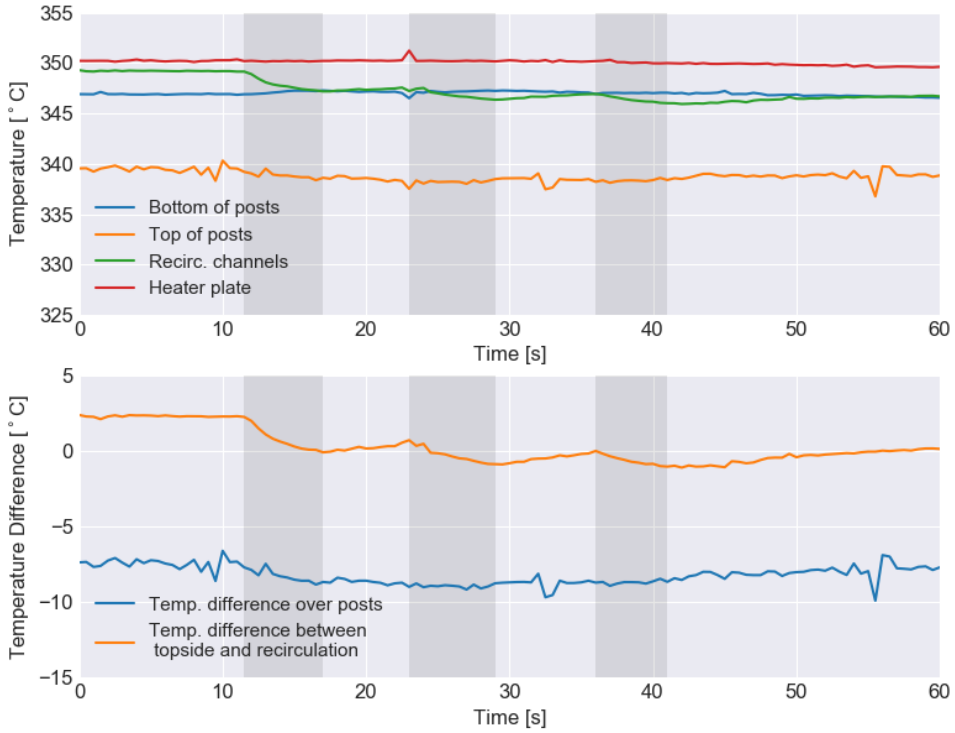

Figure 5.24 – Thermocouple response for reference case of 0.05 T magnetic field pulsing with no forced helium cooling.

The profiles in Figure 5.24 provide a further check that the temperature profiles in Figure 5.23 indicate strong, sustained TEMHD flow. This reference case pulsed a 0.05 T magnetic field for similar times at similar intervals without any cooling. The temperature gradients that are inherent in module construction and thermal distribution should therefore drive flow, but not as significantly as the cooled case. As seen in Figure 5.24, there is minimal recirculation through the module. The difference between topside and bottom side channels does decrease, indicating some mixing, but the obvious trends from the actively cooled case are not seen here. While a lower but still significant temperature gradient exists on the topside structures, it is acting in opposition to the temperature gradient in the recirculation channels. Therefore, bulk flow is not possible. Visually, slow swirling and eddy formation develops on the top surface of the lithium.

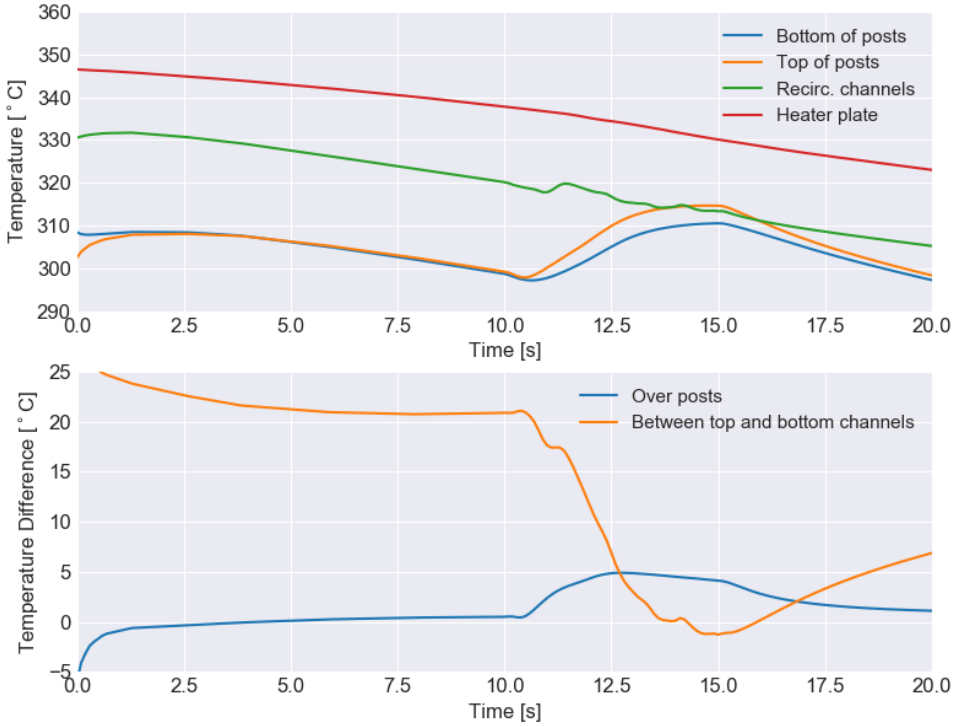

Figure 5.25 – A magnetic field pulse modeled in COMSOL, showing temperature data from similar locations as the experimental thermocouples. A magnetic field of 0.05 T is on from 10 to 15 seconds, with approximately 0.1 to 0.2 seconds of ramp time on each end.

The COMSOL simulations that were run for this work were generally initialized at a constant 300 ºC with immediate cooling and magnetic field (with exception of the immediate ramp of B that was used for the field sweeps). This is generally acceptable as a close approximation to experimental conditions, results in reliable variable profiles, and reduces computation time and instability. However, as a comparison test, a test case was run with an initial temperature gradient that more closely resembles the experimental conditions seen above. Figure 5.25 shows the temperature profile of a COMSOL simulation initialized with a temperature distribution of $340\ °C - 40\left(\frac{z}{0.03}\right)$. Cooling was immediately enabled, and the magnetic field was pulsed on between 10 and 15 seconds. While the behavior of the temperature between the posts is not identical, most likely due to the placement of the data extraction points, the bulk circulation is clearly seen through the temperature increase of the topside channels, and the equilibration of temperature between topside and bottom side bulk lithium temperature. While this is shown here as further indication of the reliability of COMSOL simulations of TEMHD flow, these types of fine-tuned simulations may warrant further study (see Section 8.6).

5.2.2 Particle Velocimetry

For initial testing of TEMHD system in the SLiDE module, PIV is currently the most reliable method for determining lithium velocity. Tracking impurity particle motion on the top surface results in a decent estimate of bulk flow speed, but potential for discrepancy remains. The general setup and concern with the method is detailed in Section 4.2. In order to quantify lithium velocity through the set of experimental conditions, videos taken of the experimental runs are converted to image series, and extensive particle tracking is done in ImageJ, using the Cell Counter plugin. Particle motion was rectified with respect to a reference point on the solid edge of the module, to remove camera or module movement. While surface eddy formation may develop due to large areas of impurity scaling or passivation regions that have 'locked' to the solid structures, the motion of small particles can generally be captured, allowing for effective flow characterization. The pulsing of the magnetic field also aids in breaking up impurity layers to better observe flow.

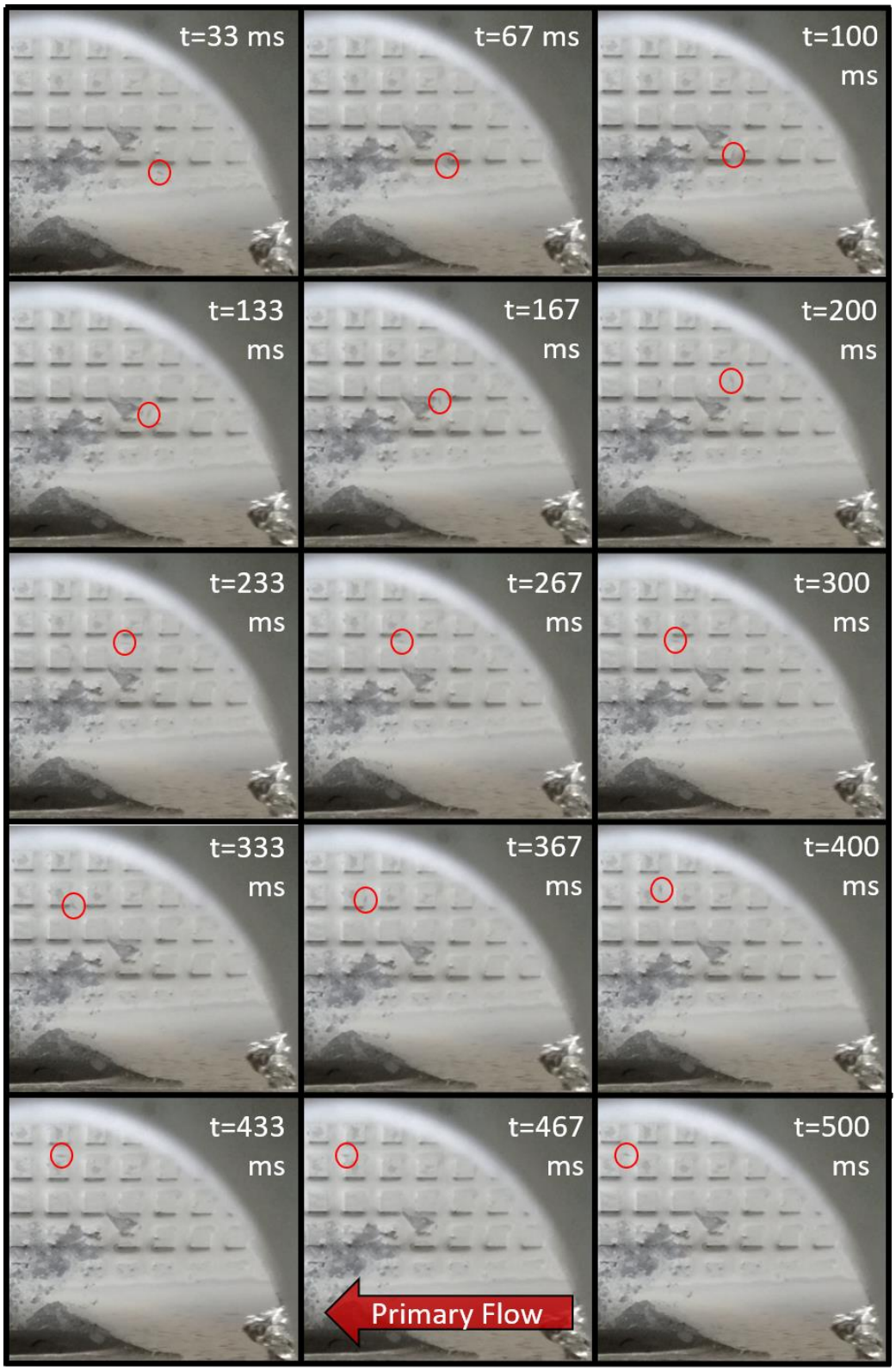

Figure 5.26 – Series of images showing particle tracing over several frames in ImageJ.

An example of a small but dark impurity particle entrained in post TEMHD flow is shown in Figure 5.26. Over the course of 15 frames totally 0.5 seconds, the particle moves through the case B_p post structure, utilizing the secondary crosstalk flow channels before accelerating into a primary flow channel. There is a wide variety of particle size and visibility throughout the sets of images, which adds to the challenge and bests basic computer vision algorithms that were attempted for particle tracking.

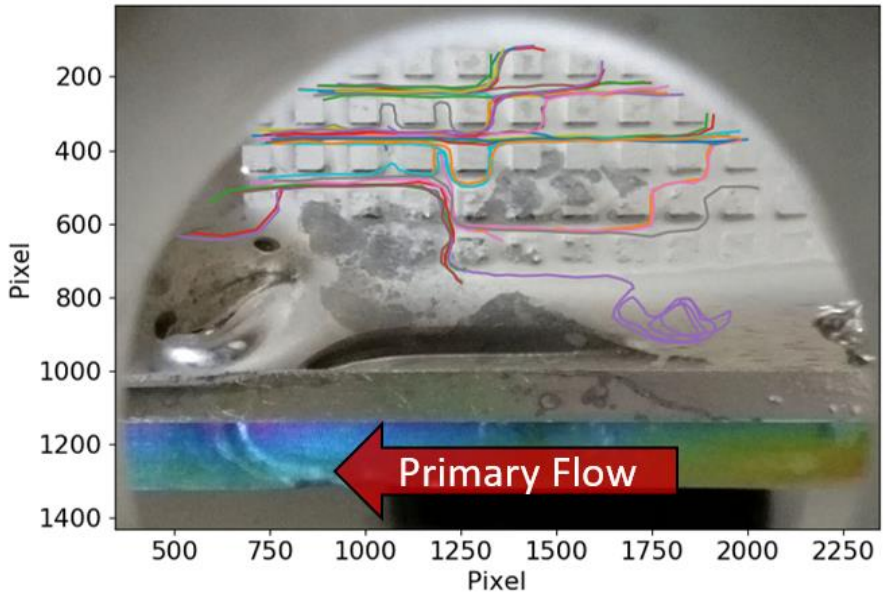

Figure 5.27 – All tracked particle traces for one pulse of TEMHD flow with a 0.07 T magnetic field, including an assortment of primary flow, secondary crosstalk, and swirling flow toward the bottom of the image.

Figure 5.27 shows an example of one pulse of tracked particle data with the particle track collocated on the first frame of the image series. Extensive flow is registered throughout the observable area of the topside surface. This example is from the case B_p structures, at a B-field of 0.07 T. There is swirling on the surface of the bulk flow that wicks up to the edge of the module, and eventually that particle is entrained in primary flow and moves through the domain. Widespread crosstalk is observed through the secondary channels, qualitatively matching the flow characteristics expected from the models. Of course, as a result of the multitudinous avenues for flow, there is a wide range of expected velocities as well.

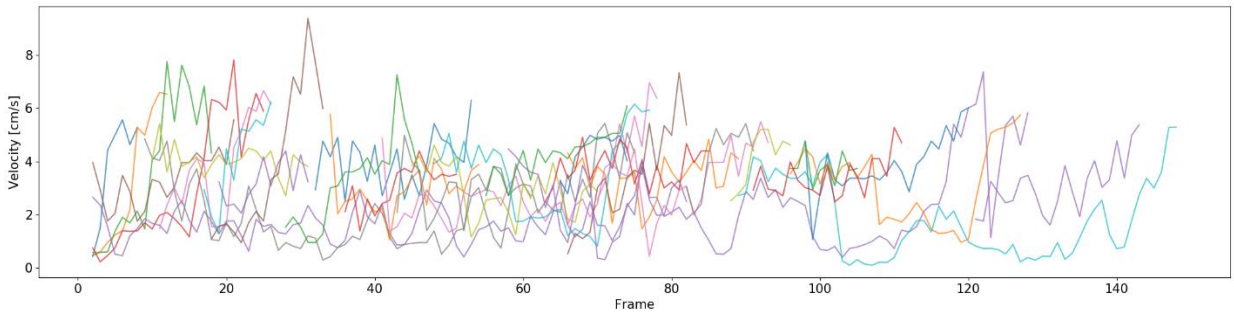

Figure 5.28 – Velocities versus frame number for all particles tracked in the representative pulse shown in Figure 5.27.

Figure 5.28 messily but accurately displays the cacophony of particle motion through the post designs. There is huge variability in particle velocity from effects such as: particle size, flow transitioning between primary and secondary flow channels, eddy formation on the surface, uneven TEMHD forcing by the posts, along with image resolution and reliable positioning while tracking. While these effects are difficult to isolate and mitigate, there are still avenues for correlating the experimental data to the modelling.

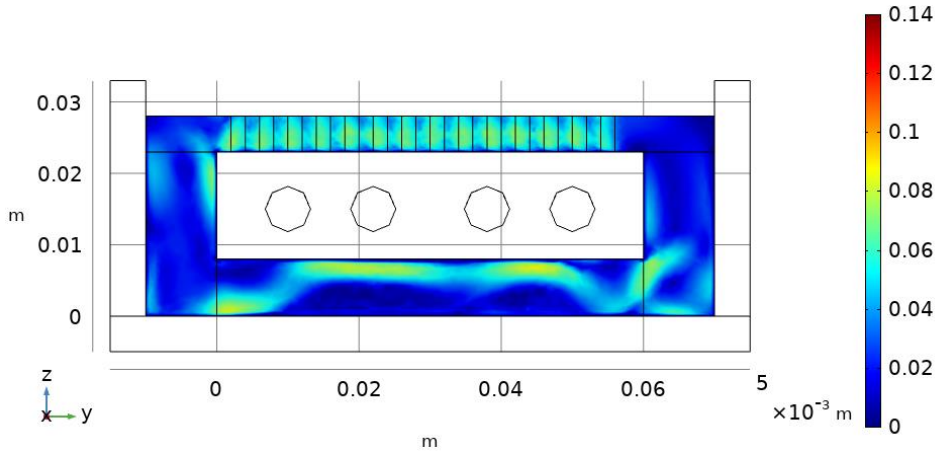

Figure 5.29 – COMSOL velocity trace for the conditions shown in the representative pulse shown in Figure 5.27.

Representative magnetic field sweeps were run in COMSOL for the same magnetic field values as were experimentally tested. For these simulations, topside heating was disabled, and the bottom heaters and cooling channels provided the thermal gradients for TEMHD flow. A representative velocity profile is shown in Figure 5.29, at a 10 second simulation time. The posts drive sustained, if uneven topside flow in the range of 6 to 7 cm/s. However, topside flow is noticeably reduced, with an average of 1.96 cm/s. The variation of topside flow speeds evident in the experiments is present in the modeling results as well. Flow recirculation is readily apparent,

with the effect of the cooling channels seen in the recirculation channel, though the slower overall flow (than the high heat flux cases) results in more eddy development, especially along the side and bottom channels.

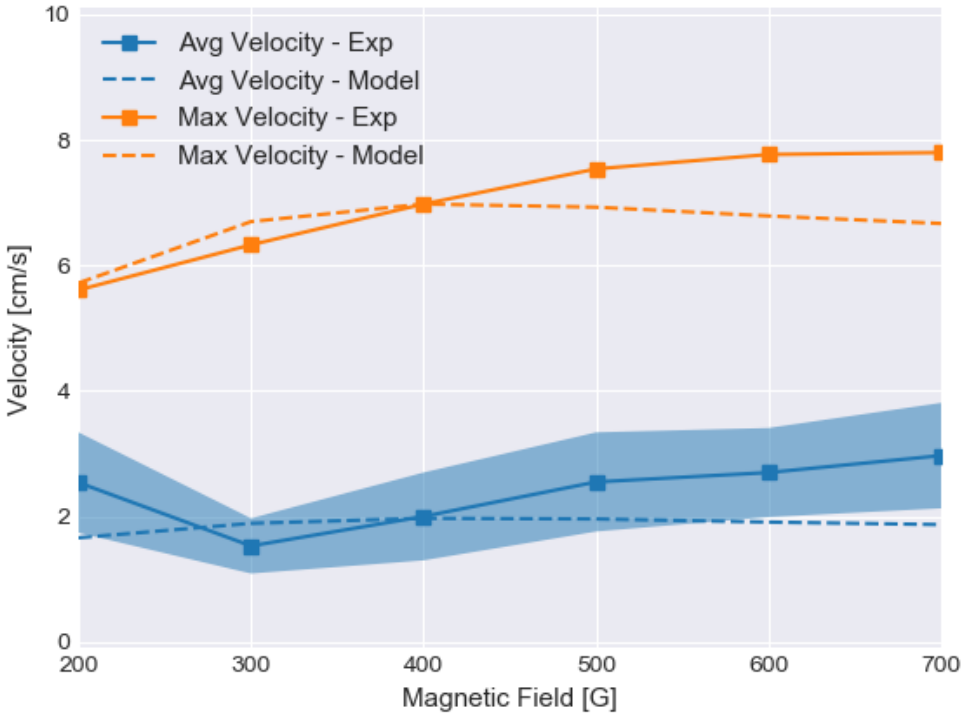

Figure 5.30 – Comparison of experimental velocity values to a SLiDE-relevant COMSOL magnetic field sweep.

In order to compare the experimental data to the models of flow, average velocities and maximum velocities are used. For the models, surface maximum and surface average derived values were used to calculate the maximum and average flow speeds for each magnetic field value, at the final time point of 10 seconds. The results are plotted in Figure 5.30.

Overall, there is impressive agreement across the range of magnetic fields, through there are some discrepancies. First, the error in the experimental curve only accounts for the standard deviation of particle averages. The fact that fewer particles moved through the domain in the low B-field cases is not included. This would likely explain the jump at 0.02 T. For 2 of the pulses only 1 particle moved through the domain, well entrained in a primary flow channel and exhibiting higher than expected velocity. There was no survey of low velocity areas to correctly account for the average velocity. The model velocities also seem to peak at a lower magnetic field than the experiments suggest. This discrepancy at higher B arises from a couple sources of error. First, while experimental cooling times and pulses were kept relatively uniform throughout testing, there

was no effort to make each part of each test exactly the same length of time. Based on natural variation, the cooling time before the beginning of the pulses varies between 8 and 11 seconds, changing the initial temperature gradients and not necessarily matching the simulation time. Second, the simulations were started from a uniform initial temperature of 300 ºC. While the 10 second simulation time smooths over a majority of this discrepancy and presents a good velocity match, the test example of a pulsed B-field shown in the temperature plots in Figure 5.25 gives some evidence that fine tuning the initial conditions could better match the data. The average velocity of that pulse simulation sits at 3.16 cm/s, higher than but within error of the experimental data. It is assumed that this holds across magnetic field values, shifting the higher B-field simulation data more in line with experiments.

CHAPTER 6 – FOAM TEMHD

A better way to ensure lithium dryout does not occur, while still providing TEMHD flow, may be through the use of large pore metallic foams. Like the passive capillary action seen in the capillary porous system (CPS) concept, the additional wicking of the lithium and its adherence to the structure can maintain the lithium level in the face of high heat fluxes that would cause dryout in an open surface trench-based system. Coupling this benefit with TEMHD pumping will allow for lithium recirculation and replenishment to avoid passivation and counter evaporation and ablation at the surface. These concepts were first proposed during the early days of TEMHD investigations at UIUC. Jaworski [61] envisioned a recirculating porous TEMHD system similar to the eventual LiMIT design, as seen in Figure 6.1. As he points out, if the pore size of the metallic foam can be controlled, the system can be engineered to find an optimal relation between TEMHD pumping, capillary action, and drag forces.

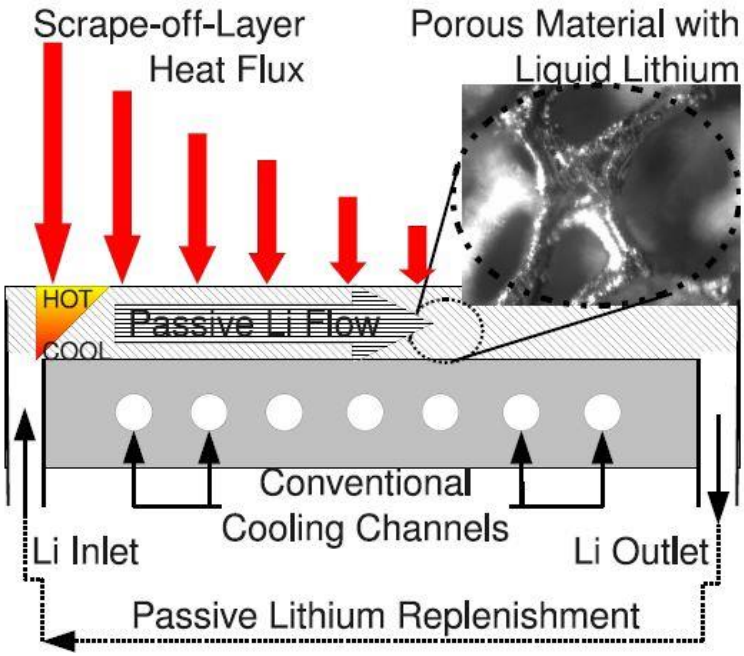

Figure 6.1 – Original concept describing the possibility of a recirculating liquid lithium in porous media [61].

6.1 Disordered Metallic Foams

CPS systems are typically comprised of disordered sub-mm pores with radii on the order of 10 to 200 μm in order to maintain efficient capillary action and maximize sorptivity, a measure of wicking speed [97]. The goal here is developing systems that can utilize the advantages of

faster open surface flow driven by TEMHD while maintaining stronger liquid surface resistance to transients, a hallmark of capillary systems. To accomplish this, large pore metallic foams are needed. Disordered foam samples were provided by Ultramet, a metals and ceramics company that also specializes in porous, open-cell foams. These foams are created by impregnating a polyurethane foam with resin and creating a carbon matrix through pyrolysis. This carbon foam is then reinforced with a metal or ceramic via CVD to create a structural composite. Ultramet provided base SiC composite foam samples with a range of 45 ppi to 3 ppi (approximately 0.5 mm to 8 mm diameters), shown in Figure 6.2.

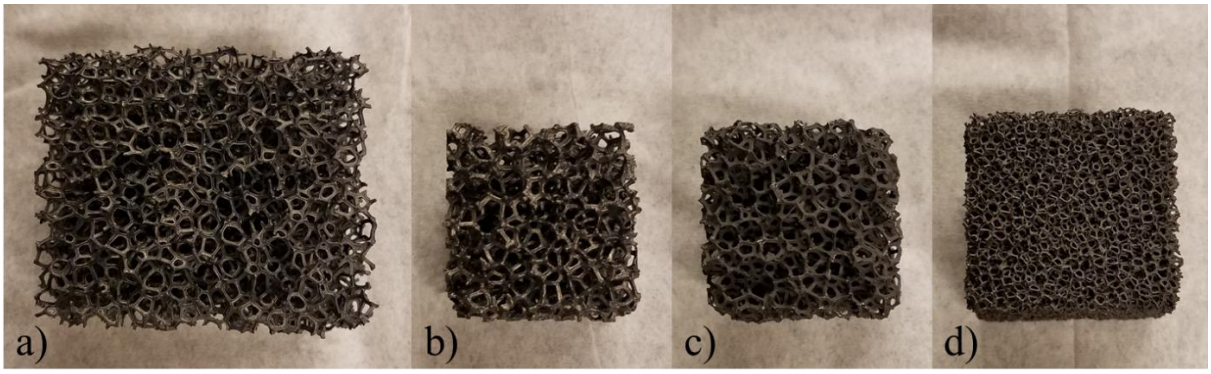

Figure 6.2 – A range of high-porosity SiC foams procured from Ultramet. Sample sizes are a) 3 ppi, b) 10 ppi, c) 20 ppi, and d) 45 ppi.

New fabrication techniques developed by Ultramet allow for the deposition of metallic layers on a base foam of SiC using PECVD. This should make resistance to liquid metal corrosion and the development of TEMHD drive possible. Tungsten coated Ultramet foam with forced helium coolant has been tested as a heat sink under e-beam bombardment as an analog for fusion conditions, resisting up to 27 MW/m^2. Heat transfer coefficients of liquid metal coolants can be orders of magnitude higher than forced gas, so these foams in conjunction with liquid lithium could drastically improve PFC design. Wanting to mimic the approximate size of standard LiMIT trenches, and aware of the potential for increased resistance to flow, 10 ppi and 3 ppi base foams were chosen for metallizing. The resultant tungsten coated foams, seen in Figure 6.3, were produced to dimensions of 120 mm by 60 mm by 10 mm for ease of preliminary testing in SLiDE. The 5% dense base foams have a nominal coating of approximately 200 μm of tungsten. As seen in Figure 6.3, this coating varies significantly toward the edges of the samples. The coating thickness around the thin edges of the sample increases by up to 300 μm, roughly doubling the

thickness of the solid structure. Surface roughness stays low, a benefit of the PECVD coatings, which is important for reliable wetting of the porous solid.

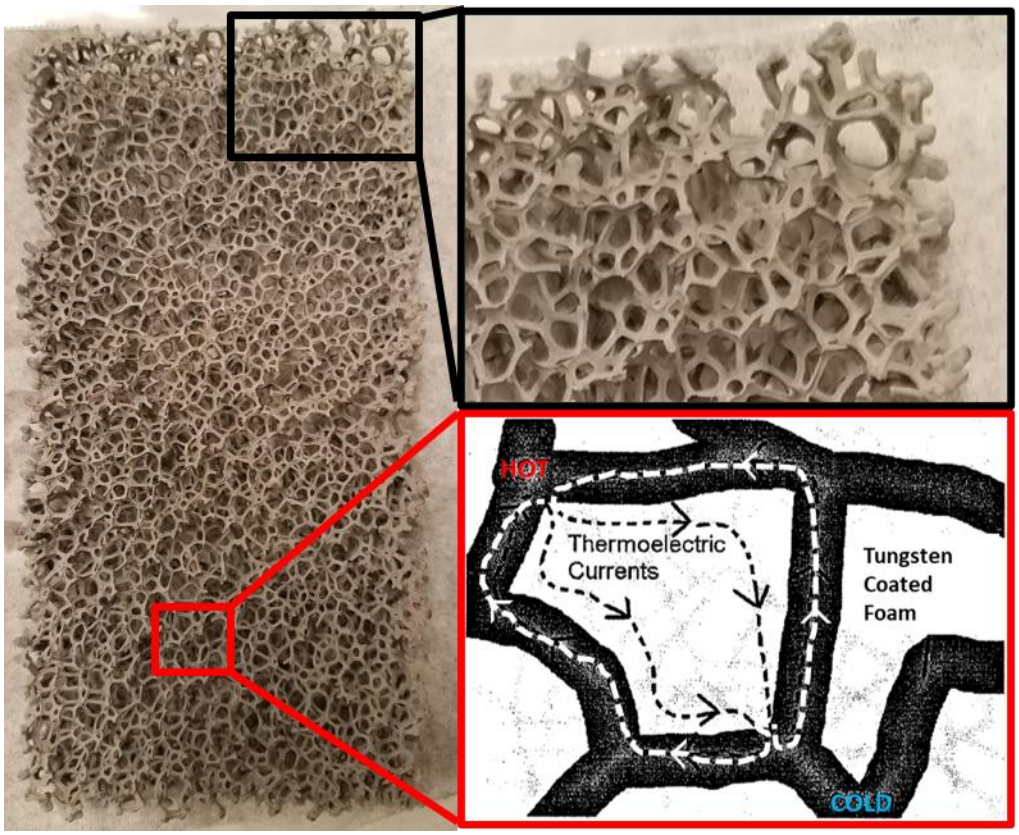

Figure 6.3 – Flow test size sample of disordered foam plate coated in tungsten. The lower inset provides a diagram of how average thermal gradients through the large pore foam should still drive thermoelectric currents for TEMHD flow, and the upper inset shows the increase in coating thickness near the edges.

6.1.1 Numerical Modeling of Porous Media

A standard approach to modelling flow in porous media is just including a constant multiplier to the equations of interest that represents the porosity of the material. Generally, this is acceptable for large domains of small pores where the macroscopic behavior is of principal interest. Alternatively, microfluidic models can be used to investigate true flow behavior over very small domains. The systems described here sit right in the middle, with a combination of large pores and highly transient conditions resulting in the desire to accurately model bulk flow in pores over a large domain

It is believed that the large-pore metallic foams will allow for ample TEMHD flow even though their base structures greatly diverge from any standard LiMIT style system that has been

tested. The standard setup for this coupled multiphysics modeling is described in Section 4.3. However, this relies on the creation of model domains using a relatively simple set of object primitives and generic CAD tools. It quickly becomes extremely difficult to build non-standard or "randomized" geometries as seen in the large-pore metallic foam samples. It is therefore beneficial to expand upon previous TEMHD modeling techniques to allow for modeling of TEMHD flow propensity in abnormal geometries. A pipeline has been developed from the basis of the work of the Tissue Biomechanics Lab at UIUC [98]. The model development pipeline can be described as follows:

1) Raw CT data acquired with support of UIUC Beckman Microscopy Suite
2) ImageJ used for thresholding stack of raw .tif images of foam
3) Stack is binarized for import into meshing program
4) Synopsys Simpleware ScanIP program allows masking of foam and fluid elements, elimination of spurious elements, and mesh creation for export
5) COMSOL simulations of foam propensity for TEMHD flow can progress

The UIUC Beckman Laboratory Imaging Technology Group contains a suite of high-resolution x-ray CT imaging systems. The SiC samples were imaged using the Xradia MicroCT scanner, providing an image stack of the foam approximately 4 cm in diameter, and 4 cm in depth. The resolution is 40.11 μm voxel size. CT data was taken for all foam sizes, in order to have references for later testing, and image processing began on 3 ppi foam.

For the purposes of this work, a new machine at Beckman provided more effective imaging capabilities of the full 120 mm by 60 mm by 10 mm foam samples. The Rigaku CT Lab GX130 is an ultra-high-speed imaging system that imaged the entire foam sample in approximately 8 seconds with 150 μm resolution.

The resultant .tif image stack was imported into ImageJ, a Java based image processing software [85]. A sample 3-D rendering of the full foam is shown in Figure 6.4. The stack of images has the background removed using Process→Image Calculator, has a threshold applied using Image→Adjust, and is binarized using Process→Binary in order to filter out background noise and eliminate spurious elements.

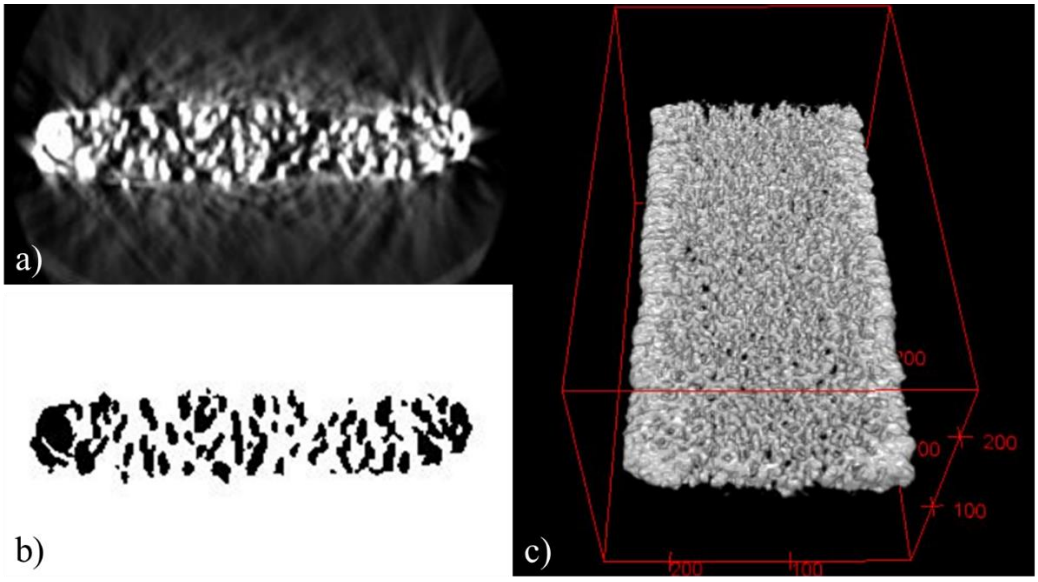

Figure 6.4 – a) Original .tif image in output stack from CT scan. b) Filtered and binarized .tif image. c) ImageJ 3D rendering of the full foam piece.

The Simpleware ScanIP software is a robust image analysis and meshing tool that is built to output mesh files for use in a variety of other programs [99]. Meshing models optimized for CAD, finite element analysis, CFD simulation, and other physics are included. While the tools for image filtering and adjustment allow changes to be made on a pixel-by-pixel basis, this level of detail was not required for the preliminary testing described here. After importing the adjusted .tif stack and fine-tuning additional filtering (Figure 6.5), the full foam was trimmed to 42 mm by 12.6 mm by 11.2 mm to more closely resemble the structured domain of the other 3-D multiphysics models.

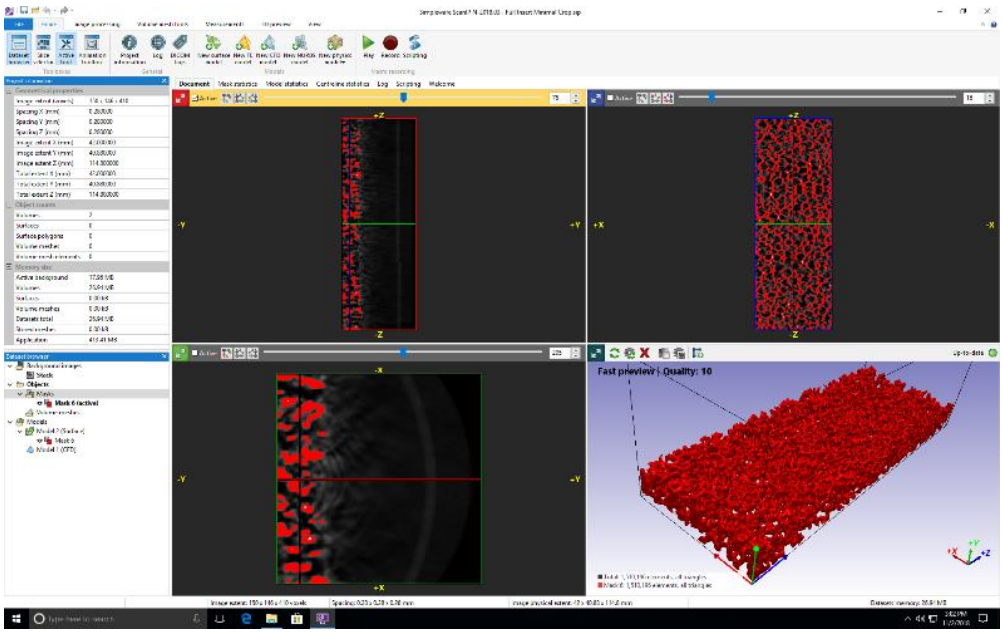

Figure 6.5 – Screenshot of Simpleware ScanIP mask of full foam.

After creating a mask for the solid foam region and inverting the mask to represent a lithium fluid domain, various CAD and CFD models were exported for use in multiphysics analysis (Figure 6.6). Decimation tests were performed on the mesh models to reduce the total number of elements. Element reduction up to 50% has been achieved without meshing errors, while reduction up to 90% may be possible. For this test, the mesh used contained 340,000 elements.

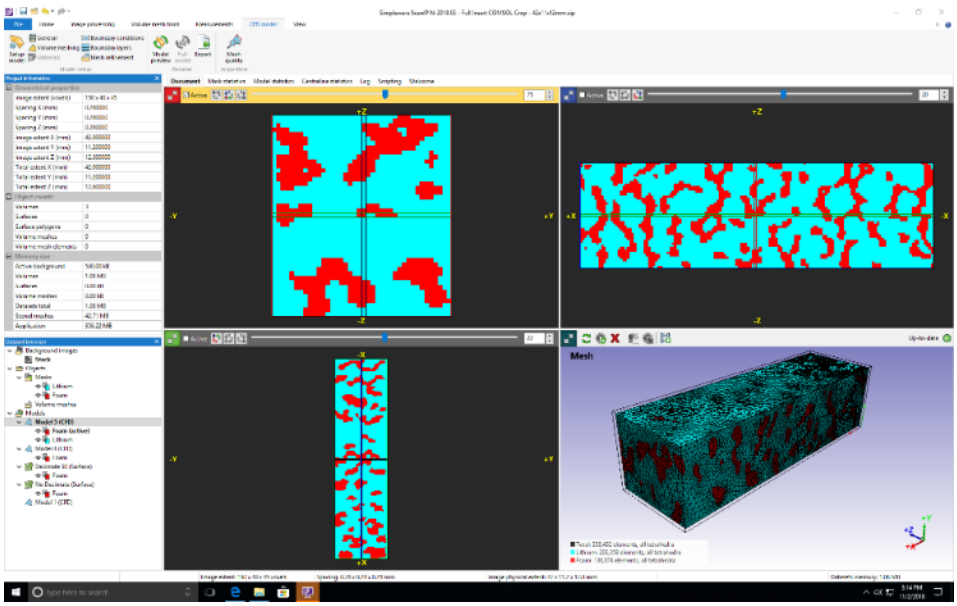

Figure 6.6 – Screenshot of Simpleware ScanIP mesh of trimmed foam sample, including the mesh of the inverted mask built to represent the lithium domain.

To test the propensity of TEMHD flow in disordered foams, the combined foam-fluid mesh is imported into COMSOL. Coupled heat transfer and electric currents modules solve for the TEMHD currents in the system, using the methods described in Section 4.3. Time-dependent simulations were run for both topside heat flux and no top heat flux cases. A sample of the current densities developed by TEMHD are given in Figure 6.7.

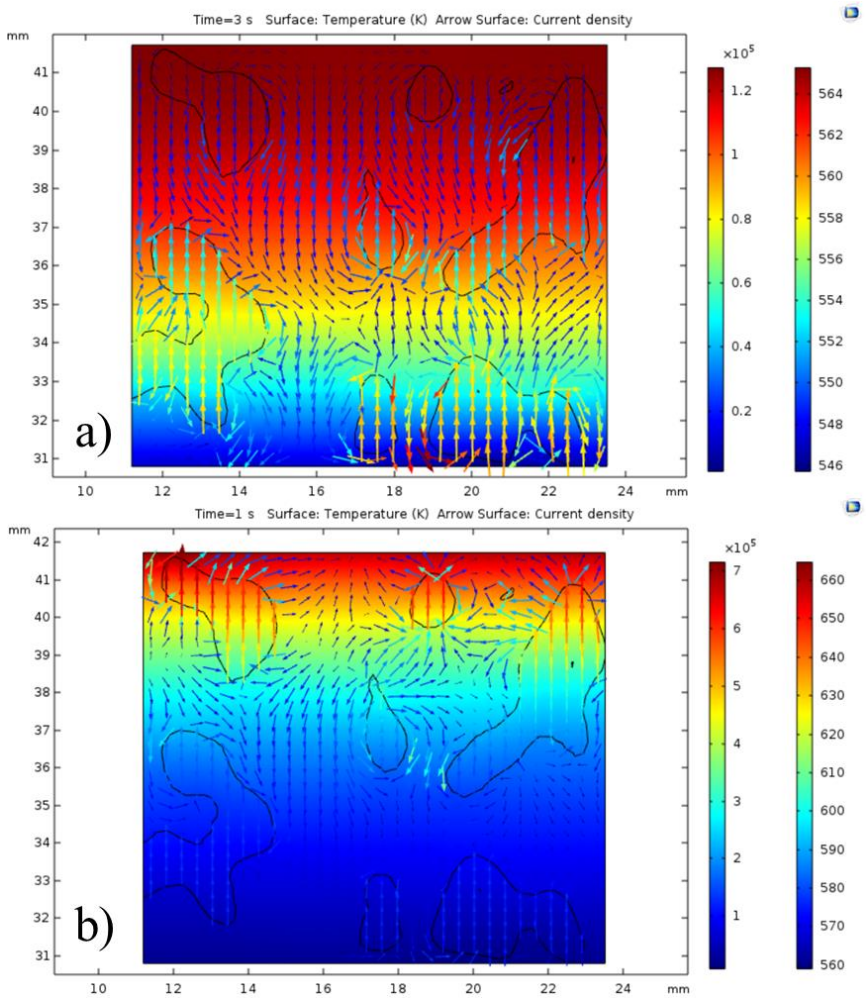

Figure 6.7 – Current density and temperature slices of the no top heat (a) and top heat (b) disordered foam simulations. The right-most color map represents the background temperature coloring in K, and the left color map corresponds to the current density in A/m^2 given by the arrow map.

The current densities in the high heat flux case are much more chaotic. The Gaussian heat flux causes thermal gradients to propagate outward upstream and downstream, as well as down through the foam (see Figure 6.8).

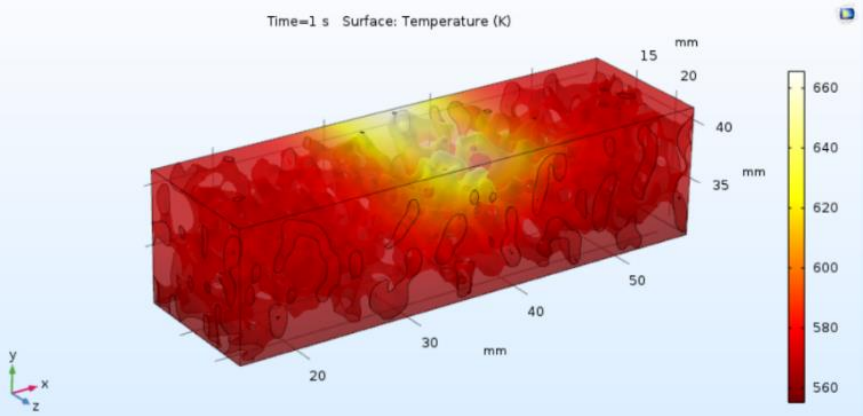

Figure 6.8 – Heat transfer in the disordered foam domain from a topside heat flux. Significant non-y-directed temperature gradients are present, leading to chaotic thermoelectric currents.

In a standard LiMIT system, the flow is more rigidly contained in the trenches, and the vertical temperature gradients dominate TEMHD flow. In the foam, however, the variety of the structure provides dissimilar metal junctions throughout the domain that capitalize on the non-vertical temperature gradients. In open pores, the average current is flowing downward, which will drive lithium downstream, but it is expected that disordered metallic foams will drastically enhance the turbulence of TEMHD flow.

In the case without a topside heat flux, the temperature gradient that develops is unidirectional, and the current profiles are ordered much more vertically. Outside of areas near bends in the foam structure, the vertical current will predominantly drive lithium downstream.

6.1.2 Experimental Testing

The high void fraction of large-pore metallic foam is expected to allow effective TEMHD flow while constraining the system against lithium dryout. To begin testing these concepts experimentally, the 3 ppi foam samples were used for initial wetting and flow tests in the MCATS and SLiDE chambers.

The Materials Characterization Test Stand (MCATS) is a multipurpose system built to facilitate materials testing tangential to the lithium flow work carried out at CPMI. The chamber has been used primarily for material compatibility and liquid metal wetting tests on a variety of fusion relevant surfaces [69], [83], [84]. Initial testing of the wetting and wicking properties of the 3 ppi foam was carried out in MCATS. A static fill of approximately 25 g of liquid lithium

was melted in a heated bucket to over 450 ºC. The 3 ppi foam was strapped onto two Watlow plate heaters with copper shim to enhance thermal conductivity to the foam. This setup is seen in Figure 6.9. The foam was lowered into the bucket until just encountering the liquid lithium and remained in that position for 1 hour. After removal, clean liquid lithium had wicked 5 mm up the foam.

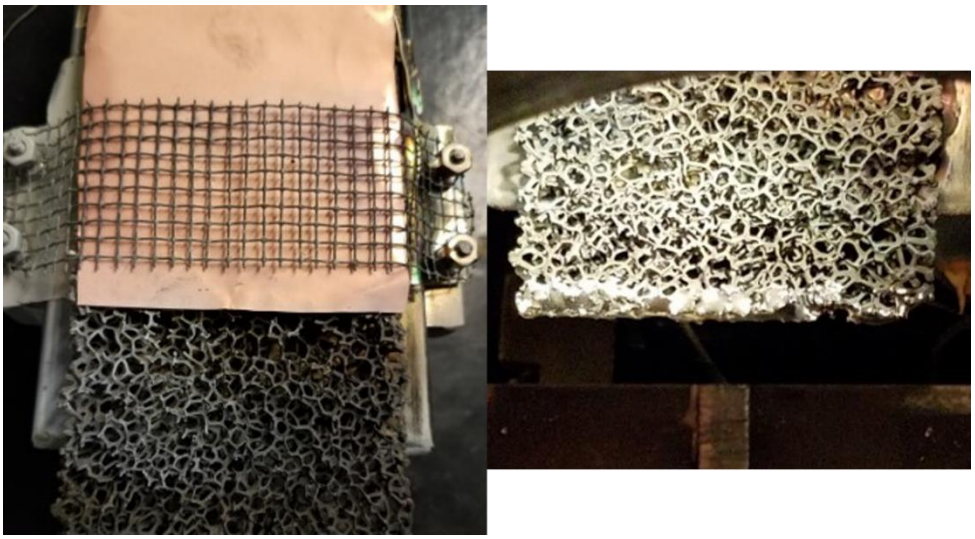

Figure 6.9 – Left: Disordered foam plate held in the dip test setup, with copper shim to improve heat transfer from the heaters on the bottom. Right: Lithium wicking through the disordered foam.

This dip test can be used to calculate the sorptivity of the foam, a measure of capillarity of a material. For a bar of porous material, the cumulative volume of liquid ingress is given by

$$V = AS\sqrt{t}$$

Where A is the wetted area, t is the time allowed for liquid absorption, and S is the sorptivity of the medium. Using the property called the cumulative liquid intake $i = V/A$, the measurable wetted length is related to sorptivity through

$$x = \frac{i}{f} = \frac{S}{f}\sqrt{t}$$

Here x is the wetted length, and f is the void fraction of the porous material. Taking a void fraction of 95% for the 3 ppi foam, the sorptivity is 0.08 mm/s$^{1/2}$. While this is quite low, it is expected that the large pore foam would not exhibit capillary strength on the order of micro-porous CPS structures. Additionally, the lack of reliable thermal contact between the heater plates and the foam base resulted in low foam temperatures. Until contact with the lithium, the

overhanging foam could not reach above 265 ºC, well below the wetting temperature for the tungsten coating. Once in contact, the foam nearest the lithium heated appreciably, but it can be assumed that temperatures between the lithium level and the heater plate fell below wetting temperatures, hindering lithium uptake and yielding a lower bound on sorptivity. If thermal conductivity to the foam could be improved, the capillary action would also enhance.

Initial flow testing was carried out in the SLiDE chamber. The foam sample was held onto the base module by gravity and simple stainless-steel shim clamps, as can be seen in Figure 6.10. In initial tests, fully even lithium loading and wetting was hindered by a lack of good thermal contact between the base module and the foam structure as well as impurities in the system.

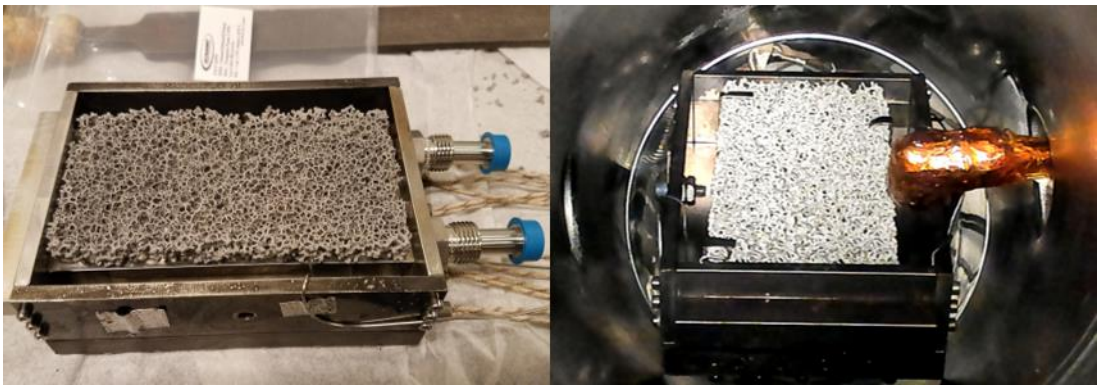

Figure 6.10 – Left: Disordered large-pore metallic foams in the test module. Right: Disordered foam plate installed in SLiDE. The Kapton tape (golden color) on the far right is the wrapped lithium injector.

Eventually, good wetting conditions were achieved through the foam, seen in Figure 6.11. Evidence of flow was observed through surface disturbance and minor impurity motion, in a no top heat flux case. Unfortunately, characterization and depiction of the flow via pictures is difficult, so more testing must be done with better filling and imaging systems. An additional difficulty was the lithium underfill in the best wetted case. This generally gives a better view of how TEMHD develops around the solid structures, but the disordered foams obstruct the view of any surface impurity motion signifying underlying fluid flow.

Figure 6.11 – Successful lithium wetting cases in disordered metallic foams. Evidence of impurity layers are seen in the left image, and the right image displays significant lithium underfill.

Ultimately the large-pore metallic foams did not live up to their hype. While the structure is generally mechanically stable, small pieces of the foam can fracture from the whole, exposing the SiC base. The SiC is not viable in a liquid lithium environment; any damage to the foam allows lithium intercalation, resulting in dissolution of the SiC and the metallic coating. Figure 6.12 shows a post-test lithium module with structurally compromised foam in the areas of strongest wetting, along with the disintegration of the foam that occurs during cleaning.

Figure 6.12 – Left: Post-test lithium module with a compromised structure. Right: Partially disintegrated metallic foam after cleaning of lithium.

A closer image of the damaged structure implies the disintegration of the SiC is the initial culprit causing loss of integrity of the foam. Figure 6.13, on the leading edge of damage, shows a hollowed-out tungsten coating, with no SiC base structure remaining. While the concept of the disordered foam structure may still hold promise as a PFC, updated designs must not include lithium incompatible materials, unless lithium ingress can be proven impossible.

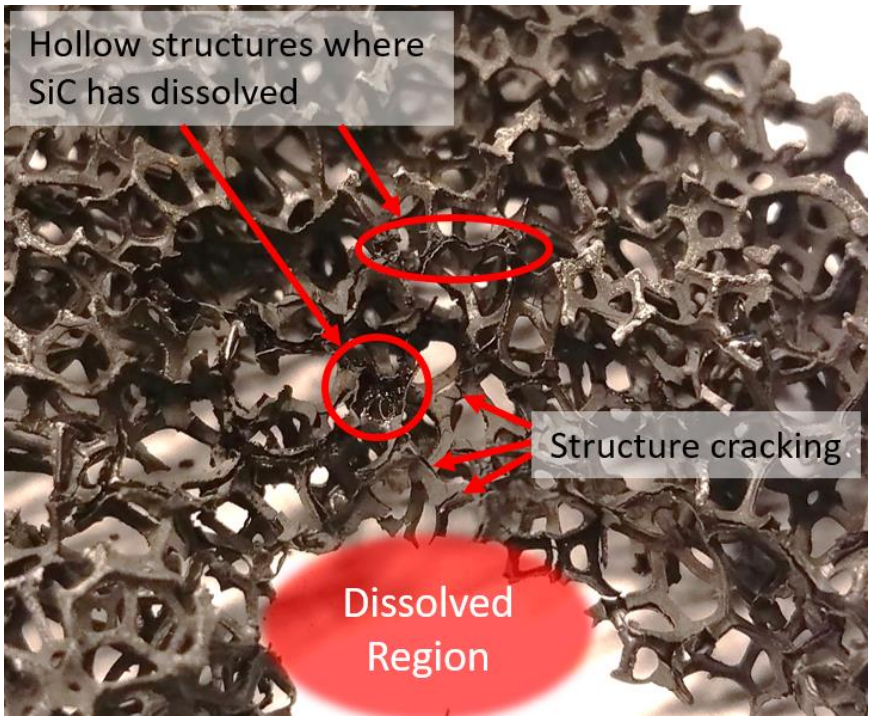

Figure 6.13 – Close-up image of damaged disordered foam sample, with regions bordering the disintegrated area exhibiting cracking and hollowness where the SiC was dissolved by the lithium.

6.2 Ordered Foams

Due to the reactivity of liquid lithium, it is likely that its lack of compatibility with other materials extends to essentially any base material upon which a metallic foam can be deposited. Additionally, the lack of heat transfer observed during the disordered foam testing reinforced the concept of using the base plate design for foam testing as well. For ease of manufacturing, it was decided the next geometry to pursue would be ordered foams. These would use an array of 'wire' sizes with similar widths and spacing to the LiMIT trenches and the posts, but extend into 3 dimensions, as seen in Figure 4.4.

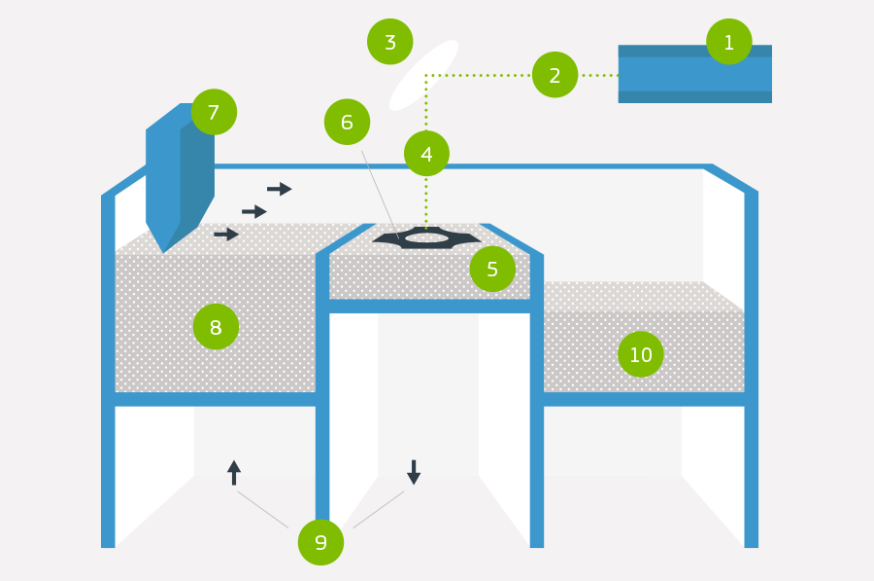

Figure 6.14 – Diagram of the DMLS process, including the laser supply (1), laser beam (2), focusing optics (3), focused beam (4), build chamber (5), part in progress (6), recoating blade (7), powder supply reservoir (8), pistons (9), and powder collection reservoir (10) [100].

Machining pure metallic ordered foams on millimeter scales is not trivial. Therefore, for experimental testing of ordered foam TEMHD, additive manufacturing was investigated as a possible avenue for structure development. Direct metal laser sintering (DMLS) uses laser heating to selectively fuse a metallic powder bed to build 3-dimensional structures layer-by-layer. Resolution of the layers is typically 20 to 30 µm, allowing structures as small as 100 µm to be reliably printed. A diagram of the DMLS process is shown in Figure 6.14. In order to save time and money in initial proof-of-concept testing, a tri-fold foam plate (Figure 6.15) was designed that incorporates three separate trench geometries, including:

A_f – 0.5×0.5 mm structure, 3 mm separation

B_f – 1×1 mm structure, 3 mm separation

C_f – 1×1 mm structure, 2 mm separation

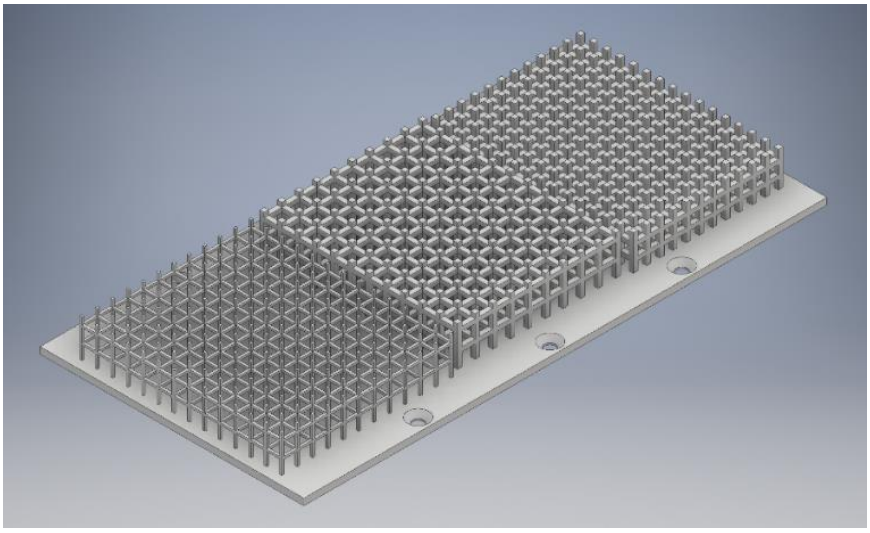

Figure 6.15 – Tri-fold ordered metallic foam geometry design, to be built on a base plate via additive manufacturing.

A variety of companies have also begun developing DMLS techniques for new materials. Various fusion relevant materials, including stainless steel, molybdenum, and even tungsten, can now be 3D printed economically. Protolabs, a rapid prototyping company with extensive machining and additive manufacturing options, was chosen to source this plate after considering price ($785), lead time (only 5 days!), and confidence in build quality and machinability. The high resolution 20 μm printer was not available due to the size of the plate, so 30 μm standard resolution was used. In order to avoid the need for supports within the foam features, which would not be removable, the part was built at a 45º angle from each axis, essentially 'corner up'. While this method introduces some additional risk of warping inherent to additive manufacturing processes, the structure cannot have additional supports. Tolerance of the standard resolution print is 0.05 mm in X and Y, and 0.1 mm in Z, plus 1 μm for each additional millimeter of build. For larger builds, warping due to thermal effects can increase these tolerances. The standard finish procedure for Protolabs's DMLS parts includes heat treatment to minimize warping, removal from platform, support removal, and surface treatment (grit, glass, and spin). The final product is shown in Figure 6.16.

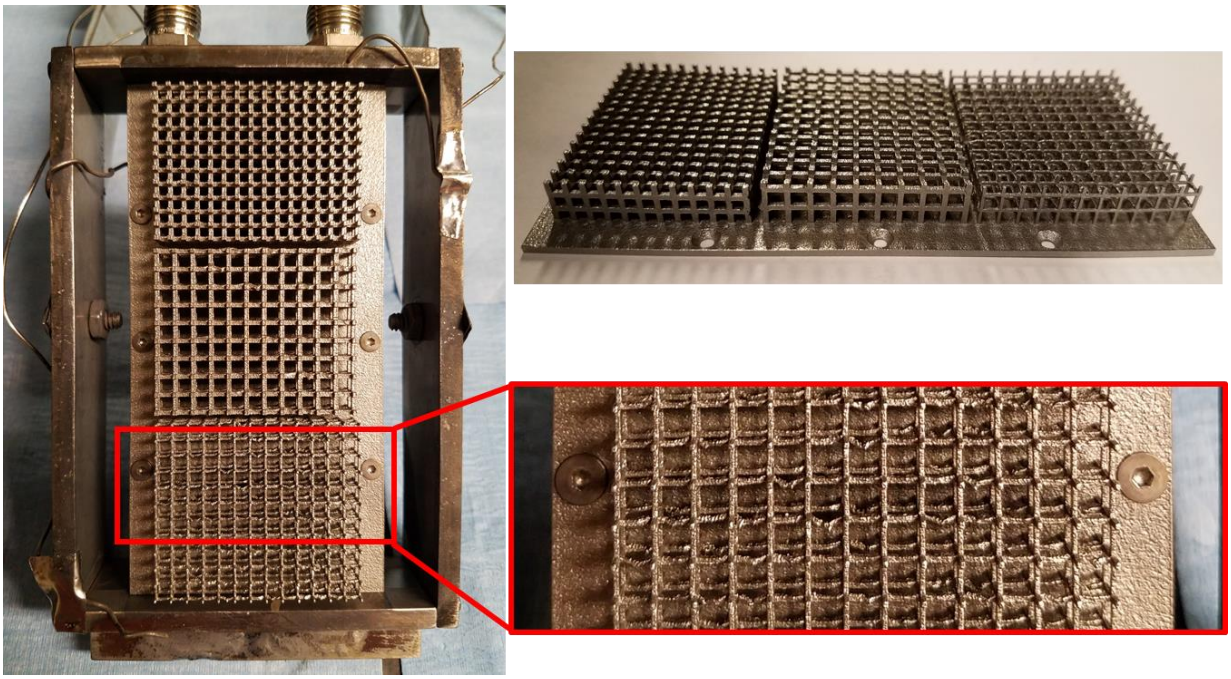

Figure 6.16 – Left: Tri-fold foam plate installed in the base module. Top Right: Side view of the tri-fold foam plate. Bottom Right: Close-up view of the case C_f foam displaying machining defects.

Overall, there is impressive build quality throughout the DMLS tri-fold plate. The nature of the foam structure precludes any additional surface finishing techniques, so native roughness is seen. The layered sintering process of DMLS creates a grainy surface with R_a value of 5 to 10 µm, obviously much higher than the wire EDM process that created the post plates. This can be a concern for effective lithium wetting. Noticeable but infrequent machining defects exist in the foam structure, concentrated predominantly in the 0.5 mm wire section. These do not affect the overall stability or average porosity of the foam sections but are an area for improvement in future designs.

6.2.1 Numerical Modeling

In order to test the TEMHD flow potential of the proposed ordered foam designs, numerical modeling was undertaken before the tri-fold plate was developed. The general COMSOL Multiphysics setup as described in Section 4.3 is used here to simulate and visualize TEMHD flow in ordered foams. As with the posts in Chapter 5, some domain adjustments had to be made to rein in spurious currents by ensuring the main flow channels in Y were bounded on either side in X by solid structure. Therefore, the thickness of the domains in X varies from 9 to 11 mm. In order to grasp the 3-D nature of the foam, 2 full layers of each structure type were included in Z,

with an additional set of posts at the top. Foregoing the topmost XY layer was done to maximize the amount of lithium flow along the top surface while still providing a solid anchor for surface stability. These adjustments result in topside domain thicknesses ranging from 8 to 11 mm.

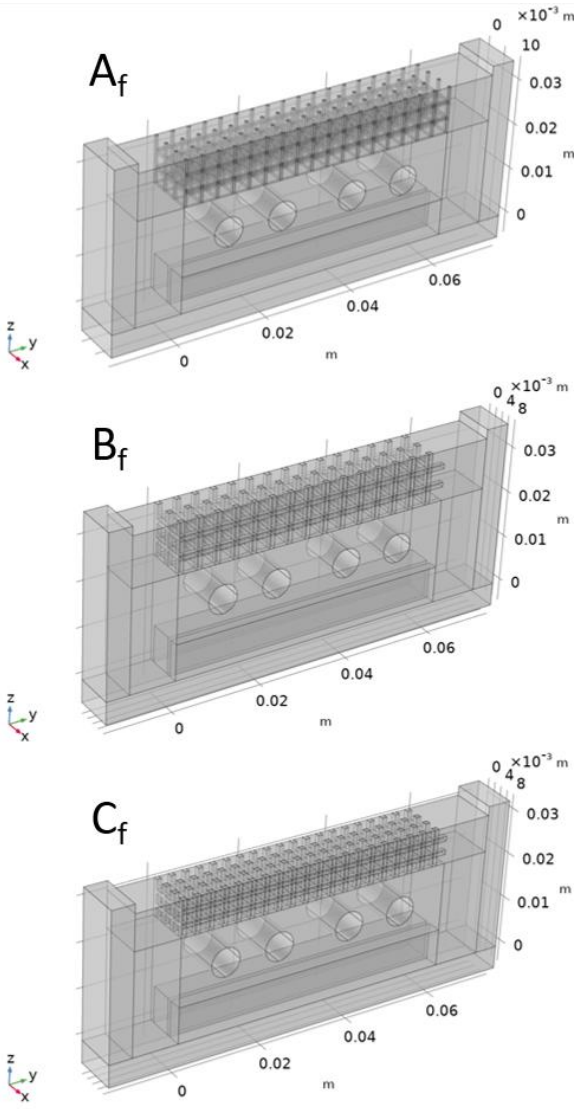

Figure 6.17 – COMSOL modeling domains for the 3 foam geometries.

Once again, snapshots of the time dependent simulations are presented in the next sections, to provide a representative sample of the profiles developing effective TEMHD flow in these domains. The test conditions are chosen to correspond to an e-beam test in SLiDE and match those presented in Chapter 5, so direct comparisons can be made. The topside heat flux is a centered Gaussian with 1 MW/m^2 peak, the B-field is a constant 0.05 T, cooling is a convective heat flux with 500 W/m^{2}K heat transfer coefficient, and the heaters provide an additional

17 kW/m^2 along the bottom surface. Where possible, scaling of the plotted values of interest are kept identical to simulations in Chapter 5, to aid in assessing the differences between geometries.

6.2.1.1 Temperature Profile

The deposition of heat from the topside heat stripe and its removal via both conduction and convection in the lithium can be seen in Figure 6.18. The thermal conductivity of the lithium allows rapid dissipation of heat down to the stainless-steel baseplate, and TEMHD convection rapidly begins to remove heat downstream. The hot lithium circulates into the underside channels, where it is cooled. In the side view shown here, the region of peak temperature seems more locally peaked than in the post geometries, though there is likely higher average resistance to flow in the foams than in the uninterrupted primary flow channels of the posts. The cooling lines work to remove heat from the system, and as the effect of the cooling reaches the bottom flow channels, TEMHD acceleration should aid in maintaining effective flow recirculation.

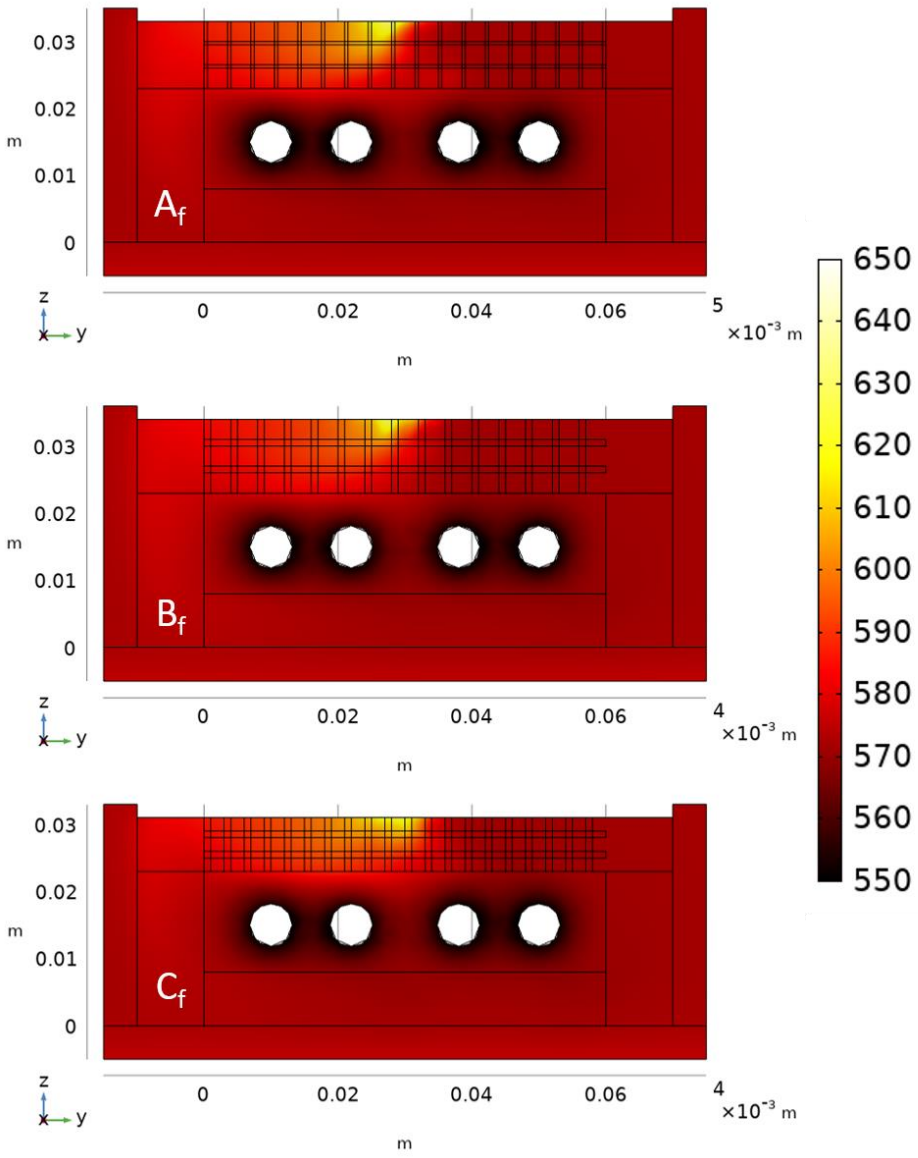

Figure 6.18 – Side view slice of the temperature profile in all foam geometries. Color bar gives temperature in K. The effect of the centered topside heat flux and subsequent flow of hot accelerated lithium is visible.

For any setup of open surface liquid lithium PFCs, the top surface temperature is important to track. Lithium is very effective at dissipating heat as the CDX-U results especially imply [30], [31]. However, the operating regime of lithium is limited due to its high vapor pressure. Lithium is low Z so ingress into the plasma is not nearly as damaging as other high Z materials but minimizing the evaporative lithium load is generally desirable. Above the 450 to 500 ºC (723 to 773 K) zone where lithium evaporation becomes significant, the vapor shielding effect comes into play. The cloud of lithium vapor is extremely effective at radiating power (recall the vapor box divertor concept), which should place a limit on open surface temperature increase. The effect of

vapor shielding is not taken into account in these simulations (see Section 8.6), though it is expected to become relevant at fusion device heat fluxes. Above all, the temperature of the solid structure under direct impingement must be kept below melting temperatures, lest high Z material be liable to enter the core. These simulations present a conservative case for heat transfer, as the solid substrate is stainless steel, notorious for its low thermal conductivity. In the 1 MW/m^2 case shown here, all foam geometries limit temperature rise to below 650 ºC. Since the foam design relies on the 3-D bulk to drive average flow due to average thermal gradients, there is less material directly under the heat stripe in the first millimeters of lithium. The posts reduce material in comparison to a typical trench system, and the foams reduce top surface material further still while still providing minimal topside structures, so the surface tension of lithium maintains surface stability.

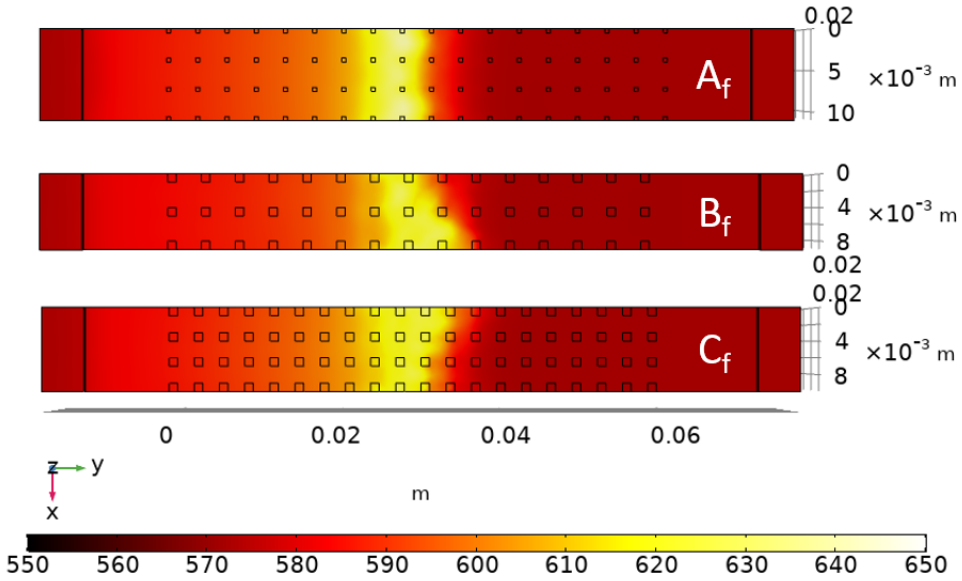

Figure 6.19 – Topside temperature profile of the 3 foam designs. The color bar gives temperature in K.

The maximum surface temperature for each geometry over time is given in Figure 6.20. As recirculation develops, the temperatures drop as cooled lithium from the recirculation channels is brought to the topside. This is most apparent in case A_f, which has the highest overall temperature peak but lowest 5 second maximum temperature. Overall, minimizing the amount of material along the open surface can reduce maximum surface temperatures in relation to the posts, though the difference is only approximately 10 K.

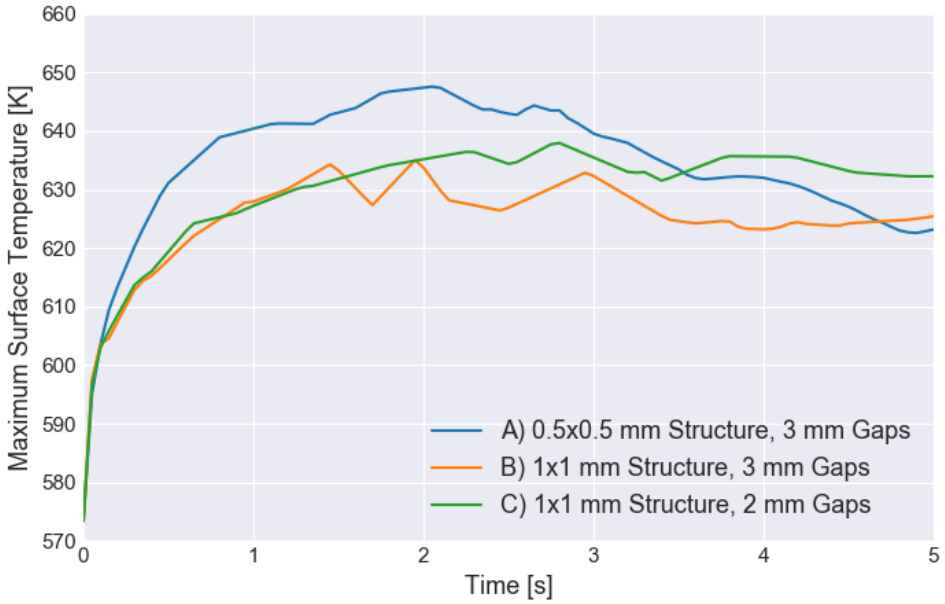

Figure 6.20 – Maximum surface temperature over time in the foam geometries for a 1 MW/m^2 peak heat flux with 0.05 T magnetic field.

6.2.1.2 Current Profile

The temperature gradients from the flow of heat through the system lead to the development of thermoelectric currents, as the liquid and solid materials have different Seebeck coefficients, and therefore have a relative thermopower. The 3-D nature of the foam and the small dimensions of the solid structure in relation to the liquid domain provide an interesting change to the typical development of TEMHD currents like those expected in a trench system. In a standard LiMIT trench, the parallel plate arrangement creates a smooth current circulation that travels up through the solid trenches and down through the lithium. In the post geometries, this same current structure dominates TEMHD drive in between the posts, though there is some disruption due to the secondary flow channels and eddy creation. In the case of the foams, a much more variable current flow develops, as seen in Figure 6.21. In between the vertical segments of the ordered structure, the main flow channels do not display an organized directional current. The presence of the horizontal segments in X further disrupts the standard expected current flow. In these structures, while there is still concentrated current density along the solid and in some parts of the lithium, there is drastically reduced current peaking in contrast to the posts. The direct results of this will be seen in the discussion on volume forces in the next section. The magnitude of the current density in the fluid volume is similar to the posts in case C_f, though it quickly becomes much lower than the post geometries in the channel centers of cases A_f and B_f.

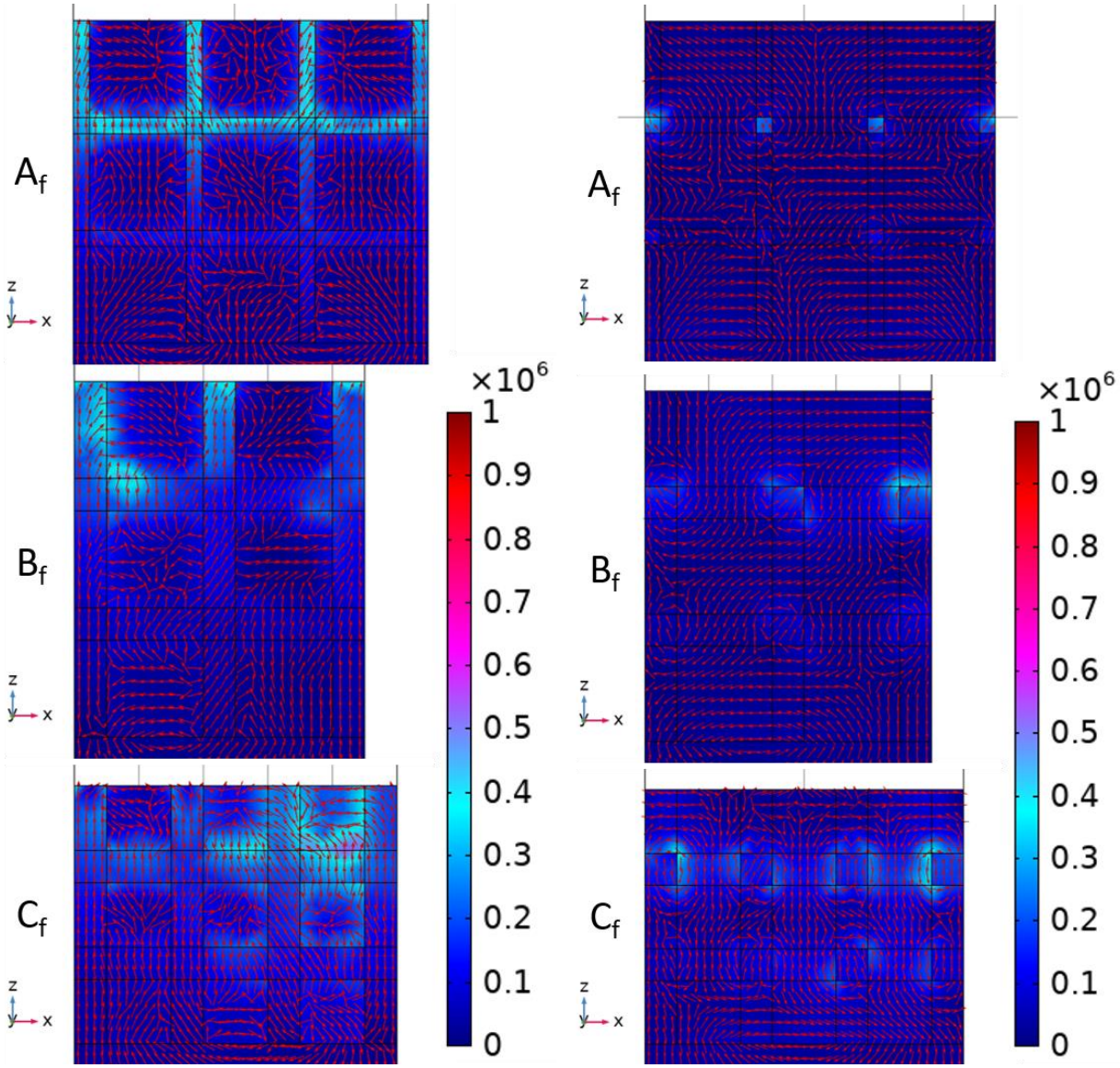

Figure 6.21 – Left: Current density plot in an XZ slice through a set of Z-directed structures near the peak of the topside heat flux, showing larger variability in these flow channels. Right: Current density plot in an XZ slice in the gap between sets of Z-directed structures near the peak of the topside heat flux, showing more uniform current density development. The color bar shows current density in A/m^2. The arrows follow XZ current direction.

Unlike the post cases, the ordered foams have continual structure along Y, and it is here in the 'gaps' between the vertical elements that a more uniform current profile develops, as seen in Figure 6.21. The Y-directed foam elements somewhat surprisingly develop a strong current circulation that is predominantly in the -Z direction. Compared to the gap currents of the posts and even a significant portion of the volume between the posts, this current density is significant. This TEMHD driving force provides the basis for the directional motion throughout the topside foam domain. Furthermore, the strongest regions of this current are in line with the X-directed

structures that create the 3-D layers along with the continued structures in Y. This means the acceleration in this region will be split by these structures and contribute to effective flow mixing in vertical directions.

The YZ current profiles in Figure 6.22 depict similar current circulation around the X-directed structures. While there is still evidence of current flow in Y under the heat strip (and low densities of current in Y upstream and downstream) the X-directed structures generate a relatively powerful current in Z. This provides extra TEMHD drive current which protects against dryout, as opposed to the strong Y-directed currents, harbingers of dryout, under the heat stripe in the post models. There is also a longer region within which there is high variability and circulation in the current, which signals mixing and lack of unidirectional drive in Z to cause dryout, unlike the thin regions in the posts with Z-directed and extensive regions with dominant currents in Y on either side.

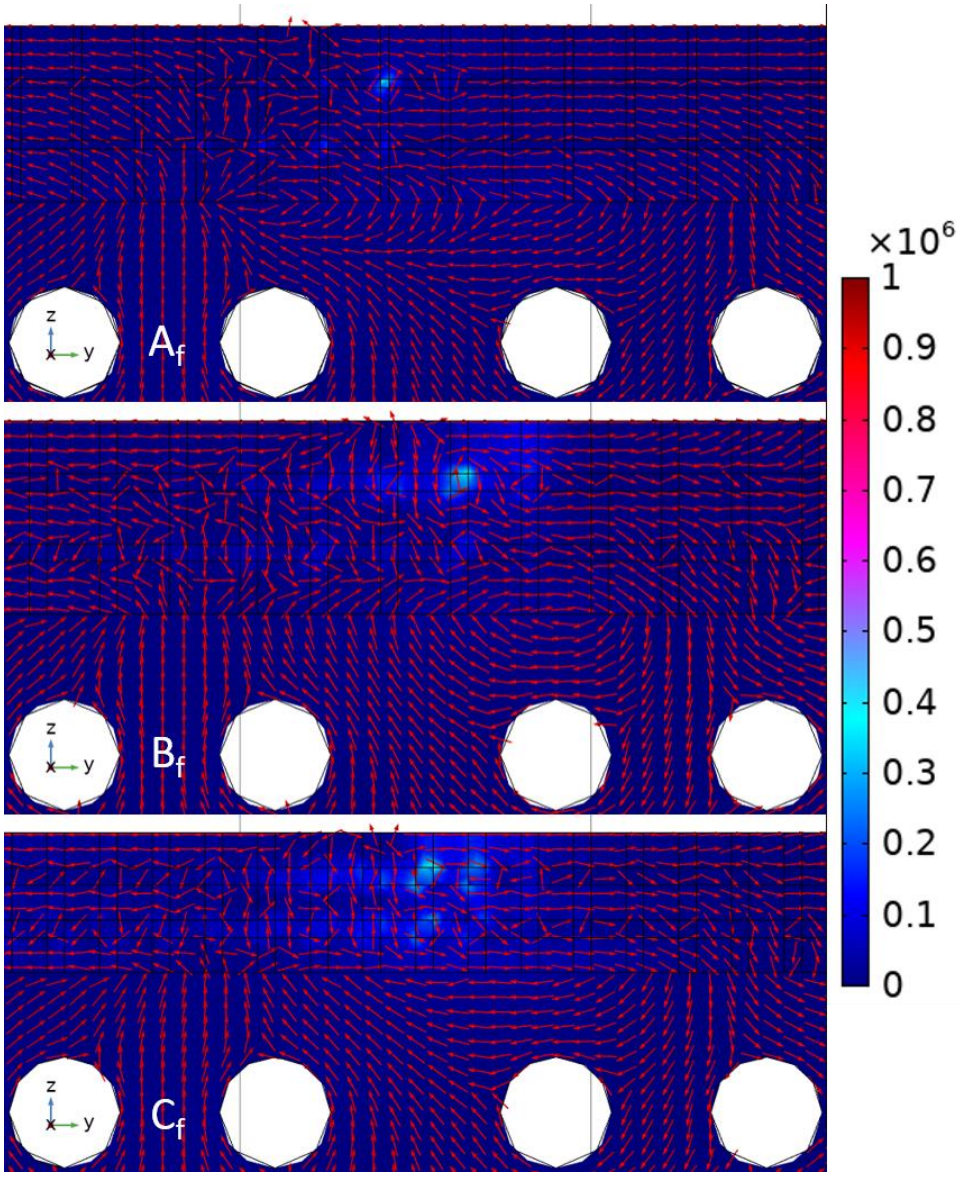

Figure 6.22 – Current density plot in a YZ slice in the center of a primary flow channel, showing the presence of the additional structures of the foam disrupting the strongest Y-directed currents that would lead to dryout. The color bar shows current density in A/m^2. The arrows follow YZ current direction.

6.2.1.3 Flow Profile

The thermoelectric currents that develop in the foams develop a Lorentz volume force in the presence of the +X magnetic field to drive TEMHD flow in the fluid domain. Figure 6.23 displays the volume force profile in the Y direction for each geometry. As indicated by the current profiles in the previous section but unique with respect to trench and post geometries, the main driving force is concentrated along the Y structures of the ordered foam. The forces are most extensive in case C_f due to the larger structure to flow area, while in the case A_f foam the volume

force is quite difficult to distinguish. For cases B_f and C_f, the magnitude of the volume force peaks resembles that of the post cases, on the order of 5×10^4 N/m^3, though the posts have more apparent peaking along corners that can reach 7×10^4 N/m^3 in small areas.

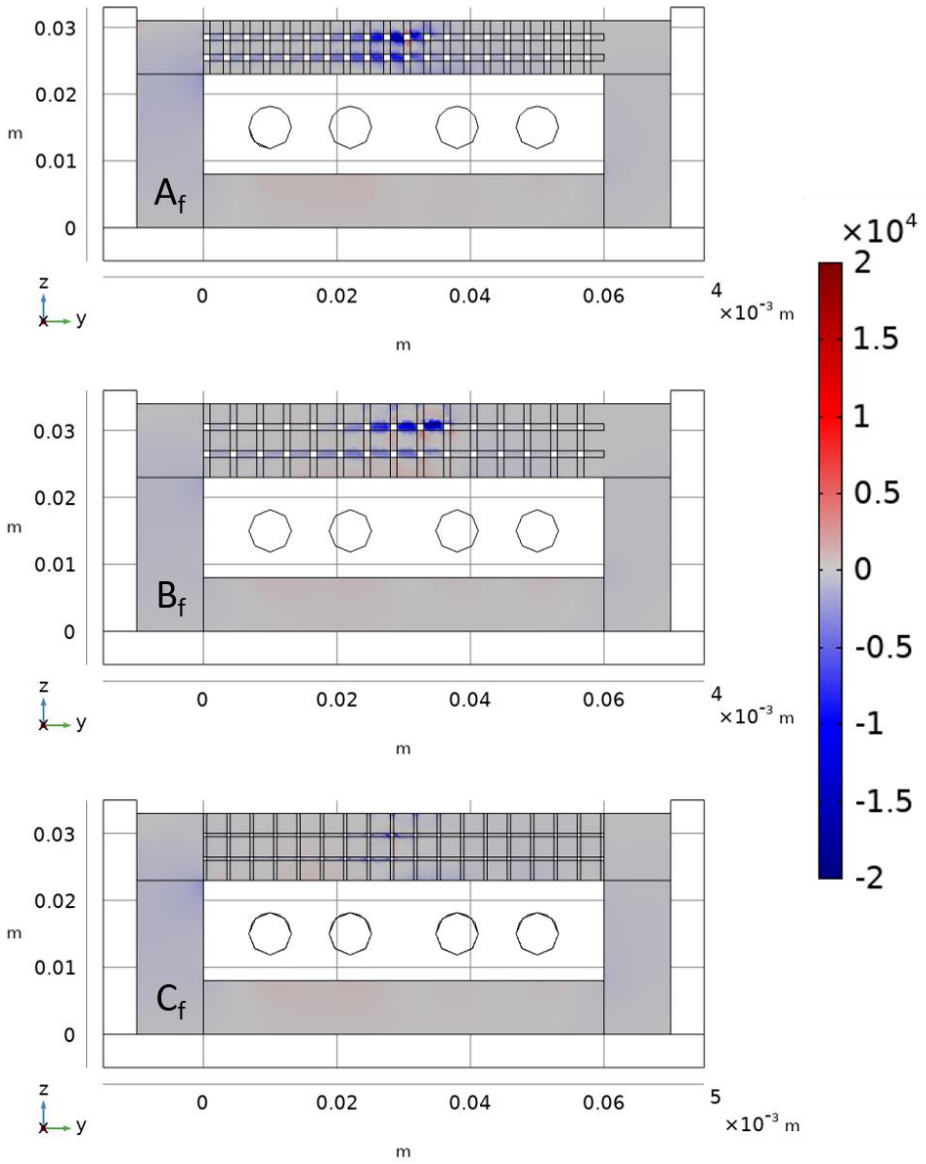

Figure 6.23 – Plot of the Y component of the volume force providing the primary TEMHD drive. The color bar gives volume force in N/m^3.

The volume forces shown above result in sustained, recirculating TEMHD flow throughout the domain, shown in Figure 6.24. At this point in time, case B_f records the highest velocity of 14 cm/s, while cases A_f and C_f exhibit 9 cm/s topside flow, though this is potentially misleading with regards to the flow profile over time. Refer to Figure 6.29 and Figure 6.30 for an examination

of maximum and average flow speeds over time. The influence of the cooling channels is evident by the 3 second mark in the simulation, especially in the recirculation channel flow. The apparent reduction in recirculation velocity in case B_f is due to differences in domain sizing leading to the slice sitting close to the channel edge where velocity goes to 0. Overall, the foams display lower sustained velocities than the posts, due to smaller structures, larger channels, and more flow disruption due to the 3-D structure. However, the foam geometries have a much smaller hallmark of dryout, which is generally seen as a sustained high velocity lithium profile that drops below the surface of the domain. Here, there is some indication of a dropping high velocity flow directly under the heat stripe, but the 3-D structure of the foam helps to immediately break up the rapidly accelerating flow, slow it down, and disperse it amongst the layered channels in Z. This is more evident in cases B_f and C_f, as the 0.5 mm structures of case A_f contribute less stabilizing current against dryout.

The Z-directed volume force responsible for dryout and pileup are plotted in Figure 6.25 at the same slice location as in Figure 6.23. While the foam cases do not contain strong dryout indicators in the velocity profile, the profiles do not suggest uninterrupted flow, so an examination of the Z-directed forces is warranted. As the heat stripe impinges on the top surface the temperature gradients in Y develop thermoelectric currents along the same direction. These currents result in volume forces that act downward on the lithium on the upstream side of the heat stripe, causing dryout, and upward on the downstream side of the heat stripe, resulting in pileup. In the foam geometries, the dryout forcing is most pronounced along the vertical components of the ordered structure, at odds with the unique driving forces for the predominant Y-directed flow, and more like the standard peak locations seen in the posts. The +Z and -Z forces are clustered closer to the central heat stripe in cases B_f and C_f, signifying any dryout forming is quickly countered by pileup forces. The presence of the horizontal structures helps to diminish the magnitude of the forces in the second and third channels from the top, in contrast to the force extent in the post designs. The horizontal structures contribute instead to the Y-directed driving force. Case A_f shows very disperse forces in Z like the Y-directed forces in Figure 6.23.

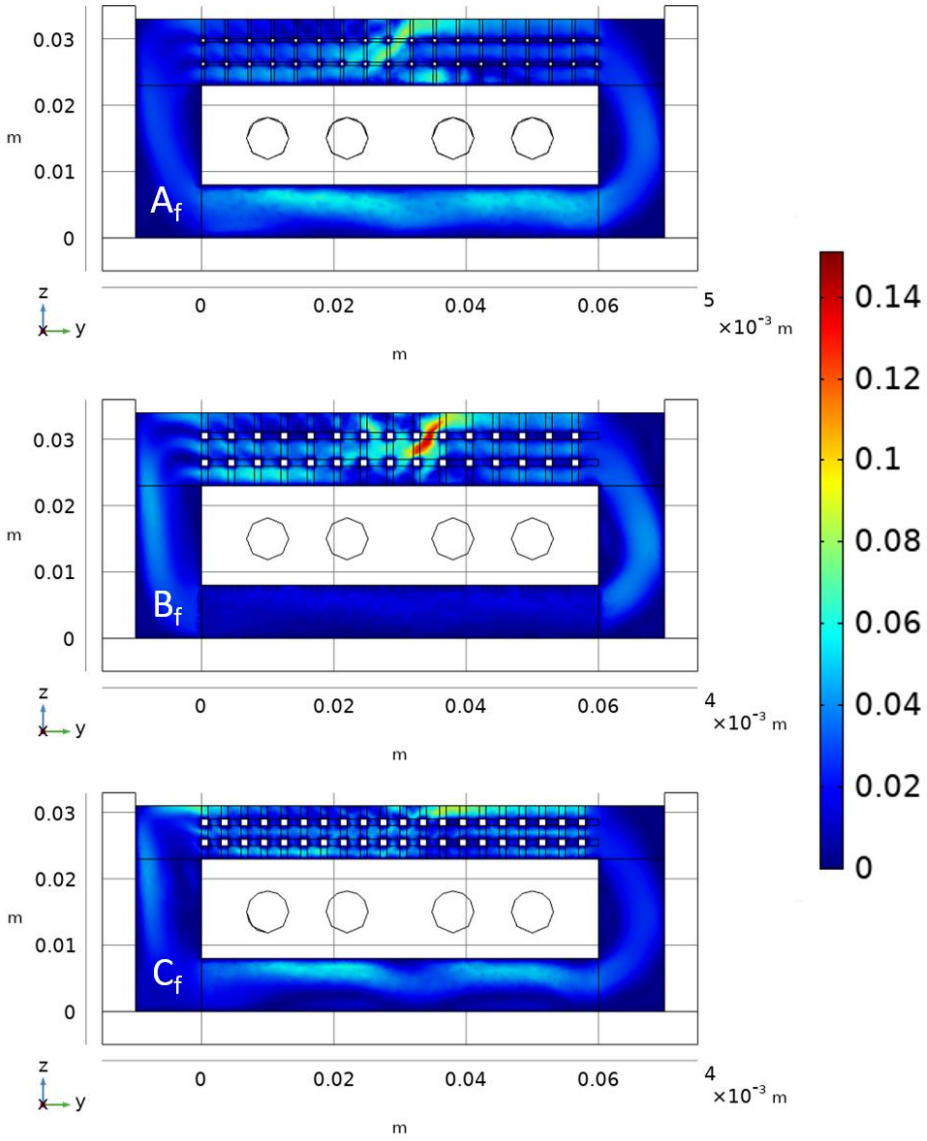

Figure 6.24 – Velocity profile at 3 seconds of simulation time, showing strong lithium circulation. The color bar gives velocity magnitude in m/s.

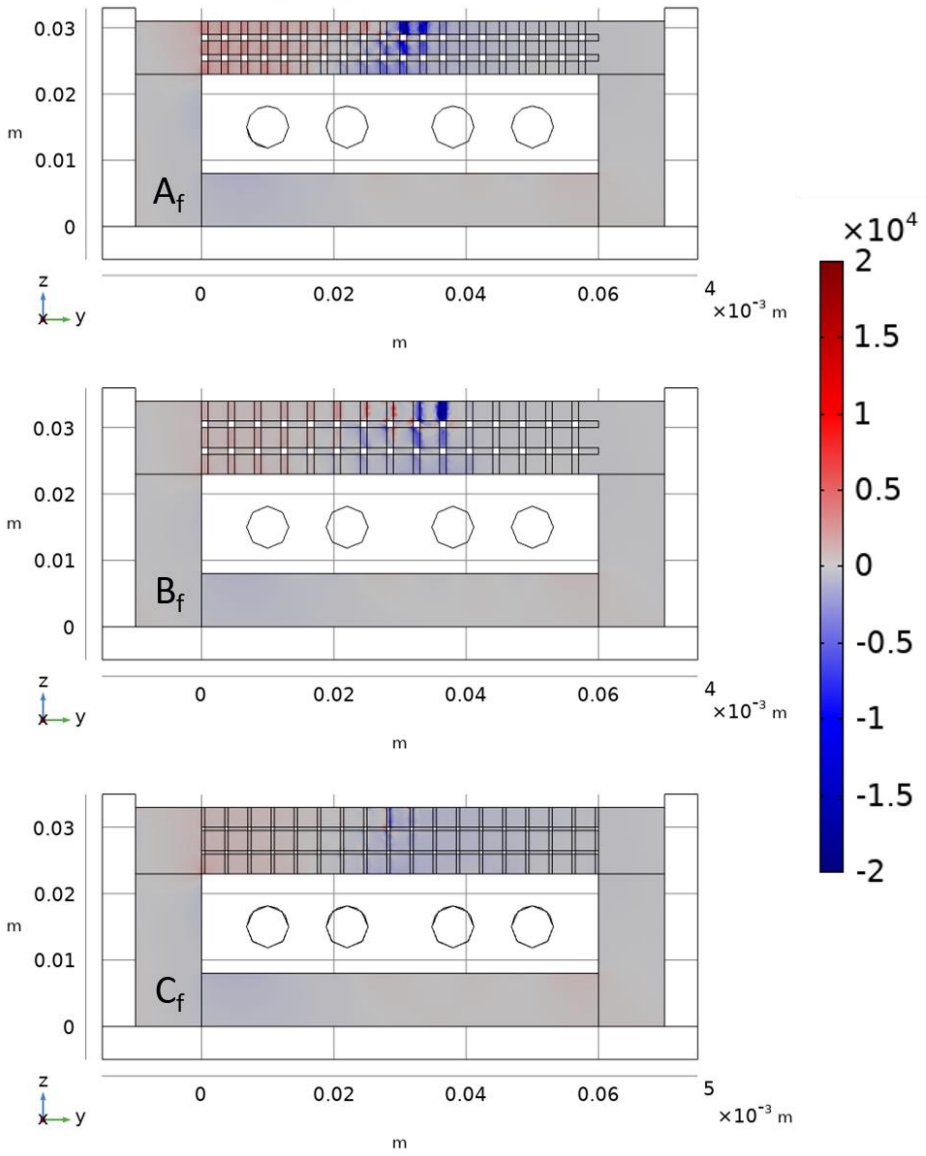

Figure 6.25 – Plot of the Z component of the volume force providing the impetus for dryout and pileup. The color bar gives volume force in N/m^3.

The time dependent characteristics of the average and minimum Y and Z volume forces are given in Figure 6.26, in order to examine the relative significance of the optimal driving forces versus the detrimental dryout forces. In all cases, the average Y volume force present at all times signifies sustained recirculation of flow through the domain. The magnitude of this drive increases from case A_f to case C_f, as expected. The 0.5 mm structures cannot drive flow as readily through the large 3 mm channels as the 1 mm structures of case B_f, and the smaller 2 mm channels of case C_f presents the most effective TEMHD drive. In all cases, the Y-directed force grows faster than the dryout force on average, though it should be noted that the average force in Z includes the

pileup forces, so this indicates dryout forcing is stronger than pileup and increases in time. This begins to dominate the driving force around 2.5 seconds in case A_f, around 4.5 seconds in case B_f, and does not overtake average driving force during the 5 second simulation time of case C_f. The average driving force magnitudes of cases A_f and B_f are on par with those of post designs Ap and C_p, while the larger structure to flow ratio of foam case C_f and post case B_p share similar TEMHD drive. The important comparison to make is in the behavior of the minimum forces, which describe the peak magnitudes of TEMHD drive (-Y) and dryout (-Z). The peak Y forces are all similar in the foam designs and lower than the post case A_p and B_p, signifying the dispersion of forces instead of peaks near the edges of the domain. Furthermore, the peak Z forces are drastically lower than those seen in the post designs, and always of very similar magnitude to the Y-directed forces. This indicates a substantially reduced potential for dryout in the foam designs, as the peak dryout forces contribute most to initial disturbance of the surface. Instead of a dominant force downward under the heat stripe, the peak forces push lithium down and out of under the heat stripe with similar magnitudes, and the 3-D nature of the foam can aid in breaking up this downward motion.

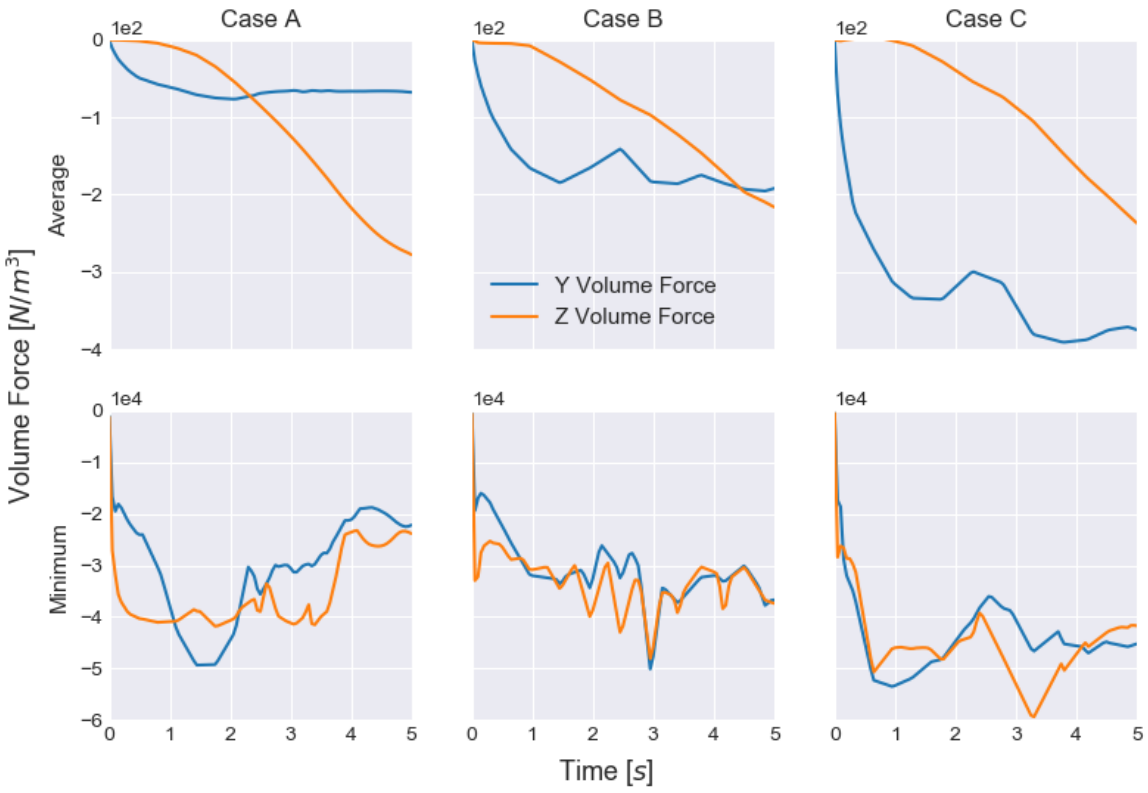

Figure 6.26 – Geometry comparison of minimum and average volume force components over time.

Ideally, the open surface of the PFC will sustain driven flow over the extent of the domain, including throughout the high heat flux region. In the foam geometries, there are strong surface flows on the order of 6 to 8 cm/s visible on the top surface downstream of the centerline, though the disruption of the heat stripe does cause slowing of surface flow. This is shown in Figure 6.27.

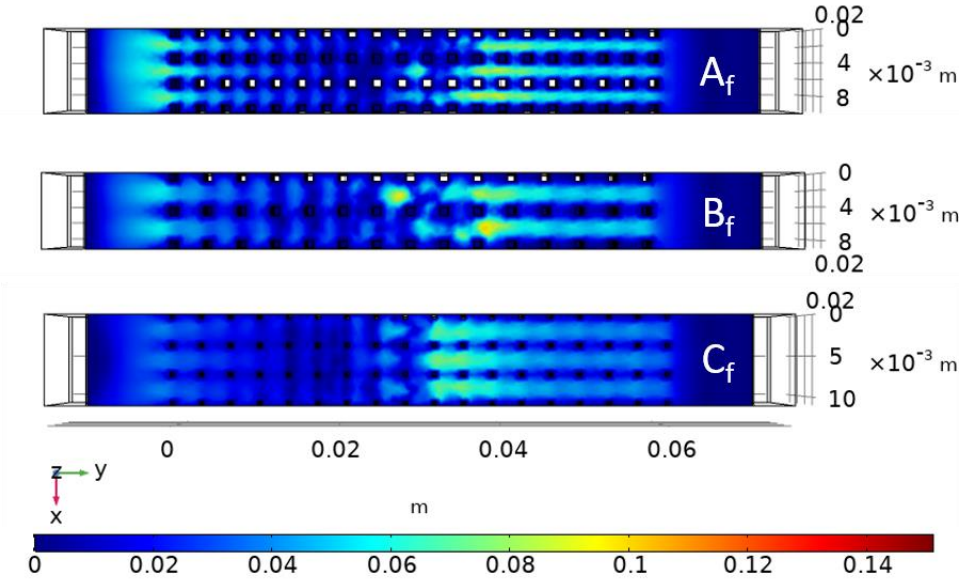

Figure 6.27 – Topside surface velocity magnitude. The color bar gives velocity in m/s.

The crosstalk between flow channels is shown in Figure 6.28 by plotting the top surface X velocity. As in the post designs, the ordered foams drive TEMHD flow while eliminating isolation between flow channels seen in the standard LiMIT trenches. The 3-D structure harnesses the thermal gradients to drive a predominantly Y-directed flow but allows for distribution between the primary flow channels. The placement of the structures and the development of thermoelectric currents around them aids in dispersing flow profiles throughout the domain, which lowers velocity magnitude but increases resilience to dryout.

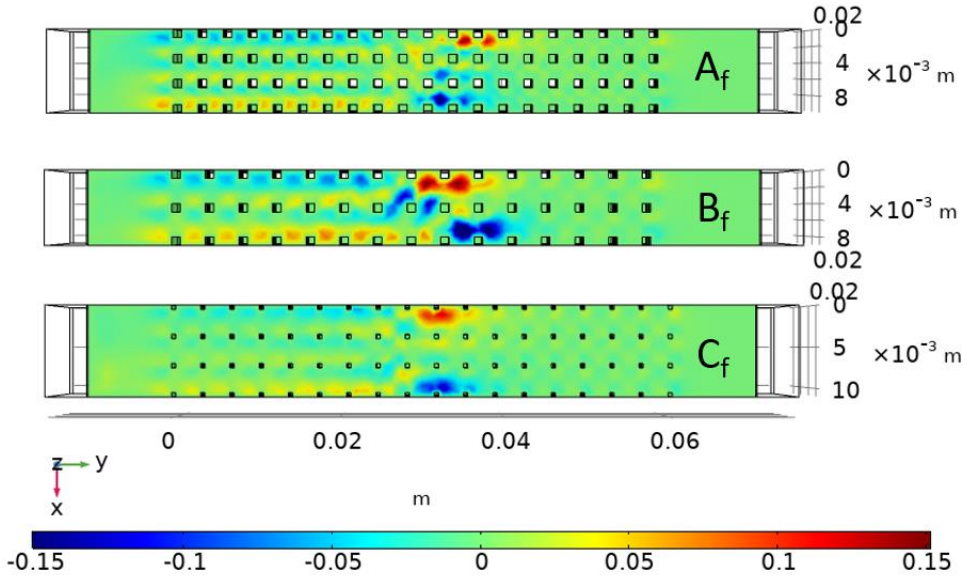

Figure 6.28 – Topside X component of velocity illustrating the crosstalk on the surface layer of the foam designs. The color bar gives velocity in m/s.

6.2.1.4 Parameter Sweep Effect on Flow

As in Chapter 5, it is useful to investigate the development of the velocity profile over time. To that end, velocity data is extracted every 0.05 seconds and plotted in Figure 6.29 and Figure 6.30. Again, it is a challenge to condense the information in these 3-D, transient models to a format that allows pertinent information to be presented. The slices plotted in the previous sections provide a representative example of how the relevant physics profiles develop, and the figures in this section describe how several key parameters vary with respect to time as topside heat flux and magnetic field are varied. The convergence and time stepping of COMSOL can vary extensively between simulations due to increasing external forces in the system, so due to computational constraints the simulation time is limited for select parameters. This is generally done for the highest heat flux and magnetic field strengths.

The curves in Figure 6.29 show velocity magnitudes for all 3 foam geometries as topside heat flux is varied from a 0.5 MW/m^2 peak to a 10 MW/m^2 peak, similar to a ramp from low e-beam heating through small fusion devices to large scale PFC applications. For these runs, the B-field is held at 0.05 T, and the heat transfer coefficient for the cooling lines is 500 W/m^{2}K. The topside heating is applied at t=0, causing rapid acceleration over the first quarter second in the bulk and mainly the first tenth of a second on the top surface. Cases A_f and B_f drive comparable

maximum velocities in the topside volume, reaching 0.35 m/s at the highest heat flux. The outliers seen in the volume and surface maximums of cases A_f and B_f are due to combining eddies at low heat flux combining to spike the velocities in a very small region of the domain. This spike is quickly damped back to expected values. Case C_f drives the slowest maximum velocities over time, reaching 0.2 m/s.

However, as described in Chapter 5, the comparison between volume and surface maximum velocity is one way to measure dryout. If the heat stripe accelerates and depresses the top surface lithium into a profile indicating potential dryout, this would be indicated by a higher volume maximum velocity than surface maximum velocity. This was apparent in the post design and can also be seen in cases A_f and B_f here. Case A_f has the largest discrepancy, with a 57% decrease at the highest heat flux, and ~50% at 3 MW/m^2. Case B_f has a drop of 43% and 25% at 10 MW/m^2 and 3 MW/m^2, respectively. Across all heat flux values, case C_f performs the best in this metric by far with a 10% drop or less between volume and surface maximum velocity. Velocities in case C_f are also remarkably stable over time. It is expected that this is caused by the larger structure to flow volume ratio. The overall velocity is lower than the other foam geometries, but it becomes more stable and resistant to dryout as a result. This is in slight contrast to the post geometries, where the higher structure to fluid ratio of case C_f allowed for larger TEMHD forces to drive equivalent velocities on average and higher surface velocities than the other designs. In the post case, the primary flow channels are less impeded, while in the foams, the overall topside flow is dispersed by the 3-D structure.

Case C_f drives average flow speeds much lower than cases A_f and B_f, and there is less increase with larger topside heat flux. While this may cause a challenge for heat removal, the resistance to dryout is an important factor. The development of cyclical patterns in the velocity profile is also observed in the foam. The behavior is more localized to directly under the heat stripe, as is suggested by the volume force plots in the previous section, which should allow the swirling and wave motion to combat dryout instead of projecting dryout downstream and disrupting flow outside of the highest heat regions. This is most clearly seen in the volume maximum curves of case A_f, though it is present to lesser extents throughout the foam designs.

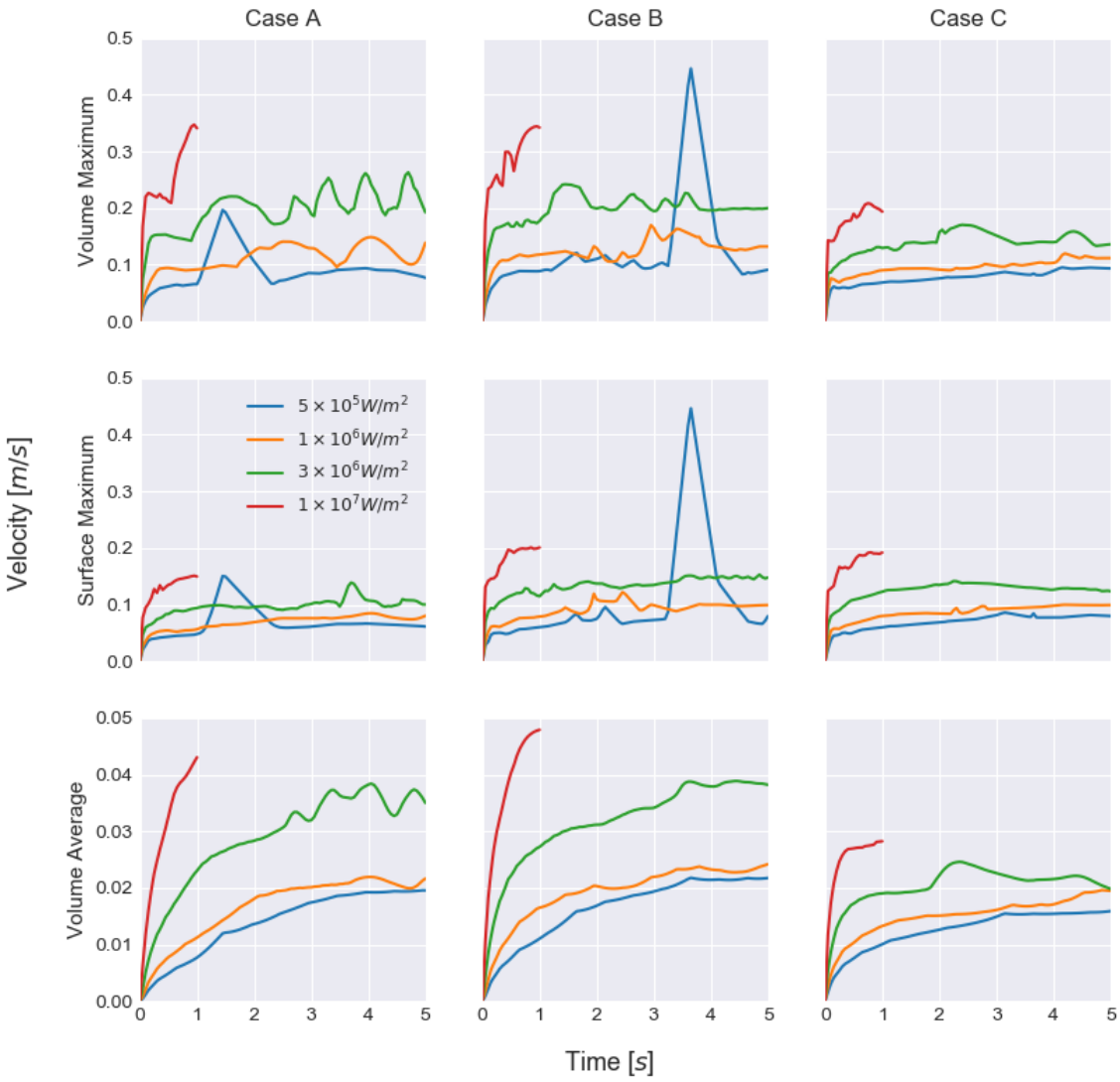

Figure 6.29 – Geometry comparison of several velocity profile characteristics over time, for various peak topside heat flux values.

The performance of the foam geometries as B-field strength is varied from 0.05 T to 0.1 T is given in Figure 6.30. The topside heat flux is kept at 1 MW/m^2. As for the magnetic field sweeps of the post geometries, the high external forces input into COMSOL as B increases tends to worsen convergence and time stepping as the source terms become large. For this reason, the domains were trimmed to a single structure width in X, and the mesh was refined. The magnetic field was ramped from 0 to the final value from t=0.1 to t=0.6 seconds. These adjustments to the simulation create variation in the flow development. The domain size adjustment results in differences between topside and recirculation channel volumes, and the magnetic field ramp changes flow conditions, especially at higher values of B, as the peak flow condition is met during startup followed by the onset of MHD drag domination of the flow.

Like the post geometries, the foam cases display counterintuitive topside maximums due to the strong driving forces caused by TEMHD. As the magnetic field increases, the Lorentz force driving term increases, and this dominates the development of maximum flow velocity in the highest heat flux regions in the topside domain. Overall, TEMHD flow should reach a peak velocity at a magnetic field strength of 0.05 to 0.1 T, depending on geometric factors, after which the larger increase in MHD drag dominates flow. The maximum velocities do not show this dependence, as that region is defined by TEMHD acceleration. It is expected that the peak B-field shifts higher in this small region, eventually dropping with extremely high levels of MHD drag. Based on the amount of the 1.0 T simulation that is captured, the peak likely shifts an order of magnitude higher, between 0.5 and 1.0 T. This counterintuitive behavior is masked by the grouping of velocity curves in case C_f. The maximum velocity is relatively immune to B-field strength over the range studied.

When B reaches 0.5 to 1.0 T, the currents and volume forces that develop result in high variability of flow, especially in the heat stripe region. The initial ramp of magnetic field is seen in many of the curves, especially the volume averages, which give insight into the expected flow profiles of true startup conditions in an experimental device. Case C_f continues to show much better agreement between volume and surface maximum velocities and maintains similar surface velocities as the other designs. Velocity change based on B-field is most apparent in case A_f, since the smaller structure provides less moderating influence on the bulk flow.

The average velocity profiles of the topside domain and recirculation channel present the expected trend of TEMHD flow as B-field increases. There is some variability in the topside average for the lower field strengths, due to the high driving force from the heat stripe, but the bottom channel follows the expected trend quite well. At the highest magnetic field strengths, the expected velocity slows to a crawl of 1 cm/s or less. The recirculation speed generally aligns with the post designs, though the topside average speed is roughly 50% lower across the board. This is expected due to the additional material and interruption of the primary flow channels due to the unique current flow and volume forces in the foam designs.

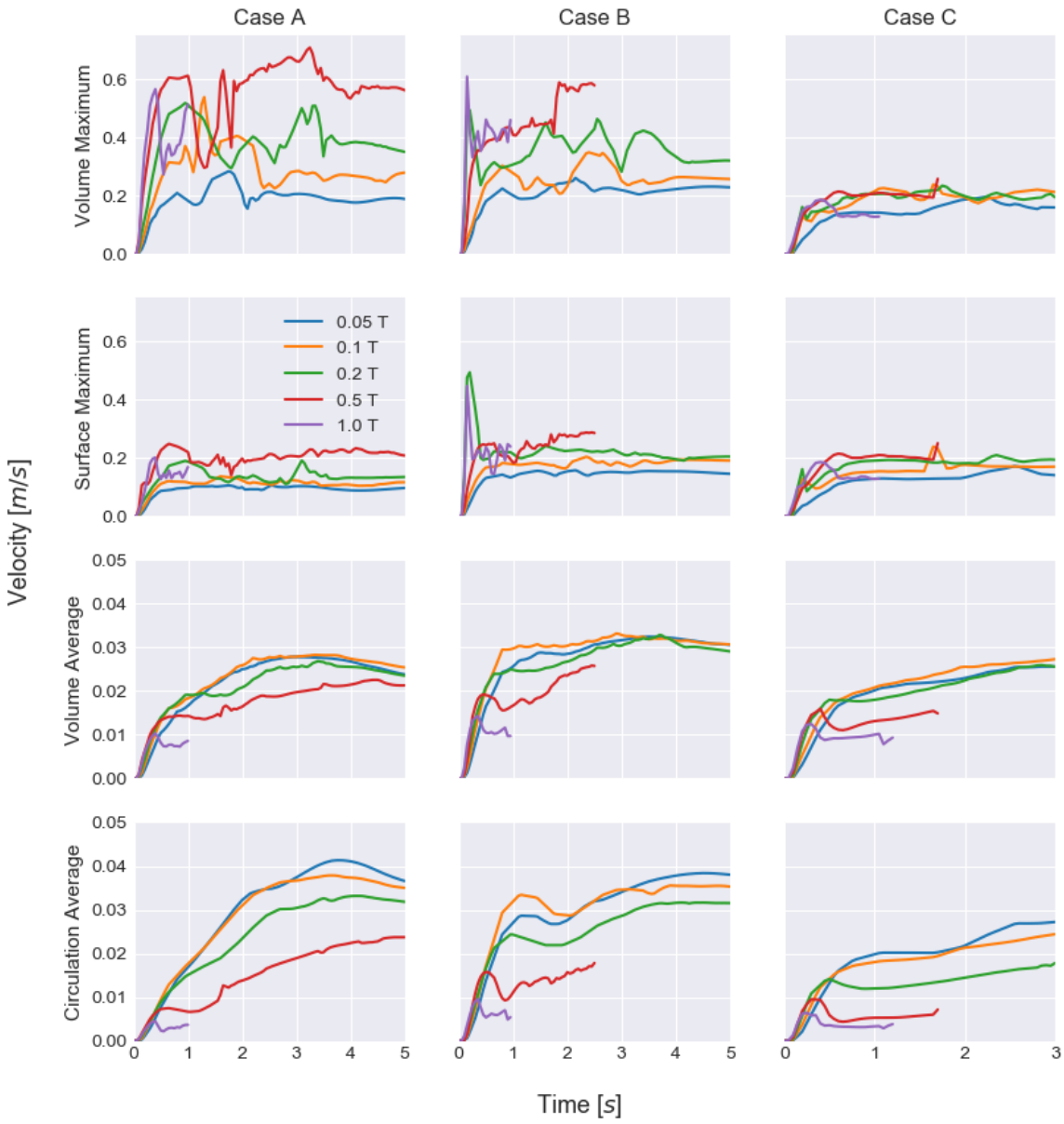

Figure 6.30 – Geometry comparison of several velocity profile characteristics over time, for various magnetic field strengths.

6.2.1.5 Relation to Heat Sink Operation

As described in Section 5.1.5, methods of describing the thermal performance of the structures are informed by studies of heat sink performance. The metrics shown here are total heat output, maximum top surface temperature, thermal resistance, and pressure drop across the topside structure. Refer to Section 5.1.5 for their definitions. These metrics are plotted in Figure 6.31 using the topside heat flux parametric sweep, since performance at high heat flux is most important.

The foam designs present similar values for total heat output in comparison to the posts up to 3 MW/m^2, though the ramp time is longer. This is likely due to the slower acceleration of flow in the foams from the smaller structure size. Computational limitations shorten the simulation time for the 10 MW/m^2 case, though the rapid increases suggest they should exhibit heat outputs similar to the post cases, just over a longer time scale. Case A_f reaches similar maximum temperatures as the post cases, while cases B_f and C_f exhibit lower temperatures. The maximum surface temperature is generally conservative because of the lack of lithium above the solid structures on the top surface and the poor thermal conduction of stainless steel. In any experimental test, lithium wicking over the structures will keep temperatures lower than this direct impingement scenario. In the post cases, the size of the post structures was more impactful to this effect. In the foam case, the effect still exists, but the primary factor with the overall smaller structures seems to be flow cooling the structures from the side and therefore the TEMHD flow propensity. The case A_f foam has the lowest TEMHD drive on the top surface, allowing higher surface temperatures. The thermal resistances through the foams are more similar between geometries than the posts. Cases A_f and C_f generally exhibit lower values, on par with case C_p of the posts. The pressure drop shares the trends seen in the post profiles, though these take place over long time scales like the total heat output. The flow startup sees negative pressure drop as the topside heat flux rapidly accelerates flow down the channel. As circulating flow develops, the pressure drop becomes positive as the topside structures affect flow. As in the post designs, the presence of the topside heat flux disrupts the development of the pressure drop due to its local TEMHD drive. The foam designs develop similar values as the posts, with less variation due to the reduction of eddy flow throughout the topside.

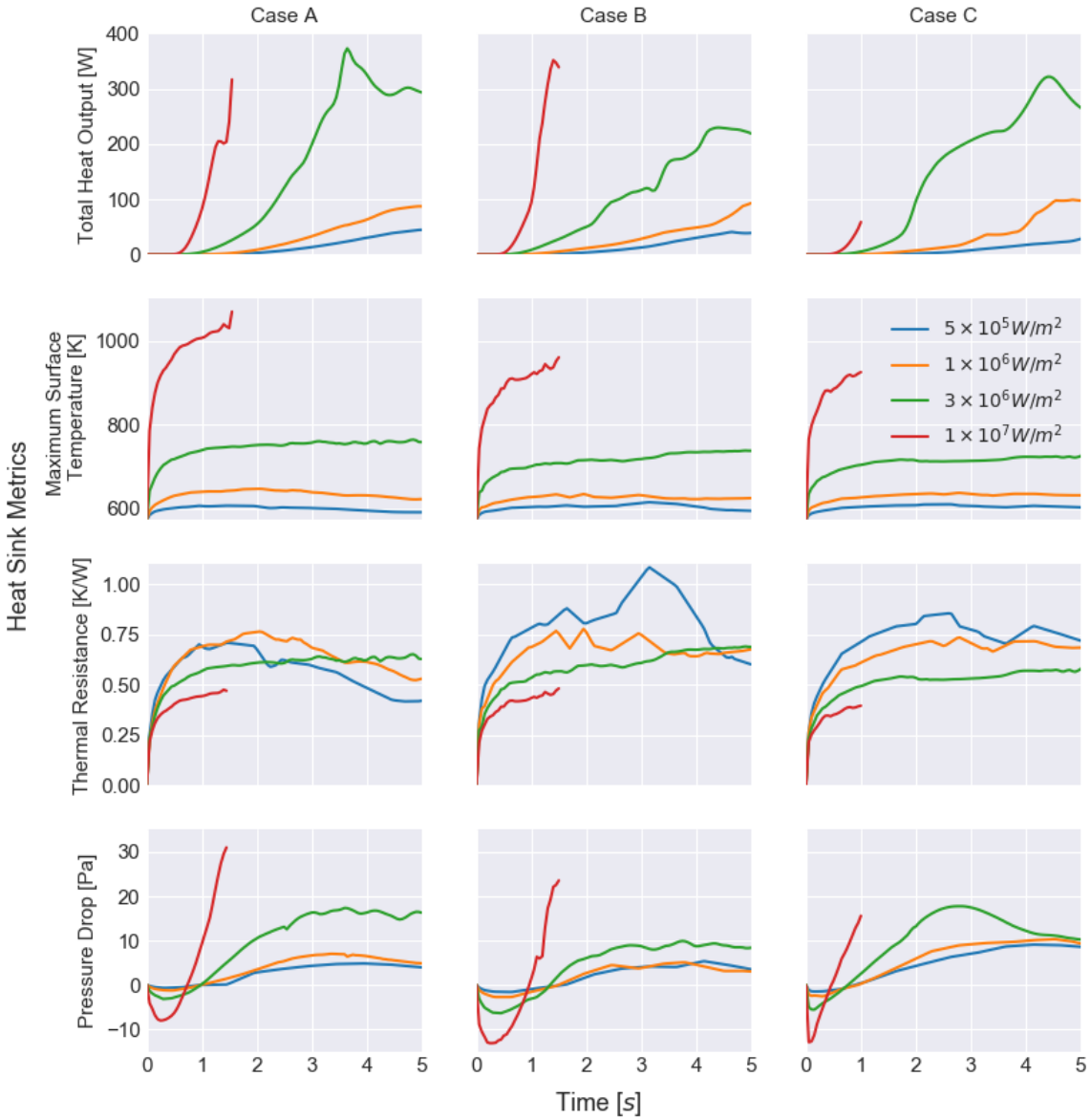

Figure 6.31 – Geometry comparison of heat sink optimization metrics over time, for various peak topside heat flux values.

6.2.2 Experimental Testing

To verify the propensity of the tri-fold foam to drive effective TEMHD flow and withstand high heat loads, the DMLS manufactured plate was installed into the SLiDE system, as seen in Figure 6.32. A more thorough description of the SLiDE experimental setup is given in Section 4.2. As in the post TEMHD testing, a thin layer of thermally conductive silver paint was added to the underside of the plate, to enhance heat transfer to the structures. The inherent roughness of the DMLS process was not a concern here, as the sides and bottom of the plate were planed and smoothed after being removed from the printer.

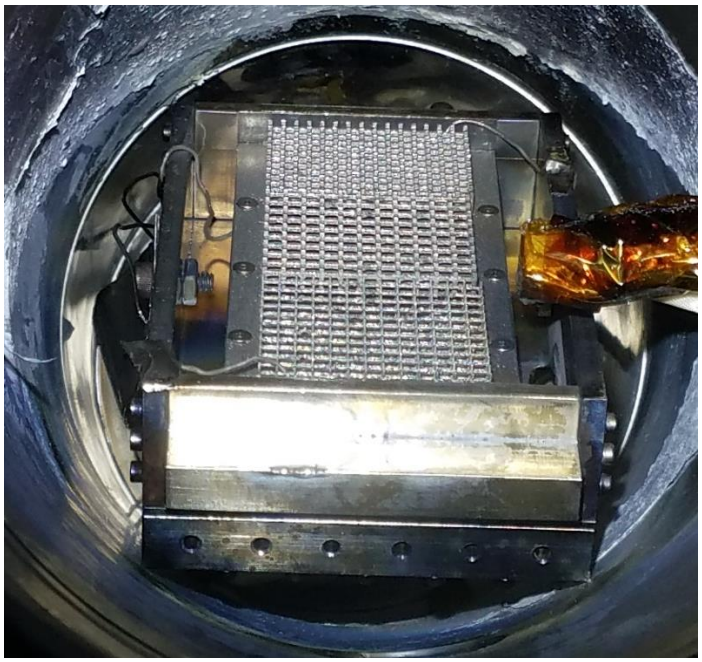

Figure 6.32 – The ordered tri-fold foam plate as installed in the SLiDE chamber.

An initial test of the ordered foam plate was ended prematurely due to issues with the lithium injection system resulting in a large underfill scenario. While this made any measurement of flow extremely difficult (though surface disruption implying flow was still seen), the test allowed for an investigation into the wetting and wicking abilities of the foams. Based on Figure 6.33, it is possible to estimate the sorptivity of the ordered foams in the same way as for the disordered foams. Based off the standard cubic structure for each foam design, the void fraction is 88.4% for case A_f, 72.0% for case B_f, and 58.3% for case C_f. The time between the 2 images is 1620 seconds, and the wetted lengths are 7.5 mm for case A_f, 16 mm for case B_f, and 12 mm for case C_f. Therefore, using the equations for sorptivity in Section 6.1.2, the values are 0.16 mm/s$^{1/2}$

for case A_f, 0.29 mm/s$^{1/2}$ for case B_f, and 0.17 mm/s$^{1/2}$ for case C_f. At worst, the ordered foams are twice as good as wicking lithium as the disordered foam sample, though a large part of this discrepancy is assumed to be due to the ineffective heat transfer to the disordered foam. Generally, in a dense porous material, the influence of gravity is negligible, due to the dominating capillary forces. In these large pore foams, there is perhaps a stronger gravitational component that would affect the apparent sorptivity of a material between the horizontal and vertical directions.

Overall, the foams display impressive wettability and wicking properties, which lends credence to their purported improvement upon standard LiMIT systems as a basis of their use in a flowing lithium PFC. The well wetted example in Figure 6.33 provides a measure of capillary action against gravity in the ordered foams. In this underfilled case, there is not enough lithium volume to entirely fill the module. From a starting condition of a side channel lithium level even with the edges of the module, the foam is able to draw down the level of lithium on the sides. This wicking height is at least 13 mm, as the final side channel lithium level lies below the base plate of the foam structures (11 mm max foam height plus 2 mm base plate thickness). The standard capillary height in a tube equation is given by

$$h = \frac{2\gamma \cos(\theta)}{\rho g r}$$

Where h is the capillary height, γ is the surface tension of the liquid, θ is the contact angle of the liquid, ρ is the density, g is the gravitational acceleration, and r is the radius of the tube. Using a 60º contact angle for lithium on roughened stainless steel [69], a tube of radius $r \approx 6\ mm$ would supply the uptake height of 13 mm observed. As these structures have at largest a diagonal dimension of 4.24 mm, it is expected they would be able to keep supplying lithium upward against gravity well over the current test height (up to 18.8 mm based on this maximum dimension), which is optimal for future application.

Once injection problems were remedied, a fill like the one seen in Figure 6.34 is possible. After injection and lithium cleaning, there is a slight impurity layer over a small portion of the surface, which should yield some particles for PIV tracking. Lithium slightly overfills the case A_f foam at the bottom of the image, while cases B_f (middle) and C_f (top) have larger areas of exact fill across their surfaces.

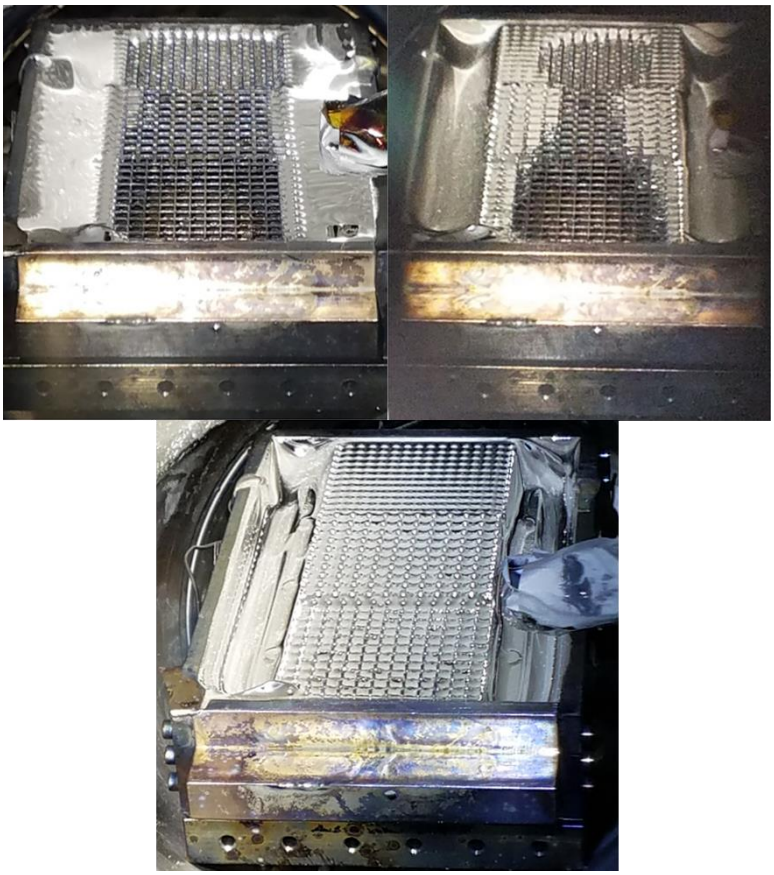

Figure 6.33 – Image series showing the strength of capillary action in the ordered foam designs. Lithium wicking continued through the foam until it was completely filled and well wetted, drawing down the lithium level in the side channels.

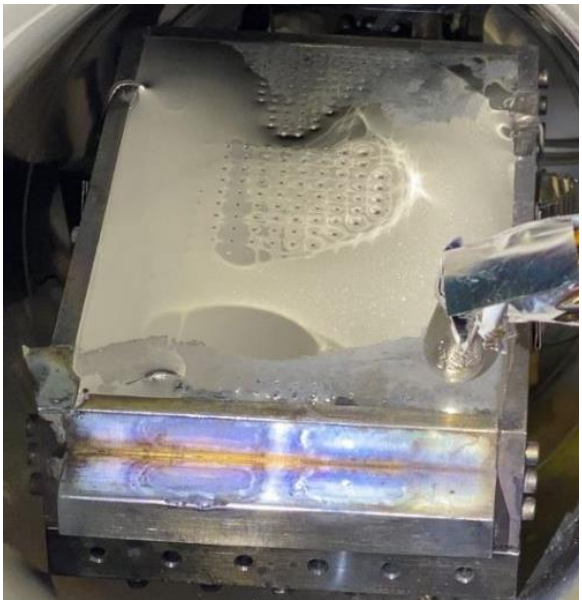

Figure 6.34 – A good foam fill exhibiting slight overfill in some regions of the device.

6.2.2.1 Proof of Concept Flow Results

Proof of concept flow testing proceeded on the tri-fold foam plate with only bottom side heating, central forced helium cooling at 20 psi, and a low magnetic field that was varied from 0.02 to 0.07 T (200 to 700 Gauss), similar to the post experimental testing. While the option exists to power the SLiDE Helmholtz coils by a bank of car batteries in order to reach 0.2 T, this option was not utilized due to safety concerns. As in the post tests, the magnetic fields are pulsed on several times (usually 3) to visualize startup from a no-flow condition after setting up the temperature gradients by cooling for 10 to 20 seconds. The B-field is engaged for 5 to 7 seconds before the knife switches that allow current to flow are disconnected.

Thermocouples monitor the temperature of the module for injection, wetting, and performance metrics. Refer to Figure 4.7 for a diagram of thermocouple placement. Unfortunately, midway through heating the system, the top of structure thermocouple began to read erroneously. Adjustment of the thermocouple wiring was not able to bring back reliable measurements over extended periods of time, so that data is omitted here. Figure 6.35 shows a representative temperature trace over the course of 3 magnetic field pulses. The magnetic field is on at 0.05 T for the periods marked in gray shading. The sharp changes in temperature behavior are immediately apparent. It is pertinent to refer to Section 5.2.1 for a discussion on reference temperature traces that show temperature response for cooling-only and B-field-only scenarios in order to appreciate the indication of flow present here.

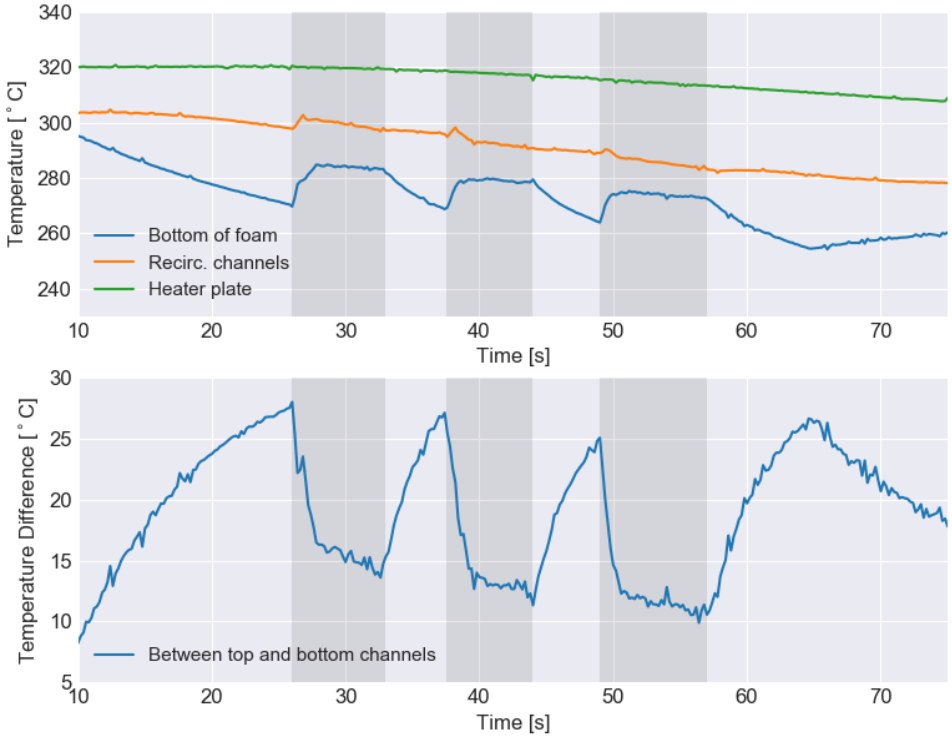

Figure 6.35 – Representative thermocouple response for a set of TEMHD pulses at 0.05 T magnetic field. The shaded bars represent the times the magnetic field is activated.

As in the post design testing, the thermocouple measurements reveal the development of sustained TEMHD flow as soon as the magnetic field is turned on. The bottom of post thermocouple responds to the cooling activation almost immediately and quickly develops a large difference in temperature with respect to the recirculation channels. As the magnets power on, the cooling trend of the topside immediately reverses as flow is driven, mixing along the topside structures occurs, and bulk recirculation exchanges hotter lithium from the recirculation channels with cooler topside lithium. The recirculation channels see a momentary jump slightly delayed from the reversal on the topside and begin cooling at a slightly increased rate due to the lithium circulation. The trend in the recirculation channels is easier to miss here than in the post design tests, due to the slower bulk flow speed and better topside mixing spurred by the 3-D foam structure. Once the magnetic field is turned off, flow stops, and the original temperature trends quickly reassert themselves as cooling continues.

In comparison to the temperature traces of the post design, the initial sharp slope downward in the temperature difference between the top and bottom channels is steeper in the foam than in the posts. The 3-D nature and denser porosity of the foam may result in a steadier startup condition

(ultimately steadier flow condition) than the swirling and eddying of the posts. This would allow for more effective bulk flow motion in the foam as flow ramps up. This explanation is bolstered by the representative COMSOL velocities shown in Figure 6.24, in comparison to that of the posts (Figure 5.11).

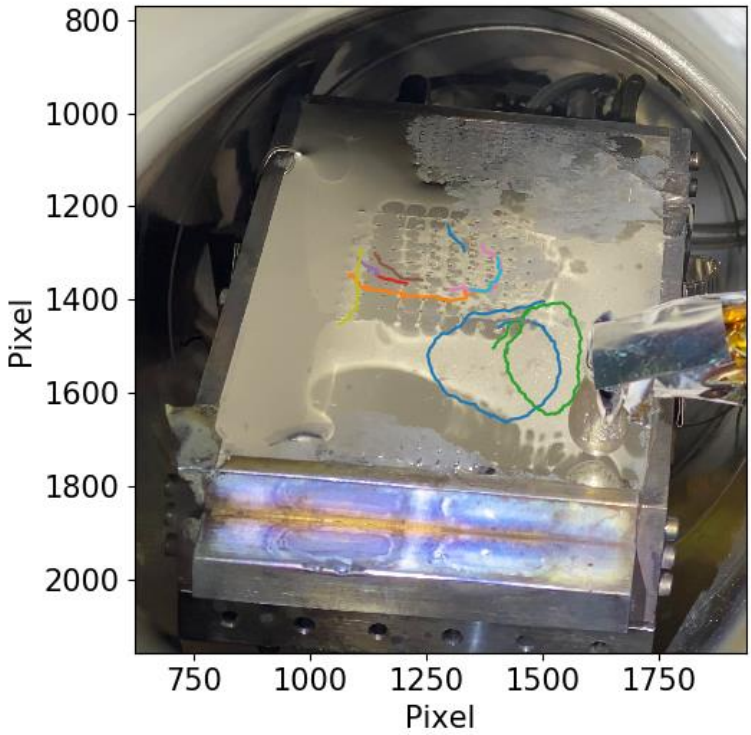

Figure 6.36 – All tracked particle traces for one pulse of TEMHD flow with a 0.07 T magnetic field, including foam surface flow and some swirling flow in the slightly overfilled region.

Particle tracking for the foam module uses the same PIV methods outlined in Section 4.2. Unfortunately, the 2.75-inch viewport directly above the flow module could not be used to track particles, as was done for the posts, due to visibility being limited to the case A_f design through that port. Therefore, the larger 8-inch viewport was used to visualize flow for the foam plate. The larger distance to the foam, however, means additional difficulty in locating and tracking impurity particle motion through the foam. Most of the particles identified were located in the case B_f foam, though there were sporadic particles visible in cases A_f and C_f. Figure 6.36 displays an example of particle tracking in the foam plate, at a 0.07 T magnetic field.

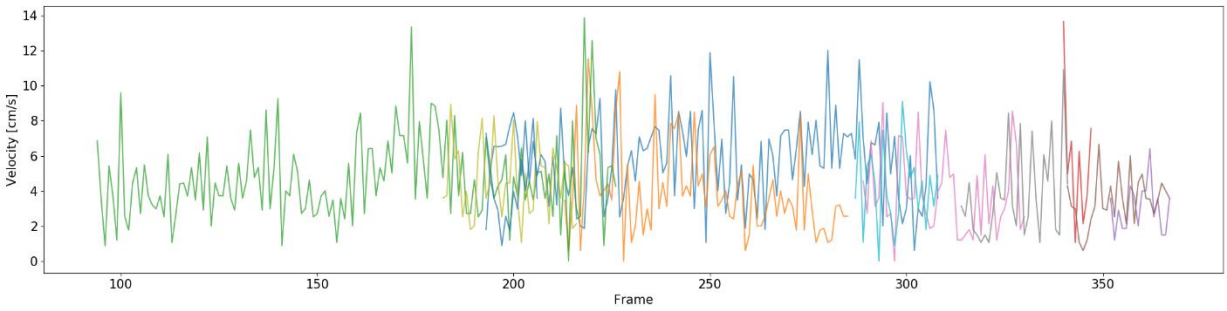

Figure 6.37 – Velocities versus frame number for all particles tracked in the representative pulse shown in Figure 6.36.

Figure 6.37 shows an example of particle velocities tracked through the foam over the single pulse from Figure 6.36. The chaos is analogous to the post design velocity traces. This results from the resolution limitations and small size of the impurities that must be tracked, and the lower numbers of particles is due to the distance from which these image series were gathered. The smallest resolvable particle is larger here than from the closer view through the 2.75-inch port.

The same model setup was adapted to run a magnetic field sweep that resembles that of SLiDE. The topside heating is disabled, and each magnetic field value is run for a simulation time of 10 seconds, to allow steady flow to develop from the thermal gradients created by the cooling lines. The 3 foam geometries establish quite smooth velocity profiles circulating around the domain. The velocity profile is smoother than the post design, which is thought to be due to the moderating influence of the porous media throughout the topside flow. The post designs exhibit uneven TEMHD drive due to the alternating presence of posts and secondary flow channels, which creates topside eddies and swirling flow. While the individual structures are quite small here, the overall influence of the foam becomes more uniform than that of the posts. The unique setup of currents driving flow, as discussed in Section, likely contributes to this effect.

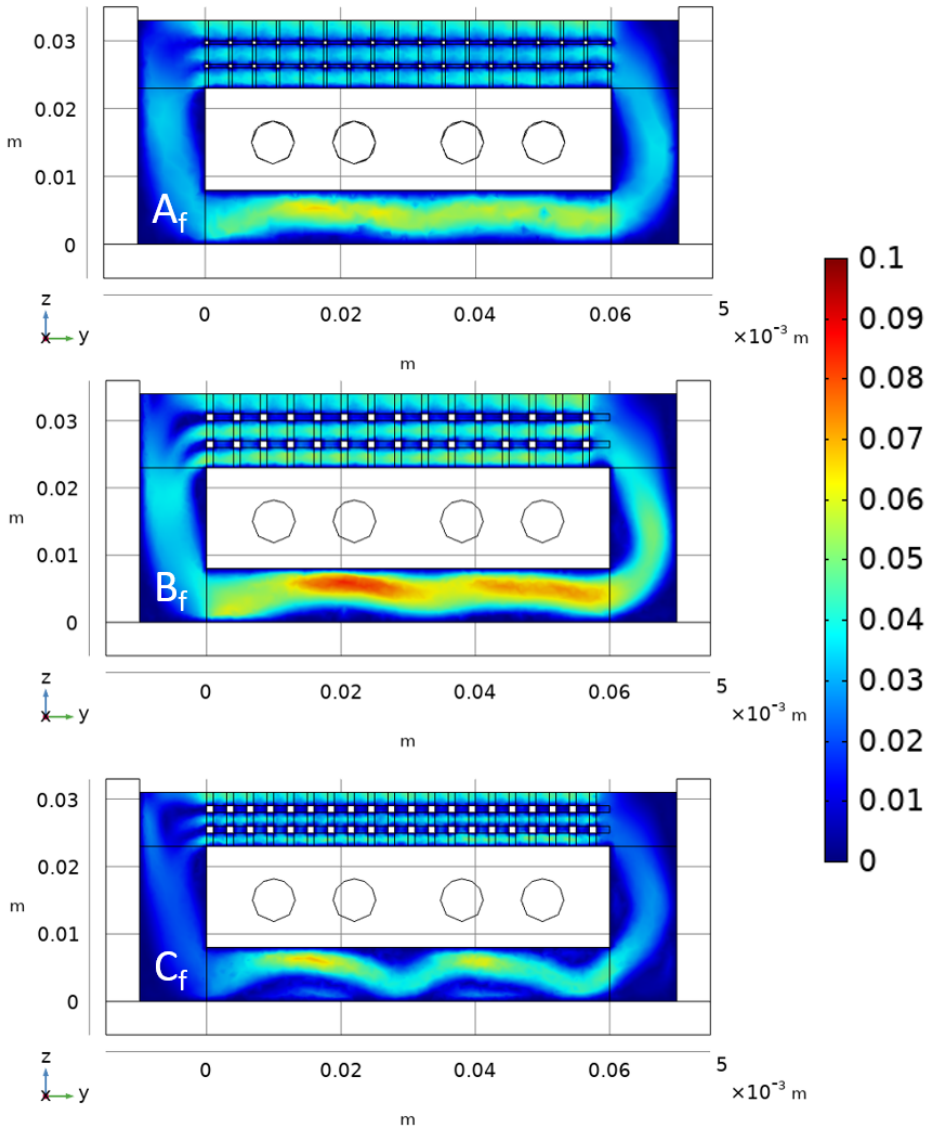

Figure 6.38 – COMSOL velocity traces for the conditions shown in the representative pulse shown in Figure 6.36.

Figure 6.39 shows the comparison of surface velocity data between the experimental tests and the COMSOL simulations of the 3 foam cases in SLiDE conditions. The 0.02 T tests did not yield particles to track, but the temperature measurements indicate sustained flow. The average and maximum surface velocities are plotted for the remainder of the magnetic field values. In these tests, the particle tracks exhibited more variation than those of the posts, so the average maximum velocity of the particles is plotted here with the shading representing the standard deviation of the maximum velocity. The same goes for the average of the particle velocities.

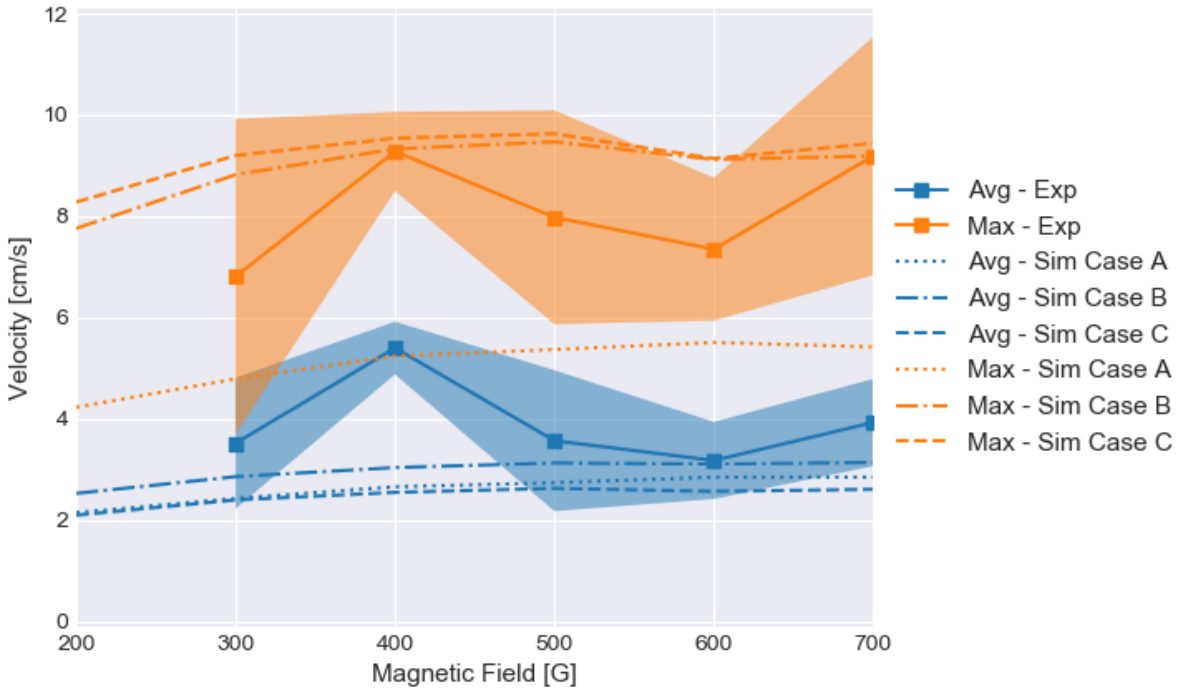

Figure 6.39 – Comparison of experimental velocity values to a SLiDE-relevant COMSOL magnetic field sweep. Experimental values are given for the tri-fold foam plate as a whole. Most tracked particles traveled through case B_f.

Overall, the experimental values show decent agreement to the velocities predicted by the multiphysics models. The average surface velocities of the modeled foams are all very similar, in the range of 2 to 3 cm/s. Experimental values trend above these curves, but are reasonably close, with the exception of 0.04 T. The average value of the 0.04 T experimental test is outside its expected value. This B-field had the least amount trackable particles, all located near the edges of the foam domain, where velocities increased. Maximum values for cases B_f and C_f lie between 9 and 10 cm/s. The interesting outlier from the models is the maximum velocity curve for case A_f. While the overall velocity profile through the foam largely resembles the other cases, the thin structures proceeding to the topside surface are not able to drive a high maximum velocity. Experimental maximum velocities showcase a much larger standard deviation but align quite well with the expected maximum values of cases B_f and C_f, which is expected due to the majority of particles being identified in case B_f.

It is important to mention some of the developments in the experimental flow profiles that affect these velocity values. During the proof of concept tests, the effects of cases A_f and C_f were observable indirectly, through the establishment of distinct flow regions. This highlights the downside to the development of a single test plate containing multiple geometries and exhibiting

differing TEMHD flow speeds. As mentioned in other parts of this work, surface PIV is quite difficult to relate to bulk flow, especially in a highly inviscid liquid, such as lithium. Impurities float on the surface and cannot sink and recirculate with the bulk flow, with the rare exception of extreme heat flux conditions.

In this experiment, and the majority of TEMHD testing at UIUC, the surface motion is easily decoupled from the bulk recirculating flow. This becomes more apparent with the inclusion of differing topside geometries. Most apparent here is the development of rapid swirling flow in the side channels. The bulk recirculation of the flow, coupled with temperature gradients that develop toward the sides of the module, can drive high speed swirling flow along the side channels. This distinct flow region easily entrains impurity particles that cannot recirculate with the bulk. As seen in Figure 6.39, while the maximum flow speeds of B_f and C_f trend together, case A_f has a reduced surface velocity maximum. In combination with the acceleration in the side channels and the presence of a slight overfill in case A_f, this results in a swirling flow that can reverse portions of the surface velocity over the case A_f foam. The particle velocity slowing in the regions of thinner overfill indicates the action of the underlying bulk attempting to counter the reverse motion, but the decoupled surface motion renders significant portions of the particle tracing unreliable. The data presented above has trimmed the particle motion through these distinct flow regions, resulting in more reliable velocity data through the foam. This was most possible for the case B_f region.

There is also noticeable wave motion in the high velocity side channel flow, in which particles can seemingly accelerate to well over 20 cm/s. It is hypothesized that it may be possible to entrain the light impurity particles in the wave motion and accelerate them to speeds faster than the bulk, but this is an avenue for future study. Ultimately, the small scale of the test modules studied at UIUC heightens the magnitude of the effect that these distinct boundary and surface flows can have on the overall surface velocity data. Larger devices, and those with external pumping, should maintain more uniform surface conditions less affected by surface mobility (and hopefully devoid of all impurities).

6.2.2.2 High Heat Flux Resistance

The true test of a theoretically improved open surface PFC is whether it can withstand the extraordinarily high fusion relevant heat fluxes. At UIUC, the SLiDE chamber comes equipped with a homemade linear e-beam for applying a thin high heat flux region on the surface of the module that mimics a divertor heat stripe in a fusion device. For a brief introduction and visualization of the e-beam placement see the experimental setup in Section 4.2, and for a deeper dive into e-beam design, construction, and commissioning, refer to [61]. This e-beam has been utilized for multiple high heat flux tests of the LiMIT device [80]. The beam circuitry has been recently rebuilt to adhere to safety protocols, and extensive operational challenges followed. After utilizing a 120/240V transformer to increase input voltage to the isolation transformers and allowing ample filament heating time (at least one hour) before acceleration voltage was turned on, reliable e-beam operation was possible. A typical initial operation condition of 10 kV acceleration voltage and 10 mA beam current is shown on the surface of the filled ordered foam module in Figure 6.40. To achieve beam focus during testing, the magnetic fields must be activated. Changing the current in the Helmholtz coils changes the length and thickness of the beam, which adjusts the ultimate heat flux impinging on the lithium surface.

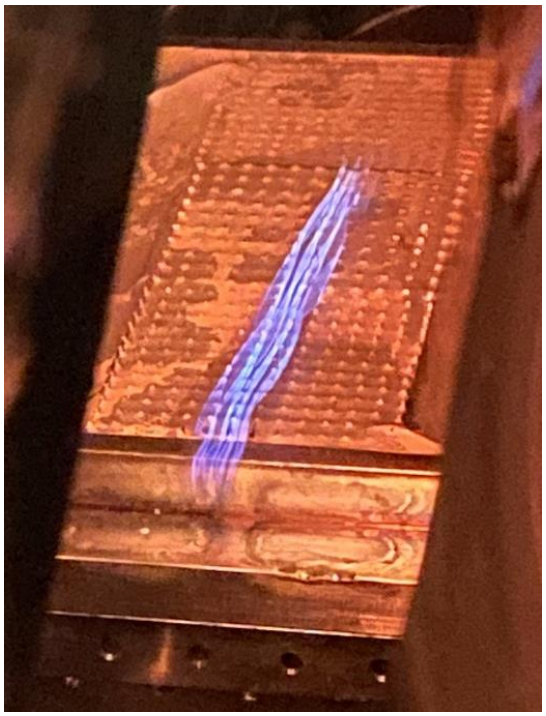

Figure 6.40 – A 10 mA e-beam hitting the surface of the lithium-filled module, with the characteristic blue glow tracing the emission from the 4 beam filaments after they are focused in the magnetic field.

The difficulties in e-beam operation led to an unintentional secondary test of lithium PFC operation. The ability to cool and restart an open surface lithium system has been an area of concern with regards to eventual long-term device operation. The lithium seen in this test was first injected for proof of concept testing of the ordered foam plate. After cooling the module, the SLiDE chamber was eventually vented with argon, opened, and the e-beam was installed. The system spent several minutes in an impure, though majority argon, atmosphere. Due to the unforeseen difficulties in achieving reliable e-beam operation, the filled module was subjected to several thermal cycles for planned operations that were scrapped over a period of 4 months. Average base pressure over that time, discounting the chamber venting, was 1.6×10^{-6} Torr, at which approximately 1 monolayer of impurities per second is estimated to grow on the surface. However, recent research into the hydrogenic species absorption of lithium shows the impurity layer is self-limiting, after which the reaction rate drops heavily to be dominated by slow diffusion to the bulk [72]. Figure 6.41 Left shows the condition of the lithium surface at the outset of e-beam operation. The lithium is liquid in this image, though the surface looks solid from the extensive impurity scaling. During e-beam operation, Figure 6.41 Right was taken, showing a drastically cleaner lithium surface. Lithium heating to dissolve impurities was limited to a brief excursion to just over 400 ºC, with the filaments heated but zero accelerating voltage to mitigate harm from lithium evaporation. This indicates much of the cleaning was due to beam/heat flux exposure. The module restart shown here provides a good initial test of system durability over time, which will prove useful in future long-term operation. Accompanying work on methods to maintain or regain a clean lithium open surface after exposure to air is ongoing at CPMI.

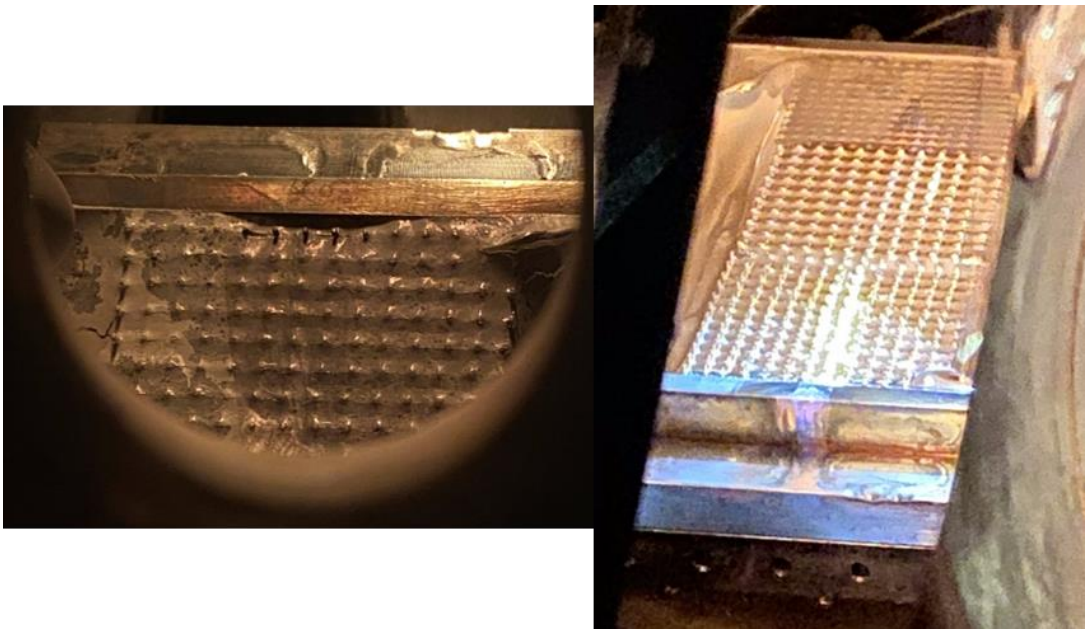

Figure 6.41 – Left: molten lithium with extensive passivation across the top surface. Right: A different view of a later point in time of the same test, showing a refreshed and shiny lithium surface.

The temperature plot of the most rigorous heat flux resistance test of the ordered foam plate is presented in Figure 6.42. Once again, the top of foam thermocouple registered faulty and inconsistent values, so it is not included here. This test was run with lower bottom side heating of 11 kW/m^2 to account for e-beam impingement, and 6.5 V, 100 A on the magnetic field power supplies, supplying a focusing field of 0.065 T. At this B-field and 10 kV acceleration voltage, the heat flux is related to the beam current by the following linear relation.

$$q_{peak}\left[\frac{MW}{m^2}\right] = 0.0225I[mA]$$

With q_{peak} as the peak heat flux magnitude and current I. Cooling is started at 5 seconds, and the beam is in standby mode at 10kV and 10 mA. At standby, temperature rise of the module in entirety is slow, and cooling is periodically activated to reset to optimal lithium temperatures. The middle subplot shows the peak heat flux value over the duration of the test. Until 2 MW/m^2, the 20 psi forced helium cooling lines can remove enough heat to keep the temperature dropping or stable. Past that point, the temperature begins to rise. At 135 seconds, the peak current of 300 mA was attained, equating to a maximum heat flux of 6.8 MW/m^2. This level was held for 5 seconds before the beam current was quickly lowered. The temperature difference between the top and bottom lithium channels never exceeded 15 ºC, indicated sustained bulk flow and mixing

throughout the device. The thermocouple at the bottom of the foam reaches 289 ºC, recording a net temperature increase of 44 ºC over 135 seconds of beam operation with cooling, and a peak-to-trough temperature increase of 62 ºC over 90 seconds of high heat flux operation over 2 MW/m2.

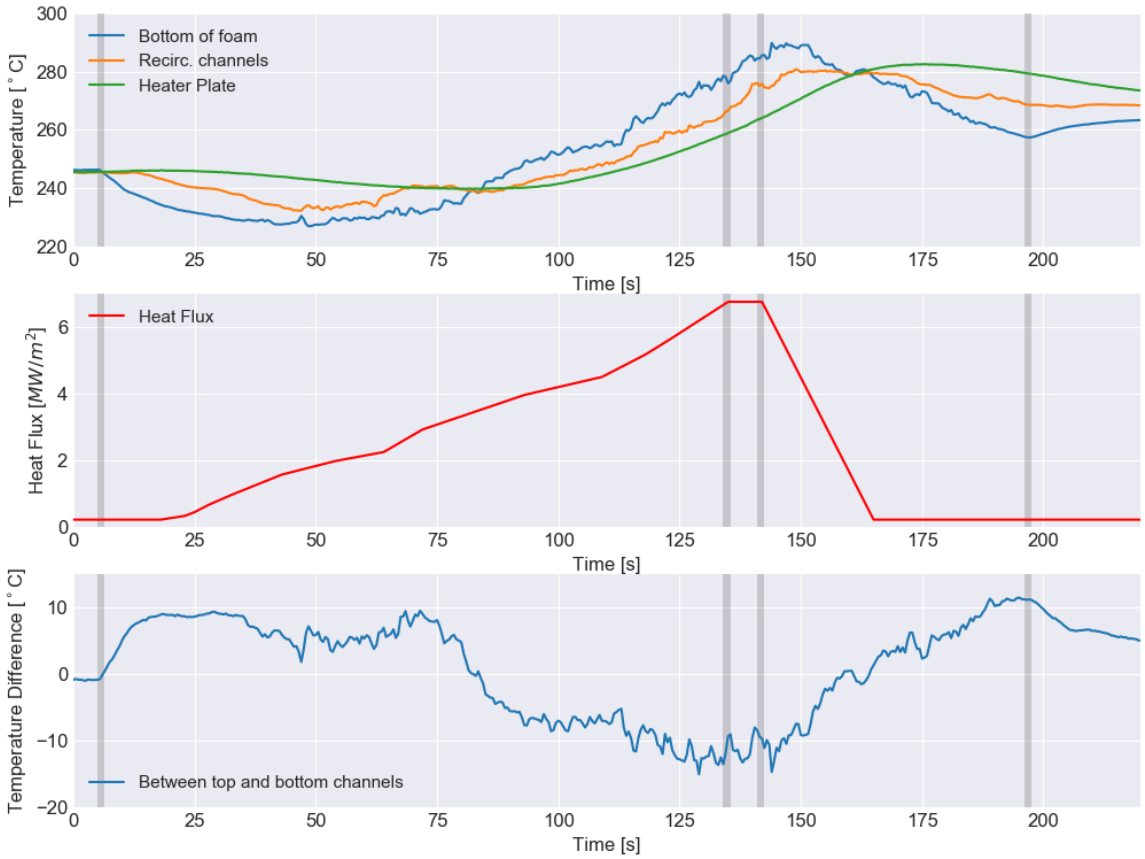

Figure 6.42 – Temperature response over of the tri-fold foam module under high heat flux e-beam heating, with the ramp of beam power included.

The image series presented in Figure 6.43 and Figure 6.44 give a better picture of the surface stability in a high heat flux environment. For these beam current ramp tests, additional light was added to the chamber for better video quality, therefore the blue Bremsstrahlung radiation emission from the beam striking the surface is less visible. The effect of the beam heating along the centerline of the flow module is still apparent, with increasing reddish glow due to the ionization of lithium at these high electron energies.

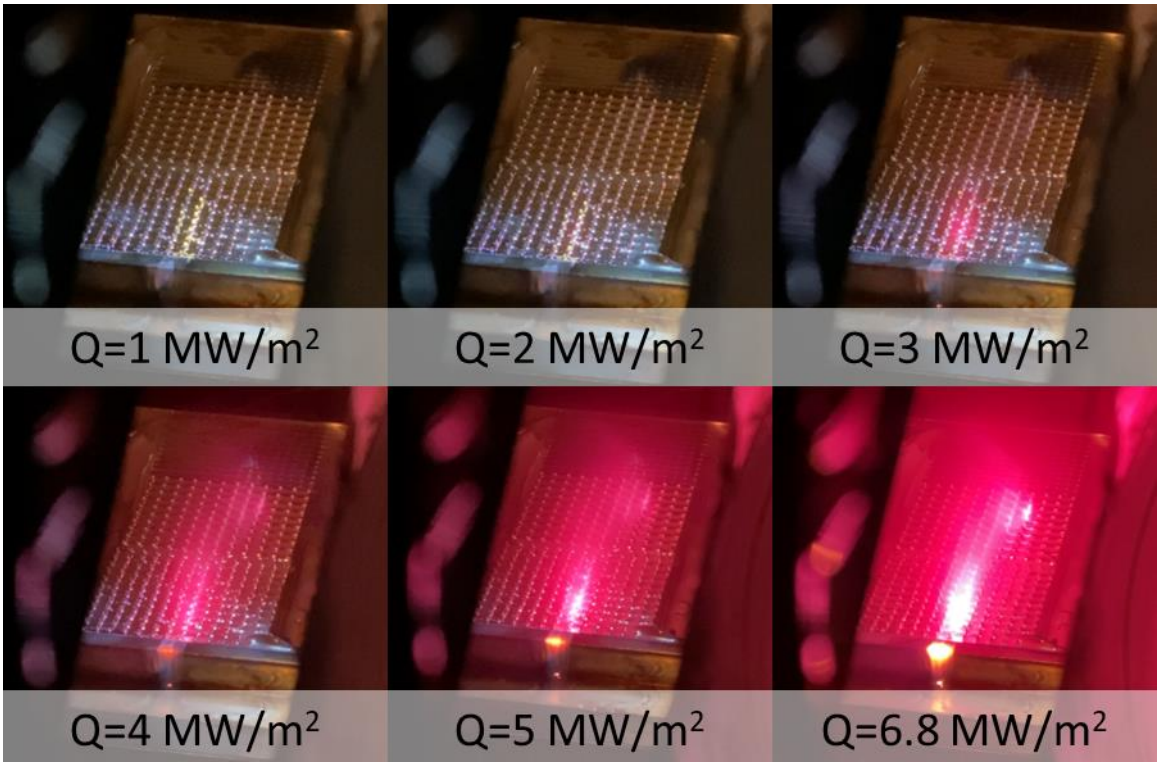

Figure 6.43 – Image series of the entire tri-fold foam plate under high heat flux exposure. The lithium surface stays stable as the leading stainless-steel edge of the module reaches potentially damaging temperatures. The red glow results from lithium ionization by the high energy electrons.

The sweep in Figure 6.43 was performed at 2 V and 32 A on the magnetic field power supplies. There is ambiguity in true peak heat flux at this focus. Beam commissioning tests estimate the peak heat flux could be as low as 25% of the 100 A settings but recognize the limitations of the profile measurements only provide this number as a lower bound. Based on the temperature response measured and visual examination of the beam, it is believed the peak heat flux closely resembles the 6.5 MW/m^2 of the 100 A magnet current, at least in the region of the case A_f foam. The beam streamers caused by the separate filaments become collocated at this focus, providing substantial heat flux. Through this view orientation, similar to the view of early dryout observation in LiMIT shown in Figure 3.7, there is no observable surface destabilization, dryout, or pileup, while the stainless steel edge of the module experiences damaging heating.

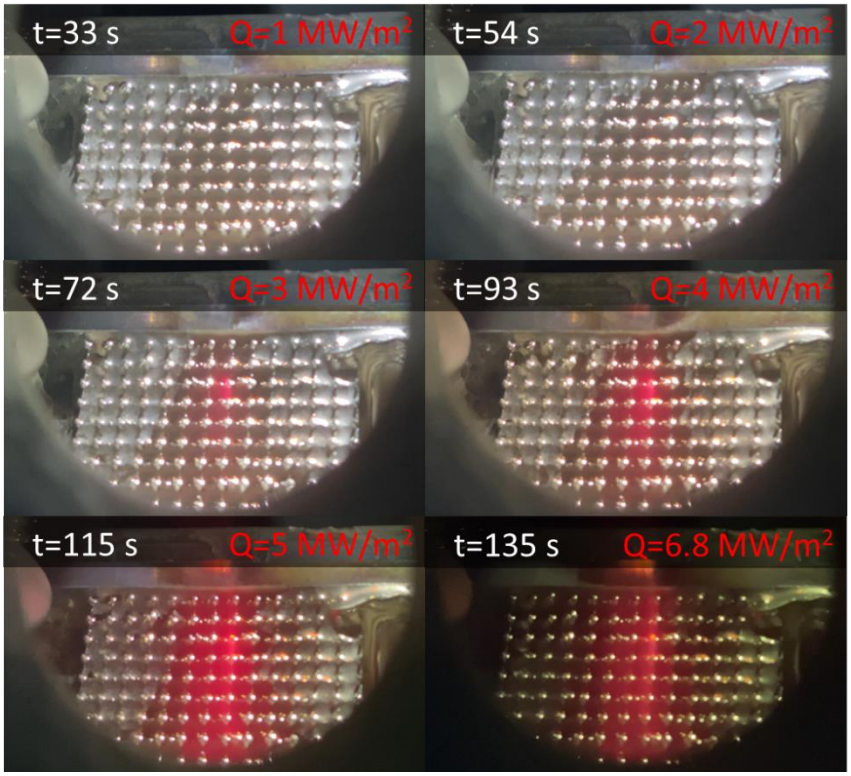

Figure 6.44 – Image series of increasing heat flux from a vantage point focusing on the case A_f foam. The closer viewpoint offers a better view of surface stability in the foams during high heat flux operation.

Figure 6.44 provides the best view to see potential dryout, over a smaller section of the tri-fold foam plate. The view from the top 2.75-inch viewport highlights the case A_f foam performance during the 6.5 V, 100 A Helmholtz condition beam ramp. The lithium surface is mirror-finish clean in a downward V-shape from the edge of the module toward the top of the images, with a thin impurity layer on the surface of the upstream and downstream regions of the foam. As the magnetic field in these tests is continuously active (deactivating the field defocuses the beam and lowers beam current), TEMHD flow through the device is already present at low speeds due to inherent temperature gradients that form through the module.

As the beam current is turned up and topside heat flux increases, rapid swirling motion is seen in tiny impurity particles in multiple cells of the topside surface of the foam. Surface circulation is also seen in the side channels. There is no observable evidence of diminishing surface stability throughout the heat flux ramp, as the surface tension of the liquid lithium acts in the foam structure to anchor the surface against dryout. This is true up to the maximum 6.8 MW/m^2, which the foam withstands for at least 5 seconds before the beam heating is decreased.

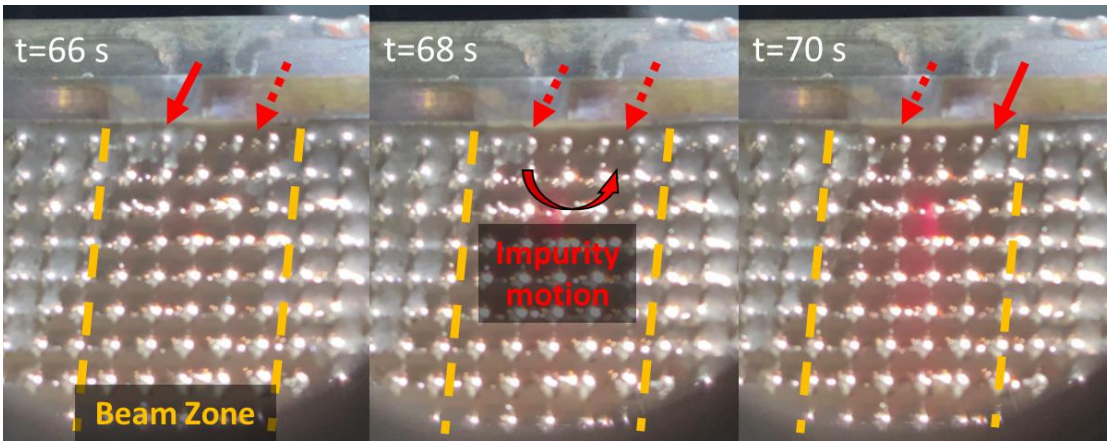

Figure 6.45 – Image series of impurity motion moving under the lithium surface, indicating dryout forces are present but stabilized by the foam structures. Solid red arrows indicate impurities are present, dashed red arrows indicate impurities are not present.

At the 2.5 to 3 MW/m^2 range, approximately 65 to 75 seconds into the duration of the test, centerline impurities near the module edge (top of the images) seem to indicate the Z-directed (into and out of the page) dryout and pileup forces are still present but can be countered by the flow, capillary action, and mixing of the foam. Impurities on the upstream side of the heat stripe appear to drop into the lithium as they are entrained in rapid motion just beneath the surface. Between 3 and 4 seconds later, new impurities are seen coming to the surface on the downstream side of the high heat flux region. This is a very rare case of impurity motion below the surface of the lithium, which is likely due to the large volume forces present in that region, and potentially the local temperature change starting to allow impurity dissolution into the bulk. This process is displayed in the images in Figure 6.45. Ultimately, the lithium surface remained stable through this event.

The high heat flux e-beam tests discussed in this section provide the strongest evidence for improvement to TEMHD driven, open surface, liquid lithium PFCs utilizing advanced geometries to stabilize the surface while maintaining the propensity for bulk flow. The operating regime for a LiMIT-style TEMHD system was improved by 127%, from 3 MW/m^2 to 6.8 MW/m^2. Furthermore, this level of peak heat flux was sustained for at least 5 seconds with no evidence of impending dryout, pileup, or material failure, over a span of high heat flux impingement lasting 140 seconds total.

CHAPTER 7 – TRUE FREE SURFACE FLOW MODEL

Multiphysics modeling of the TEMHD system has been a large component of the UIUC approach to continued design of open surface liquid lithium PFCs, as has been demonstrated in the earlier chapters of this work. A vast majority of TEMHD fluid simulations have been developed using COMSOL Multiphysics due to its excellence in coupling multiple physics interfaces. The TEMHD system is a highly coupled thermal, electromagnetic, and fluid flow problem. Due to limitations in computational power and fluid solver capabilities, the simulations describing TEMHD flow in LiMIT systems have been constrained surface models, where the lithium free surface is approximated using a slip boundary condition, but the lithium domain is a fixed block. These models provide reasonably accurate descriptions of flow development and match proof-of-concept experimental profiles, allowing for studies of TEMHD flow propensity and more rapid examination of how changing conditions affect flow behavior. However, no topology change is allowed with a constrained surface. Until the focus of LiMIT development shifted to dryout resistance, this could suffice. In order to truly investigate the fluid behavior of open surface PFCs along with their potential to resist dryout, the motion of the free surface must be captured.

Numerical modeling of free surface fluids is a notoriously difficult problem to solve. Resolving and tracking the motion of an interface between multiple fluids introduces sharp gradients in material properties and therefore the introduction of large surface forces. While an encompassing review of the techniques used for multiphase CFD simulations is not possible here, a brief summary of potential methods is given, leading to the model choice for initial free surface flow simulations in this work.

There are generally 2 types of multiphase flow: separated flow, where immiscible fluids exist in disparate phases that can be separated by an interface, and dispersed flow, where one phase is spread throughout another and interface separation of the many instances of small phase inclusions is not feasible [101]. Separated flow examples include melting or solidification, film boiling, and annular flow. Dispersed flows include sprays, bubbly flows, and solid particulates moving in a fluid. Sometimes a third type of multiphase flow is defined, mixed flow, which includes both separated and dispersed regimes, such as slug flow and bubbly annular flow.

The type of multiphase flow model used depends on the types of flow regimes the scenario includes. A LiMIT style PFC system falls squarely into the separated, free surface flow regime, so the choice of model is narrowed to those that can resolve and advect an interface between the phases. There are 2 standard approaches to resolving an interface in separated multiphase flow modeling: interface tracking and interface capturing. While these terms sound very similar there are important distinctions. Interface tracking methods, including the marker-and-cell and front tracking methods, physically render the interface between the phases as a geometrical surface, and physically modify the size and shape of the phase domains on either side of the interface as the interface moves. Interface capture methods, including volume of fluid, level set, and phase field methods, represent the multiple phases as a field on a fixed background mesh, and the interface is captured within the static mesh based on the values in the field [102].

COMSOL Multiphysics is chosen as the modeling software of choice due to its ability to couple multiple physics interfaces with relative ease. For separated open surface multiphase flow, COMSOL contains 4 types of flow models: stationary free surface, moving mesh (as seen in the initial 2-D dryout simulations), level set, and phase field. The stationary free surface model is a way of approximating the changing height of a 'free surface' based on solving a stationary flow model and adjusting the height of the surface based on the solution profiles of the velocity and pressure. While it is useful in some instances and allows for a single fluid flow solver to yield an estimate of free surface motion, this is essentially a plotting scheme and it does not actively track an interface between flow phases. The moving mesh model is an interface tracking method that explicitly defines the interface as a boundary along the mesh. This model produces an exact interface, but the high resolution requires a very fine mesh, displacements of the surface quickly necessitate remeshing since the physical mesh elements are stretching and compressing, and no topology change is possible. The moving mesh model is able to resolve impressively accurate surface curvatures in select applications, since a change in topology breaks the model without difficult prediction schemes that COMSOL has not implemented [88].

The level set and phase field schemes are field-based methods that capture the interface within a fixed mesh. The multiple phases are represented by the level set function or phase field function, and the interface is defined as a contour as a specific value of those functions. The interface is advected by the fluid physics interface coupled to the method. This allows topology

change and droplet formation with relative ease. However, both methods entail lower interfacial accuracy because the boundary between the phases is a smooth gradient in the function, and mesh density should be high wherever the interface resides. The methods solve the following equation to advect the interface.

$$\frac{\partial \emptyset}{\partial t} + \nabla \emptyset \cdot u = F$$

The level set uses a right-hand-side term that includes higher order derivatives of the level set function, while the phase field method utilizes a term that is used to minimize the free energy of the surface. Based on the nuances between the models, the phase field method tends to yield better shape accuracy in small systems with high surface tension and high interface curvature like wetting droplets and meniscus formation. In contrast, the level set method is best for macroscopic systems with bulk fluid flow where the exact shape of the interface is less important. Of course, the TEMHD driven lithium system entails characteristics from both categories. It is a highly transient bulk flow with high surface tension and the possibility of developing dryout and pileup effects whose shape is important to accurately represent. Ultimately, the level set model is chosen due to its success in solving bulk flow and its stability and convergence with less tuning in trial simulations.

7.1 Level Set Model

As mentioned in the previous section, free surface TEMHD flow was developed in COMSOL based on its ability to efficiently couple system physics, and the level set method is chosen as the multiphase flow implementation due to its stability and speed. In a broad sense, a level set method is any method that uses an implicit level set function $\emptyset$ to describe a shape or surface that can then be advected through an independent grid. The level set function is a signed distance function that is continuous and smoothly varies from +1 on one side of the interface to -1 on the other. The shape is represented as the 0-level isosurface of the level set function. The method allows for topology changes that would be extremely difficult to describe using an explicitly defined boundary, like droplet breakup or flame propagation. Developed by Osher and Sethian in 1988, level set methods were originally used for tracking interfaces in computer graphics [103]. Sussman et al. devised the original theory for applying the level set method to

multiphase CFD problems in 1994, allowing for large density and viscosity variation across the interface and the inclusion of surface tension [104].

The COMSOL Multiphysics implementation of the level set method is based upon the work of Olsson and Kreiss, who proposed a method for improving conservation of the level set method by utilizing a smoothed Heaviside function as the level set function [105]. In this version, one fluid has a value of 0, while the second fluid has a value of 1, with smooth variation between the two along the interface region. The interface is defined as the isosurface at $\emptyset = 0.5$. Their methods improve the mass conservation in the system without creating a hybrid of schemes (like coupled LSVOF), maintaining the simplicity of the level set method. Fluid motion is still governed by the standard incompressible Navier Stokes equations.

$$\rho \frac{\partial \boldsymbol{u}}{\partial t} + \rho(\boldsymbol{u} \cdot \nabla)\boldsymbol{u} = \nabla \cdot [-p\boldsymbol{I} + \mu(\nabla \boldsymbol{u} + \nabla \boldsymbol{u}^T)] + \boldsymbol{F}_g + \boldsymbol{F}_{st} + \boldsymbol{F}_{ext} + \boldsymbol{F}$$

$$\nabla \cdot \boldsymbol{u} = 0$$

Where ρ is the density, $\boldsymbol{u}$ is the velocity vector, p is the pressure, $\boldsymbol{I}$ is the identity matrix, μ is the dynamic viscosity, $\boldsymbol{F}_g$ is the gravity force, $\boldsymbol{F}_{st}$ is the surface tension force, $\boldsymbol{F}_{ext}$ is the user defined external contribution to free energy (only used in the phase field method), and $\boldsymbol{F}$ is the user defined volume force [106]. These fluid equations are solved by whichever fluid solver is included along with the multiphase flow scheme. The interface is advected using the following additional equation specific to the level set method.

$$\frac{\partial \emptyset}{\partial t} + \boldsymbol{u} \cdot \nabla \emptyset = \gamma \nabla \cdot \left[\varepsilon \nabla \emptyset - \emptyset(1 - \emptyset) \frac{\nabla \emptyset}{|\nabla \emptyset|} \right]$$

Here $\emptyset$ is the level set function, γ is the reinitialization parameter, and ε is the parameter controlling interface thickness. This shows the interface is advected by the velocity vector, solved via the coupled fluid physics interface.

The density and dynamic viscosity of the fluids are automatically adjusted with respect to the level set function, so variation across the interface is accurate.

$$\rho = \rho_1 + \emptyset(\rho_2 - \rho_1)$$

$$\mu = \mu_1 + \emptyset(\mu_2 - \mu_1)$$

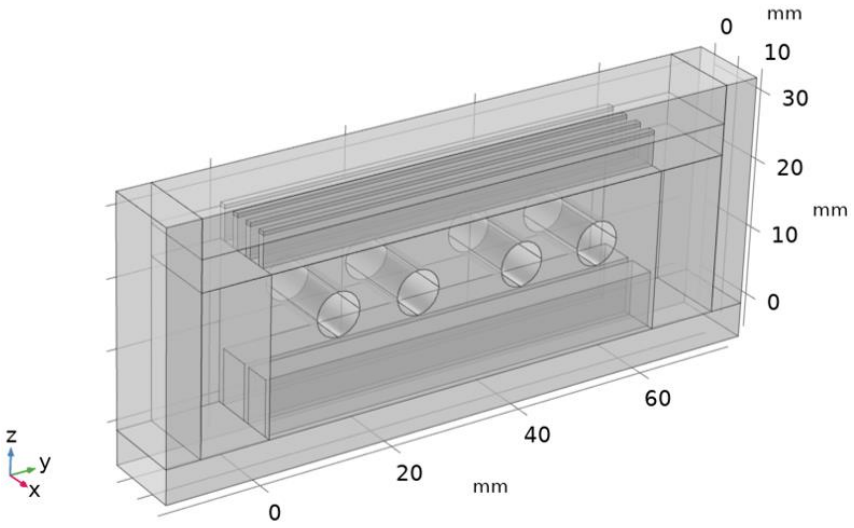

Figure 7.1 – Example COMSOL domain for multiphase modeling, including 2 topside domains to allow motion of the free surface.

Ultimately, the level set method will be applied to a domain that is very similar to the fixed surface setup. This is shown in Figure 7.1. The second topside domain represents the secondary fluid, in this case air. The density and pressure of the air are very small compared to the lithium and there is no concern about passivation, as these COMSOL models do not account for surface chemistry. Therefore, the air domain is acting as a stand-in for vacuum, to allow the free surface of the lithium to respond to the transient forces of TEMHD flow with a high heat flux region.

7.2 Model Development

The important thing to note is that the level set (LS) interface only truly couples to the laminar flow (LF) interface (or whatever fluid physics interface is being used). COMSOL v5.4 does not include any direct coupling of its multiphase flow setup to other physics interfaces, such as heat transfer in fluids (HT) or electric current (EC), necessary for TEMHD modeling. The largest effect of this omission is seen in the material properties settings of these interfaces.

In general, the materials interface provides properties of the multiple materials included in the model as well as the selection of domains that these materials occupy. For the vast majority of potential simulation types, including the constrained surface TEMHD modeling shown throughout this work, the setup works well, as the material properties within a domain never change, outside of expected variation due to temperature or pressure, etc. that can be included as a function of the dependent variable of the physics interface. For multiphase flow, the interface between the fluid phases must move smoothly between domains, and boundary conditions and volumetric physics must respond correctly as the fluid properties change. The properties can no longer be initialized within a domain and remain unchanged in that domain. Instead, all physics interfaces acting on the fluid domains and their boundaries must incorporate the volume fraction of the fluid into the material properties, so the movement of the interface successfully captures the response of the system to the multiple fluid phases.

This section details the adjustments made to the COMSOL model setup described in Chapter 4 to incorporate multiphase flow, and simultaneously outlines the major steps taken in the development of these free surface TEMHD flow simulations. 2-D models were used to test initial performance of the physics interfaces, and to learn how to apply necessary adjustments to the setting in a less rigorous domain. After the HT and EC physics were deemed operational and coupled to the LF/LS system, the extension to 3-D was performed.

7.2.1 Laminar Flow and Level Set Interfaces

While this seems backwards from the model development as described in Section 4.3, it is important to begin by ensuring the coupling of the LF and LS physics is working as it should before attempting to include additional physics. Initially, a simple 2-D rectangular domain was tested for free surface flow, with half of one boundary being an inlet and half of the other boundary an outlet. Almost immediately, the limitations of the multiphase fluid solvers in COMSOL were apparent. As the lithium entered the domain, a negative relative pressure developed immediately above the inlet region. This would draw the lithium up the wall above the inlet over time, which is obviously unphysical. At the outlet, the lithium would hit the boundary and react as if no outlet existed. The liquid level would increase and eventually fill the domain. COMSOL Knowledgebase article 1239 provides some insight into these issues, and along with a blog post

on multiphase flow modeling presents a jumping point for diving into the world of COMSOL multiphase CFD [107], [108].

When including inlets and outlets in multiphase systems, the inlet and outlet should encompass a full boundary, as in a wall or other boundary condition should not be present along the same line as the inlet or outlet. If possible, they should also border domains that fully contain a single fluid. This is most important for the inlet. It is also suggested that the initial conditions of the fluid (i.e. velocity) match from inlet to simulation domain if possible. The outlet issues were fixed by disabling the setting to compensate for hydrostatic pressure. This is meant to be used when the outlet also borders a single fluid domain, or if a constant level of liquid is desired, instead of flow draining until the liquid thickness equilibrated to the mass flow rate through the domain. This could not ultimately be achieved, so a dam is used instead, as a stopgap measure to test the remainder of the physics involved in TEMHD. The resulting domain is shown in Figure 7.2.

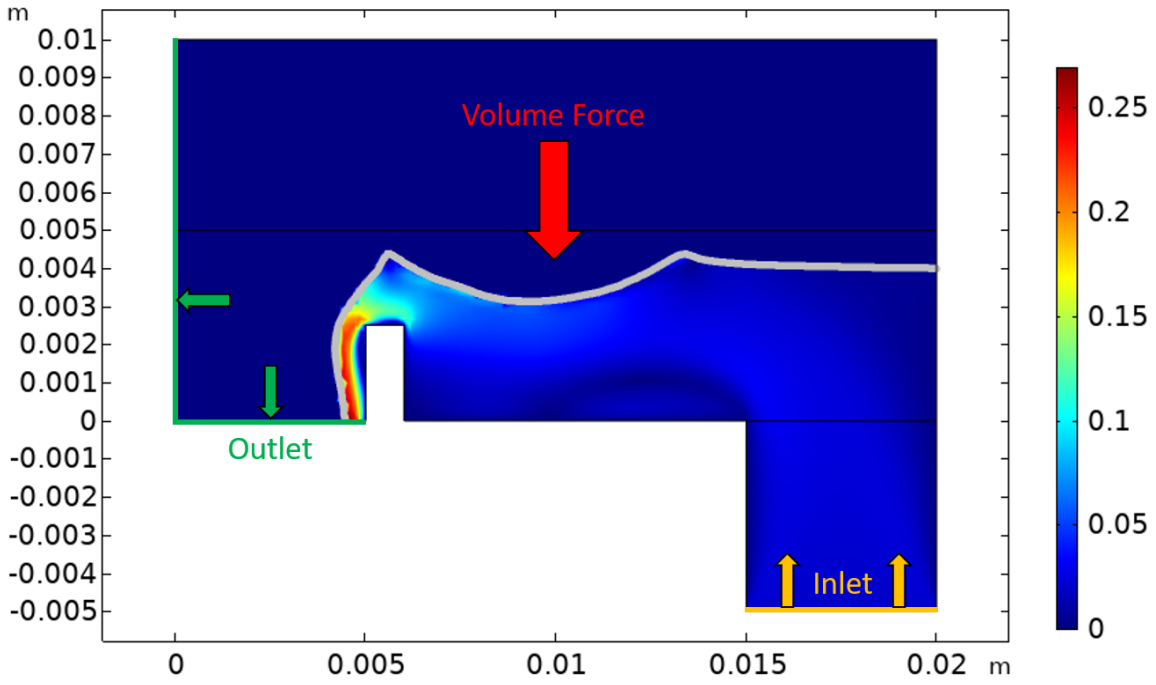

Figure 7.2 – 2-D physics test domain with a test volume force applied to the fluid surface centered at 0.01 m. The interface is marked in gray and the color bar describes velocity magnitude, plotted in the fluid of interest.

The inlet and outlet zones are labeled, and the lower block is initialized as fully liquid. Testing of free surface flow began with water and proceeded to lithium once development progressed to the EC module. The interface is initialized at y=0 between x=0.015 m and x=0.02 m.

The inlet has a velocity normal to the boundary at 2 cm/s, and standard gravity is included. Over time, the liquid fills the area that is dammed before cresting the boundary and spilling into the outlet.

After this simple flow testing succeeded, volume force testing proceeded. To test surface evolution in response to a volume force, a pulse in the -Y direction was included. A Gaussian function was defined at location 1 with standard deviation 0.1, and an analytical function turned that into a gaussian pulse in time, by defining the expression as gp1 and dependent variable as time t. The force variable is then defined as

$$F = F_0[an1(t)]e^{-(x-0.01)^2/0.002^2}$$

This yields a Gaussian pulse in space and time that peaks at x=0.01 m at t=1 s, which was applied as a -Y volume force in the LF interface. Various values of F_0 were included, from 25 to 2500 (similar magnitudes to those seen in dryout conditions), as a quick investigation of surface depression and droplet formation due to splashing. Figure 7.2 shows the $F_0 = 1000$ simulation 10 ms after the peak of the volume force.

There are several other considerations of LF/LS settings that should be noted. Standard settings of the LF interface as described in Section 4.3 continue to apply. The pressure point constraint and reference position should remain collocated to preempt any issues with reference pressures. Note that the point should not be chosen along the interface, as frequent changes in material properties and therefore pressures could occur here. A point in the corner of the air domain furthest from any potential multiphase activity is chosen. The LS boundary conditions should match those in the LF interface, in terms of walls, symmetries, inlet/outlet, etc. The parameter controlling interface thickness should be ½ the maximum mesh dimension along the interface. By default, this value is set to ½ the overall maximum mesh dimension, which can cause the interface to be much larger than desired. In changing this value, the entire region over which the interface will propagate should be considered. The reinitialization parameter should be defined as the maximum expected velocity. Defaulting to 1, this term can be refined after an initial result yields more accurate velocity data.

7.2.2 Heat Transfer Interface

As mentioned previously, additional physics interfaces included in the model beyond a fluid solver do not directly couple to the LS interface. For example, this means that when a temperature boundary condition is enabled in the model at x=0.02 m from y=0 to 0.005 m, the temperature response does not change as lithium fills along that boundary. The default material property settings of 'from material' respond to the material properties of the domains as initialized, and do not react to the motion of the interface between the fluids. To correct this, the material properties are changed to a user defined linear combination of the 2 possible fluids, in the form

$$Property = property_{fluid1} \cdot ls.Vf1 + property_{fluid2} \cdot ls.Vf2$$

Where $property$ is thermal conductivity k, density ρ, heat capacity at constant pressure C_p, or ratio of specific heats γ. How these variables are written depends on the parameter naming convention of the user. The volume fractions of the respective fluids are given in COMSOL by $ls.Vf1$ and $ls.Vf2$. After these adjustments, the temperature response to heating and cooling along the boundaries correctly reacted to the changing fluid.

In the fixed surface models presented in the previous chapters of this work, the topside heating was applied as a heat flux boundary condition. With the extension to free surface flow, there is no fixed boundary at the interface on which a heat flux can be supplied. The topside of the system is now an air domain which has an extremely low thermal conductivity. Any heat flux applied to the surface rapidly heats the air and diffuses before reaching the liquid. A method is needed to improve thermal conductivity to the liquid or selectively apply heat to mobile interface.

The first attempts to remedy this issue revolved around adjusting the value and directionality of thermal conductivity in air so the air domain would pass heat directly to the liquid surface. The thermal conductivity of air in the materials interface was changed from isotropic to diagonal with only a k_{22} (k in Y) value, and the magnitude was increased to quickly pass heat deposited on the boundary through the air to the interface. This does not automatically pass into the HT physics, since the properties are reliant on linear combinations of the parameters. Therefore, the HT thermal conductivity was changed to anisotropic and included a directional conductivity of air in the Y direction.

These modifications do not work. The directional thermal conductivity and high magnitude of k in air rapidly rises the temperature in a sharp heat stripe under the applied heat flux. As the liquid rises from the inlet domain and begins to pass under the heat stripe, the temperature instantly decreases to the liquid temperature along the vertical line from the leading edge of the interface. The temperature of the liquid never increases. This highly nonphysical result comes from the limitations imposed on the movement of heat through the air. Since the air domain can only pass heat vertically, it has no choice but to cool instantly as the liquid moves into the hot air domain because that is the trivial solution.

The next method focuses on ways to apply heat directly to the interface between the liquid and air domains, instead of changing parameter directionality and lessening relation to the physical system. User defined surface physics seems to not be common in COMSOL multiphase flow systems. Some insight into surface application of heat in COMSOL level set modeling was gained through literature on selective laser melting for additive manufacturing [109] and melt pool dynamics in laser welding [110]. The heat deposition requirements for these applications are very similar to the modeling needs here. These references mention utilizing the delta function of the level set variable to identify the interfacial surface and apply heat at that location. Searching COMSOL documentation and example walkthroughs yields a method for smoothing the gradient of the level set function to approximate a delta function $\delta(\emptyset)$ over the interface. This is given by

$$\delta(\emptyset) = 6|\emptyset(1-\emptyset)||\nabla\emptyset|$$

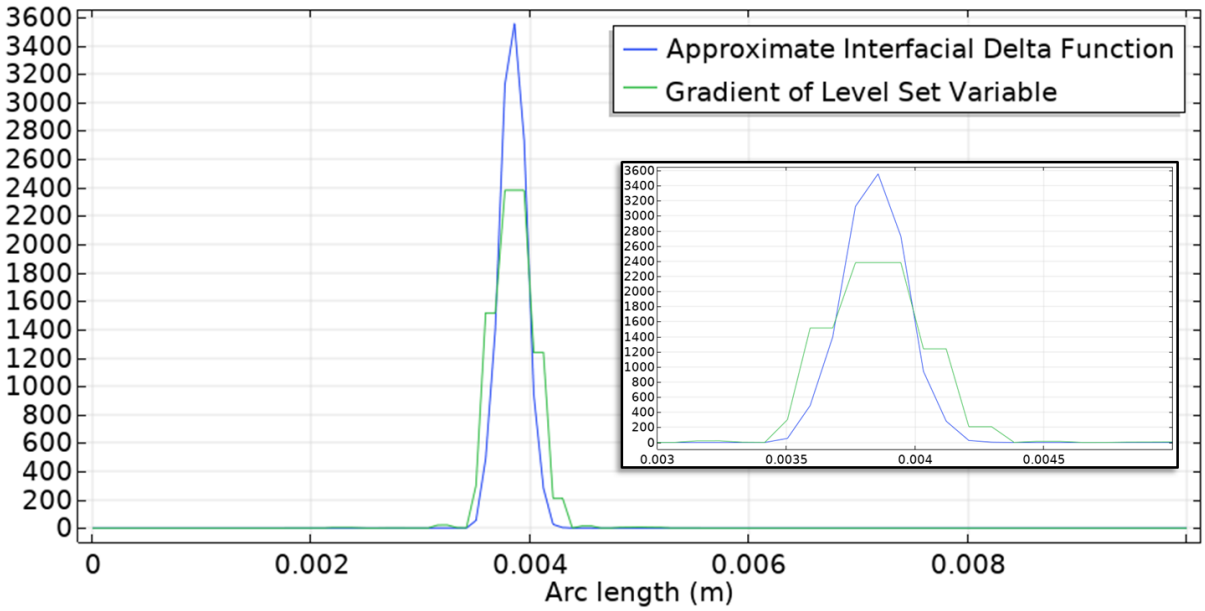

Figure 7.3 – Line plot along x=0.01 m showing the gradient of the level set function and the adjusted approximation of the interfacial delta function. The inset gives a closer view.

The plot of both the gradient of the level set function $\nabla\emptyset$ and the delta function approximation $\delta(\emptyset)$ are shown in Figure 7.3 along a line located at x=0.01 and swept from y=0 to y=0.01. While the gradient is stepped as a result of the mesh shaping near the boundary, the delta function approximation smooths the steps and provides a sharp peak where the interface is taken at the 0.5 level isosurface.

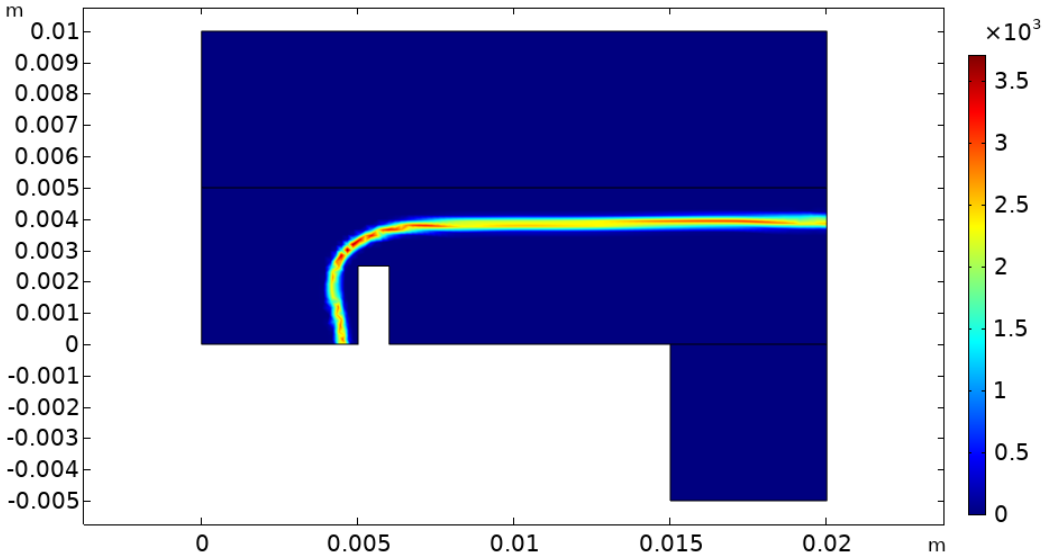

Figure 7.4 – 2-D physics test domain with the interfacial delta function equation plotted throughout the surface. The color bar represents the function value.

When plotted over the 2-D test domain, the delta function smoothly tracks the interface, as seen in Figure 7.4. There is some variation in peak magnitude due to the placement of mesh elements, but overall, the interface is clearly defined. Note this example does not include the volume force pulse used to test surface disruption in the LF/LS testing, and the surface stays smooth through t=1 second. When the volume force is included, the delta function still correctly follows the interface.

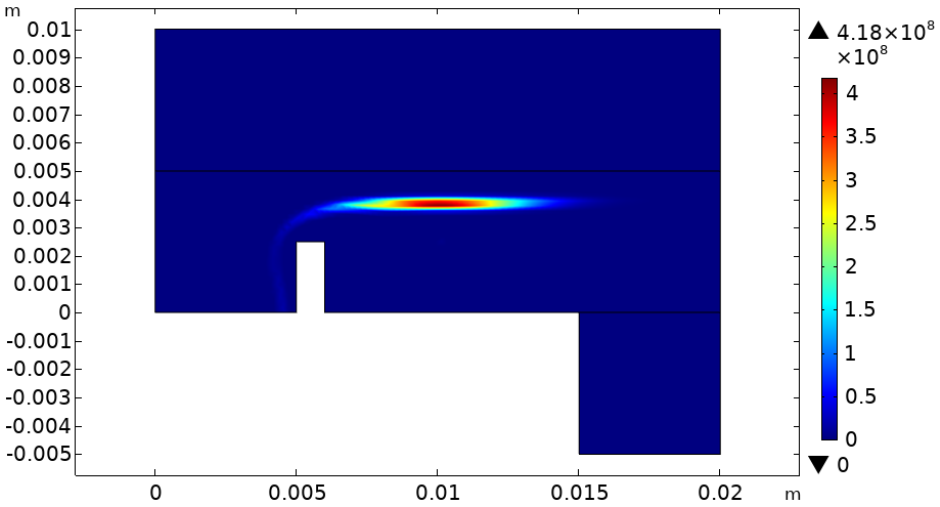

Figure 7.5 – 2-D physics test domain with Gaussian heat source applied to the interface using the interfacial delta function approximation. The color bar gives total heat source in W/m^3.

With the delta function, application of a heating zone to the surface of the liquid is possible via the application of a domain heat source in the HT interface. The delta function approximation is multiplied by a spatial Gaussian of the same standard form as in the fixed surface simulations. To create the heat source shown in Figure 7.5, it is written as

$$Q = q_0\left(e^{-(x-0.01)^2/0.003^2}\right)|\emptyset(1-\emptyset)||\nabla\emptyset|$$

Where q_0 is the peak magnitude of the beam or heat stripe. The heat source is written in COMSOL as

$$Q = topheat * abs\big(phils * (1 - phils)\big) * abs(ls.gradphi)$$

$$topheat = peakheat * \exp\left(-(x - 0.01)\text{^}2/0.003\text{^}2\right)$$

Here $topheat$ is a user defined variable that defined the spatial Gaussian in X and $peakheat$ is a user defined parameter that is the magnitude of the Gaussian peak. These

improvements to the HT interface change material properties so heat transfer accounts for the motion of the 2 fluid phases and correctly apply heat to the level set interface in a way that mimics the e-beam pulse or divertor heat stripe impinging the liquid surface.

7.2.3 Electric Currents Interface

After getting the HT interface to correctly model temperature distribution and heat transfer through the domain, the next step is turning the temperature gradients into thermoelectric currents. To begin, the materials properties settings were changed to functions of the volume fraction of each liquid, using the same method as for the HT interface shown above. This fixes the issue of the lack of coupling between the EC interface and the LS interface. When applying the external current density source term that spurs development of the thermoelectric currents, it is important to separate out the electrical conductivity and make sure it is written as a linear combination of volume fractions in these settings as well.

Past attempts at including EC physics for modeling multiphase current distributions with a static interface resulted in current density spiking at the fluid interface and breaking the simulation. In initial simulations with the new domain, using water as the liquid phase, the current seemed to flow correctly near the interface and there were no observable nonphysical increases in current density. At this point, the liquid phase was switched to lithium throughout the physics interfaces, to ensure all simple steps were working with lithium before true coupling to the fluid motion was included via the addition of the TEMHD volume force. As should be expected, lithium initially broke the model. After stepping back and ensuring individual physics interfaces worked effectively, the issue remained in the EC module. Again, sharp nonphysical gradients in current density were visible along the 1 to 2 mesh elements directly above the level set interface and near sharp corners of the domain. Corners tend to cause peaking of the current density, but this is observable in working TEMHD models, such as the fixed surface simulations. The issue ultimately stems from the difference in electrical conductivity magnitudes between air and lithium. The value for air is input as 1×10^{-9} S/m, while water is 5×10^{-2} S/m and lithium, as a metal, is 3.6×10^{6} S/m. COMSOL has trouble handling 0 values in material properties, especially when dealing with a property change over the interfacial gradient and physics such as electric currents. When the liquid material was shifted to lithium, the 15-order-of-magnitude difference in electrical

conductivity is on the order of machine epsilon, and the COMSOL solvers exhibit an error prone response. Since the 7-order-of-magnitude difference between water and air resulted in accurate solutions, the electrical conductivity of air is increased to 1×10^{-1} S/m. This solves the issue, and the conductivity of the air domain remains negligible with respect to that of lithium.

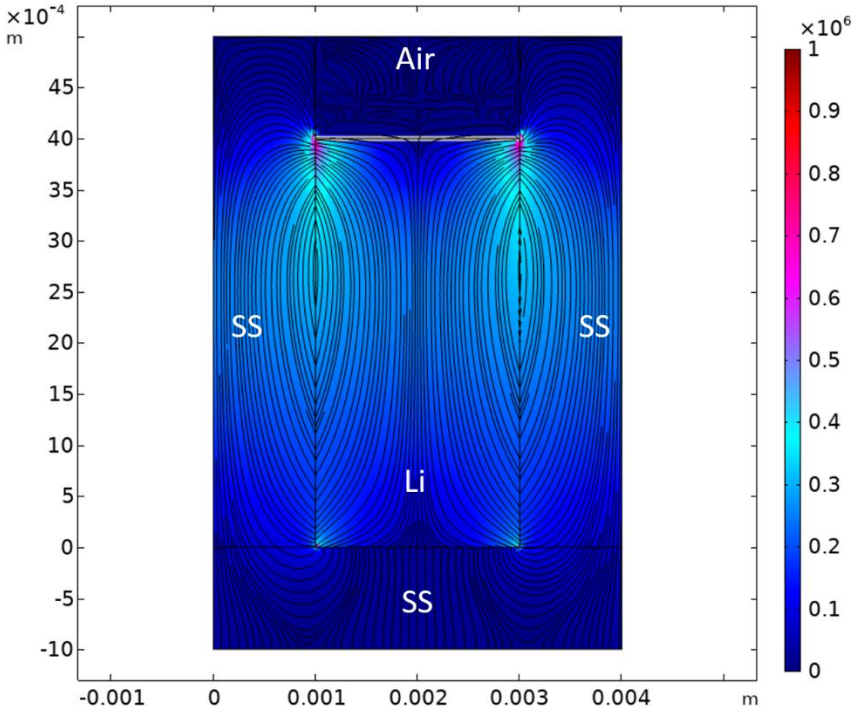

Figure 7.6 – 2-D physics test domain of a LiMIT trench cross section showing thermoelectric current developments due to a topside temperature gradient. The interface is marked in gray, the color bar gives current density in A/m^2, and the streamlines follow current flow.

In order to ensure the thermoelectric currents develop as expected, an additional 2-D domain was built to showcase the standard current density profile in a LiMIT trench. The trench is bounded on 3 sides by stainless steel, with a small air domain above the lithium. This model solves for all physics, though there is no volume force included to drive flow. A high heat flux condition with 1 MW/m^2 peak is set on the fluid interface, generating current densities very similar to the early modeling of LiMIT trenches as well as the post and foam TEMHD models in this work. The typical peaking of the current at the corners of the lithium domain exists, and the current circulates accurately through the stainless steel and lithium domains while falling to essentially 0 in the air domain.

7.3 3-D Free Surface TEMHD Flow

After the physics interfaces involved in TEMHD flow were adjusted and tested in concert with the addition of level set multiphase flow, the 2-D test domain representing a cross section of a LiMIT trench, shown in Figure 7.6, was expanded to 3-D. Here, a single simple trench is recreated with no recirculation channel. Similar testing of the coupling between the physics interfaces is carried out, with volume forces disabled but the fluid motion (stability) and level set interface still solved for. An example of the resultant current density is shown here in Figure 7.7, while other plots from this test are described in Chapter 3 as illustrations of the development of lithium dryout.

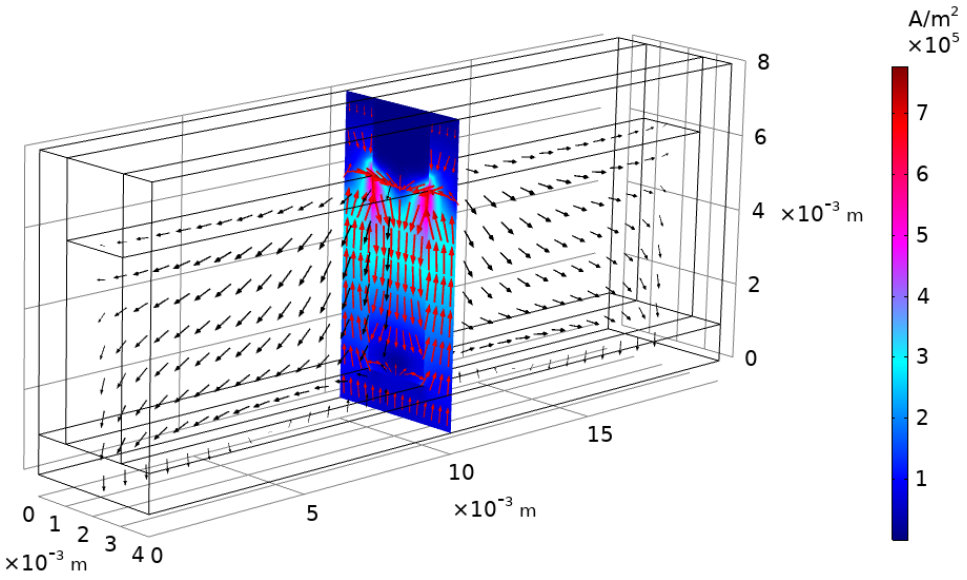

Figure 7.7 – 3-D test domain of a single LiMIT trench displaying a centered XZ current density slice, a collocated XZ arrow surface in red showing current circulation through the trenches and lithium, and a YZ arrow surface in black showing the nonuniformity of current circulation direction on either side of the topside heat flux. The color bar gives current density in A/m^2.

The current density plot in Figure 7.7 shows an XZ current density slice with an arrow volume in red plotted at the slice location in Y describing the directional swirling of the current. This is placed directly under the centered Gaussian heat flux applied to the fluid interface. The black arrow volume plotted along the trench in YZ at the central X location displays the nonuniformity that develops due to the spatially transient nature of the heat flux. This works to create the volume forces that cause dryout and pileup.

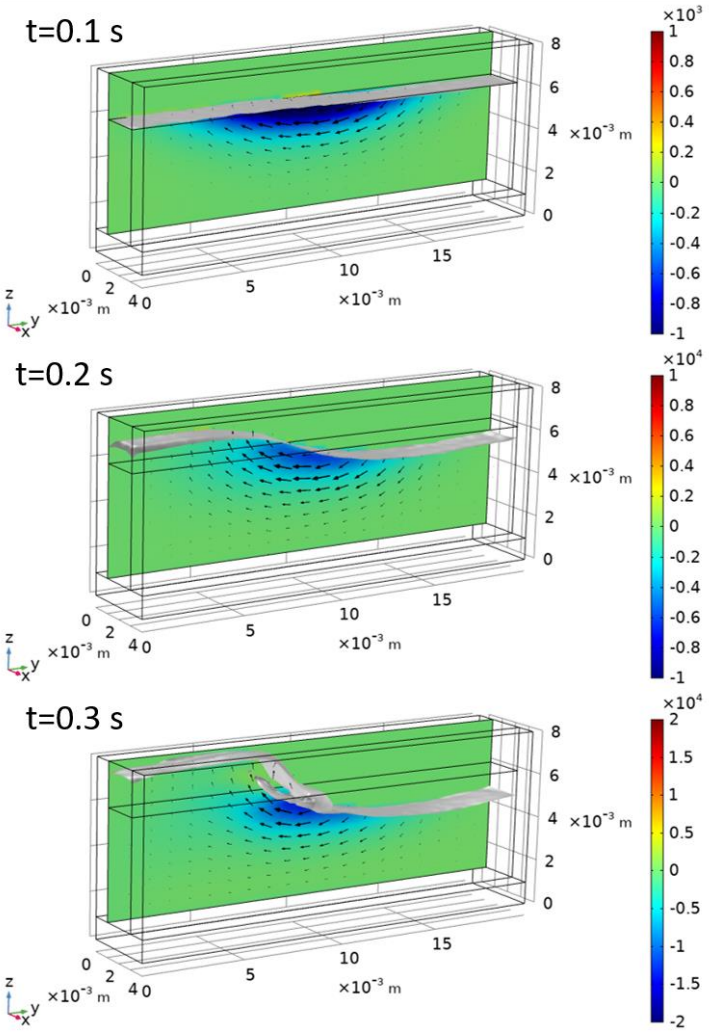

Figure 7.8 – Image series of the bounded 3-D single trench when TEMHD volume forces are enabled, showing the upstream lithium depression and downstream pileup caused by the local heat flux when there is no flow through the system. The interface isosurface is plotted in gray, the slice plots the Y component of the volume force in the lithium volume, and the arrow surface follows the total volume force. The color bar gives the Y component of the volume force in N/m^3. Note the changes in scale.

In a closed system, the volume forces are enabled, allowing TEMHD drive to move the liquid and advect the interface. The trench does not include an inlet or outlet but the image series in Figure 7.8 shows the rapid development of TEMHD driving forces that then act to depress the lithium on the upstream side of the heat stripe and raise the lithium on the downstream side. The slice shows the magnitude of the volume forces; note the change in scale for the last image in the series. The arrow volume plotted in YZ at the location of the slice shows the direction of the volume force circulating around the high heat flux region. The lithium forced downstream eventually piles up and falls back on itself, as the system is closed, but this provides a good test of the TEMHD effect with level set.

From there, a standard LiMIT trench design with the same dimensions as the fixed surface simulations was built into the level set model. See Section 4.3 for a description of this model domain. The lithium domain was set 0.5 mm above the level of the trenches, to begin with a very slight overfill condition. Simulations were run with a 0.5 mm underfill initial condition as well, though the overfill condition more accurately describes the issue with dryout exposing the underlying solid structure. It is not recommended to initialize level set interfaces in a coplanar arrangement with other boundaries, such as an exact fill case where the initial surface would lie at the same height of the trenches. This increases risk of instability and additional error in the LS physics as the solution initializes and progresses in time. Surface tension is not yet included in these simulations.

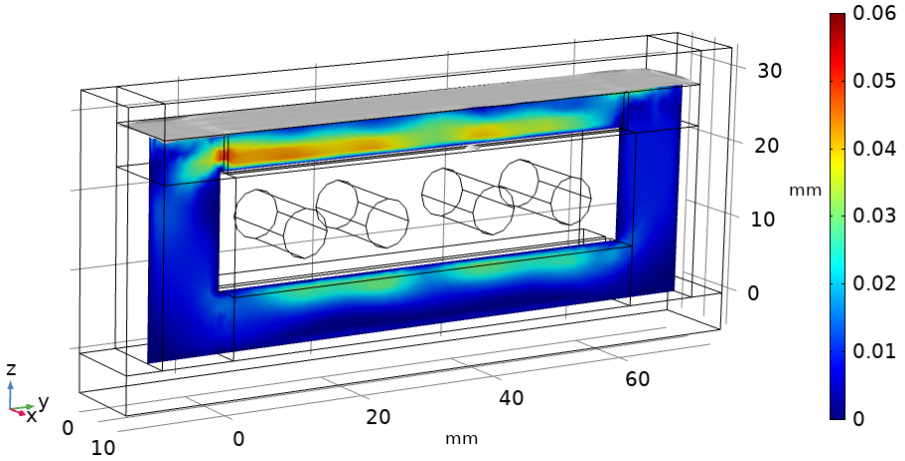

Figure 7.9 – Full 3-D LiMIT module domain with free surface TEMHD flow. This case shows flow development from module cooling, absent topside heat flux. The color bar gives velocity magnitude in m/s, and the lithium surface is plotted in gray.

Before investigating the appearance of dryout under high heat flux conditions, it is important to test for the stable development of TEMHD flow under proof of concept conditions. With only bottom side heating and cooling enabled, Figure 7.9 shows the smooth circulation of TEMHD flow through the trench module. The maximum velocity is approximately 6 cm/s, as expected for a low heat flux scenario at 0.05 T magnetic field. The temperature gradients from the cooling lines dominate the development of flow, and the higher velocities are seen toward the lower parts of the topside trenches and in the characteristic pattern along the recirculation channel from the slight additional separation between the left and right pairs of cooling lines. The surface of the lithium remains very stable over the course of the 2 second simulation time, signifying smooth, effective TEMHD flow.

7.3.1 Dryout in LiMIT Trenches

It is expected that once a high topside heat flux impinges the surface of the lithium the high local temperature gradients and thermoelectric currents will drive volume forces through the lithium domain that cause a depression in the lithium surface, exposing the underlying trenches and causing dryout. A more thorough description of the development of the dryout phenomenon is provided in Chapter 3. With the free surface TEMHD model displaying effective lithium flow in the simulation domain, the next step is applying heat to the lithium surface to mimic the divertor heat stripe or e-beam heating. This is applied using a volumetric heat source in the same way the heating is applied for the 2-D testing. In order to maintain stability and effective convergence in the solvers, the topside heat flux is ramped from 0 to 100% using a ramp function in COMSOL at a location of 0.05, a slope of 2, and smoothing over a transition zone of 0.1 at the start and end of the ramp. An analytic function then converts this to a function of time, which is multiplied by the rest of the topside heat equation as seen in Section 7.2.2. Note the center point and standard deviation values of the spatial Gaussian are adjusted to match this domain and the standard fixed surface heat flux. This serves to ramp the topside heating over the course of approximately 0.6 seconds.

The set of images in Figure 7.10 shows the response of the LiMIT trenches at increasing peak values of heat flux after 2 seconds of simulation time. Dryout formation is already apparent with the lowest peak heat flux, though the effect is minimal and the surface stays quite smooth. The low topside heat flux case drives a local velocity increase to 12 cm/s. When increasing the peak heat flux to 1×10^6 MW/m^2, the topside high velocity flow increases to 20 cm/s, and more rapid sustained flow exists throughout the trench regions and recirculation channels. Dryout becomes pronounced at this level, clearly exposing over 1 cm of trench tops near the heat stripe.

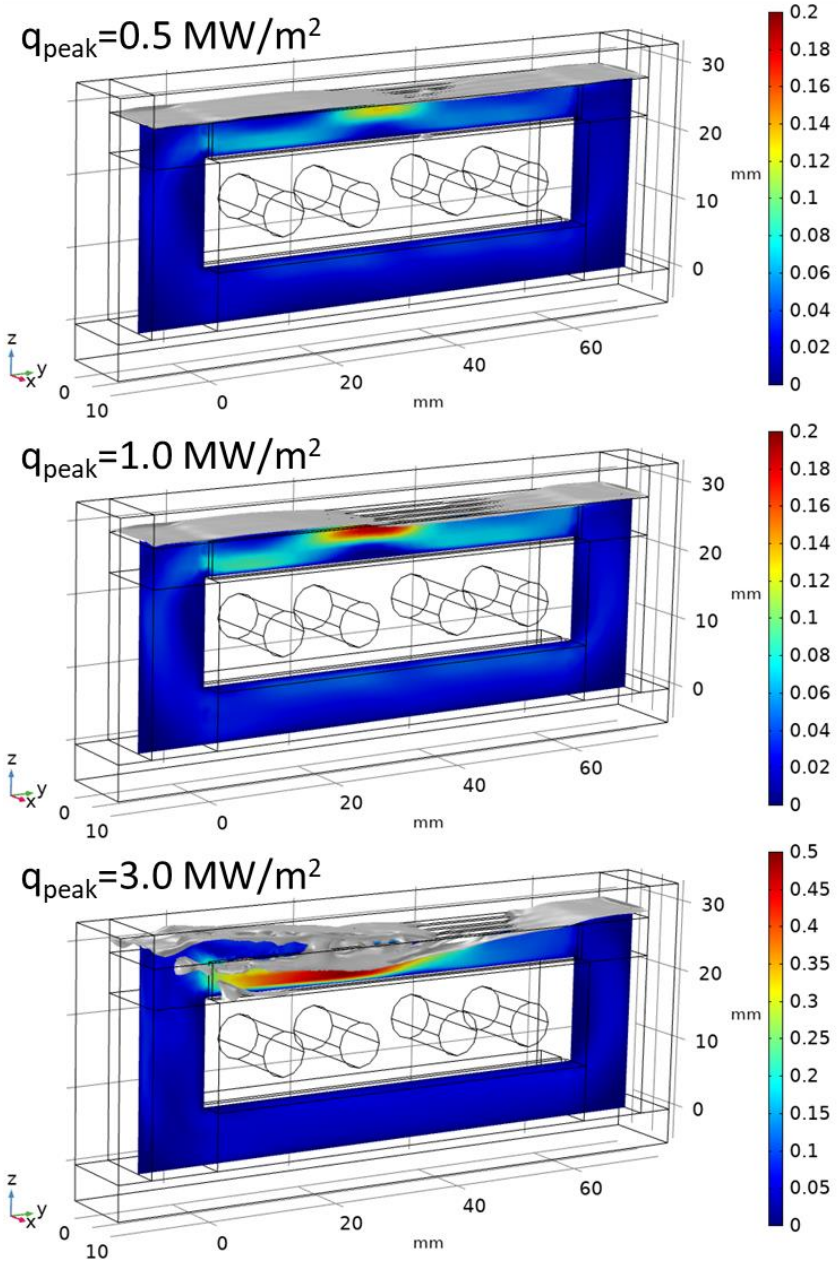

Figure 7.10 – Images of free surface dryout in LiMIT trenches for increasing peak topside heat fluxes. The lithium surface is plotted in gray, and the color bar gives velocity magnitude in m/s. Note the change in scale for the final image.

At the highest heat flux shown here, the dryout and pileup exhibit much larger turbulence. The high velocity lithium accelerated by the heat stripe enhances pileup downstream, resulting in a hydraulic jump condition that causes wave cresting and swirling flow. The scale was changed here to capture the velocity profile, showing maximum TEMHD velocities of 50 cm/s under the dryout depression. This behavior displays impressive agreement with the experimental behavior seen in high heat flux LiMIT testing as well as the Magnum-PSI dryout example at 3×10^6 MW/m^2.

However, these test cases do not include surface tension, which is expected to stabilize the lithium surface. It seems that in the trench case, the lack of surface tension happens to result in a similar flow profile as the poor recirculation system in the Magnum-PSI module. While these are separate effects, the resultant dryout is quite similar.

7.3.2 Dryout Resistance in Posts and Foams

To investigate the base dryout mitigation ability of the advanced TEMHD geometries, case B_p and case C_f (see Chapter 5 and Chapter 6 for naming conventions) were built into the level set model. The highest heat flux case presented in the previous section, 3×10^6 MW/m^2, was applied to the post and foam geometry. The velocity profile and surface contours are plotted in Figure 7.11.

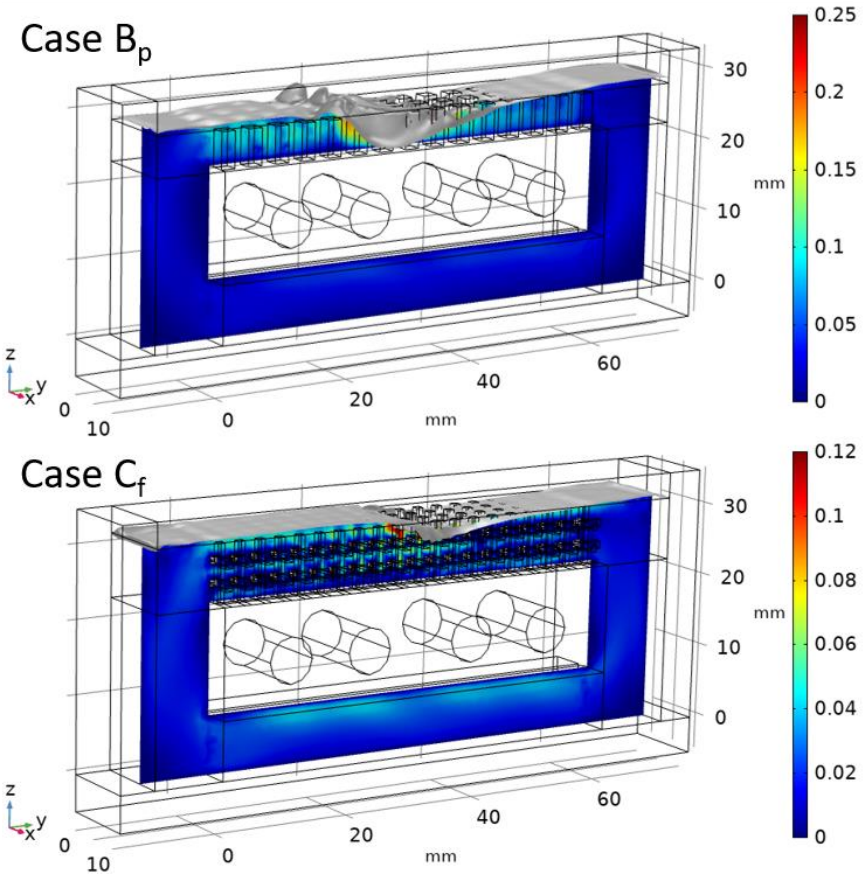

Figure 7.11 – Free surface TEMHD circulation and dryout resistance in post case B_p and foam case C_f. The lithium surface is plotted in gray, and the color bar gives velocity magnitude in m/s.

Even in this base case with no surface tension, the adjustment of the standard LiMIT trench to 2 and 3 dimensions of flow channels starts to mitigate the dryout effect. The post geometry still exhibits some chaotic wave motion, dryout and pileup, but the effect is less widespread than in the standard trenches. The addition of the secondary flow channels allows for crosstalk and slows the flow overall, lowering the maximum velocities near the dryout depression to 25 cm/s. This is slightly lower than expected velocity maximums predicted by the fixed surface post models. While steady dryout is expected to increase lithium velocities above fixed surface predictions due to the lowered flow area, the effect is more nuanced once the dryout and pileup effects begin interacting. When there is a hydraulic jump and the wave starts to progress back toward the central heat stripe dryout, velocity magnitude can decrease due to enhanced turbulence and swirling. This is what is seen here. In comparison to the trenches, the pileup effect does not rapidly propagate to the edge of the module and the dryout depression does not cause widespread hydraulic jump conditions. This maybe happening close to the heat stripe location in the area of highest disturbance, but the post design localizes the effect.

The trench geometry further mitigates dryout through the structure alone, while maintaining steady TEMHD circulation through the module. Most of the surface remains stable, and dryout is localized to just upstream of the heat stripe. Dryout progression is halted by the first horizontal layer in the foam structure, both by the presence of material there and by the additional thermoelectric currents and volume forces that develop from these structures (see Chapter 6 for further discussion on these unique profiles). The flow resistance in the foam lowers maximum surface velocity to 12 cm/s. This matches the expected maximum velocities predicted by the fixed surface models. It is expected that as dryout is reduced, the mobile surface effects in changing velocity profiles should be reduced, which is supported by these results.

7.3.3 Effects of Surface Tension

The effects of surface tension are notoriously difficult to accurately capture in multiphase CFD modeling. The large forces or energies that result from the inclusion of surface tension naturally reside on the interface, creating sharp gradients at the fluid boundaries that are liable to cause solution errors and reduce convergence and interface reconstruction accuracy. As a result, multiphase modeling of high surface tension fluids with methods that allow for topology change

is essentially never attempted. Literature on modeling 'high' surface tensions sometimes do not even reach the value of air-water surface tension, 0.072 N/m, and instead focus on values orders of magnitude lower [111]. In these and similar studies, standard droplet breakup, droplet coalition, and droplet splash benchmark simulations aim to very finely reproduce the shape of the surface. Studies of wetting angle and reproduction of droplet pinching in contact with surfaces are also common applications. It is very difficult to locate attempts to model bulk flow systems that include surface tension, let alone with a surface tension coefficient approximately 5 times greater than the air-water value. As a liquid in the temperature ranges typical for PFC operation, the lithium-air/lithium-vacuum surface tension is reported to be between 0.3 N/m and 0.4 N/m [112].

In COMSOL multiphase modeling, the brief discussion at the beginning of the chapter still applies. Phase field models achieve more accurate surface curvature than level set methods in surface tension scenarios, level set outperforms phase field in bulk flow cases. It is expected that including high surface tensions in these models will inject large sources of error. However, the high surface tension of lithium is part of what allows lithium to be an effective PFC material, and a large part of the expected improvements of these advanced TEMHD geometries. Therefore, an attempt is made to improve the free surface modeling by including surface tension.

COMSOL includes surface tension in the LF/LS coupling via the $\boldsymbol{F}_{st}$ source term in the incompressible Navier Stokes equations. This force is defined as

$$\boldsymbol{F}_{st} = \sigma\delta\kappa\boldsymbol{n} + \delta\nabla_s\sigma$$

Where σ is the surface tension coefficient (it is indeed regrettable that COMSOL uses sigma to represent both surface tension and electrical conductivity), δ is the delta function approximation over the interface given in Section 7.2.2, and $\boldsymbol{n}$ is the vector normal to the interface. The curvature κ is defined by

$$\kappa = -\nabla \cdot \boldsymbol{n}$$

The surface gradient operator ∇_s is defined by

$$\nabla_s = (\boldsymbol{I} - \boldsymbol{n}\boldsymbol{n}^T)\nabla$$

Where $\boldsymbol{I}$ is the identity matrix. The surface tension coefficient is included in the two-phase flow, level set multiphysics settings window, where either predefined values for a range of materials can be included or the user can define a specific value. For the following results, mesh and solver adjustments allowed for solutions to converge up to at least 0.3 N/m, and the values presented are 0.072 N/m (water-air), 0.15 N/m, and 0.3 N/m. All simulations were run with the 3×10^6 MW/m^2 peak heat flux.

As seen in Figure 7.12, the inclusion of surface tension has an immediate effect on the flow profile of the post geometry under high heat flux. At the 0.072 N/m case, the lithium surface is already much steadier than the no surface tension case. Dryout is drastically reduced, and while pileup is visible, the interaction between the dryout and pileup effects is minimized, which mitigates the hydraulic jump condition seen in the previous section. Maximum lithium velocities remain approximately 25 cm/s under the heat stripe, which is lower but close to the predicted fixed surface velocities. As surface tension is increased, dryout and pileup is reduced in the 0.15 N/m case and eliminated in the 0.3 N/m case. At the highest surface tension value, growing effects of spurious wave motion are visible, but the dryout effect under the high heat flux zone is gone, while lithium acceleration in that region remains. This signifies effective dryout reduction in the post geometry.

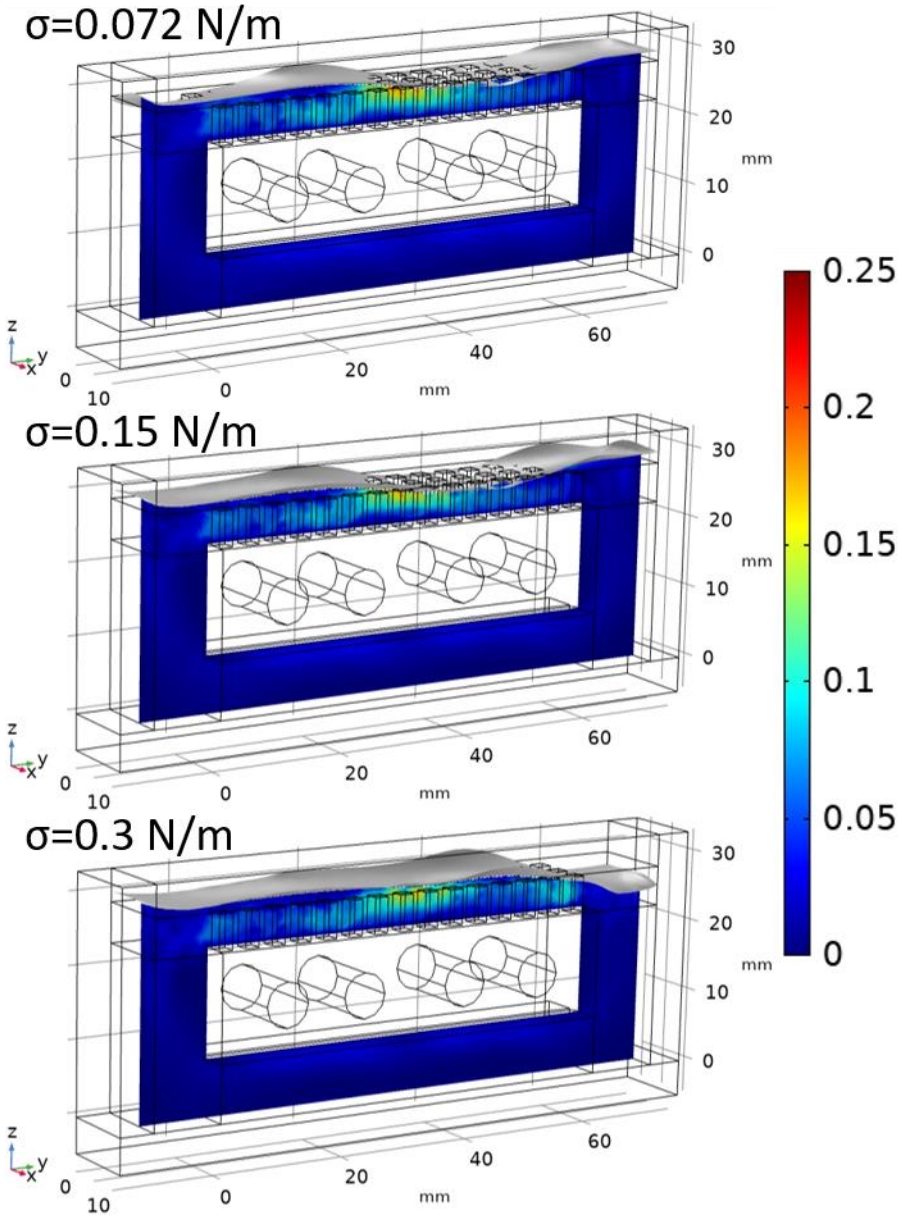

Figure 7.12 – Increasing surface tension in the post B_p case eliminates observed dryout in a simulation with a 3 MW/m^2 peak topside heat flux. The lithium surface is plotted in gray, and the color bar gives velocity magnitude in m/s.

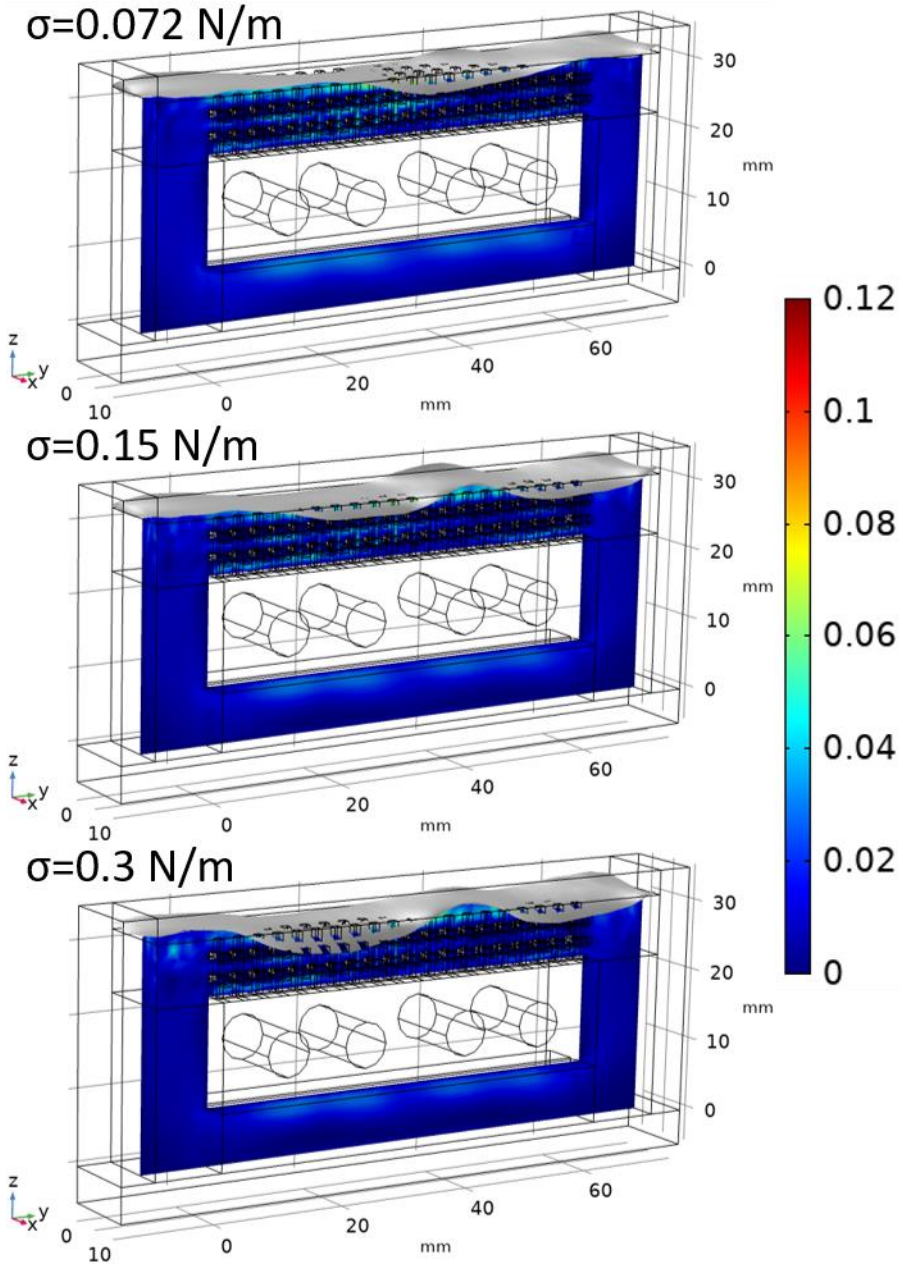

Figure 7.13 – Increasing surface tension in the foam C_f case eliminates observed dryout in a simulation with a 3 MW/m^2 peak topside heat flux but increases spurious wave motion due to large surface forces. The lithium surface is plotted in gray, and the color bar gives velocity magnitude in m/s.

The foam structure, depicted in Figure 7.13, also shows impressive reduction in dryout magnitude in the 0.072 N/m surface tension test. Dryout mitigation is better than the post design, as expected. By the 0.15 N/m case, the direct dryout and pileup effects caused by the high local heat flux are completely eliminated. However, at this value and the 0.3 N/m case, the development of spurious waves due to the large surface tension forces is more pronounced than in the post

geometry. These wave forms develop as the simulation begins, and slowly grow over the course of the simulation. Dryout and pileup effects, when present, begin to dominate as the heat flux is ramped from 0 over the first 0.6 seconds of simulation time. The reduction and elimination of the dryout phenomenon can therefore still be concluded via these simulations, as the location and development of the lithium depression and pileup differ from the wave effects. Unfortunately, the default discretization of the laminar flow interface (first order) and level set method (linear) means the addition of large surface forces is liable to instill dispersion error and create spurious waves as seen in the high surface tension cases. Improvements to interfacial stability can likely result from either an increase in the LF and LS discretization to P2+P2 and quadratic, respectively or additional mesh refinement via global mesh improvements or adaptive mesh refinement along the interface. Both methods have the potential to drastically increase solution times, but improved surface accuracy should result.

CHAPTER 8 – CONCLUSIONS AND FUTURE WORK

The successful harnessing of nuclear fusion has the potential to significantly change the world for the better, providing nearly limitless amounts of clean energy with very limited waste products. In order to achieve and sustain fusion energy production, fusion technologies must overcome nuclear repulsion forces by heating hydrogenic fuel species to extremely high temperatures and confining these energetic species in a dense environment. At these temperatures, the fuel species become ionized and exist as a plasma, allowing electric and magnetic fields to govern the motion of the particles. The most promising methods for developing fusion energy production rely on toroidal confinement of the fusing plasma, which theoretically traps particle motion along field lines that never end as they circle the device. In practice, particle drifts and the nuances of plasma physics in a toroidal configuration lead to instabilities and disruptions that lessen confinement and send hot plasma out toward the walls. Additionally, there is a need to exhaust reaction products and fuel species, so plasmas are diverted toward regions of the device where pumping can occur. These practical considerations coupled with the extreme environments in fusion devices lead to rigorous requirements for plasma facing components, with the most robust materials exhibiting melt damage, radiation embrittlement, nanostructure formation, and enhanced surface erosion.

Liquid metal PFCs have been proposed as systems that can mitigate many of the concerns inherent to solid materials. Liquid lithium specifically has shown amazing benefits to plasma operation along with providing a surface that is highly resistant to damage. These benefits are summarized in Chapter 1. While there are several potential methods for liquid lithium inclusion in PFCs, as described in Chapter 1, the CPMI has pioneered a free surface, medium-flow system known as LiMIT. The LiMIT design utilizes the power of TEMHD to harness the heat and magnetic fields already present in fusion devices to passively drive liquid lithium flow through a series of trenches. This system, described in more detail in Chapter 2, has undergone extensive testing at the CPMI at UIUC as well as in larger devices around the world.

Several concerns have been raised by the fusion community regarding the efficacy of free surface liquid metal flow concepts, namely surface stability, wetting control, fuel retention, and heat flux handling. Research at the CPMI has methodically addressed the first three of these

concerns, as described in Chapter 2. The fourth main concern with the LiMIT system is heat flux handling, especially the transient phenomenon of lithium dryout. When struck with a large localized heat flux, ideal unidirectional TEMHD forces are disrupted due to highly local temperature gradients. The additional forces act to depress the lithium surface under the high heat flux region, exposing the underlying solid material and risking material damage. The large lithium acceleration in the high heat flux zone increases the removal rate of lithium from the most sensitive areas. The thermal gradients downstream of the heat stripe, coupled with the high velocity lithium flow, lead to lithium pileup that can result in drainage issues, spilling, or droplet ejection as the bulk surface becomes untethered from the solid structure.

This work uses a multifaceted approach to tackle the issue of heat flux handling in a LiMIT-style system. Through the modeling, design, development, and experimentation of advanced TEMHD geometries, a better understanding of the dryout phenomenon and its mitigation is gained. Major achievements and conclusions are summarized below. For further discussion and conclusions regarding specific topics, continue to the following sections.

- Increasing the dimensionality of the standard LiMIT concept from the initial 1-D trench system to 2-D post TEMHD and 3-D foam TEMHD maintains strong sustained propensity for flow and improves the viability of the system by reducing isolation between primary flow channels. This is seen in modeling and experiments.
- Dryout risk is best characterized as an interplay between Y (primary flow) and Z (depression and pileup) forces. Minimizing peaking in the volume forces and maximizing the ratio of Y to Z forces yields the best dryout resistance
- Time-dependent, fixed surface COMSOL multiphysics modeling of the post and foam geometries yields a wealth of information on flow development and dryout resistance. Based on the consideration of all metrics, including heat flux response, magnetic field response, and heat transfer efficiency, B_p is suggested as the most effective post design and C_f is put forward as the best foam design out of the designs considered.
- The arsenal of multiphysics modeling capabilities is greatly expanded via the development of a CT-scan-to-computational-model pipeline that can be used for

any arbitrary surface structures, as well as the successful creation of free surface TEMHD modeling using the level set method that can include the surface tension of the liquid lithium.

- The free surface modeling with surface tension shows dryout mitigation in the post and foam designs, and is especially important for further investigation of surface stability in the face of plasma impulse and heat flux impingement
- Experimental electron beam testing of all 3 foam designs on the tri-fold foam plate successfully improved the operating window for a LiMIT style device by 127%, from 3 MW/m^2 peak heat flux to 6.8 MW/m^2, with no material damage and no signs of surface depression or dryout. This displays the reliability of the advanced TEMHD geometries and suggests viability at much larger peak heat fluxes, readying the system for the next generation of large-scale fusion devices.

8.1 Post TEMHD

Chapter 5 examines the propensity for TEMHD flow through arrays of posts, expanding the single dimension of the LiMIT trench to 2-D. These designs allow for the development of TEMHD flow through primary flow channels and enable crosstalk between the flow channels. Channel crosstalk is expected to be prominent in the post designs and aid in refilling the primary flow channels hardest hit by any reduction in lithium levels. The removal of solid material to open the secondary flow channels also reduces the amount of solid structure at risk under the heat stripe while still providing an anchor for the surface tension of lithium to stabilize the surface. Three designs were considered, including

A_p – 1×1 mm posts with 2 mm separation
B_p – 2×2 mm posts with 2 mm separation
C_p – 2×2 mm posts with 4 mm separation

Modeling of the posts shows strong sustained flow through all post module designs. The presence of the posts and de-isolation of flow channels creates current density behavior that differs from trench flow. The patterned presence and lack of parallel plate TEMHD drive structure leads to current dispersal and swirling that leads to eddy creation in the flow. The secondary flow channels also aid in eddy formation. The flow swirling presents a much more complicated picture

of temp gradients, and therefore current, as rapidly heated lithium travels around the posts. The existence of the high velocity lithium depression in the models suggests dryout may still become an issue for the post geometries, though this seems more pronounced in transient startup.

As topside peak heat flux is increased, the posts show similar increasing velocity profiles, reaching maximum velocities greater than 0.9 m/s. As magnetic field is increased, topside maximum velocities become decoupled from the expected trends due to the dominance of the thermoelectric driving force. Average velocities through the topside domain and the recirculation channels offer expected decreases in velocity as magnetic field increases. The post designs offer impressive heat transfer capabilities, with the potential to remove large amounts of heat from the surface. One shortcoming of the fixed surface models is the exact fill scenario studied here does not account for the presence of lithium on the top surface of the post structures, inflating topside maximum temperatures. In practical applications there will always be a thin layer of wetted lithium covering the post surface or a thin level of overfill, even in cases when light to moderate dryout occurs. This lithium will drastically improve conduction of heat to the bulk, helping cool the tops of the solid structures.

Proof of concept experimental testing of the posts shows impressive agreement between modeled velocities and experimental velocities determined through PIV. The response of the thermocouples placed through the system provide a reliable indicator of flow circulation between the topside structures and the recirculation channels. While the pulse-to-pulse initial conditions are variable enough to any differences due to the magnetic field, especially because the range tested sits right at the TEMHD velocity peak, it may be possible to utilize a temperature-based technique to quantify flow with larger testing ranges and higher resolution. Extensive crosstalk is observed through the secondary channels, providing ample evidence that the addition of these channels will aid in flow distribution in larger scale testing.

8.2 Foam TEMHD

In Chapter 6, the foam TEMHD system extends the basic LiMIT concept another step, to include 3 dimensions of potential flow channels. While TEMHD drive is expected to be lower in these designs due to the smaller structure sizes, the bulk temperature gradients through the structure still work to drive TEMHD in one predominant direction. The foam concept attempts to

combine the benefits of both LiMIT and CPS systems, enhancing capillary action to stabilize the surface in the face of high heat flux while maintaining steady TEMHD flow with the large pores.

The disordered foam system was based on the development of randomized large pore foams by Ultramet. These SiC base foams are coated in tungsten using CVD/PECVD methods. Since the randomized structure of the disordered foam is nearly impossible to build in a modeling software, a new modeling pipeline was developed. This procedure can be used for investigating the TEMHD flow propensity in any arbitrary design, provided it can be scanned using CT imaging. Using these methods, the disordered foam is shown to display significant propensity for TEMHD flow, though current densities and volume forces are lower than the post cases. While fewer direct results from this modeling setup are presented here, this pipeline is an important improvement for use in future design where CAD representations of the geometries are difficult to create.

Unfortunately, the disordered foam did not live up to the hype in experimental testing. The lack of thermal contact between the foam and the base module proved to be a major hindrance for lithium loading and wetting, with very slow uptake in the large pore foam. It may be possible to improve this issue by 3-D printing a foam that melds into a solid baseplate, which is a capability advertised by Ultramet. As it stands, the most important showstopper for the disordered foam is its lack of compatibility with liquid lithium. In the face of prolonged exposure (greater than 1 hour), any break in the metallic coating allows lithium ingress to the SiC base structure, resulting in disintegration of the foam. While the foam blocks were mechanically stable overall, the breakage of a few single strands was not uncommon, and this is enough to quickly destabilize the foam. While it may be possible to fully metallize the disordered foam structure, and this is an exciting avenue for future study, the investigation of the disordered foams was necessarily abandoned in this work.

Moving forward, the foray into ordered foam TEMHD proved much more successful. These designs are built from an ordered cubic structure. The designs studied are

A_f – 0.5×0.5 mm structures with 3 mm gaps
B_f – 1×1 mm structures with 3 mm gaps
C_f – 1×1 mm structures with 2 mm gaps

Modeling of the foams shows unique development of thermoelectric currents and volume forces due to the thin structures placed in each main axis direction. The Y-directed elements in the gaps between the vertical elements drive the most sustained TEMHD flow in the primary flow direction. Furthermore, the X-directed elements develop current profiles that aid in fighting dryout. Taken together with the flow disruption present due to the 3-D structure, the flow profiles that develop are more resilient to the dryout effect. In the foam designs more so than the post designs, the fixed surface models present a conservative velocity profile because of the necessary neglect of surface tension which is expected to improve top surface stability. Accelerated regions of flow under the topside heat flux do not depress and propagate to the extent seen in the post designs. Overall, the foams display lower average flow due to the smaller structures and larger flow channel gaps.

As topside peak heat flux is increased, the foams exhibit expected increases in flow velocities, though at a lower magnitude than the foams and with better agreement between surface and volume maximum velocities. The dominance of the thermoelectric drive on the top surface is still apparent in the magnetic field sweep, but like the post designs the foam geometries display expected decreases in average velocity with increasing magnetic field. While increases in simulation complexity limited the simulation time of the highest heat flux test, the posts display similar heat output and slightly lower maximum surface temperatures. As mentioned in the previous section, this value is a very conservative estimate, as lithium presence above the structure, even in a thin film, will help keep temperature increase lower than these simulations suggest. Surprisingly, the foam simulations display similar pressure drops over the top of the module, though this measure is likely skewed by the large driving forces present along the top structures. The foams as a whole show a lower thermal resistance than the posts, improving this metric of heat sink efficacy.

Experimental testing shows the DMLS 3-D printing process creates a robust material that is lithium compatible. Repeated testing of the tri-fold foam plate shows mechanical stability after repeated testing and lithium cleaning cycles. Even with the large roughness that is inherent in DMLS-printed materials, the foams exhibited impressive wetting ability and wicking through the bulk. In one test, the foam plate, drew lithium up into the foam, lowered the surrounding lithium level, and maintained a stable wetted surface against gravity, showing enhanced capillary action.

Proof of concept testing displayed sustained lithium flow through the bulk, with the temperature response signifying effective mixing and recirculation of bulk lithium. Velocity magnitudes match numerical modeling of the proof of concept magnetic fields quite well, with some discrepancy due to the lower resolution of the imaging setup and the presence of all 3 foam designs allowing effective decoupling of the surface motion.

High heat flux testing with the SLiDE e-beam produced some of the most important results. To a lesser extent, it first showed restart of an open surface PFC is doable, within the bounds of the conditions that happened to be experienced by the filled module. While no conclusive study has yet been performed, this first step is significant for eventual long-term operation. More importantly, the e-beam testing expanded the tested viability limit a LiMIT-style open surface PFC system to 6.8 MW/m^2, a 127% increase from the 3 MW/m^2 failure case observed in Magnum-PSI testing. This line comes from current limits of the e-beam components, not from system failure. The stability of the surface was closely observed in the case A_f foam and no indication of lithium dryout or structural damage in the solid was seen, indicating the dryout mitigation of the foam TEMHD system extends well beyond this tested value.

8.3 Free Surface TEMHD Modeling

While fixed surface simulations provide a reliable numerical representation of the physics that develops TEMHD flow, the response of the surface of transient effects is negated. The behavior of the free surface is especially important in the case of highly transient effects, such as the application of extreme localized heat fluxes that lead to dryout and pileup of the topside lithium. The simulations presented in Chapter 7 showcase a new addition to modeling capabilities for the simulation of TEMHD flow in liquid lithium PFCs. The development of true free surface flow models using the level set method further validates the physics basis of the TEMHD models used to inform design decisions. The transient phenomenon of dryout development matches what is seen in experiments and implied in fixed surface modeling. In initial testing without the inclusion of surface tension, the case B_p post and case C_f foam design shows reduction in dryout magnitude in comparison to standard LiMIT trenches.

Large surface tension values are generally very difficult for fluid solvers to include, due to the large surface forces at play. After adjusting the mesh and solver settings, the COMSOL level

set method was able to find stable solutions including surface tension coefficients up to 0.3 N/m, very close to the accepted value of liquid lithium at PFC temperatures. The inclusion of surface tension leads to immediate and extensive dryout reduction in the advanced geometries studied here, with the foam geometry exhibiting no characteristic dryout depression. Unfortunately, the surface also exhibits spurious wave motion due to instability in handling the large surface forces. Refinement of the mesh at interface could help this issue, and COMSOL includes the possibility of using adaptive mesh refinement to localize the improvement of mesh quality around the interface. The spurious waves could also likely be reduced by increasing the discretization of the level set and laminar flow modules. The additional computational complexity of these potential solutions will likely drastically increase computation time.

An additional limitation of the model is seen in the heat deposition method. The current adaptation uses the fluid interface to locate regions of heat deposition. If dryout occurs, the heat flux does not continue impinging the solid structure, reducing the applicability of thermal damage studies.

8.4 General Considerations

There are several geometry independent considerations that should be mentioned. These designs all show sustained TEMHD flow, and a major benefit to these systems is that they exhibit dryout reduction throughout the structure. Unlike potential trench shaping solutions, these geometries do not need to be tailored to specific plasma shapes or operating conditions and can be machined along any surface. It is possible to fine tune the system with some tailoring, such as adjusting the size, shape, or spacing of posts or foam in broad areas expected to have the potential to experience high heat flux. In other areas, constraints can ease. These adaptations allow for better control of the flow profile throughout the PFC surface, improving ultimate efficiency.

Machinability should move to the forefront as an important design consideration moving forward. As it stands, machinability is an advantage for the post geometries, as EDM machining is simple and rapid, while DMLS is slow and requires careful design to ensure supports are not placed within the flow channels. However, most potential design changes as discussed in the future work section diminish this advantage. It should still be possible to mill the trench geometries, but the complexity and required time increases drastically. It may quickly be more

cost effective to resort to DMLS or other additive manufacturing methods to produce both post and foam designs. For large scale application, casting remains in play as a manufacturing option for the posts, but research and development efforts will be required to focus on additive manufacturing.

In this work, both simulations and experiments present a conservative case for heat transfer due to the use of stainless steel. Large scale testing will likely use molybdenum, TZM, or tungsten, so thermal conductivity will improve tenfold. For the simulations, the initial condition of 0 velocity is a conservative setup since the no-flow start condition allows the topside heat flux to dominate flow startup. This makes dryout more liable to develop. As early simulations with larger bottom heating have shown, stronger flow driving into the topside does lessen the risk for dryout. This will be the case in PFC applications, as the move to looping systems will encompass EM pumping and/or steady flow startup with latent heat before device pulsing and high heat flux operation.

8.5 Suggestions for Dryout Resistance

Overall, both modeling and experimental studies described throughout this work have shown impressive TEMHD drive through advanced LiMIT-style geometries. The post and foam systems have improved resistance to lithium dryout due to additional flow channels and enhanced capillary action. This section distills some of the most important criteria that affect flow profile development and dryout resistance in these geometries and offers suggestions for what geometries to pursue.

Through the investigation of the profiles in temperature, current density, volume force, and velocity, the dryout and pileup effects are best described via the volume forces and the interplay between Y (primary flow) and Z (depression and pileup) forces. Geometries that maximize Y force while minimizing Z forces perform the best under high heat flux impingement. The volume forces also tend to be highly peaked at the solid-liquid junction, and especially the corners of these junctions, as expected due to thermoelectric current flow. Minimizing the peaking in the volume forces and maximizing the ratio of Y to Z forces yields the best dryout resistance.

The relative strengths of the volume forces are also affected by the proportion of TEMHD driving area versus open flow channel. Post cases A_p and C_p have a 2:1 open channel to solid boundary ratio, while case B_p is 1:1. Case B_p displays better volume force ratios over time. A related measure is the post density, which affects flow resistance and therefore pressure drop. Cases A_p and C_p have equivalent open channel to solid boundary ratios, but Case A_p has a higher post density. This increases the pressure drop of the fluid moving through the foam. The effect on flow velocity is balanced by the more pronounced TEMHD volume forces. For the foam designs, this becomes a discussion of void fraction. Void fraction for the base cubic structure is 88.4% for case A_f, 72.0% for case B_f, and 58.3% for case C_f. Case C_f exhibits better volume force relationships.

Extensive metrics of system performance are plotted over the course of Chapter 5 and Chapter 6. Based on the examination of the velocity profile in the geometries, the relation of Y and Z directed volume forces is deemed to be the largest contributing factor to dryout. Overall, the foams minimize this difference, while the posts have large peaking in the Z volume force. It is still important to consider system behavior as heat flux and magnetic field are increased and investigate the heat transfer metrics. Final suggestions of optimal flow geometries out of the designs studied are given below, with notable pros and cons listed to show advantages as well as areas for future improvement in the design. Metrics that are not listed can be assumed to be roughly equivalent to other geometries.

And the awards go to:

Winner: Post Category – Case B_p – 2×2 mm posts with 2 mm separation

Pros – volume force comparison, lower difference between volume and surface maximum velocities, less eddy formation, low pressure drop

Cons – larger velocity decrease with larger B, larger thermal resistance, larger topside maximum temperature

Winner: Foam Category – Case C_f - 1×1 mm structure with 2 mm gaps

Pros – volume force comparison, lower difference between volume and surface maximum velocities, lower topside maximum temperature, lower thermal resistance

Cons – lower average velocity

Winner: Overall – Foam Designs, specifically Case C_f

While all designs studied here improve upon the standard LiMIT design, the foam designs show the largest improvements across several metrics. The foam has also demonstrated effective dryout mitigation during high topside heat flux testing.

8.6 Future Work

There are numerous avenues for continuing this work, as the development of open surface TEMHD driven PFCs continues to develop toward effective large-scale application. The study of potential post and foam designs was by no means exhaustive.

Additional Designs

Studies of heat sink efficacy have identified a multitude of potential designs. These include diamonds, cylinders ellipses, and pyramids [91], [93], [94]. Literature and initial simulations of cylinders and ellipses suggest these shapes should smooth eddy formation due to the lack of corners and perform best as heat sinks [93], [94]. Staggering the post array has shown to improve flow breakup. These changes may improve dryout resistance. A study with respect to heat sink efficiency would be warranted, including TEMHD flow propensity studies. Additional adjustments can be made to potentially improve the stability of TEMHD drive while maintaining channel crosstalk. The spacing of the posts in X and Y does not need to be equal, and the X and Y dimensions of the posts do not need to be the same. Making the posts longer in Y would enable smoother TEMHD drive over a larger portion of the topside length, and small breaks would still allow crosstalk. The eddy formation and flow swirling observed in the posts, especially case C_p, strengthens the case for elongated posts. For post designs, a staggered array of ellipses, with a radius of 1.5 to 2 mm along the primary flow direction, a radius of 0.5 to 1 mm in the secondary

flow direction, and spacing of 2 to 3 mm should improve heat transfer efficiency and reduce dryout. For the

Other potential options include topside mesh placement to mimic a small layer of CPS structures, or developing CPS trenches, posts, or foam with additive manufacturing techniques. CPS designs built with 3-D printing techniques have become quite complex and developing a base structure of microporous CPS may prove more resilient to extreme heat fluxes while still containing enough solid material to drive bulk TEMHD flow.

While the disordered foams tested here were not compatible with liquid lithium, the geometry is still a valid option for porous TEMHD. Ultramet seems capable of fully metallizing the foam structure, eliminating SiC and hopefully making the foam impervious to lithium attack. If this were the case, the disordered foam could also be melded into a metallic baseplate to drastically improve thermal contact. This has at least been used in a cylindrical arrangement to test a heat sink in fusion relevant heat fluxes, and Ultramet can manufacture plate designs as well. It would be useful to perform a more thorough study of disordered foam TEMHD flow, to compare and contrast the velocity profiles that develop and resistance to dryout.

In the cubic foam structures, the main TEMHD drive results from the Y-directed structures, which is strongest in line with the X-directed structures. The flow accelerated in this region hits the X-directed structures and splits, which aids in dryout disruption. It would be interesting to attempt to fine tune the shape of these X-directed structures into angled fins to preferentially provide additional lift to the flow against dryout.

Additional concepts for ordered foam geometries could improve machinability with respect to the cubic ordered foam. Designs incorporating diamonds, spheres, triangular prisms, and more could be built without the need for support or the corner-up build orientation that avoided supports in the cubic foam designs. This improved machinability would allow for better resolution and fewer structural defects in future foam designs. An ordered diamond mesh with 1 mm structures and 2 to 3 mm gaps could be tessellated to provide improved machinability, enhanced surface stability due to additional posts along the surface (depends on where the pattern is cut off), and sustain effective TEMHD flow with extra breakup of dryout forces.

Experimentation

Future improvements to experimental tests should focus on ways to improve the measurement of TEMHD flow. If PIV must continue to be used, adjusting lighting or camera techniques to provide better contrast between bulk lithium and impurity particles could improve particle tracking. Use of grayscale IR imaging showed promise in this respect. If contrast can be reliably improved and colors remain relatively unchanged over the test surface, computer vision techniques can be applied to identify and track the particle trajectories.

As was discussed in Chapter 6, surface flows are easily decoupled from the bulk motion due to both the nature of liquid lithium and the presence of impurities. Since the impurities float and are confined to the surface in standard operating temperature regimes, they can develop surface swirling that does not represent the motion of the bulk lithium. This makes PIV a relatively unreliable method of determining liquid lithium velocity in these applications. Surface visibility is also not guaranteed in future testing, especially in large scale devices, so better methods of flow measurement are needed. It is possible that with better temperature measurement and more accurate modeling initial conditions, the thermocouple response to flow could be used to measure velocity quantitatively. Other avenues of investigation include capacitive or resistive probes that can move in the flow or current probes to measure hall effects.

As looping systems become more common and EM pumping is used to supply and recirculate lithium, surface velocities may be of less importance. In that case, flow velocity in supply and/or return tubing can be assumed via EM pumping conditions or directly measured through a number of methods already developed for liquid metal pipe flow. As the recirculating module system transfers to loop concepts, the distribution of lithium from the inlet tubing into the structures must be studied and improved. This work is already underway.

Overall, it is important to work towards more extensive high heat flux testing, both on geometries already machined and new designs. The next experimental steps also entail large scale device testing and incorporation of the advanced TEMHD geometries into full liquid lithium loop systems.

Modeling

The goal of these models has generally been to examine the bulk flow through a LiMIT style PFC system, and while this works well and provides engineering insight, little details can get lost. Improving mesh refinement for all simulations or including adaptive mesh refinement over areas of interest as flow develops could elucidate some of these details in the flow. Examples include eddy flow development in the secondary flow channels and how that effects heat transfer or primary velocity profiles, or more accurate free surface motion and its interaction with different structures.

To more accurately model experimental conditions, there are several adjustments that can be made to the simulations. Setting up temperature gradients before 'pulsing' the magnetic field would provide more accurate comparisons to proof of concept testing. One pulse test was attempted and discussed in Chapter 5. Care must be taken to ensure the solver does not start taking time steps that are too large and jump over the sudden development of TEMHD or lose stability and diverge when these rapid changes occur. Intelligent ramping of parameters and fine tuning of solver settings is key. More accurate descriptions of large-scale testing can be achieved with magnetic field variation over the length of the system to investigate how velocity profiles will change within the device. Sweeping of the high heat flux stripe can also be included.

COMSOL includes daunting amounts of solver settings that can be refined and fine-tuned for specific applications. Examples include the damping factors for each interface, nonlinear method, pivoting perturbation in the PARDISO solver, factor in error estimate, stabilization and acceleration settings, and more. While many changes were made to the default settings, the focus was simulation convergence and solution time. A more thorough examination of solver parameters and their effects on solution convergence is warranted. In order to improve general convergence, more extensive use of parameter ramping can be included. In this work, ramping of magnetic field and surface tension was included to the effect of drastically improving solution convergence. Identifying and ramping other parameters that highly effect convergence, like topside heat flux, would be encouraged. It is probably most effective and most similar to realistic scenarios, to focus on constant ramp rate instead of ramp time (as was done here).

As simulation complexity increases and modeled conditions become more extreme, it may be apt to attempt turbulent flow modeling of the TEMHD system. This increases computational complexity, but especially in dryout scenarios the velocity profile (Reynolds number) and turbulence in the wave motion would be more accurately described by turbulent methods.

For multiphase modeling, there is a wealth of other potential modeling techniques that can be explored. While COMSOL is used for its ability to couple extra physics, codes and software such as ANSYS Fluent, OpenFOAM, and Gerris are highly optimized for solving multiphase fluid problems. These are generally VoF models, but it is useful to look into phase field and even higher order methods like coupled level set, volume of fluid. All of these methods are single fluid models, since the two-fluid model is too complex to be applicable outside of a few simple cases. However, smoothed particle hydrodynamics lies outside of these 2 frameworks. This Lagrangian method is mesh free and highly parallelizable, which lends itself well to tackling complex fluid systems like free surface flow. Additional physics kernels can be included to represent the additional requirements of TEMHD flow.

Theory

This work has displayed a highly applied approach to the modeling and experimentation. Continuation of the concepts investigated here could also be approached theoretically. The TEMHD system under high heat flux impingement is a highly transient system, in both time and spatial dimensions. This could warrant a mathematical examination of transient phenomena with relation to dryout development. A theoretical study of flow in porous media could also provide new insights into flow profiles in the foam TEMHD designs. While this field is sprawling, there have been some recent attempts to describe porous flows using fractional calculus, which could be an interesting avenue of further study.

Next Steps

As this work finds its place in the systematic improvements to the LiMIT-style liquid metal PFC concept, the next steps for development in both experiments and modeling lie in combining the multiple facets of recent work in TEMHD driven systems and extending the applicability to large scale devices. Material studies should be performed, since solid structures in fusion devices will be predominantly molybdenum, TZM, or tungsten. The effects of evaporation and vapor

shielding, surface transport, and impurity concentrations and their effects on TEMHD should be studied in more detail. Robust testing of PFC restart capabilities should be undertaken, including methods of preserving the surface during long-term atmospheric exposure, to improve applicability in future power systems.

This study has worked to tackle the heat flux handling issue of open surface PFCs. As the multitude of previous work on flowing liquid lithium PFCs comes together, the technologies will ultimately integrate into a full-scale lithium loop, complete with reservoir systems and EM pumping, wetting control, lithium filtration systems, distillation systems for recovery of fuel species, and a flowing open surface PFC geometry stable to ejection in the face of plasma impulse and unchanging in the face of fusion power heat fluxes.

REFERENCES

[1] J. P. Freidberg, *Plasma Physics and Fusion Energy*. Cambridge University Press, 2007.

[2] T. E., A. Wingen, J. G., and K. Heinz, "A Conceptual Model for the Nonlinear Dynamics of Edge-localized Modes in Tokamak Plasmas," in *Nonlinear Dynamics*, InTech, 2010.

[3] J. D. Lawson, "Some criteria for a power producing thermonuclear reactor," *Proc. Phys. Soc. Sect. B*, vol. 70, no. 1, pp. 6–10, 1957.

[4] J. D. Lindl *et al.*, "The physics basis for ignition using indirect-drive targets on the National Ignition Facility," *Physics of Plasmas*, vol. 11, no. 2. pp. 339–491, 2004.

[5] J. Ongena, R. Koch, R. Wolf, and H. Zohm, "Magnetic-confinement fusion," *Nature Physics*, vol. 12, no. 5. pp. 398–410, 2016.

[6] R. J. Goldston, "Heuristic drift-based model of the power scrape-off width in low-gas-puff H-mode tokamaks," *Nucl. Fusion*, vol. 52, no. 1, 2012.

[7] A. Herrmann *et al.*, "Stationary and transient divertor heat flux profiles and extrapolation to ITER," in *Journal of Nuclear Materials*, 2003, vol. 313–316, no. SUPPL., pp. 759–767.

[8] H. Bolt *et al.*, "Plasma facing and high heat flux materials - Needs for ITER and beyond," *J. Nucl. Mater.*, vol. 307–311, no. 1 SUPPL., pp. 43–52, 2002.

[9] "JET: The Joint European Torus," *Culham Center for Fusion Energy*. [Online]. Available: https://ccfe.ukaea.uk/research/joint-european-torus/.

[10] A. Skyman, H. Nordman, and P. I. Strand, "Particle transport in density gradient driven TE mode turbulence," *Nucl. Fusion*, vol. 52, no. 11, 2012.

[11] P. K. Shukla and J. Weiland, "Toroidal electron-temperature-gradient driven electromagnetic drift wave instability," *Phys. Lett. A*, vol. 137, no. 3, pp. 132–136, 1989.

[12] P. N. Guzdar, L. Chen, W. M. Tang, and P. H. Rutherford, "Ion-temperature-gradient instability in toroidal plasmas," *Phys. Fluids*, vol. 26, no. 3, pp. 673–677, 1983.

[13] J. M. Finn and J. F. Drake, "Magnetic curvature-drift instability," *Phys. Rev. Lett.*, vol. 53, no. 24, pp. 2308–2311, 1984.

[14] F. Wagner *et al.*, "Regime of improved confinement and high beta in neutral-beam-heated divertor discharges of the ASDEX tokamak," *Phys. Rev. Lett.*, vol. 49, no. 19, pp. 1408–1412, 1982.

[15] D. F. Valcárcel *et al.*, "The JET real-time plasma-wall load monitoring system," *Fusion Eng. Des.*, vol. 89, no. 3, pp. 243–258, Mar. 2014.

[16] G. Janeschitz *et al.*, "Divertor Design and its Integration into the ITER Machine."

[17] J. W. Coenen *et al.*, "Evolution of surface melt damage, its influence on plasma performance and prospects of recovery," *J. Nucl. Mater.*, vol. 438, no. SUPPL, 2013.

[18] G. Federici *et al.*, "Effects of ELMs and disruptions on ITER divertor armour materials," in *Journal of Nuclear Materials*, 2005, vol. 337–339, no. 1-3 SPEC. ISS., pp. 684–690.

[19] G. De Temmerman *et al.*, "Effect of high-flux H/He plasma exposure on tungsten damage due to transient heat loads," *J. Nucl. Mater.*, vol. 463, pp. 198–201, 2015.

[20] J. Knaster, A. Moeslang, and T. Muroga, "Materials research for fusion," *Nature Physics*, vol. 12, no. 5. pp. 424–434, 2016.

[21] J. Wesson, *Tokamaks*, 4th ed. New York City: Oxford University Press, 2011.

[22] A. Kallenbach *et al.*, "Impurity seeding for tokamak power exhaust: From present devices via ITER to DEMO," *Plasma Phys. Control. Fusion*, vol. 55, no. 12, pp. 124041–124051, 2013.

[23] O. I. Buzhinskij and Y. M. Semenets, "Review of in Situ Boronization in Contemporary

Tokamaks," *Fusion Technol.*, vol. 32, no. 1, pp. 1–13, 2017.
[24] R. W. Conn, R. P. Doerner, and J. Won, "Beryllium as the plasma-facing material in fusion energy systems - Experiments, evaluation, and comparison with alternative materials," *Fusion Eng. Des.*, vol. 37, no. 4, pp. 481–513, 1997.
[25] M. A. Abdou *et al.*, "On the exploration of innovative concepts for fusion chamber technology," *Fusion Eng. Des.*, vol. 54, no. 2, pp. 181–247, 2001.
[26] R. F. Mattas *et al.*, "ALPS - advanced limiter-divertor plasma-facing systems," *Fusion Eng. Des.*, vol. 49–50, pp. 127–134, 2000.
[27] J. N. Brooks *et al.*, "Overview of the ALPS program," in *Fusion Science and Technology*, 2005, vol. 47, no. 3, pp. 669–677.
[28] D. K. Mansfield *et al.*, "Observations concerning the injection of a lithium aerosol into the edge of TFTR discharges," *Nucl. Fusion*, vol. 41, no. 12, pp. 1823–1834, 2001.
[29] A. A. Tuccillo *et al.*, "Overview of the FTU results," *Nucl. Fusion*, vol. 49, no. 10, 2009.
[30] R. Majeski *et al.*, "CDX-U operation with a large area liquid lithium limiter," in *Journal of Nuclear Materials*, 2003, vol. 313–316, no. SUPPL., pp. 625–629.
[31] R. Majeski *et al.*, "Recent liquid lithium limiter experiments in CDX-U," *Nucl. Fusion*, vol. 45, no. 6, pp. 519–523, 2005.
[32] J. C. Schmitt *et al.*, "High performance discharges in the Lithium Tokamak eXperiment with liquid lithium walls," *Phys. Plasmas*, vol. 22, no. 5, 2015.
[33] H. W. Kugel *et al.*, "The effect of lithium surface coatings on plasma performance in the National Spherical Torus Experiment," *Phys. Plasmas*, vol. 15, no. 5, 2008.
[34] M. A. Jaworski, A. Khodak, and R. Kaita, "Liquid-metal plasma-facing component research on the National Spherical Torus Experiment," *Plasma Phys. Control. Fusion*, vol. 55, no. 12, 2013.
[35] R. Maingi *et al.*, "The effect of progressively increasing lithium coatings on plasma discharge characteristics, transport, edge profiles and ELM stability in the National Spherical Torus Experiment," *Nucl. Fusion*, vol. 52, no. 8, Aug. 2012.
[36] D. K. Mansfield *et al.*, "Transition to ELM-free improved H-mode by lithium deposition on NSTX graphite divertor surfaces," *J. Nucl. Mater.*, vol. 390–391, no. 1, pp. 764–767, 2009.
[37] L. R. Baylor *et al.*, "High frequency ELM pacing by pellet injection on DIII-D and implications for ITER," in *39th EPS Conference on Plasma Physics 2012, EPS 2012 and the 16th International Congress on Plasma Physics*, 2012, vol. 1.
[38] A. Bortolon *et al.*, "High frequency pacing of edge localized modes by injection of lithium granules in DIII-D H-mode discharges," *Nucl. Fusion*, vol. 56, no. 5, 2016.
[39] G. L. Jackson *et al.*, "Effect of lithium in the DIII-D SOL and plasma-facing surfaces," *J. Nucl. Mater.*, vol. 463, pp. 1160–1164, 2015.
[40] J. S. Hu *et al.*, "An overview of lithium experiments on HT-7 and EAST during 2012," in *Fusion Engineering and Design*, 2014, vol. 89, no. 12, pp. 2875–2885.
[41] J. S. Hu *et al.*, "New Steady-State Quiescent High-Confinement Plasma in an Experimental Advanced Superconducting Tokamak," 2015.
[42] P. Fiflis, M. Christenson, M. Szott, K. Kalathiparambil, and D. N. Ruzic, "Free surface stability of liquid metal plasma facing components," *Nucl. Fusion*, vol. 56, no. 10, 2016.
[43] D. Alegre, E. Oyarzabal, and F. L. Tabarés, "Micro and nano-porous materials as support of liquid metals for fusion energy," in *85th IUVSTA Workshop on Nanoporous Materials for Green Energy Conversion and Storage*, 2018.

[44] A. Vertkov *et al.*, “Technological aspects of liquid lithium limiter experiment on FTU tokamak,” *Fusion Eng. Des.*, vol. 82, no. 15–24, pp. 1627–1633, 2007.
[45] V. A. Evtikhin, A. V. Vertkov, I. E. Lyublinski, B. I. Khripunov, V. B. Petrov, and S. V. Mirnov, “Research of lithium capillary-pore systems for fusion reactor plasma facing components,” *J. Nucl. Mater.*, vol. 307–311, no. 2 SUPPL., pp. 1664–1669, Dec. 2002.
[46] R. J. Goldston, R. Myers, and J. Schwartz, “The lithium vapor box divertor,” in *Physica Scripta*, 2016, vol. 2016, no. T167.
[47] Q. Yang *et al.*, “Development of the flowing liquid lithium limiter for EAST tokamak,” *Fusion Eng. Des.*, vol. 124, pp. 179–182, Nov. 2017.
[48] J. Ren *et al.*, “First results of flowing liquid lithium limiter in HT-7,” in *Physica Scripta*, 2014, vol. T159.
[49] A. Moeslang, V. Heinzel, H. Matsui, and M. Sugimoto, “The IFMIF test facilities design,” *Fusion Eng. Des.*, vol. 81, no. 8-14 PART B, pp. 863–871, Feb. 2006.
[50] H. Nakamura *et al.*, “Latest design of liquid lithium target in IFMIF,” *Fusion Eng. Des.*, vol. 83, no. 7–9, pp. 1007–1014, Dec. 2008.
[51] E. Kolemen, M. Hvasta, R. Majeski, R. Maingi, A. Brooks, and T. Kozub, “Design of the Flowing LIquid Torus (FLIT),” *Nucl. Mater. Energy*, vol. 19, pp. 524–530, May 2019.
[52] J. A. Shercliff, “Thermoelectric magnetohydrodynamics,” *J. Fluid Mech.*, vol. 91, no. 2, pp. 231–251, 1979.
[53] S. Molokov, R. Moreau, and H. K. Moffatt, *Magnetohydrodynamics – Historical Evolution and Trends*. Springer, 2007.
[54] J. F. Osterle and S. W. Angrist, “The Thermoelectric-Hydromagnetic Pump,” *J. Heat Transfer*, vol. 86, no. 2, p. 166, 2012.
[55] M. A. Perlow and K. A. Davis, “The development of the SNAP-10 thermoelectric pump,” *Trans. Am. Nucl. Soc.*, vol. 8, p. 160, 1966.
[56] J. A. Shercliff, “Thermoelectric magnetohydrodynamics in closed containers,” *Phys. Fluids*, vol. 22, no. 4, pp. 635–640, 1979.
[57] J. A. Shercliff, “Thermoelectric MHD with walls parallel to the magnetic field,” *Int. J. Heat Mass Transf.*, vol. 23, no. 9, pp. 1219–1228, Feb. 2005.
[58] J. A. Shercliff, “The Pipe End Problem in Thermoelectric MHD,” 1980.
[59] J. Shercliff, “Thermoelectric MHD affects heat flow in liquid lithium,” *Proc. 9th Symp. Eng. …*, 1981.
[60] J. A. Shercliff, “Non-Uniqueness in Thermoelectric Magnetohydrodynamic Heat Convection,” *Proc. R. Soc. A Math. Phys. Eng. Sci.*, vol. 382, no. 1783, pp. 273–293, 1982.
[61] M. A. Jaworski, “Thermoelectric Magnetohydrodynamic and Thermocapillary Driven Flows of Liquid Conductors in Magnetic Fields,” University of Illinois at Urbana-Champaign, 2009.
[62] D. N. Ruzic, W. Xu, D. Andruczyk, and M. A. Jaworski, “Lithium-metal infused trenches (LiMIT) for heat removal in fusion devices,” *Nucl. Fusion*, vol. 51, no. 10, 2011.
[63] W. Xu, D. Curreli, D. Andruczyk, T. Mui, R. Switts, and D. N. Ruzic, “Heat transfer of TEMHD driven lithium flow in stainless steel trenches,” *J. Nucl. Mater.*, vol. 438, no. SUPPL, 2013.
[64] W. Xu, D. Curreli, and D. N. Ruzic, “Computational studies of thermoelectric MHD driven liquid lithium flow in metal trenches,” in *Fusion Engineering and Design*, 2014, vol. 89, no. 12, pp. 2868–2874.

[65] W. Xu *et al.*, “Vertical flow in the Thermoelectric Liquid Metal Plasma Facing Structures (TELS) facility at Illinois,” *J. Nucl. Mater.*, vol. 463, pp. 1181–1185, 2015.
[66] G. Z. Zuo *et al.*, “Liquid lithium surface control and its effect on plasma performance in the HT-7 tokamak,” in *Fusion Engineering and Design*, 2014, vol. 89, no. 12, pp. 2845–2852.
[67] J. Ren *et al.*, “Investigations on interactions between the flowing liquid lithium limiter and plasmas,” *Fusion Eng. Des.*, vol. 102, pp. 36–43, 2016.
[68] P. Fiflis *et al.*, “Performance of the lithium metal infused trenches in the magnum PSI linear plasma simulator,” *Nucl. Fusion*, vol. 55, no. 11, 2015.
[69] M. Szott *et al.*, “Wetting of lithium on nanostructured surfaces for first wall components,” in *Proceedings - Symposium on Fusion Engineering*, 2016, vol. 2016-May.
[70] S. Hammouti *et al.*, “Wetting of liquid lithium on fusion-relevant materials microtextured by femtosecond laser exposure,” *J. Nucl. Mater.*, vol. 508, pp. 237–248, 2018.
[71] M. Szott, “Flow Control and Associated Technologies to Advance the Application of TEMHD-Driven Liquid Lithium in Fusion Devices,” UIUC, 2016.
[72] M. Christenson, “The Design and Development of Hydrogen Isotope Extraction Technologies for a LiMIT-Style Liquid Lithium Loop,” University of Illinois at Urbana-Champaign, 2018.
[73] M. Christenson, C. Moynihan, and D. N. Ruzic, “A distillation column for hydrogen isotope removal from liquid lithium,” *Fusion Eng. Des.*, vol. 135, pp. 81–87, Oct. 2018.
[74] S. I. Krasheninnikov, L. E. Zakharov, and G. V. Pereverzev, “On lithium walls and the performance of magnetic fusion devices,” in *Physics of Plasmas*, 2003, vol. 10, no. 5 II, pp. 1678–1682.
[75] Z. Ma, Y. Nina, S. Qiu, W. Tian, and G. Su, “Application of Film Dryout Model in Liquid Metal CHF Prediction,” 2014, p. V02AT09A023.
[76] M. Jeltsov, W. Villanueva, and P. Kudinov, “Parametric Study of Sloshing Effects in the Primary System of an Isolated Lead-Cooled Fast Reactor,” *Nucl. Technol.*, vol. 190, no. 1, pp. 1–10, 2015.
[77] M. Vanderhaegen and A. Le Belguet, “A Review on Sodium Boiling Phenomena in Reactor Systems,” *Nucl. Sci. Eng.*, vol. 176, no. 2, pp. 115–137, 2014.
[78] F. J. Arias, “Critical heat flux -CHF in liquid metal in presence of a magnetic field with particular reference to fusion reactor project,” *J. Fusion Energy*, vol. 29, no. 2, pp. 146–149, 2010.
[79] V. V Buryak, A. A. Kolesnichenko, A. F. Kolesnichenko, and S. Smolentsev, “Free-surface mhd flows as a potential tool for high heat flux removal in fusion applications,” *Magnetohydrodynamics*, vol. 48, no. 4, pp. 651–666, 2012.
[80] W. Xu, “Experimental and Numerical Analysis of Thermoelectric Magnetohydrodynamic Driven Liquid Lithium Flow in Open Channels for Fusion Applications,” University of Illinois at Urbana-Champaign, 2015.
[81] M. Szott and D. N. Ruzic, “2-D moving mesh modeling of lithium dryout in open surface liquid metal flow applications,” 2020.
[82] “COMSOL Multiphysics Reference Manual, Version 4.3,” 2014.
[83] P. Fiflis, A. Press, W. Xu, D. Andruczyk, D. Curreli, and D. N. Ruzic, “Wetting properties of liquid lithium on select fusion relevant surfaces,” in *Fusion Engineering and Design*, 2014, vol. 89, no. 12, pp. 2827–2832.
[84] S. A. Krat *et al.*, “Wetting properties of liquid lithium on lithium compounds,” *Fusion*

Eng. Des., vol. 117, pp. 199–203, 2017.
[85] J. Schindelin *et al.*, "Fiji: An open-source platform for biological-image analysis," *Nature Methods*, vol. 9, no. 7. pp. 676–682, 2012.
[86] Ff. Developers, "FFmpeg." 2020.
[87] M. Szott, Z. Wang, and D. N. Ruzic, "Reconstruction and analysis of exploding wire particle trajectories via automatic calibration of stereo images," *Rev. Sci. Instrum.*, vol. 89, no. 10, p. 10K118, Oct. 2018.
[88] "COMSOL Multiphysics Reference Manual, Version 5.4," 2019.
[89] K. S. Kanekar and D. B. Meshram, "No Title," *IJRET Int. J. Res. Eng. Technol.*, 2015.
[90] A. A. Bhuiyan and A. K. M. S. Islam, "Thermal and hydraulic performance of finned-tube heat exchangers under different flow ranges: A review on modeling and experiment," *International Journal of Heat and Mass Transfer*, vol. 101. Elsevier Ltd, pp. 38–59, 01-Oct-2016.
[91] A. Mohammadi and A. Koşar, "Review on Heat and Fluid Flow in Micro Pin Fin Heat Sinks under Single-phase and Two-phase Flow Conditions," 2018.
[92] K. NAWAZ, "Metal Foams As Novel Materials For Air-Cooling Heat Exchangers," 2011.
[93] W. A. Khan, J. R. Culham, and M. M. Yovanovich, "Optimization of microchannel heat sinks using entropy generation minimization method," *IEEE Trans. Components Packag. Technol.*, vol. 32, no. 2, pp. 243–251, 2009.
[94] Z. S. Abdel-Rehim, "Optimization and thermal performance assessment of pin-fin heat sinks," *Energy Sources, Part A Recover. Util. Environ. Eff.*, vol. 31, no. 1, pp. 51–65, 2009.
[95] P. Dupuis, Y. Cormier, M. Fenech, A. Corbeil, and B. Jodoin, "Flow structure identification and analysis in fin arrays produced by cold spray additive manufacturing," *Int. J. Heat Mass Transf.*, vol. 93, pp. 301–313, Feb. 2016.
[96] D. Ansari and K. Y. Kim, "Hotspot management using a hybrid heat sink with stepped pin-fins," *Numer. Heat Transf. Part A Appl.*, vol. 75, no. 6, pp. 359–380, 2019.
[97] J. W. Coenen *et al.*, "Liquid metals as alternative solution for the power exhaust of future fusion devices: Status and perspective," in *Physica Scripta*, 2014, vol. T159.
[98] M. E. Kersh, "3D Volumetric Data to Finite Element Analysis: Applications in Musculoskeletal Biomechanics Using the Beckman Vis Lab." 2018.
[99] "Simpleware ScanIP." 2018.
[100] Protolabs, "Direct Metal Laser Sintering (DMLS)," 2020. [Online]. Available: https://www.protolabs.com/services/3d-printing/direct-metal-laser-sintering/.
[101] E. Fontes, "Modeling and Simulation of Multiphase Flow in COMSOL: Part 1," *COMSOL Blog*, 2020. [Online]. Available: https://www.comsol.com/blogs/modeling-and-simulation-of-multiphase-flow-in-comsol-part-1/.
[102] B. S. Mirjalili, S. S. Jain, and M. S. Dodd, "Interface-capturing methods for two-phase flows : An overview and recent developments," *Cent. Turbul. Res. Annu. Res. Briefs*, no. 1, pp. 117–135, 2017.
[103] S. Osher and J. A. Sethian, "Fronts propagating with curvature-dependent speed: Algorithms based on Hamilton-Jacobi formulations," *J. Comput. Phys.*, vol. 79, no. 1, pp. 12–49, Nov. 1988.
[104] M. Sussman, "A level set approach for computing solutions to incompressible two-phase flow," *J. Comput. Phys.*, vol. 114, no. 1, pp. 146–159, Sep. 1994.
[105] E. Olsson and G. Kreiss, "A conservative level set method for two phase flow," *J.*

Comput. Phys., vol. 210, no. 1, pp. 225–246, Nov. 2005.
[106] "CFD Module Users Guide -COMSOL Multiphysics v5.4," 2019.
[107] "Two Phase Flow Modeling Guidelines," *COMSOL Knowledgebase*. [Online]. Available: https://www.comsol.com/support/knowledgebase/1239.
[108] E. Fontes, "Two Methods for Modeling Free Surfaces in COMSOL Multiphysics," *COMSOL Blog*, 2018. [Online]. Available: https://www.comsol.com/blogs/two-methods-for-modeling-free-surfaces-in-comsol-multiphysics/.
[109] T.-W. Tsai *et al.*, "Selective Laser Melting of Metal Powders in Additive Manufacturing," *Avestia Publ. J. Fluid Flow, Heat Mass Transf.*, vol. 5, pp. 2368–6111, 2018.
[110] M. Courtois, M. Carin, P. Le Masson, S. Gaied, M. Balabane, and el Balabane, "A complete model of keyhole and melt pool dynamics to analyze instabilities and collapse during laser welding A com-plete model of keyhole and melt pool dynamics to analyze instabilities and collapse during laser welding A complete model of keyhole and melt pool dynamics to analyze instabilities and collapse during laser welding," *J. Laser Appl.*, vol. 26, no. 4, p. 42001, 2014.
[111] H. Z. Yuan, Z. Chen, C. Shu, Y. Wang, X. D. Niu, and S. Shu, "A free energy-based surface tension force model for simulation of multiphase flows by level-set method," *J. Comput. Phys.*, vol. 345, pp. 404–426, Sep. 2017.
[112] H. W. Dauison, "COMPILATION OF THERMOPHYSICAL PROPERTIES OF LIQUID LITHIUM."